Observational Constraints on Tropospheric Chlorine Cycling

Jessica D. Haskins

A dissertation

submitted in partial fulfillment of the

requirements for the degree of

Doctor of Philosophy

University of Washington

2020

Reading Committee:

Joel Thornton, Chair

Lyatt Jaeglé

Becky Suess

Program Authorized to Offer Degree:

Atmospheric Sciences

University of Washington

Abstract

Observational Constraints on Tropospheric Chlorine Cycling

Jessica D. Haskins

Chair of the Supervisory Committee:
Prof. Joel Thornton
Atmospheric Sciences

The multiphase photochemical cycling of chlorine has a widespread influence on the chemical composition of the troposphere, affecting climate, the oxidant budget, acid deposition to the biosphere, and the chemistry of primary and secondary pollutants such as nitrogen oxides, nitrate aerosols, and ozone. There have been relatively few observations to constrain chlorine chemistry in the troposphere, often resulting in either its exclusion from global chemistry climate models or inclusion with limited verification. This work catalogues critical constraints on tropospheric chlorine chemistry utilizing data collected in 2015 during the Wintertime Investigation of Transport, Emissions, and Reactivity (WINTER) aircraft campaign.

Using WINTER data, the contribution of various oxidants, including Cl atoms from nitryl chloride ($ClNO_2$) photolysis, on a regional basis are quantified, and I show that multiphase reactions between gas-phase NO_x reservoirs and chlorine containing aerosol particles controls

greater than 70% of the oxidizing capacity of polluted air during winter. I use observations from WINTER in a chemical box model to constrain a laboratory-based mechanism of chlorine gas (Cl_2) production from $ClNO_2$ uptake on acidic particles. To reproduce Cl_2 concentrations observed during WINTER, the model required the $ClNO_2$ reaction probability to be more than an order of magnitude lower than those determined in previous laboratory experiments on acidic surfaces. I show the availability of Cl^- and particle volume limit the efficiency of the reaction in the atmosphere, compared to the laboratory.

By 2015, when the WINTER campaign took place, strict emissions controls on NO_x and SO_2, which impact anthropogenic emissions of chlorine compounds, particle pH, and $ClNO_2$ formation, had already been enacted across the United States. Using deposition data collected from precipitation samples across the US, I show that the mean wet deposition flux of non-sea salt chloride has decreased at sites throughout the Northeastern US over a 20-year span and are well correlated with anthropogenic HCl emissions decreases, suggesting that industry emissions controls have decreased the tropospheric atmospheric Cl_y burden and implying that its impacts on the oxidant budget were larger in the past than they are today.

TABLE OF CONTENTS

List of Figures ii
List of Tables iv

Chapter 1 Introduction

1.1 Impacts of Tropospheric Chlorine Chemistry 1
1.2 History of Tropospheric Chlorine Chemistry 2
1.3 Sources of Inorganic Chlorine to The Troposphere 4
1.4 Production & Loss of HCl 5
1.5 Reactive Tropospheric Chlorine Cycling 7
1.6 Removal of Tropospheric Chlorine Compounds 15
1.7 Motivating Questions for this work 16
1.8 References 18
1.9 Figures 25

Chapter 2 Anthropogenic control over wintertime oxidation of atmospheric pollutants

2.1 Introduction 27
2.2 WINTER Field Campaign Overview 30
2.3 Measurement Methods 31
2.4 Instantaneous Radical Source Calculations 34
2.5 Daily Integrated Radical Source Calculations 35
2.6 F0AM Box Modeling 37
2.7 Results and Analysis 39
2.8 Estimates of HONO production from pNO_3^- 46
2.9 Impacts of Increased Oxidants 49
2.10 Conclusions 50
2.11 References 54
2.12 Tables 62
2.13 Figures 63

Chapter 3 Observational Constraints on the Formation of Cl_2 From the Reactive Uptake of $ClNO_2$ on Aerosols in the Polluted Marine Boundary Layer

3.1 Introduction 81
3.2 WINTER Campaign & Observations 85
3.3 Calculating Aerosol Growth Factors 86
3.4 Estimating Wet Surface Area Density from AMS mass 87
3.5 Aerosol Thermodynamics 89
3.6 Multiphase Chemical Box Model 91

3.7 Results & Discussion 93
3.8 Model Sensitivity 103
3.9 Conclusions 108
3.10 References 110
3.11 Tables 118
3.12 Figures 120

Chapter 4 Significant U.S. decreases in deposition of anthropogenic chloride from emission controls

4.1 Introduction 131
4.2 Methodology 134
4.3 Results & Discussion 137
4.4 Conclusions 153
4.5 References 157
4.6 Figures 163

Chapter 5 Conclusions

5.1 Summary of Results 171
5.2 Potential Future Research Directions 174
5.3 References 183

Appendix List of Collaborators 185

LIST OF FIGURES

Chapter 1

Figure 1.1 Summary of Proposed Cl_y impacts on Tropospheric Oxidants 25
Figure 1.2 GEOS-Chem Cl Deposition Patterns during WINTER..... 26

Chapter 2

Figure 2.1 WINTER Campaign Flights 63
Figure 2.2 WINTER Nighttime HCHO 64
Figure 2.3 Determining VOC Concentrations from CO 65
Figure 2.4 F0AM Gas Phase Concentrations..... 66
Figure 2.5 Summary of F0AM Operation..... 67
Figure 2.6 Downwind NO_x & $ClNO_2$ Evolution 68
Figure 2.7 Instantaneous Morning Estimates of $ClNO_2$ Photolysis..... 69
Figure 2.8 Contribution of Alkene Ozonolysis to Radical Budget 70
Figure 2.9 F0AM Radical Production..... 71
Figure 2.10 Mechanism for O_3, HCHO Enhancements from Cl 72
Figure 2.11 F0AM Enhancements in O_3, HCHO Production 73
Figure 2.12 Daily Integrated Oxidants from Precursors 74
Figure 2.13 Cumulative Distribution of Radical Sources 75
Figure 2.14 Daily Integrated Oxidants, Including pNO_3 Photolysis 76
Figure 2.15 pNO_3 and HONO Compared to Parameterizations 77
Figure 2.16 Impact of pNO_3^- photolysis on HNO_3 concentrations 78
Figure 2.17 Standard Emissions vs. High Oxidant Simulations 79
Figure 2.18 Changes in GEOS-Chem from Enhanced Oxidants 80

Chapter 3

Figure 3.1 Estimating Particle Surface Area from Total AMS Mass 120
Figure 3.2 Timeseries of $ClNO_2$ and Cl_2 during 3 Flights 121
Figure 3.3 Correlations between Cl_2, $ClNO_2$, and HOCl..... 122
Figure 3.4 MOSAIC Input Constraints from WINTER..... 123
Figure 3.5 MOSAIC Outputted Size Resolved pCl^- and Aerosol pH 124
Figure 3.6 Modeled Evolution of Selected Plumes 125
Figure 3.7 WINTER Constraints on φ_{Cl2} and γ_{ClNO2} 126
Figure 3.8 Multi-linear fits of Modeled $\gamma(ClNO_2)$ 127
Figure 3.9 Mechanistic Differences between Atmosphere & Lab..... 128
Figure 3.10 Determining First and Second Order Rate Coefficients 129
Figure 3.11 Time series of HOCl, Cl_2, $ClNO_2$..... 130

Chapter 4

Figure 4.1 Changes in HCl emissions and NSS Cl^- deposition 163

Figure 4.2 Total Cl^- Deposition 164
Figure 4.3 Sen's Slopes in NSS Cl^- and SO_4^{2-} 165
Figure 4.4 Regional Changes in Na^+, Cl^- and Precipitation..... 166
Figure 4.5 Determining Regional Emissions Factors 167
Figure 4.6 Predicted Changes in NSS Cl^- from HCl Emissions 168
Figure 4.7 Temporal Correlation in HCl Emissions & NSS Cl^- deposition 169

Chapter 5

Figure 5.1 Comparisons of GEOS-Chem Vertical Profiles to WINTER …….. 177

LIST OF TABLES

Chapter 2

Table 2.1 Summary of WINTER Observations Used..... 62

Chapter 3

Table 3.1 Reactions & Rate Constants included in 0-D Box Model. 118
Table 3.2 Summary of Box Model Results & Corresponding Observations..... 119

ACKNOWLEDGEMENTS

First and foremost, I would like to thank my advisors, Joel Thornton and Lyatt Jaeglé who patiently guided me through this part of my journey to become a scientist. Working with Joel has taught me to always question the integrity of measurement methodologies, the relevancy of results to big picture questions, and to never underestimate the value of explaining science simply. Conversely, working with Lyatt has taught me to pay attention to details in experiment design, data presentation, and quantitative methodologies. Having heard countless horror stories of being a co-advised graduate student, I am deeply thankful for their enthusiastic cooperation.

I am grateful to the former and current members of the Thornton, Jaeglé, and Alexander groups that I had the privilege to work with including Felipe Lopez-Hilifiker, Viral Shah, Qiaoyun Peng, Shuting Zhai, Lexie Goldberger, Carly Fredrickson, Phil Rund, Jiayue Huang, Brett Palm, and Cassandra Gaston, many of whom collected the data that I have been fortunate to use herein. I'm particularly thankful to our Postdoc turned Research Scientist, Ben Lee, for answering every dumb question I never took to Joel and I will be forever thankful to Emma D'Ambro for making our office an enjoyable place to be and for her support at every science meeting we went to together. I would also like to thank Hannah Horowitz for her friendship, mentorship, and support of my research and career beyond UW.

To all the exceptional teachers and mentors that helped me see the world beyond middle Georgia, thank you. I would never have found my passion for Atmospheric Chemistry if it were not for Mrs. Perkins encouraging me to pursue my 7th grade project on the "harmful effects of auto emissions and how to prevent them", Coach Groeper's Chemistry class, and the Georgia Governor's Honors Program. I am extremely thankful to Susan Solomon for enthusiastically mentoring me at MIT, for instilling in me optimism for our environment, and for helping me decide where to apply for graduate school.

Finally, I would like to thank my family and friends. I would never have found my home in Seattle if it weren't for my brass band, the Filthy FemCorps, who aggressively reinforced the idea that that no matter what age you are, it's never too late to try something new. Thanks to my Dad, brother, and Michael for really making me find the simplest way to explain science. Special thanks to my fiancé, who always propped me up when I lacked motivation. And thanks to my Mom, who found the strength to let me move across the country to pursue this dream, and who never stopped showing me that she loved and supported me.

Chapter 1

Introduction

1.1 Impacts of Tropospheric Chlorine Chemistry

The multiphase photochemical cycling of chlorine has a widespread influence on the chemical composition of the atmosphere, affecting climate, the stratospheric ozone layer, and air quality. However, it has only been within the last 30 years that the realization of the extent to which chlorine chemistry within the troposphere can impact the oxidant budget, acid deposition to the biosphere, and the chemistry of primary and secondary pollutants, has come about. The broad influence of chlorine chemistry on air quality and climate stems from the high reactivity of chlorine atoms (Cl) with most volatile organic compounds (VOC) relative to the hydroxyl radical (OH) [Simpson et al., 2015]. The reaction rate of methane (CH_4) with Cl is roughly 14 times faster than its reaction rate with OH [Sander et al., 2006]. Although the global abundance of Cl is much less than that of OH, in part because of this difference in reaction rate, reactions of Cl with methane are estimated to be nearly 1% of the total methane sink [Wang et al., 2019]. Therefore, Cl atoms play an important role in controlling the lifetime of this greenhouse gas [Atkinson, 1997]. Cl atoms also have faster rate constants than OH for reactions with other VOC, with potential impacts on secondary organic aerosols (SOA) production, and ozone (O_3) formation. Sherwen et al. (2016) suggested that the oxidation of VOCs like ethane, acetone and propane by Cl atoms can be globally significant accounting for ~15-27% of their loss. Cl atoms can also serve as an oxidizer for other environmentally relevant compounds such as dimethyl sulfide [Chen et al., 2017; Hoffmann et al., 2016], and mercury [Horowitz et al., 2017]. However, the

abundances of Cl atoms within the troposphere and its precursors are poorly known, and the mechanisms responsible for the oxidation of chloride to more reactive forms (Cl, ClO, Cl_2, BrCl, HOCl, $ClNO_2$, etc.; collectively referred to as Cl^*) are incompletely understood.

With connections to the rapid cycling of hydrogen oxides ($HO_x \equiv OH + HO_2$) and nitrogen oxides ($NO_x \equiv NO + NO_2$), the cycling of reactive chlorine Cl* within the troposphere can have competing impacts on local and downwind air quality (**Figure 1.1**). The dominant fate of Cl atoms depends on the availability of non-methane hydrocarbons (NMHC). In remote regions, its estimated that 46% of Cl atoms react with methane (Wang et al., 2019), the remaining fraction react with O_3. As NO_x is low, the fate of CH_3O_2 is to react with HO_2, leading to a net sink of O_3 and HO_x. In polluted regions, with higher concentrations of NMHC, reactions of Cl atoms with NMHC are more competitive, accounting for an estimated 20% of the global loss for ethane [Wang et al., (2019)], and with less available to react with O_3. Higher NO_x in these regions lead to rapid propagation of the corresponding RO_2 into HO_2 and OH, thereby increasing HO_x and net O_3 production. Without observational constraints on the abundance of Cl*, its relative cycling, and formation pathways, it has, historically, been difficult to fully assess the impacts of reactive chlorine on tropospheric chemistry and climate, given these competing pathways.

1.2 History of Tropospheric Chlorine Chemistry

The first direct observations of elevated chlorine species in tropospheric coastal air were published in 1993 via mist chamber measurements [Pszenny et al., 1993]and in 1998 via mass spectrometry [Spicer et al., 1998]. Only as recently as 1996, the first modeling studies [Vogt et al., 1996], based upon these measurements indicated that the marine boundary layer (MBL) was

impacted by reactive halogens. Since then rapid advances in measurement technologies have occurred, allowing direct simultaneous measurements of various chlorine compounds via Chemical Ionization Mass Spectrometry (CIMS), [Kercher et al., 2009]. The deployment of this instrument at various ground, aircraft, and ship based campaigns has occurred in the 11 years since [Crisp et al., 2014; Riedel et al., 2014; Young et al., 2014]. However, until the 2015 Wintertime Investigation of Transport, Emissions, and Reactivity (WINTER) aircraft campaign, the deployment of the CIMS to measure chlorine compounds had not taken place on a broad regional basis during wintertime [Lee et al., 2018]. Lower temperatures, less sunlight, and lower water vapor typical of wintertime, together promote the multiphase reactions critical in activating Cl atoms from sea salt aerosols, and decrease the availability of other radical sources, making chlorine chemistry relatively more important in winter.

Because of how recently widespread measurements of various chlorine compounds within the troposphere have become available, the inclusion of comprehensive, tropospheric chlorine chemistry within global chemistry climate models only first occurred in 2007 [Sarwar et al., 2007]. Many of the relevant inorganic chlorine species are highly reactive, and thus present at low concentrations difficult to generate reproducibly for calibration of instruments. Moreover, their production and loss often depend on variable environmental factors such as VOC, particle pH, liquid water content, temperature, and aerosol surface area. Thus, atmospherically relevant laboratory constraints on chlorine chemistry mechanisms in the troposphere have been limited in the past [Sander et al., 2006]. With few existing observations in the atmosphere to test parameterizations or suggested mechanisms of tropospheric chlorine chemistry, the relative importance, seasonal and temporal changes, and impacts of different chemical pathways remained in question. Utilizing data collected in 2015 during the Wintertime Investigation of

Transport, Emissions, and Reactivity (WINTER) aircraft campaign, as well as deposition data from the National Atmospheric Deposition Program, this work provides critical constraints for such parameterizations and model representations of tropospheric chlorine chemistry.

1.3 Sources of Inorganic Chlorine to The Troposphere

Throughout the troposphere, inorganic reactive chlorine compounds are expected to be primarily in the form of hydrochloric acid (HCl) and particulate chloride (pCl^-), with minor contributions from hypochlorous acid (HOCl), nitryl chloride ($ClNO_2$), and chlorine gas (Cl_2) [Keene et al., 1999]. The primary global source of total inorganic chlorine (^TCl_y= pCl^-+ HCl+ $ClNO_2$ + $2Cl_2$ + HOCl+ $ClNO_3$) is from the emission of inorganic particulate chloride (pCl^-) from sea-salt aerosol (SSA) produced at the ocean's surface via bursting bubbles [Graedel and Keene, 1995; Keene et al., 1999]. The amount of emitted SSA and the associated pCl^- varies over several orders of magnitudes as a function of wind velocity and sea surface temperature [Graedel and Keene, 1995, Jaeglé et al., 2011], with tropospheric concentrations decreasing sharply above the marine boundary layer. The inland transport of super-micron SSA is small since they have a relatively short lifetime against deposition (~1.5 days) [Erikson et al., 1999; Keene et al., 1999]. However, submicron sea salt has a lifetime of 1-2 weeks and can be transported inland further making it a potentially important source even in areas not immediately adjacent to an ocean [Tegen et al, 1997].

Outside of coastal regions, direct emissions of HCl into the atmosphere can influence ^TCl_y concentrations and can be emitted through coal combustion, industrial processes, waste incineration, road salt application, fugitive dust, and biomass burning [Andreae et al., 1996; Keene et al., 1999; Lobert et al., 1999; McCulloch et al., 1999; Sarwar et al., 2012; Kolesar et al.,

2018]. HOCl and Cl_2 can also be directly emitted through various industry processes such as water treatment and within coal fired power plant emissions [Chang et al., 2002; Lee et al., 2018]. Although these non-sea salt (NSS) emissions of $^{T}Cl_y$ are much smaller in magnitude (together < 6.7 Tg yr^{-1}, globally in 1999) [Keene et al., 1999], relative to the source from SSA, they are potentially important as inland sources of reactive chlorine compounds [Haskins et al., 2018; Thornton et al., 2010]. As global models have begun to incorporate comprehensive chlorine chemistry, the relevancy of including NSS sources of $^{T}Cl_y$ and how those sources have changed since emissions inventories were compiled and created in the 1990s has remained an open question. Additionally, as air quality regulations in Europe and the US have tightened in the last two decades, requiring industry emitters to control NO_x and SO_2 emissions more tightly, emissions control technologies such as Flue Gas Desulfurization (FGD) technologies, and Selective Catalytic Reactors (SCR) have been widely installed. Although these technologies were invented to remove SO_2 and NO_x, respectively, both remove HCl with efficiencies greater than 90% as a by-product resulting in large decreases in anthropogenic HCl emissions in the last two decades in both the US and Europe. The consequences of this decrease in emissions is discussed further in Chapter 4, which utilizes deposition collected across the US over the last 20 years to address the importance of considering these inland anthropogenic sources.

1.4 PRODUCTION & LOSS OF HCL

HCl(g) can exist in equilibrium with its hydrated form in the aerosol at typical atmospheric conditions. However, it undergoes rapid dissociation yielding H^+ (aq) and Cl^- (aq), as a strong acid. This dynamic equilibrium (1.1) depends on highly local multiphase parameters like particle pH, liquid water content, relative humidity, and solute activity, all of which are influenced by ambient temperature, pressure, and atmospheric composition. It is important to

highlight that the backward reaction of this equilibrium can occur, allowing ambient HCl to replenish available pCl^- for other reactions in areas where there is no significant primary source of pCl^-.

$$HCl\,(g) \leftrightharpoons H^+(aq) + Cl^-(aq) \qquad (1.1)$$

The presence of other acid gases such as HNO_3 and H_2SO_4 can perturb this equilibrium and produce HCl, mobilizing Cl^- from the aerosol to the gas phase (1.2).

$$HNO_3 + Cl^-(aq) \rightarrow HCl(g) + NO_3^-(aq) \qquad (1.2)$$

$$H_2SO_4 + Cl^-(aq) \rightarrow HCl(g) + HSO_4^-(aq) \qquad (1.3)$$

This volatilization of HCl from primarily marine aerosol via acid displacement reactions is estimated to be the largest global source of HCl [Keene et al., 1999]. As NO_x and SO_2 (US EPA, 2014) concentrations have decreased over the past 20 years across the US, the question of the degree to which corresponding particle pH and acid displacement mechanisms have changed the magnitude of this dominant HCl source remains to be assessed and will be addressed in Chapter 5.

HCl can be directly converted to Cl atoms through reaction with OH (Pechtl & von Glasow, 2007).

$$HCl + OH \rightarrow Cl + H_2O \qquad (1.4)$$

However, this reaction alone is too slow to maintain significant levels of Cl atoms for typical HCl levels in the remote atmosphere (Erickson et al., 1999; Harris et al., 1992). Wang et al., (2019) recently estimated that only 19% of HCl is activated to reactive Cl* through this mechanism.

1.5 Reactive Tropospheric Chlorine Cycling

It has been suggested that pCl^- can undergo a number of multiphase reactions which ultimately convert pCl^- into reactive gas phase Cl*, which can subsequently undergo rapid cycling within the troposphere, with a widespread impact on air quality and climate. However, not all cycling and heterogeneous reaction mechanisms have been confirmed to occur in the troposphere by direct observations, and the rates at which some of these reactions take place are not well constrained [Simpson et al., 2015]. Those that are confirmed to occur have production mechanisms that vary seasonally and diurnally, and the importance of multiphase chemistry as a net source and the resulting cycling between phases and compounds, complicates the confirmation of reasonable representations of these reactions in models. This section describes relevant heterogenous reactions that will be discussed throughout this work and the remaining questions surrounding these production mechanisms. Figure 1.1 shows a synopsis of the chemical cycles and their resulting impacts on tropospheric oxidants and secondary pollutants described here.

1.5.1 *Formation of $ClNO_2$*

The multiphase reaction of dinitrogen pentoxide (N_2O_5) on chlorine containing particles to form $ClNO_2$ (1.5(1.9), represents a critical connection between chlorine and the cycling of NO_x, which can impact air quality and climate by regulating tropospheric O_3 production and OH abundances [Finlayson-Pitts et al., 1989; Behnke et al., 1997].

$$NO_2 + O_3 \rightarrow NO_3 + O_2 \qquad (1.5)$$

$$NO_2 + NO_3 \leftrightharpoons N_2O_5 \qquad (1.6)$$

$$NO_3 + NO \rightarrow NO_2 \qquad (1.7)$$

$$N_2O_5 + H_2O\ (l) \xrightarrow{\gamma(N2O5)} (2-\Phi)HNO_3 \qquad (1.8)$$

$$N_2O_5 + Cl^-\ (aq) \rightarrow NO_3^- + \Phi ClNO_2 \qquad (1.9)$$

$$Cl + RH \xrightarrow{+O_2} HCl + RO_2 \qquad (1.10)$$

N_2O_5 production, and therefore $ClNO_2$ production, occurs primarily at night, owing to the rapid photolysis of the N_2O_5 precursor, the nitrate radical (NO_3) during the day at wavelengths typical of the troposphere, and its reaction with nitric oxide (NO) to produce NO_2. At night, NO_3 can directly oxidize assorted VOC, or can subsequently react with NO_2 to form N_2O_5. Once formed, N_2O_5 can react on particles with some reaction probability, $\gamma_{(N2O5)}$, to form HNO_3, or if there is ample pCl^- available, to form some yield, Φ, of $ClNO_2$. The lower temperatures typical of winter promote the formation of N_2O_5 relative to its thermal decomposition and the longer nights allow for more production of $ClNO_2$.

At night, $ClNO_2$ remains relatively unreactive, but photolyzes upon sunrise with a photolysis frequency approximately a factor of 60 lower than that of NO_2, releasing Cl atoms and NO_2 (1.7). Therefore, $ClNO_2$ serves as a nighttime NO_x reservoir moving NO_2 downwind from source regions, which can lead to enhanced O_3 (and therefore OH) formation in the morning. Reactions of NO_3 with VOC or of N_2O_5 on particles has been previously estimated to account for ~50% of NO_x removal in polluted regions [Brown et al., 2004; Dentener & Crutzen, 1993], underscoring the importance that the production of $ClNO_2$ plays as a NO_x reservoir. Additionally, this mechanism serves to mobilize pCl^- from the particle into the gas phase as Cl*. Cl atoms released from $ClNO_2$ photolysis can serve as an important early morning oxidant source for assorted VOC, because the wavelength needed to photolyze $ClNO_2$ is longer than that

needed to begin photochemical production of OH [Riedel et al., 2013].

$ClNO_2$ production has recently represented a major focus of research into tropospheric Cl-atom sources. Over the course of an entire day, photolysis of $ClNO_2$ could account for 45% of the integrated Cl atom production in polluted offshore regions of the US (Riedel et al., 2012), where [$ClNO_2$] can reach ~1 ppbv. Other studies prior to the WINTER campaign, have also showed that Cl atoms from photolysis of $ClNO_2$ could contribute significantly to the total oxidizing capacity of the troposphere [Bannan et al., 2015; Osthoff et al., 2008; Phillips et al., 2012; Tham et al., 2014]. Reported concentrations of $ClNO_2$ ranged between a few parts per trillion and 4 ppb [Saiz Lopez et al., 2012]. Some studies in rural northern China, where the direct emission of photolytic chlorine containing compounds from coal-fired power plants is larger, the contribution of $ClNO_2$ to the total Cl-atom budget can be smaller, ranging from 16-21% [Liu et al., 2017; Liu et al., 2018], though this may not be the case for other regions.
It was hypothesized that colder temperatures and less photochemical production of OH typical of winter, could increase the relative importance of multiphase interactions, like the formation of $ClNO_2$ [Riedel et al., 2013]. However, no measurements of $ClNO_2$ had been made during winter and the degree to which its formation transported NO_x downwind and impacted the oxidant budget the following morning had not been assessed during this season when it was expected to be most important. Such an analysis, using data collected during the WINTER campaign, is presented in Chapter 2.

1.5.2 *Tropospheric Cycling of Cl**

Prior to the discovery of $ClNO_2$ production in the troposphere, past work on tropospheric Cl-atom sources often focused on BrCl or Cl_2, which are produced from multiphase chemistry or

emitted directly from industrial processes [Faxon et al., 2015; Finley et al., 2006; Keene et al., 2007; Lawler et al., 2011; Lee et al., 2018a; Liao et al., 2014; Pszenny et al., 1993; Pszenny et al., 2004; Riedel et al., 2012; Spicer et al., 1998; Tanaka et al., 2000;]. In-situ production of tropospheric Cl_2 has been proposed to occur via several mechanisms, including the daytime reaction of OH on chlorine-containing particle surfaces [Knipping et al., 2000; Laskin et al., 2003], snowpack chemistry [Custard et al., 2017; Pratt et al., 2013], and reactive uptake of hypochlorous acid (HOCl) and chlorine nitrate ($ClONO_2$) on SSA [Vogt et al., 1996]. Reported tropospheric mixing ratios of Cl_2 tend to be < 100 pptv, and typically on the order of 10 pptv [Faxon et al., 2015; Finley et al., 2006; Keene et al., 2007; Lawler et al., 2011; Pszenny et al., 1993; Pszenny et al., 2004; Riedel et al., 2012; Spicer et al., 1998;].

Cl atoms released from the photolysis of $ClNO_2$ that do not oxidize VOC and reform HCl via reaction (1.10, can react with O_3 to form the radical, hypochlorite (ClO) via reaction 1.11.

$$Cl + O_3 \rightarrow ClO + O_2 \qquad (1.11)$$

Unlike other halogen oxides, ClO does not rapidly photo-dissociate, and therefore has a longer photolytic lifetime allowing it to accumulate in the troposphere (direct observations suggest between 15-30 pptv) [Platt & Honniger, 2003; Saiz-Lopez et al., 2012]. However, because the hydrogen-chlorine bond strength is similar to that of organic carbon-hydrogen bonds, the Cl atom reaction with hydrocarbons via (1.10, typically outcompetes the O_3 depleting pathway via reaction 1.11 [Platt & Honniger, 2003]. Additionally, the loss of ClO to nitric oxide (NO) via R4 can dominate ClO's fate in polluted regions [Riedel et al., 2012]. This suggests that in polluted marine regions, the impact of $ClNO_2$ photolysis, increasing the Cl atom budget will increase O_3 production in the net, by transporting NO_2 downwind, rather than decreasing O_3 through catalytic loss from ClO cycling described below.

If formed, ClO can undergo a variety of reactions with itself of other halogen oxides (XO, where X=Cl, Br, I), which generally destroy ozone and either conserve radicals or produce dihalogens, like Cl_2, that rapidly photolyze during the day releasing Cl atoms (reaction 1.14).

$$XO + XO \rightarrow X_2 + O_2 \quad (1.12a)$$

$$XO + XO \rightarrow 2X + O_2 \quad (1.11b)$$

$$XO + XO \rightarrow OXO + X \quad (1.11c)$$

$$XO + NO \rightarrow X + NO_2 \quad (1.13)$$

$$X_2 + h\nu \rightarrow 2X \quad (1.14)$$

Cross halogen reactions (those of ClO with BrO or IO) are typically an order of magnitude faster than self-reactions, emphasizing the critical role that the coupling of bromine and iodine chemistry to chlorine chemistry can play. However, these reactions only occur when high concentrations of BrO or IO are available (such as in the Arctic and Antarctic lower troposphere during spring). In other regions, these reactions are typically slow, and other reactions dominate.

ClO can also undergo reactions with NO_2 or HO_2 to form either chlorine nitrate ($ClONO_2$) or hypochlorous acid (HOCl), respectively. However, the availability of ClO can be a limiting step in the formation of HOCl and $ClONO_2$, especially in the polluted troposphere, owing to the loss of ClO to NO via reaction 1.13.

$$ClO + NO_2 + M \rightarrow ClONO_2 \quad (1.15)$$

$$ClO + HO_2 \rightarrow HOCl + O_2 \quad (1.16)$$

$ClONO_2$ can also be converted to HOCl on aerosol particles via heterogenous reaction 1.17. And, HOCl can photolyze with a typical tropospheric lifetime on the order of minutes, returning Cl atoms (reactions 1.18).

$$ClONO_2 + H_2O(l) \rightarrow HOCl + HNO_3 \quad (1.17)$$

$$HOCl + h\nu \rightarrow Cl + OH \quad (1.18)$$

Breton et al., (2018) recently reported $ClONO_2$ measurements in the troposphere with concentrations peaking at night and being sustained around 15 pptv at a semi-rural site northwest of Beijing. However, the reported behavior of $ClONO_2$ is not consistent with daytime production or heterogenous loss, and the reproducibility of the calibration needed to quantify observed concentrations is unclear. Concentrations of HOCl have been observed routinely between 5-40 pptv (Lawler et al., 2009; Haskins et al., 2018;) with daytime peaks. Considering these observed concentrations, conversion of $ClNO_3$ to HOCl and subsequent photolysis compounds could yield an atmospherically relevant concentration of Cl atoms. Lawler et al. (2011) suggested a fast daytime HOCl source from a hypothetical light-dependent Cl^- oxidation pathway to account for high daytime HOCl concentrations (>100 pptv) observed at Cape Verde, but models have struggled to recreate those observed concentrations [Wang et al., 2019], and no other observations of HOCl at elevated concentrations similar to those have since been made.

The photochemical cycling of these liberated chlorine compounds can then couple back to multiphase chemistry via the uptake of $ClONO_2$ or HOCl on aerosols containing particulate chloride, pCl^- in the condensed phase to produce Cl_2.

$$ClONO_2 + Cl^-(aq) + H^+(aq) \xrightarrow{\gamma(ClONO2)} Cl_2 + HNO_3 \quad (1.19)$$

$$HOCl + Cl^-(aq) + H^+(aq) \xrightarrow{\gamma(HOCl)} Cl_2 + H_2O \quad (1.20)$$

Using tropospheric observations of Cl_2 and HOCl, Lawler et al., (2011) estimated a reaction probability for HOCl, γ(HOCl), via reaction 1.20, of 1.7×10^{-3} to best explain observed Cl_2 levels and the rate of evening conversion of HOCl to Cl_2 in a pristine marine environment.

This field-derived γ(HOCl) value is an order of magnitude above those inferred from laboratory experiments using acidified SSA by Pratte & Rossi (2006). γ(HOCl) values from Lawler et al. (2011) imply nearly complete conversion of HOCl into Cl_2 over a night at typical tropospheric temperatures and aerosol surface area density, while those from Pratte & Rossi (2006) imply 5 to 10% conversion. Ultimately, these studies suggest conversion of HOCl to Cl_2 could be significant in the troposphere but highlight the differences in field and laboratory estimates of such uptake processes.

Riedel et al., (2012) hypothesized that the fate of $ClONO_2$ on aerosol particles was particularly important in polluted regions, since even a slow conversion of $ClONO_2$ to HOCl via reaction 1.17 and subsequent conversion to Cl_2 via 1.19, could lead to production of ~40 pptv of Cl_2 at night, even if $ClONO_2$ production was slowed by NO during the preceding day. Although laboratory constraints on the heterogeneous reaction of $ClONO_2$ with HCl to form Cl_2 exist under stratospheric conditions [Hanson & Ravishankara, 1994], few laboratory measurements at typical tropospheric temperatures exist. These studies suggest a wide range in the efficiency of uptake on particles or surfaces containing NaCl with γ ($ClONO_2$) estimates ranging from 4.6 x 10^{-3} to 0.14, though all agree the yield of Cl_2 is 100% [Burkholder et al., 2015;].

Reaction 1.20 and cross halogen reactions either initiated by BrO instead of ClO in reaction 1.11 or through HOCl's reaction with Br^- instead of Cl^- in reaction 1.20 is of particular interest when considering partitioning of available oxidants. Starting from one halogen radical atom, Cl, and following the sequence of reactions 1.11, 1.16, 1.20, and 1.14 gives the net reaction:

$$Cl + HO_2 + Cl^-(het) + h\nu \rightarrow 2Cl + OH^- \quad (1.21)$$

An analogous series of reactions involving bromine is termed the "bromine-explosion"

since it is ultimately an autocatalytic cycle that builds up the pool of reactive halogen radicals in the atmosphere. However, the net effect of this cycle on the radical budget, which starts with one Cl atom (and one HO_2 radical), is to produce two Cl atoms. This series, then, is a conversion of HO_x radicals to Cl atoms. Therefore, although this shift within the available radical pool has consequences for the oxidation of various VOC, particularly alkanes, the net impact of such a series, is not to increase the available radical pool within the atmosphere. However, it should be noted that this process ultimately consumes protons from the aqueous phase shifting the pH of aerosol surfaces to be less acidic, which can impact other heterogenous halogen chemistry [Simpson et al., 2015]. In polluted continental outflow, Riedel et al., (2012) found that these reactions only enhanced Cl_2 in the early morning hours, initiated by the photolysis of $ClNO_2$, when the NO/NO_2 ratio was low enough that reaction 1.13 did not suppress the formation of HOCl and $ClONO_2$, which otherwise lead to the production of a few pptv of Cl_2 at night.

Another possible pathway that pCl^- can be mobilized from the particle into the reactive gas phase is through the heterogenous uptake of $ClNO_2$ on acidic particles, proposed in Roberts et al., (2008). Laboratory studies have shown the nocturnal production of $ClNO_2$ from dinitrogen pentoxide (N_2O_5) uptake leads to Cl_2 via reaction on acidic aerosols (1.22) is possible, following a mechanism analogous to the formation of Br_2 from $BrNO_2$ on Br^- containing substrates.

$$Cl^-(aq) + ClNO_2(g) + H^+(aq) \xrightarrow[\gamma(ClNO_2)]{} Cl_2(g) + HONO(aq) \qquad (1.22)$$

Given that $ClNO_2$ has routinely been observed in the troposphere exceeding 1 ppbv [Osthoff et al., 2008; Thornton et al., 2010; Mielke et al., 2011, 2013; Phillips et al., 2012; Riedel et al., 2012; Riedel et al., 2013; Tham et al., 2014; Bannan et al., 2015; Faxon et al., 2015; Wang et al., 2016; Haskins et al., 2018; Yun et al., 2018], this production channel suggests significant Cl_2 production, on the order of 1 ppbv, which would result in a considerable Cl atom source upon

the photolysis of Cl_2. Chapter 3 utilizes WINTER data to constrain the degree to which this mechanism occurs in the troposphere.

1.6 Removal of Tropospheric Chlorine Compounds

Although chlorine can cycle through many forms within the troposphere, its removal occurs primarily through the deposition of pCl^- and HCl. Wang et al. (2019) estimated that of the 13 Tg Cl yr^{-1} released as reactive chlorine Cl^*, 98.4% eventually returned as HCl before being deposited. The atmospheric lifetime of HCl is primarily controlled by wet and dry deposition. The dry deposition velocity of HCl in marine environments has been estimated to range between 1 and 5 cm s^{-1} [Finlayson-Pitts and Pitts, 1999]. At deposition rate of 1 cm s^{-1}, the lifetime against dry deposition is 1.2 and 1.7 days at a boundary layer height of 1 km and 1.5 km, respectively. The 24-hour averaged lifetime of HCl with respect to OH oxidation is roughly 15 days (k_{OH+HCl} (298 K) = 8×10^{-13} cm^3 $molecule^{-1}$ s^{-1} and $[OH]_{24\,h} = 1 \times 10^6$ molecules cm^3). However lower OH levels in winter, this lifetime against OH oxidation is likely even longer, making wet and dry deposition the primary removal mechanism of HCl from the troposphere. Simulations by Wang et al. (2019) suggest that deposition is the dominant sink of Cl_y gases in the atmosphere, accounting for > 95% of the simulated losses in GEOS-Chem, with dry deposition accounting for 49%, wet depositions accounting for 51%. HCl readily dissolves in particles with pH typical of even acidic rainwater, making wet deposition a major HCl removal processes, particularly over land. Chapter 4 addresses changes in deposition patterns of pCl^- over the US from anthropogenic emissions of HCl changes.

Super-micron sea salt aerosols have a relatively short lifetime against deposition (~1.5 days) [Erikson et al., 1999; Keene et al., 1999] comparable to that of HCl against dry deposition while submicron sea-salt has a lifetime of ~1-2 weeks. Figure 1.2 shows the different modeled

deposition of HCl and pCl^- during the WINTER campaign over the eastern US highlighting where each of these processes dominate removal pathways. Although uptake of pCl^- by alkaline particles in inland regions could serve as an important replenisher to pCl^- for heterogenous reactions in non-source regions, global estimates from Wang et al., 2019 suggest this only accounts for ~5% of the global sink of Cl_y.

1.7 MOTIVATING QUESTIONS FOR THIS WORK

This work utilizes a new observational data set with simultaneous measurements of many of the precursors to Cl atom production, including N_2O_5, $ClNO_2$, Cl_2, HOCl, NO_2, O_3, HCl, pCl^-, among others during winter. The motivating questions guiding the analysis presented herein are as follows:

Chapter 2: Anthropogenic Control over Wintertime Oxidation of Atmospheric Pollutants [Haskins et al., 2019b]

(1) What radical precursors control the radical budget and what is the magnitude of the production of Cl atoms from $ClNO_2$ photolysis in the polluted marine boundary layer during winter?

(2) To what degree do Cl atoms impact downwind O_3 formation and VOC oxidation?

Chapter 3: Observational Constraints on the Formation of Cl_2 From the Reactive Uptake of $ClNO_2$ on Aerosols in the Polluted Marine Boundary Layer [Haskins et al., 2019a]

(1) Is there observational support for the uptake of $ClNO_2$ to form Cl_2 on acidic aerosols?

(2) Can laboratory and observational uptake mechanisms be reconciled, and if so, what causes discrepancies?

Chapter 4: Significant U.S. decreases in deposition of anthropogenic chloride from emission controls [in prep]

(1) To what degree have depositional patterns of anthropogenic Cl^- changed as emissions of NO_x and SO_2 have declined in the last 20 years?

(2) Is there evidence of changes in the acid displacement of HCl because of NO_x and SO_2 emissions changes?

Chapter 5: Conclusions

(1) What is the significance of the insights contained in this work?

(2) What questions remain on the topics presented herein & what future research may be needed to further understanding of these topics?

1.8 REFERENCES

Andreae, M. O.: Emission of trace gases and aerosols from biomass burning – an updated assessment, Atmos. Chem. Phys., 19, 8523–8546, https://doi.org/10.5194/acp-19-8523-2019, 2019.

Atkinson, R.: Gas-Phase Tropospheric Chemistry of Volatile Organic Compounds: 1. Alkanes and Alkenes, J. Phys. Chem. Ref. Data, 26, 215–290, 1997.

Bannan, T. J., Booth, A. M., Bacak, A., Muller, J. B. A., Leather, K. E., Le Breton, M., … Percival, C. J. (2015). The first UK measurements of nitryl chloride using a chemical ionization mass spectrometer in central London in the summer of 2012, and an investigation of the role of Cl atom oxidation. Journal of Geophysical Research: Atmospheres, 120(11), 5638–5657. https://doi.org/10.1002/2014JD022629

Behnke, W., George, C., Scheer, V., and Zetzsch, C.: Production and decay of $ClNO_2$ from the reaction of gaseous N_2O_5 with NaCl solution: Bulk and aerosol experiments, J. Geophys. Res.-Atmos., 102, 3795–3804, https://doi.org/10.1029/96JD03057, 1997.

Brown, S. S., et al. (2004), Nighttime removal of NOx in the summer marine boundary layer, Geophys. Res. Lett., 31, L07108, doi:10.1029/2004GL019412.

Burkholder, J. B., Sander, S. P., Abbatt, J. P. D., Barker, J. R., Huie, R. E., Kolb, C. E., et al. (2015). Chemical kinetics and photochemical data for use in atmospheric studies: Evaluation number 18. Pasadena, CA: Jet Propulsion Laboratory, National Aeronautics and Space Administration.

Chang, S., McDonald-Buller, E., Kimura, Y., Yarwood, G., Neece, J., Russell, M., Tanaka, P., and Allen, D.: Sensitivity of urban ozone formation to chlorine emission estimates, Atmos. Environ., 36, 4991–5003, https://doi.org/10.1016/S1352-2310(02)00573-3, 2002.

Chen, Q., Schmidt, J. A., Shah, V., Jaeglé, L., Sherwen, T., and Alexander, B.: Sulfate production by reactive bromine: Implications for the global sulfur and reactive bromine budgets, Geophys. Res. Lett., 44, 7069–7078, https://doi.org/10.1002/2017GL073812,

Crisp, T. A., Lerner, B. M., Williams, E. J., Quinn, P. K., Bates, T. S., and Bertram, T. H. (2014), Observations of gas phase hydrochloric acid in the polluted marine boundary layer, J. Geophys. Res. Atmos., 119, 6897– 6915, doi:10.1002/2013JD020992.

Custard, K. D., Raso, A. R. W., Shepson, P. B., Staebler, R. M., & Pratt, K. A. (2017). Production and release of molecular bromine and chlorine from the Arctic coastal snowpack. ACS Earth and Space Chemistry, 1(3), 142–151. https://doi.org/10.1021/acsearthspacechem.7b00014

Dentener, F. J., and P. J. Crutzen (1993), Reaction of N_2O_5 on tropospheric aerosols: Impact on the global distributions of NO_X, O_3, and OH, J. Geophys. Res., 98(D4), 7149–7163, doi:10.1029/92JD02979.

Erickson, D. J. I., Suezaret, C., Keene, W. C., & Gong, S. L. (1999). A general circulation model-based calculation of HCI and CINO2 production from sea salt dechlorination: Reactive Chlorine Emissions Inventory annual production of sea distributions of via direct scavenging or chemical production from the generation of se. J. Geophys. Res., 104(D7), 8347–8372.

Faxon, C., Bean, J., & Hildebrandt-Ruiz, L. (2015). Inland concentrations of ClNO2 in Southeast Texas suggest chlorine chemistry significantly contributes to atmospheric reactivity. Atmosphere, 6 (Atmospheric Composition Observations), 1487–1506. https://doi.org/ 10.3390/atmos6101487

Finlayson-Pitts, B. J., Ezell, M. J., & Pitts, J. N. (1989). Formation of chemically active chlorine compounds by reactions of atmospheric NaCl particles with gaseous N2O5 and ClONO2. Nature, 337(6204), 241–244. https://doi.org/10.1038/337241a0 Fortems-Cheiney, A., Chevallier, F., Pison, I., Bousquet, P., Saunois, M., Szopa, S., et al. (2012). The formaldehyde budget as seen by a global-scale multi-constraint and multi-species inversion system. Atmospheric Chemistry and Physics, 12(15), 6699–6721. https://doi.org/ 10.5194/acp-12-6699-2012

Finley, B. D., & Saltzman, E. S. (2006). Measurement of Cl2 in coastal urban air. Geophysical Research Letters, 33, L11809. https://doi.org/ 10.1029/2006gl025799

Graedel, T. E., & Keene, W. C. (1995). Tropospheric budget of reactive chlorine. Global Biogeochemical Cycles, 9(1), 47–77. https://doi.org/10.1029/94GB03103

Hanson, D. R., & Ravishankara, A. R. (1994). Reactive uptake of ClONO2 onto sulfuric acid due to reaction with HCl and H2O. The Journal of Physical Chemistry, 98(22), 5728–5735. https://doi.org/10.1021/j100073a026

Harris, G. W., Klemp, D., and Zenker, T.: An upper limit on the HCl near-surface mixing ratio over the Atlantic measured using TDLAS, J. Atmos. Chem., 15, 327–332, 1992.

Haskins, J. D., Jaeglé, L., Shah, V., Lee, B. H., Lopez-Hilfiker, F. D., Campuzano-Jost, P., et al. (2018). Wintertime gas-particle partitioning and speciation of inorganic chlorine in the lower troposphere over the Northeast United States and Coastal Ocean. Journal of Geophysical Research: Atmospheres, 123, 12,897–12,916. https://doi.org/10.1029/2018JD028786

Haskins, J. D., Lee, B. H., Lopez-Hilifiker, F. D., Peng, Q., Jaeglé, L., Reeves, J. M., et al. (2019a). Observational constraints on the formation of Cl2 from the reactive uptake of ClNO2 on aerosols in the polluted marine boundary layer. Journal of Geophysical Research: Atmospheres, 124, 8851–8869. https://doi.org/10.1029/2019JD030627

Haskins, J. D., Lopez-Hilfiker, F. D., Lee, B. H., Shah, V., Wolfe, G. M., DiGangi, J., … Thornton, J. A. (2019b). Anthropogenic Control Over Wintertime Oxidation of Atmospheric Pollutants. Geophysical Research Letters, 46(24), 14826–14835. https://doi.org/10.1029/2019GL085498

Hoffmann, E. H., Tilgner, A., Schrödner, R., Bräuer, P., Wolke, R., and Herrmann, H.: An advanced modeling study on the impacts and atmospheric implications of multiphase dimethyl sulfide chemistry, P. Natl. Acad. Sci. USA, 113, 11776–11781, https://doi.org/10.1073/pnas.1606320113, 2016.

Horowitz, H. M., Jacob, D. J., Zhang, Y., Dibble, T. S., Slemr, F., Amos, H. M., Schmidt, J. A., Corbitt, E. S., Marais, E. A., and Sunderland, E. M.: A new mechanism for atmospheric mercury redox chemistry: implications for the global mercury budget, Atmos. Chem. Phys., 17, 6353–6371, https://doi.org/10.5194/acp-17-6353-2017, 2017.

Hossaini, R., Chipperfield, M. P., Saiz-Lopez, A., Fernandez, R., Monks, S., Feng, W., Brauer, P., and von Glasow, R.: A global model of tropospheric chlorine chemistry: Organic versus inorganic sources and impact on methane oxidation, J. Geophys. Res.-Atmos., 121, 14271-14297, https://doi.org/10.1002/2016JD025756, 2016.

Jaeglé, L., Quinn, P. K., Bates, T. S., Alexander, B., and Lin, J.-T.: Global distribution of sea salt aerosols: new constraints from in situ and remote sensing observations, Atmos. Chem. Phys., 11, 3137–3157, https://doi.org/10.5194/acp-11-3137-2011, 2011.

Keene, W. C., Aslam, M, Khalil, K., Erickson Iii, D. J., Mcculloch, A., Graedel, T. E., (1999). Composite global emissions of reactive chlorine from anthropogenic and natural sources: Reactive Chlorine Emissions Inventory. JOURNAL OF GEOPHYSICAL RESEARCH, 104(20), 8429–8440. https://doi.org/10.1029/1998JD100084

Keene, W. C., Jacob, D. J., Fan, S., Maben, J. R., Zetwo, M. P., et al. (1993). Evidence of inorganic chlorine gases other than hydrogen chloride in marine surface air. Geophysical Research Letters, 20(8), 699–702. https://doi.org/10.1029/93gl00047

Keene, W. C., Pszenny, A. A. P., Jacob, D. J., Duce, R. A., Galloway, J. N., Schultz-Tokos, J. J., Sievering, H., and Boatman, J. F. (1990), The geochemical cycling of reactive chlorine through the marine troposphere, Global Biogeochem. Cycles, 4(4), 407– 430, doi:10.1029/GB004i004p00407.

Keene, W. C., Stutz, J., Pszenny, A. A., Maben, J. R., Fischer, E. V., Smith, A. M., et al. (2007). Inorganic chlorine and bromine in coastal New England air during summer. Journal of Geophysical Research, 112, D10S12. https://doi.org/10.1029/2006JD007689

Kercher, J. P., Riedel, T. P., and Thornton, J. A.: Chlorine activation by N_2O_5: simultaneous, in situ detection of $ClNO_2$ and N_2O_5 by chemical ionization mass spectrometry, Atmos. Meas. Tech., 2, 193–204, https://doi.org/10.5194/amt-2-193-2009, 2009.

Knipping, E. M., Lakin, M. J., Foster, K. L., Jungwirth, P., Tobias, D. J., Gerber, R. B., et al. (2000). Experiments and simulations of ion-enhanced interfacial chemistry on aqueous NaCl aerosols. Science, 288(5464), 301–306. https://doi.org/10.1126/science.288.5464.301

Kolesar, K. R., Mattson, C. N., Peterson, P. K., May, N. W., Prendergast, R. K., and Pratt, K. A.: Increases in wintertime $PM_{2.5}$ sodium and chloride linked to snowfall and road salt application, Atmos. Environ., 177, 195–

202, https://doi.org/10.1016/j.atmosenv.2018.01.008, 2018.

Laskin, A., Moffet, R. C., Gilles, M. K., Fast, J. D., Zaveri, R. A., Wang, B., et al. (2012). Tropospheric chemistry of internally mixed sea salt and organic particles: Surprising reactivity of NaCl with weak organic acids. Journal of Geophysical Research, 117, D15302. https://doi. org/10.1029/2012JD017743

Lawler, M. J., Sander, R., Carpenter, L. J., Lee, J. D., Von Glasow, R., Sommariva, R., & Saltzman, E. S. (2011). HOCl and Cl2 observations in marine air. Atmospheric Chemistry and Physics, 11(15), 7617–7628. https://doi.org/10.5194/acp-11-7617-2011

Lee, B. H., Lopez-Hilfiker, F. D., Veres, P. R., McDuffie, E. E., Fibiger, D. L., Sparks, T. L., et al. (2018). Flight deployment of a high-resolution time-of-flight chemical ionization mass spectrometer: Observations of reactive halogen and nitrogen oxide species. Journal of Geophysical Research: Atmospheres, 123, 7670 –7686. https://doi.org/10.1029/2017JD028082

Liao, J., Huey, L. G., Liu, Z., Tanner, D. J., Cantrell, C. A., Orlando, J. J., et al. (2014). High levels of molecular chlorine in the Arctic atmosphere. Nature Geoscience, 7, 91. https://doi.org/10.1038/ngeo2046

Liu, X., Qu, H., Huey, L. G., Wang, Y., Sjostedt, S., Zeng, L., et al. (2017). High levels of daytime molecular chlorine and nitryl chloride at a rural site on the North China Plain. Environmental Science & Technology, 51(17), 9588–9595. https://doi.org/10.1021/acs.est. 7b03039

Liu, Y., Fan, Q., Chen, X., Zhao, J., Ling, Z., Hong, Y., et al. (2018). Modeling the impact of chlorine emissions from coal combustion and prescribed waste incineration on tropospheric ozone formation in China. Atmospheric Chemistry and Physics, 18, 2709–2724. https://doi. org/10.5194/acp-18-2709-2018

Lobert, J. M., Keene, W. C., Logan, J. A., and Yevich, R. (1999), Global chlorine emissions from biomass burning: Reactive Chlorine Emissions Inventory, J. Geophys. Res., 104(D7), 8373– 8389, doi:10.1029/1998JD100077.

McCulloch, A., Aucott, M. L., Benkovitz, C. M., Graedel, T. E., Kleiman, G., Midgley, P. M., and Li, Y.-F. (1999), Global emissions of hydrogen chloride and chloromethane from coal combustion, incineration and industrial activities: Reactive Chlorine Emissions Inventory, J. Geophys. Res., 104(D7), 8391– 8403, doi:10.1029/1999JD900025.

Mielke, L. H., Furgeson, A., & Osthoff, H. D. (2011). S.I.: Observation of ClNO in a mid-continental urban environment. Environmental Science & Technology, 45, 8889–8896. https://doi.org/10.1021/es201955u

Osthoff, H. D., Roberts, J. M., Ravishankara, A. R., Williams, E. J., Lerner, B. M., Sommariva, R., et al. (2008). High levels of nitryl chloride in the polluted subtropical marine boundary layer. Nature Geoscience, 1(5), 324–328. https://doi.org/10.1038/ngeo177

Pechtl, S. and von Glasow, R.: Reactive chlorine in the marine boundary layer in the outflow of polluted continental air: A model study, Geophys. Res. Lett., 34, L11813, doi:10.1029/2007GL029761, 2007.

Phillips, G. J., Tang, M. J., Thieser, J., Brickwedde, B., Schuster, G., Bohn, B., et al. (2012). Significant concentrations of nitryl chloride observed in rural continental Europe associated with the influence of sea salt chloride and anthropogenic emissions. Geophysical Research Letters, 39, L10811. https://doi.org/10.1029/2012GL051912

Platt, U., & Hönninger, G. (2003). The role of halogen species in the troposphere. Chemosphere, 52(2), 325–338. https://doi.org/https://doi.org/10.1016/S0045-6535(03)00216-9

Pratte, P. and Rossi, M. J.: The heterogeneous kinetics of HOBr and HOCl on acidified sea salt and model aerosol at 40–90% relative humidity and ambient temperature, Phys. Chem. Chem. Phys., 8, 3988–4001, 2006.

Pszenny, A. A. P., Keene, W. C., Jacob, D. J., Fan, S., Maben, J. R., Zetwo, M. P., et al. (1993). Evidence of inorganic chlorine gases other than hydrogen chloride in marine surface air. Geophysical Research Letters, 20(8), 699–702. https://doi.org/10.1029/93gl00047

Pszenny, A.A.P., Moldanová, J., Keene, W.C., Sander, R., Maben, J.R., Martinez, M., et al. (2004). Halogen cycling and aerosol pH in the Hawaiian marine boundary layer. Atmospheric Chemistry and Physics, 4(1), 147–168. Retrieved from https://hal.archives-ouvertes.fr/ hal-00295390

Riedel, T. P., Bertram, T. H., Crisp, T. A., Williams, E. J., Lerner, B. M., Vlasenko, A., et al. (2012). Nitryl chloride and molecular chlorine in the coastal marine boundary layer. Environmental Science and Technology. https://doi.org/10.1021/es204632r

Riedel, T. P., Wagner, N. L., Dubé, W. P., Middlebrook, A. M., Young, C. J., Öztürk, F., et al. (2013). Chlorine activation within urban or power plant plumes: Vertically resolved ClNO2 and Cl2 measurements from a tall tower in a polluted continental setting. Journal of Geophysical Research: Atmospheres, 118, 8702–8715. https://doi.org/10.1002/jgrd.50637

Riedel, T. P., Wolfe, G. M., Danas, K. T., Gilman, J. B., Kuster, W. C., Bon, D. M., Vlasenko, A., Li, S.-M., Williams, E. J., Lerner, B. M., Veres, P. R., Roberts, J. M., Holloway, J. S., Lefer, B., Brown, S. S., and Thornton, J. A.: An MCM modeling study of nitryl chloride ($ClNO_2$) impacts on oxidation, ozone production and nitrogen oxide partitioning in polluted continental outflow, Atmos. Chem. Phys., 14, 3789–3800, https://doi.org/10.5194/acp-14-3789-2014, 2014.

Roberts, J. M., Osthoff, H. D., Brown, S. S., & Ravishankara, A. R. (2008). N2O5 Oxidizes Chloride to Cl2 in Acidic Atmospheric Aerosol. Science, 321(5892), 1059.

Sander, S. P., Golden, D. M., Kurylo, M. J., Moortgat, G. K., Wine, P. H., Ravishankara, A. R., et al. (2006). Chemical kinetics and photochemical data for use in atmospheric studies, Evaluation Number 15. Pasadena, CA: JPL Publication 07-10, Jet Propulsion Laboratory.

Sarwar, G. and P.V. Bhave, 2007: Modeling the Effect of Chlorine Emissions on Ozone Levels

over the Eastern United States. J. Appl. Meteor. Climatol., 46, 1009–1019, https://doi.org/10.1175/JAM2519.1

Sherwen, T., Schmidt, J. A., Evans, M. J., Carpenter, L. J., Großmann, K., Eastham, S. D., Jacob, D. J., Dix, B., Koenig, T. K., Sinreich, R., Ortega, I., Volkamer, R., Saiz-Lopez, A., Prados-Roman, C., Mahajan, A. S., and Ordóñez, C.: Global impacts of tropospheric halogens (Cl, Br, I) on oxidants and composition in GEOS-Chem, Atmos. Chem. Phys., 16, 12239–12271, https://doi.org/10.5194/acp-16-12239-2016, 2016.

Simpson, W. R., Brown, S. S., Saiz-Lopez, A., Thornton, J. A., & Von Glasow, R. (2015). Tropospheric Halogen Chemistry: Sources, Cycling, and Impacts. Chemical Reviews, 115(10), 4035–4062. https://doi.org/10.1021/cr5006638

Spicer, C. W., Chapman, E. G., Finlayson-Pitts, B. J., Plastridge, R. A., Hubbe, J. M., Fast, J. D., & Berkowitz, C. M. (1998). Unexpectedly high concentrations of molecular chlorine in coastal air. Nature, 394(6691), 353–356. https://doi.org/10.1038/28584

Tanaka, P. L., Oldfield, S., Neece, J. D., Mullins, C. B., & Allen, D. T. (2000). Anthropogenic sources of chlorine and ozone formation in urban atmospheres. Environmental Science & Technology, 34(21), 4470–4473. https://doi.org/10.1021/es991380v

Tegen, I., P. Hollrig, M. Chin, I. Fung, D. Jacob, and J. Penner (1997), Contribution of different aerosol species to the global aerosol extinction optical thickness: Estimates from model results, J. Geophys. Res., 102(D20), 23,895 – 23,915.

Tham, Y. J., Yan, C., Xue, L., Zha, Q., Wang, X., & Wang, T. (2014). Presence of high nitryl chloride in Asian coastal environment and its impact on atmospheric photochemistry. Chinese Science Bulletin, 59(4), 356–359. https://doi.org/10.1007/s11434-013-0063-y

Thornton, J. A., Kercher, J. P., Riedel, T. P., Wagner, N. L., Cozic, J., Holloway, J. S., Dubé, W. P., Wolfe, G. M., Quinn, P. K., Middlebrook, A. M., Alexander, B., and Brown, S. S.: A large atomic chlorine source inferred from mid-continental reactive nitrogen chemistry, Nature, 464, 271–274, https://doi.org/10.1038/nature08905, 2010.

Vogt, R., Crutzen, P. J., & Sander, R. (1996). A mechanism for halogen release from sea-salt aerosol in the remote marine boundary layer. Nature, 383(6598), 327–330. Retrieved from http://dx.doi.org/10.1038/383327a0

Wang, X., Jacob, D. J., Eastham, S. D., Sulprizio, M. P., Zhu, L., Chen, Q., Alexander, B., Sherwen, T., Evans, M. J., Lee, B. H., Haskins, J. D., Lopez-Hilfiker, F. D., Thornton, J. A., Huey, G. L., and Liao, H.: The role of chlorine in global tropospheric chemistry, Atmos. Chem. Phys., 19, 3981–4003, https://doi.org/10.5194/acp-19-3981-2019, 2019.

Wang, X., Wang, H., Xue, L., Wang, T., Wang, L., Gu, R., et al. (2017). Observations of N2O5 and ClNO2 at a polluted urban surface site in North China: High N2O5 uptake coefficients and low ClNO2 product yields. Atmospheric Environment, 156, 125–134. https://doi.org/10.1016/J.ATMOSENV.2017.02.035

Young, A. H., W. C. Keene, A. A. P. Pszenny, R. Sander, J. A. Thornton, T. P. Riedel, and J. R.

Maben (2013), Phase partitioning of soluble trace gases with size-resolved aerosols in near-surface continental air over northern Colorado, USA, during winter, J. Geophys. Res. Atmos., 118, 9414–9427, doi:10.1002/jgrd.50655

Yun, H., Wang, W., Wang, T., Xia, M., Yu, C., Wang, Z., et al. (2018). Nitrate formation from heterogeneous uptake of dinitrogen pentoxide during a severe winter haze in southern China. Atmospheric Chemistry and Physics, 18, 17,515–17,527. https://doi.org/10.5194/acp-18-17515-2018

1.9 FIGURES

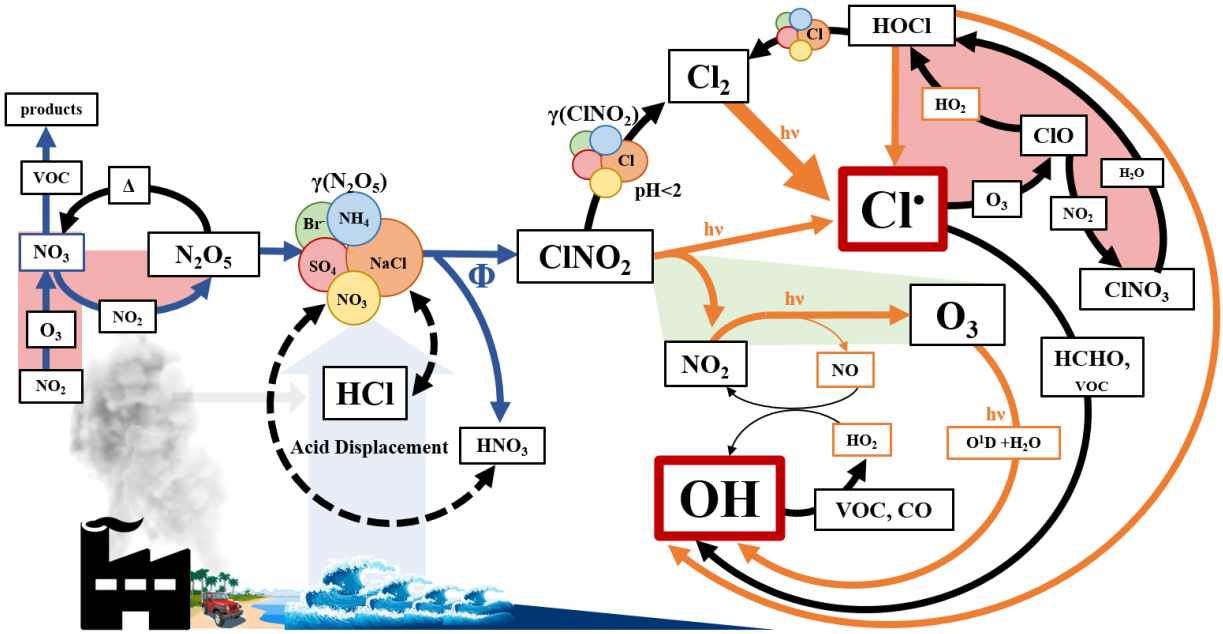

Figure 1.1 Summary of Proposed Cl_y impacts on Tropospheric Oxidants

Summary of the activation, mobilization, and chemical cycling of Cl_y compounds relevant to the tropospheric oxidant budget (excluding bromine connections), and their connection to the NO_x and HO_x cycles. Orange arrows indicate daytime reactions, while blue arrows indicate nighttime reactions. Red shaded ares indicate reaction series that net destroy ozone, while green shaded ares indicate reaction series that net produce ozone.

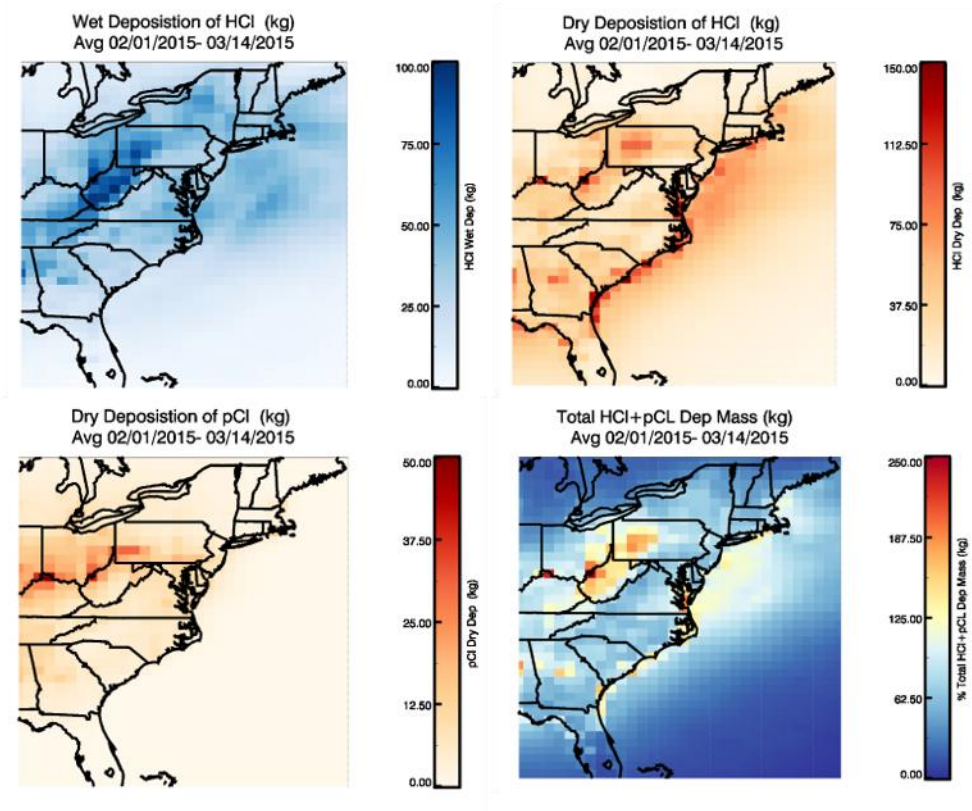

Figure 1.2 GEOS-Chem Cl Deposition Patterns during WINTER

Average wet and dry deposition of HCl and pCl^- within the WINTER campaign domain during the WINTER campaign predicted within GEOS-Chem.

Chapter 2

Anthropogenic control over wintertime oxidation of atmospheric pollutants

2.1 INTRODUCTION

Atmospheric primary radicals, formed from the photolysis of closed-shell molecules, initiate, and sustain oxidation cycles during air pollution episodes. Understanding the sources of these radicals is a key scientific challenge for designing pollution mitigation strategies because they drive conversion of primary pollutants into secondary pollutants such as ozone (O_3) and fine particulate matter ($PM_{2.5}$). In summer, production of hydroxyl radicals (OH) through O_3 photolysis is often the dominant daily integrated primary radical source due to high water vapor, O_3, and solar radiation.

$$O_3 + h\nu\ (\lambda < 320\ nm) + H_2O \rightarrow 2OH + O_2 \qquad (2.1)$$

Other smaller summertime sources of hydrogen oxide radicals ($HO_x = OH + HO_2$) can include formaldehyde (HCHO) and nitrous acid (HONO) photolysis [Michoud et al 2012; Volkamer et al 2010; Whalley et al., 2018; Young et al., 2014].

During winter, reaction 2.1 is slower by more than an order of magnitude due to reduced sunlight and reduced water vapor [Yienger et al., 1999], suggesting greater importance of other less well quantified radical sources. Moreover, colder temperatures and less photochemical oxidation increase the importance of multiphase interactions, between trace gases, particulate

matter, and cloud and fog droplets, in driving the chemical evolution of primary pollutants. The sources of atypical radical precursors that might drive photochemical oxidation, multiphase chemical processing, and the interplay between these processes remain highly uncertain, and indubitably cause some of the problems air quality models have in describing wintertime air pollution [Edwards et al., 2014; Gao et al., 2016; Heald et al., 2012].

HONO photolysis (2.2) can be an important OH radical source at low light levels typical of winter [Kleffman et al., 2007; VandenBoer et al., 2013; Wong et al., 2012;].

$$HONO + h\nu\ (\lambda<400\ nm) \rightarrow OH + NO \qquad (2.2)$$

HONO is directly emitted from combustion [Kirchstetter et al., 1996], and formed *in situ* from the heterogeneous uptake of NO_2 on surfaces [Stutz et al., 2002; Kleffman et al., 2007]. Daytime HONO concentrations in excess of that expected from these sources are routinely observed [Sorgel et al., 2011; Vander Boer et al., 2013; Wong et al., 2012], leading to numerous *in situ* multiphase production mechanisms being proposed [Spataro & Ianniello, 2014]. However, there is not yet consensus on the abundance, production mechanisms, and seasonality of daytime HONO.

Photochemical oxidation of hydrocarbons in the presence of nitrogen oxide radicals (NO_x = NO + NO_2) can amplify the primary radical sources by leading to photo-labile intermediates such as HCHO [Levy, 1971].

$$HCHO + h\nu\ (\lambda< 340\ nm) + 2O_2 \rightarrow 2HO_2 + CO \qquad (2.3)$$

In the lowest kilometer of the atmosphere, oxidation of the biogenic hydrocarbon, isoprene, is typically the largest regional source of HCHO during summer [Wolfe et al., 2016]. During winter, negligible biogenic isoprene emissions and lower radical concentrations are expected to reduce the production and abundance of HCHO. Thus, the importance of HCHO as a radical

source in winter will depend upon direct emissions of HCHO and potential precursors from inefficient combustion, manufacturing processes, and consumer products, all of which remain poorly constrained [Sigsby et al., 1987; Altshuller, 1993; Anderson et al., 1996; Kelly et al., 1999; McDonald et al., 2018]).

Coincident with seasonal shifts in photochemistry, multiphase chemical processes that occur in aerosol particles and clouds are promoted in winter relative to summer [Shah et al., 2018]. A prime example is dinitrogen pentoxide (N_2O_5), formed from the reaction of NO_2 with O_3 to generate the nitrate radical (NO_3), which, subsequently reacts with another NO_2 molecule (2.4 – 2.5) [Platt et al., 1984]. N_2O_5 hydrolysis on aqueous particles (2.6a) is a major sink of NO_x during winter, which in turn limits daytime radical cycling [Dentener & Crutzen, 1993].

When particles contain chloride, N_2O_5 reactions can also form $ClNO_2$ [Finlayson-Pitts et al., 1989; Behnke et al., 1997], which undergoes photolysis via 2.7 during the early morning, releasing NO_x and highly reactive chlorine atoms (Cl). Cl atoms initiate the oxidation of various hydrocarbons (RH), in some cases up to 100 times faster than OH [Orlando et al., 2003].

$$NO_2 + O_3 \rightarrow NO_3 + O_2 \quad (2.4)$$

$$NO_2 + NO_3 \leftrightharpoons N_2O_5 \quad (2.5)$$

$$N_2O_5 + H_2O\ (het) \rightarrow 2HNO_3 \quad (2.6a)$$

$$N_2O_5 + Cl^-\ (het) \rightarrow NO_3^- + ClNO_2 \quad (2.6b)$$

$$ClNO_2 + h\nu \rightarrow Cl + NO_2 \quad (2.7)$$

$$Cl + RH \xrightarrow{+O_2} HCl + RO_2 \quad (2.8)$$

Resolving whether the multiphase chemistry of N_2O_5 is a net sink of radical precursors (via 2.6a), or source of radical precursors (2.6b) during winter is a key challenge.

In this work, we utilize recent observations from the Wintertime Investigation of Transport, Emissions, and Reactivity (WINTER) campaign to assess the wintertime primary radical sources in polluted regions of the eastern United States. We find that in polluted air, the regional daily integrated primary radical source is dominated by $ClNO_2$, HCHO, and to a lesser extent HONO.

2.2 WINTER FIELD CAMPAIGN OVERVIEW

The NSF/NCAR C-130 aircraft was utilized during the WINTER campaign to make airborne observations of many of the above radical precursors as well as related primary and secondary pollutants from February 1 – March 15, 2015. The main observing platform was the instrumented NSF/NCAR C-130 research aircraft, which was based out of the NASA Langley Research Center, located in Hampton, VA. The C-130 made a total of 13 research flights (Figure 2.1), typically lasting 8 hours, for a total of 96 flight hours. About 50% of flight time occurred during daylight hours while the other half occurred in the dark. Additionally, a similar number of research flight hours were spent over land as in the marine boundary layer off the eastern coast of the U.S., from north of Cape Cod, Massachusetts to central Florida. The majority (70%) of sampling occurred within the first 1.5 km of the Earth surface to focus on the near-field evolution of atmospheric pollutant in the planetary boundary layer, although all research flights included periodic vertical profiling through the boundary layer and into the middle free troposphere to characterize the composition of overlying air masses. The typical maximum altitude sampled during WINTER flights was ~ 5 km above sea level.

2.3 MEASUREMENT METHODS

Table 2.1 lists the instrumentation operated aboard the C-130 during WINTER. Most of these instruments are well described in the literature as operated during WINTER, and the associated references should therefore be consulted for more details. In this manuscript, we utilize observations from a iodide high-resolution time of flight chemical ionization mass spectrometer (I-ToF-CIMS), a high-resolution aerosol mass spectrometer (AMS), a cavity ringdown instrument to measure N_2O_5 via thermal dissociation and direct absorption of NO_3, a multi-channel speciated reactive nitrogen (NO_y) instruments based on thermal dissociation and optical detection of NO_2, a total reactive nitrogen (NO_y) and nitric oxide (NO) instrument based on chemiluminescence from the reaction of NO with ozone (O_3), and a formaldehyde laser-induced fluorescence instrument. Sparks et al. (2019) provide a detailed comparison reactive nitrogen measurement on the C-130.

2.3.1 *University of Washington HRToF-CIMS*

The UW HRToF-CIMS used Iodide adduct ionization as described previously, [Lee et al., 2014; Lee et al., 2018] to detect a suite of reactive nitrogen, halogen and organic compounds, with the most relevant for this work being N_2O_5, $ClNO_2$, Cl_2, and HNO_3, at parts per trillion detection limits. The ability of Iodide CIMS to detect these species at high time resolution (1 Hz), has been well established [Kercher et al., 2009; Mielke et al., 2011; Lee et al., 2014; Bannan et al., 2015; Iyer et al., 2016]. The general performance of the instrument and detailed upgrades to the sampling inlet, background determinations, calibrations and ionization region during the WINTER campaign are presented in Lee et al., (2018). A few of these upgrades are discussed below in the context of the in-flight operation.

2.3.2 *Formaldehyde LIF*

The in-Situ Airborne Formaldehyde instrument (ISAF) was used to detect gas-phase formaldehyde (HCHO) during the WINTER campaign, operating at 1 Hz, as previously described in Cazorla et al. (2015). Estimated accuracy of reported HCHO mixing ratios is estimated at ±10 %, based on calibration against IR and UV absorption of a primary HCHO standard. At 1 Hz, precision is > 20% above 100 pptv, which was typical of the nocturnal WINTER measurements used in this work (see Figure 2.2). At low mixing ratios, uncertainty in the signal background contributes more to the variability in precision. Detection limits at 1 Hz for a signal to noise ratio of 2 is 36 pptv for 10 mW of laser power.

2.3.3 *Chemiluminescence NO_y*

NO, NO_y, and O_3 were measured with the National Center for Atmospheric Research (NCAR) Chemiluminescence Detector (CL) [Walega et al., 1991; Weinheimer et al., 1993] with accuracies for O_3, NO, and NOy of 5%, 10%, and 50% respectively [Sparks et al., 2019]. NO_y. NO_y and O_3 are sampled through a Teflon temperature controlled, rear facing inlet to avoid the intake of large particles. NO_y is measured via catalytic conversion of its component species to NO which in turn is detected by means of its chemiluminescent reaction with reagent O_3 that is added to the airstream [Walega et al., 1991]. O_3 is measured via the same chemiluminescent reaction but produced by the addition of reagent NO to the airstream [Ridley et al., 1992].

2.3.4 *Cavity Ring-Down Spectrometer*

NO, NO_2, O_3, NO_y, and N_2O_5 were measured with a NOAA custom built cavity ring-down spectrometer (CRDS) following the methods described in Fuchs et al. [2009]), Washenfelder et al. [2011].), and Wild et al., (2014). The accuracy for NO_2, NO, and O_3 during WINTER were better than 4% for research flights 4-13 (McDuffie et al., 2018a). A quartz oven (650° C) was used to convert reactive nitrogen oxides (NO_y) to NO_2 (or NO) allowing for detection using methods following Wild et al. [2014]. The accuracy and detection limits for NO_y were better than 12% and between 50-380 pptv (2σ, 1s), respectively. N_2O_5 was measured after thermal dissociation (130°C) to NO_3 and subsequent subtraction of ambient NO_3, which was measured in a separate channel by direct absorption at 662 nm [Dubé et al., 2006]. The accuracy and detection limits for CRDS N_2O_5 were better than 12% and ranged from 1.3-4.4 pptv (2σ, 1s), respectively.

2.3.5 *High-Resolution Aerosol Mass Spectrometer*

A highly customized high-resolution time of flight aerosol mass spectrometer (HR-ToF-AMS, Aerodyne Research Inc, referred to as "AMS") measured non-refractory composition of PM_1. The theory and operation of the AMS has previously been described in detail [Jayne et al., 2000; DeCarlo et al., 2006; Canagaratna et al., 2007; Dunlea et al., 2009; Jimenez et al., 2009; Kimmel et al., 2011]. In-field calibrations for both nitrate and chloride were performed multiple times throughout the campaign. Detection limits for nitrate and chloride were 0.07 μg sm^{-3} for a 1-sec sampling interval (sm^{-3} refers to standard cubic meters at 273 K and 1 atm). Accuracy for AMS detection of inorganic species is estimated as +/-35% [Bahreini et al., 2008]. Semi-refractory species, such as $NaNO_3$ (sodium nitrate) and Na_2SO_4 (sodium sulfate), are

inefficiently detected by the AMS [Hayes et al., 2013] and AMS data have sometimes been used to estimate the fractions of ammonium nitrate and organic nitrates using the measured NO_2^+/NO^+ ion ratio from the AMS [Fry et al., 2013; Farmer et al., 2010]. However, in this study, the presence of particulate nitrite and the likely partial detection of $NaNO_3$ made that method indeterminate. For that reason, in addition to total measured nitrate, estimates were made of total inorganic nitrate concentrations based on comparisons of the AMS data to the IC-based instruments. For this campaign, the chloride signal was corrected for a recently discovered small vaporizer interference [Hu et al., 2017] when sampling under high particulate nitrate conditions. Other operational specifics for the AMS during the WINTER campaign can be found in Schroder et al., (2018).

2.3.6 *TDLIF (sum PNs)*

NO_2, the sum of peroxy nitrates (ΣPNs), the sum of alkyl nitrates (ΣANs), and HNO_3 were measured by the University of California Berkeley Thermal Dissociation – Laser Induced Fluorescence Instrument (TD-LIF) (Day et al., 2002; Wooldridge et al., 2010; Kenagy et al., 2018). The accuracy and detection limits of the TD-LIF measurements of ΣPNs, ΣANs, and HNO_3 depend on the accuracy of the primary measurement of NO_2, the precision of the calibration in the different detection cells, the conversion efficiency in the inlet, and the transmission efficiency of the inlet. The estimated accuracy of the NO_2 measurements during WINTER was 5%, with a detection limit of 20 pptv.

2.4 INSTANTANEOUS RADICAL SOURCE CALCULATIONS

We use two approaches to estimating the source of radicals important to atmospheric

oxidation from the *in-situ* observations made during WINTER: instantaneous and daily integrated (Section 2.5). Apart from alkene ozonolysis and HO_x production from Cl reaction with alkenes, most atmospheric radicals are produced from photolysis of closed shell precursors. Therefore, the instantaneous source of radicals throughout the majority of the WINTER domain will be the sum of local photolysis rates for each precursor, as shown in equations 2.1 and 2.2.

$$P_i(t) = n_i j_i(t)[X_i(t)] \qquad \text{[molec cm}^{-3}\text{ s}^{-1}\text{]} \qquad (2.1)$$

$$P_{total}(t) = \sum_i n_i j_i(t)[X_i(t)] \qquad \text{[molec cm}^{-3}\text{ s}^{-1}\text{]} \qquad (2.2)$$

In equations 2.1 and 2.2, *n* are species specific stoichiometric coefficients representing the number of radicals produced per photolysis event of species X_i. The j_i is the time (and thus also space) dependent photolysis frequencies of species X_i. We use *in situ* measurements of both j_i values and precursor concentrations and literature values of n_i to calculate the instantaneous radical production rate for a given species. We then sum across these rates for all species considered to obtain the total. These instantaneous radical source calculations carry the fewest assumptions but can only be calculated from daytime data and cannot provide accurate estimates of radical sources which may have already undergone photolysis prior to intercepting the air mass with the C-130. Therefore, we also calculate estimates of a daily integrated version of equations 2.1 and 2.2, discussed below.

2.5 Daily Integrated Radical Source Calculations

There is a wide distribution in the atmospheric lifetimes of potentially important radical sources. For example, the local noon lifetime of $ClNO_2$ is approximately 30 minutes, while that for O_3 undergoing reaction 2.1 is on the order of a day. Moreover, $ClNO_2$ production is negligible during the daytime, such that for most of the day [$ClNO_2$] ~0, even though its

photolysis may have resulted in a significant source of Cl atoms in the first few hours after sunrise. Therefore, to obtain a more complete picture of the importance of various short-lived radical sources we calculate daily integrated radical production rates.

$$P_i(24h) = \int n_i j_i(t)[X_i(t)]dt \quad (2.3)$$

Noting that for $ClNO_2$, Cl_2, and HONO, which we assume are not produced during the day and which have lifetimes due to photolysis that are shorter than ~4 hours, then from mass balance considerations, equation 2.3 simplifies to:

$$P_i = n_i[X_i]_{t0} \quad (2.4)$$

where $[X_i]_{t0}$ is the concentration of precursor X present at sunrise. We use the concentrations of species observed at night or in the very early morning as an approximation. In Section 2.7, we discuss an extrapolation of values observed at night to a representative sunrise concentration, where the extrapolation is based on known chemistry. But, in general we use only the observed values, which may then underestimate the appropriate concentration for use in equation 2.4 if there is continued production of the precursor from the measurement time to sunrise time. Thus, for $ClNO_2$ and HONO, our estimates of its contribution are likely conservative, in that they could be larger given the potential for continued production (or emission in the case of HONO) throughout the night.

For O_3 and HCHO a better approximation is that their concentrations are constant throughout the day. This assumption accounts for the slower photochemical losses and allows for some photochemical production during the day offsetting the loss due to photolysis. We did not observe a strong dependence of boundary layer average [O_3] and [HCHO] on time of day, consistent with this approximation. In this case, equation 2.3 simplifies to equation 2.5.

$$P_i = n_i[X_i]_{t0} \int j_i(t)dt \quad (S5)$$

The j_i values for equation 2.5 are obtained from the average measured photolysis frequencies within the boundary layer throughout the WINTER campaign. The daily integrated source calculations assume there is no significant recycling of radical precursors throughout the day, which may not be the case for HONO or Cl_2, and neglects dilution due to plume spreading or entrainment. This latter assumption depends strongly on the vertical distribution of precursors throughout the planetary boundary layer and the extent of vertical mixing that occurs throughout the day. As the C-130 was most often within the residual layer of the convectively mixed boundary layer at night, or the mixed layer during the day, this assumption is reasonable. While high concentrations of precursors, such as HONO are highly localized in the first 100 m above the surface at night, the C-130 did not sample those concentrations very often (on the 0.1 to 1 Hz observation frequency used herein) and so the averages shown in our results minimize their impact on our conclusions.

2.6 F0AM Box Modeling

The Framework for 0-D Atmospheric Modeling (F0AM) was initialized using concentrations of N_2O_5, $ClNO_2$, HNO_3, and HONO from the CIMS, HCHO from the ISAF, and NO, NO_2, and O_3 from the CRDS, at the point of observation of when the maximum concentration of $ClNO_2$ was observed, which occurred on RF 08 at 06:36 local time on 3/1/2015 off the coast of Long Island. Additionally, the model was initialized earlier in that morning (06:16 local time) when $ClNO_2$ concentrations (400 pptv) were close to the median of observed $ClNO_2$ concentrations at night within the boundary layer during this flight to test the median impacts of Cl on the oxidant budget, in addition to the extremes, within the WINTER boundary.

Measurements of VOCs from the NCAR Trace Organic Gas Analyzer (TOGA) were not

available on this flight due to an instrumental problem. Therefore, observations from Research Flight 3, which sampled a similar spatial domain when the TOGA was operational, were used to correlate all observed VOCs with CO to derive a separate linear fit for each observable VOC (propane, formaldehye, iso-butene, n-butane, acetaldehyde, methylbromide, isopentane, n-pentane, methanol, ethanol, acrolein, propanal, acetone, 2-methylpentane, 3-methylpentane n-hexane, dichloromethane, methacrolein, butanal, methyl-ethyl-keytone, chloroform, ethylnitrate, benzene, n-heptane, dibromoethane, toluene o-xylene, 1-2-4-trimethylbenzene 1-2-3-trimethylbenzene, tertbutylnitrate, 2-butylnitrate, n-butyloxy). These fits were then used to estimate VOC concentrations on Research Flight 8 based on the measured CO as shown below in Figure 2.3. This model does not include the dynamics of mixing, or deposition, but does assume a constant dilution rate of 1 s^{-1} and is initialized with concentrations within the well-mixed residual layer.

Photolysis frequencies were calculated using the TUV radiation model under the observed conditions assuming clear sky conditions and scaled to match observed photolysis frequencies at the time of intercept. The model was run for a period of 4 days to allow sufficient spin-up time, starting at the time of observation holding only CH_4 and CO constant, updating the solar parameters in 30-minute time steps. At the end of each full day, the observed concentrations were set back to their observation (at 6:36:49 local time), while concentrations of VOCs that were not initialized came into steady state and accumulated in concentration, while still undergoing a diurnal cycle. A 4 day spin up was required for these non-observed VOCs to come into steady state (same end of day and beginning of day concentrations), after which, increasing the spin up period had little effect on the non-observed VOC concentrations. The concentrations of the unobserved VOCs do not accumulate unencumbered, as they respond to the

diurnal cycle of other compounds. For example, in Figure 2.4 several observed (HCHO) and unobserved VOCs (PAN, APN) are shown. It can be seen here that the profiles of the unobserved VOCs begin the day and end the day with the same concentration at the end of the spin up period. Sensitivity simulations preformed using only a 2 day spin up period showed radical budget changes were not greater than 3%. The results presented here, therefore, are not significantly sensitive to the selected spin up time, given that most changes occur within a single day.

At the end of the 3rd day of the spin up period, all compounds could freely evolve while CH_4 and CO were held constant. Results shown are from the 4th day of the simulation during the free evolution period. Figure 2.5 summarizes the flow of WINTER observations, TUV model input and spin up operation within F0AM. Reactions included are from the Master Chemical Mechanism version 3.3.1 and the Riedel et al. (2014) chlorine reaction mechanism. Heterogeneous N_2O_5 formation is implemented by assuming a constant source of wet aerosol surface area density of 3.61×10^{-6} cm^2 cm^{-3} derived from onboard measurements of dry aerosol number distributions at the time of plume intercept, following the method described in McDuffie et al. (2018), and a constant aerosol uptake coefficient of 0.006. Heterogeneous $ClNO_2$ formation was implemented assuming a yield of 1.0. These uptake and yield values were chosen arbitrarily and do not affect the radical budget calculated following the next day since the concentrations of $ClNO_2$ and N_2O_5 are set back to observations at the end of the night before the radical budget is allowed to freely evolve as the sun rises the following morning.

2.7 Results and Analysis

Using the suite of *in situ* observations made during WINTER, we can assess the

contribution of each radical source discussed above to the oxidative capacity of the wintertime troposphere. For example, observations of all components involved in the conversion of NO_x to N_2O_5 and its multiphase reaction products (Figure 2.6) were made during a flight downwind of New York City, when westerly winds exported urban NO_x emissions into the marine boundary layer (MBL) over the Atlantic Ocean. Mixing ratios of $ClNO_2$, N_2O_5, HNO_3, and HONO measured by mass spectrometry, together with NO and NO_2 measured by chemiluminescence and cavity ring-down spectroscopy (Figure 2.6, top panels) explain the independently measured sum total of reactive nitrogen oxides (NO_y= NO_x + 2* N_2O_5 +$ClNO_2$ +HNO_3 +HONO + alkyl nitrates (ANs) + peroxy acetyl nitrates (PNs)) at all points along this flight (Figure 2.6, bottom). Our observations show that ~25-60% of NO_x is converted to N_2O_5 on this flight, with ~93% reacting in the MBL to form HNO_3 and $ClNO_2$ [Jaeglé et al., 2018], highlighting the importance of multiphase chemistry under such conditions.

We use the observed nighttime concentrations of O_3, $ClNO_2$, HCHO, and HONO together with average WINTER measured photolysis frequencies to calculate the total integrated concentration of radicals that would be produced by these precursors over the following day (Section 2.5). Other radical sources, such as alkene ozonolysis or dihalogen (Cl_2) photolysis (See Chapter 3), were < 5% on a regional basis during WINTER (Figure 2.7, Figure 2.8). While the nocturnal surface layer is poorly mixed over land, vertical profiling performed by the aircraft allowed us to assess the vertical extent of these radical precursors. We found the MBL to be well mixed up to 800-1500 m altitude (e.g Figure 2.7), allowing more straightforward calculations of radical sources from measured concentrations.

During the flight shown in Figure 2.6, $ClNO_2$ becomes the largest measured radical reservoir, contributing at least 38% to the calculated next-day integrated radical source, with

similar contributions from HCHO and O_3 (reactions 2.1 and 2.3), but negligible contributions from HONO. This integrated radical source calculation is based upon measurements made before local midnight, and several more hours of $ClNO_2$ production could be expected. Assuming N_2O_5 formation continued as observed NO_2 and O_3 would suggest, and an N_2O_5 reactivity on aerosols from in situ observations [McDuffie et al., 2018a; McDuffie et al., 2018b], we estimate $ClNO_2$ concentrations would increase throughout the night and account for as much as 80% ($[ClNO_2]$~1500 pptv) of the integrated radical source the next day. This result, assuming no further changes to O_3, HCHO, or HONO, highlights the important role of anthropogenic NO_x emissions in wintertime radical sources. Estimates of $ClNO_2$ contributions to the summertime radical budget have been substantially less (8-20%) [Young et al., 2014].

During a second WINTER flight, a stalled high-pressure system offshore of New Jersey (Figure 2.7) allowed us to probe the instantaneous morning radical source (Section 2.4) in pollution from the New York City area that had aged overnight in the MBL. As the sun rose, vertical profiles (Figure 2.7) with the aircraft revealed that the observed instantaneous radical source from $ClNO_2$ photolysis, $j_{ClNO2}(t)*[ClNO_2(t)]$, was 60-80% of the total instantaneous radical source throughout the entire MBL.

During this flight, HONO photolysis was the next largest instantaneous radical source. Contributions from Cl_2 were low, given small (<15 pptv) observed concentrations [Haskins et al., 2018]. $ClNO_2$ reactive uptake to form Cl_2, which would amplify the radical source stemming from N_2O_5 chemistry, was also small [Haskins et al., 2019, Chapter 3]. Reaction 2.1 was negligible in the flight shown in Figure 2.7. O_3 mixing ratios are often suppressed in NO_x-rich air masses during the night and morning, in part due to nighttime N_2O_5 chemistry which removes O_3 (reactions 2.2-2.4) [Brown et al., 2006;]. The aircraft departed the area (segment E, Figure 2.7a)

flying above the MBL where we find that the radical source is dominated by that from O_3 photolysis (reaction 2.1), as expected, given the steep gradients in $ClNO_2$ between the polluted boundary layer and free troposphere.

To further evaluate the implications of these results, we use a chemically explicit Master Chemical Mechanism based 0-D model (F0AM [Wolfe et al., 2016]) to simulate radical chemistry during the full day following the interception of these plumes. We perform two simulations, including and excluding reactions of Cl atoms with various VOCs (reactions 2.8b-2.10), using the mechanism described in Riedel et al. (2014). The model is initialized with WINTER measurements of VOCs and other gas-phase species including HCHO, HONO, O_3, N_2O_5, and $ClNO_2$. Figure 2.9 shows the modeled instantaneous radical production occurring for 16 hours following our interception of the maximum $ClNO_2$ concentration (6:36AM, location "D", Figure 2.7). A time series of the modeled concentrations of relevant species is shown in Figure 2.4 for the simulations with and without chlorine reactions. Like other box models, nighttime RO_2+RO_2 reaction rates in the absence of NO are highly uncertain (Stevens et al., 1997), resulting in considerable uncertainty in the simulated nighttime RO_2 concentrations. We also initialized the model with median $ClNO_2$ concentration from all intercepts in this flight, and results presented in parenthesis below are all for the simulation using the initialized median $ClNO_2$ concentrations.

Consistent with our above observational analysis, the model predicts an instantaneous radical production rate from $ClNO_2$ that is a factor of 5-12 larger than the next largest radical source between 6 am and 11 am (Figure 2.9). $ClNO_2$ also dominates the total daily integrated radical source predicted with the model. The simulation including chlorine chemistry produced 2.5 ppbv of radicals ($Cl + HO_x + RO_2$) by day's end, which is a factor of 3.75 larger than that

predicted without chlorine chemistry. The increase in radical production stems from Cl radicals from $ClNO_2$ photolysis, a secondary 114% enhancement (0.62 ppbv) in HCHO due to Cl radical initiated VOC oxidation and an increase in ozone production (as described in Figure 2.10). Using median $ClNO_2$ concentrations similarly led to the total radical source being a factor of 3.1 larger than when neglecting Cl radical chemistry. The magnitude of the HO_x enhancement could be different for different locations and time periods, especially with a different mix of VOC, but these results underscore that including Cl-atom chemistry from $ClNO_2$ is necessary to represent wintertime oxidation, given the secondary impacts of Cl atoms on HCHO and O_3.

The underestimate in the total integrated daily radical budget observed in F0AM from excluding reactions involving chlorine occurs primarily from excluding the early morning source of Cl radicals from $ClNO_2$ photolysis, but also from a 114% (40%) enhancement or 0.62 ppbv (0.1 ppbv) in the integrated daily [HCHO] that occurred because of an increase in VOC oxidation by those Cl radicals and an increase in the daily integrated ozone production of 4.7 ppbv (1.5 ppbv), thereby increasing the local source of OH from O_3 photolysis. Figure 2.11 a and b show that most of the increase in the production of O_3 and HCHO that results occurs early in the day immediately following $ClNO_2$ photolysis. The increase in production of HCHO that occurs in the simulation including chlorine reactions primarily results from an increase in the concentration of CH_3O, an oxidation product of VOCs + Cl, primarily CH_4, in the early morning, but also from Cl oxidation of CH_3OH, which occurs faster than its oxidation by OH as shown in Figure 2.11 c and d. The loss rates of HCHO also significantly increase in the simulation including chlorine reactions compared to that without, though not at the same time of day as the production of HCHO does, such that the simulation including Cl_y reactions shows the largest difference in predicted HCHO concentration in the hours immediately following $ClNO_2$

photolysis at around 11am local time (Figure 2.4). It is possible that the enhancement in HO_x shown above, could be larger, given that the measured VOC concentrations used in the spin up are a lower limit to total VOC concentrations, since they exclude some number of alkenes that are highly reactive with Cl, such as fossil fuel derived alkenes (not including aromatics), that may not be well represented in a box model that does not take into account direct emissions. Therefore, the total speciation of alkenes in the wintertime may extend the anthropogenic impact of emissions on the oxidant budget during winter beyond what we are able to constrain and show here, by impacting HCHO, and therefore HOx yields.

We apply the above daily integrated radical source analysis to the wider set of flights (Section 2.5) using predicted photolysis rates and observations of the radical precursors made at night and early morning within 1 km of the surface. Daytime observations underestimate the overall contributions of HONO and $ClNO_2$ to the total primary radical source because both species photolyze rapidly and may not be reformed until night. The results, shown in Figure 2.12, illustrate that >70% of the wintertime radical source in polluted air (represented by increasing NO_x) stems not from reaction 2.1 as it would in summer, but from $ClNO_2$, HCHO, and HONO photolysis. $ClNO_2$ and HCHO tend to dominate, but with a strong spatial (vertical and horizontal) dependence reflecting distribution of emission sources, relative lifetimes, and mixing.

Figure 2.13 shows a broader comparison of the different radical sources constrained by the WINTER observations. The panels show cumulative distribution functions for the contribution of each specific radical source to the total daily integrated source derived from measurements over land (a) and in the marine boundary layer (b) to demonstrate how often a particular radical source made a given contribution to the overall radical budget. We relaxed our

selection criteria compared to the calculations shown in Figure 2.12, requiring only that NO_x> 2ppb and the C-130 altitude < 1 km, but otherwise the data used for Figure 2.13 is the same as in Figure 2.12. These distributions illustrate that over land, $ClNO_2$ is only rarely a major component of the daily radical source, contributing less than 20% of the total radical source in more than 80% of the determinations. In half the measurements over land, HCHO and HONO accounted for ~50% and ~30%, respectively, of the total daily radical source. In over half the measurements in the MBL, $ClNO_2$ represented about 40% of the total daily radical source, with minimal importance from HONO. These statistics do not include a potential source of HONO from pNO_3^- photolysis.

The control of local and regional anthropogenic emissions on primary radical sources during winter is evident when considering the contributions of HCHO. HCHO contributes most to the observed radical budget outside of the MBL (Figure 2.6 and Figure 2.12). Jaeglé et al., (2018) showed that the standard GEOS-Chem model underestimated observed HCHO during WINTER by a factor of 2 but increasing anthropogenic emissions of HCHO from 10% to 30% of the total HCHO source brought the model into agreement. Increasing emissions of short-lived anthropogenic HCHO precursors, such as ethene and other primary alkenes, followed by their oxidation to form HCHO would also be consistent with the WINTER observations. The extent to which measured alkenes explain the HCHO should be evaluated. Ultimately, the resulting modeled wintertime HCHO is primarily from anthropogenic sources, in stark contrast to summer. Although smaller than the isoprene dominated source in summertime [Fortems-Cheiney et al., 2012; Luecken et al., 2012; Wolfe et al., 2016], the total HCHO source we estimate during WINTER demonstrates the seasonally varying sensitivity of the radical budget to both anthropogenic and biogenic VOC emissions.

2.8 ESTIMATES OF HONO PRODUCTION FROM pNO_3^-

Given that the above analysis does not rule out a role for pNO_3^- photolysis as a source of HONO, for comparison with the results shown in the main manuscript, we include in our estimates of the daily integrated radical source pNO_3^- photolysis to form HONO as prescribed by Ye et al. (2016) using a pNO_3^- photolysis enhancement factor (EF) of either 300 or 30 [Romer et al., 2018]. The results of those calculations, similar to those shown in Figure 2.12, are presented in Figure 2.14. The importance of the HONO source from pNO_3^- photolysis is largest in polluted air (light and dark gray bars). The relative importance of pNO_3^- photolysis as a daytime HONO production channel, and therefore OH source relative to other oxidant sources, largely depends the photolysis EF chosen, underscoring the need for further constraints on this process. At maximum, both over land and in the MBL pNO_3^- photolysis could account for up to 11 – 33% of the total daily radical source if using an EF of 300, though this is likely an overestimation. More in line with our far field HONO measurements, this pathway only accounts for 1-4% of the total daily radical source if using an EF of 30 (Romer et al., 2018).

The measured nighttime HONO concentrations during WINTER imply it is a small but non-negligible contributor to the primary daytime radical source, especially in urban areas close to the surface (<100 m), but not in the MBL. For example, HONO contributed a maximum of 8% to the projected daily radical budget on the flight shown in Figure 2.6, but over land HONO contributed 10-20% to the radical budget at the lowest altitudes surveyed, consistent with its main sources being tied to anthropogenic emissions. Somewhat surprisingly, our observations suggest a smaller role for HONO on a regional basis in the daily integrated radical budget than might be inferred from ground-based observations [Whalley et al., 2018]. Near-source

measurements in a poorly mixed nocturnal atmosphere may tend to overestimate the regional impact of this source [Febo et al., 1996; Stutz et al., 2002; Wong et al., 2012].

The photolysis of nitrate on surfaces and in the condensed phase to produce NO_x and HONO has been well documented in laboratory studies and snow packs [Zhou et al., 2003; Zhu et al., 2010; Du et al., 2011; Baergen et al., 2013;]. Recently, Ye et al. (2016) showed that nitrate photolysis in aerosol particles (pNO_3^-) could produce HONO at rates capable of explaining HONO mixing ratios observed in the summertime marine boundary layer of the western Atlantic Ocean, just south of the typical WINTER flight domain. Romer et al., (2018) provided an upper limit on how much more efficiently pNO_3^- could photolyze relative to HNO_3, during 6 different aircraft campaigns, given that the fastest proposed photolysis rate is inconsistent with observed NO_x to HNO_3 ratios. Using the proposed parameterization of pNO_3^- photolysis, which is referenced to gas-phase HNO_3 photolysis frequencies, and constrained with observed values of $j(HNO_3)$ and j(HONO), we predicted daytime HONO mixing ratios using both a pNO_3^- photolysis EF of 300 (Ye et al., 2016) and 30 (Romer et al., 2018) with the AMS pNO_3^- measurements and the filter measurements of pNO_3^- that were made in WINTER.

The comparison between predicted and observed daytime enhancements in HONO observed below 1 km for the WINTER campaign are shown in Figure 2.15. Potential biases could arise from direct emissions of HONO sampled near urban areas and ships. Therefore, we show results where we bin the comparison to different ranges in the NO_x/NO_y, which is an indicator of air mass age since NO_x emissions occurred. In all plumes, better correlation between parameterization predictions of HONO and observations are seen using the filter measurement of pNO_3^- ($D_p < 4.1$ μm) than the AMS pNO_3^- ($D_p < 1$μm). This is likely because of the more complete sampling of the size distribution of pNO_3^- captured from the filter measurements given

the low cutoff of the AMS inlet during WINTER. At the lowest NO_x/NO_y ratio, in air less affected by direct HONO emissions, the observed enhancement of HONO is low and better correlated using a pNO_3^- EF of 30, but regardless of which pNO_3^- measurement is used, the enhancement in HONO is near the limit of detection of the I^- CIMS (see above). This indicates that in aged air, if HONO is indeed created from secondary processes like the photolysis of pNO_3^-, the enhancement is too low for our instrument to confidently detect.

At the highest NO_x/NO_y ratios, in areas of fresh NO_x emissions, the observed and predicted HONO concentrations are better correlated using an EF of 300. However, direct emission of HONO from industrial processes in NO_x rich air could be contributing to the observed concentrations, in which case, this method of analysis is not appropriate for extracting an EF. Predictions from the F0AM modeling presented above indicate that requiring a sink of total nitrate using an EF of 300 under WINTER conditions would be an order of magnitude faster than $OH+NO_2$ creating total nitrate, such that the total nitrate lifetime becomes unrealistically short (e.g. < 12 hours) with predicted total nitrate concentrations falling to 0 before sunset, as shown in Figure 2.16.

The results in Figure 2.15 suggest that pNO_3^- photolysis as fast as the Ye et al. (2016) parameterization, would tend to overestimate HONO during the WINTER campaign away from relatively fresh NO_x emissions, while using a pNO_3^- photolysis EF of 10-30 from Romer et al., (2018), would generally tend to explain observed HONO. However, given that all of the far field measurements of HONO during WINTER are at or below the limit of detection, our measurements cannot quantify an appropriate EF for pNO_3^- photolysis producing daytime HONO, but do provide further evidence of an EF lower than 300, given the chemical lifetime inconsistencies that would arise if total nitrate was lost so quickly at the observed conditions. We

conclude from this analysis that pNO_3^- photolysis may be an important source of daytime HONO but that our data does not robustly support such a source. Uncertainties in the HONO observations, which in the daytime are typically within a factor of 2 of our estimated limits of detection, and the limited availability of data having both high pNO_3^- and $jHNO_3$ preclude a more direct conclusion.

Recent studies suggest particulate nitrate (pNO_3^-) photolysis may be an important daytime HONO source, but the rate remains debated [Ye et al., 2016; Romer et al., 2018]. We use early morning observations of HONO to predict the production of radicals resulting from its photolysis, assuming no daytime production or further emission of HONO in the analysis presented in Figure 2.12. Therefore, we would under-predict the contribution from HONO to the primary radical sources if photolysis of pNO_3^- or other daytime HONO sources are significant. Our simultaneous observations of pNO_3^- and HONO suggest a slow daytime production of HONO from pNO_3^- photolysis, similar to the rate presented in Romer et al., (2018), which would increase the total radical source shown in Figure 2.12 by ~4% over land, with smaller contributions in the polluted MBL (Figure 2.15). Daytime HONO concentrations were often at or below our detection limit (30 pptv), thus we can only constrain an upper limit source of daytime HONO.

2.9 Impacts of Increased Oxidants

HCHO emissions, the multiphase chemistry of NO_x, and aerosol processes that produce and directly affect $ClNO_2$, pNO_3^-, and HONO concentrations, are highly parameterized components of air quality and chemistry-climate models, if included at all [Evans & Jacob et al., 2005; Riemer et al., 2003]. Increasing anthropogenic HCHO sources [Jaeglé et al., 2018] and

implementing the production of $ClNO_2$ [Shah et al., 2018] in the GEOS-Chem model, we find significant impacts on primary and secondary pollutant abundance and air quality metrics relative to the standard model run (shown in Figure 2.17). For example, $PM_{2.5}$ components, such as SOA and sulfate increase by 0.3 $\mu g/m^3$ (20-30%) and 0.12 $\mu g/m^3$ (2-6%), respectively, while nitrate decreases by up to 0.25 $\mu g/m^3$ (0-5%) [Jaeglé et al., 2018;], and NO_x shifts further into its labile reservoirs, such as peroxy acetyl nitrate (PAN, see Figure 2.18). Given PAN's longer lifetime in winter, this transports NO_x further downwind than during summer. These changes are driven by 40-80% increases in HO_x and RO_2 radical concentrations across the WINTER domain from increased HCHO photolysis and VOC + Cl reactions, with concomitant increases in ozone production.

Wintertime sulfate is often underestimated by air quality models, while pNO_3^- and nitrate deposition over land have been overestimated [Tesche et al., 2002; Heald et al., 2012; Walker et al., 2012; Gao et al., 2016]. The increases in regional radical sources and changes to NO_x multiphase chemistry we suggest reduce such discrepancies [Jaeglé et al., 2018; Shah et al., 2018] and also halve GEOS-Chem underestimates (from 30% to 15% bias) of measured total peroxy nitrates (such as PAN). Recent results show that while models of the WINTER domain predict organic aerosol (OA) from primary sources, most OA sampled is formed secondarily in processes like those that occur during summer [Schroder et al., 2018]. Ultimately, our results provide support for increased oxidation initiated by atypical radical precursors, and increased export of NO_x reservoirs to the global free troposphere.

2.10 CONCLUSIONS

We have shown that anthropogenic emissions of NO_x, and HCHO and its precursors,

exert control over radical sources in polluted air during winter. We provide novel and unique observational confirmation that conversion of NO_2 to $ClNO_2$ represents a critically important wintertime radical source throughout the polluted MBL. In polluted maritime regions, we find that Cl atoms from direct $ClNO_2$ photolysis are both the dominant early morning radical source and the dominant integrated daily radical source, and that their presence amplifies the OH source by increasing HCHO formation from VOC + Cl reactions, and increased O_3 production. HCHO is the largest radical source on a regional basis over land, and the dormant wintertime biosphere implies the HCHO sources are dominated by local or regional anthropogenic contributions, either through direct emissions and/or emissions of short-lived precursors, such as primary alkenes.

As the HCHO source evaluation implies, it is possible some reactive VOC, such as alkenes, went unmeasured during the WINTER campaign. Ozonolysis of alkenes produces hydroxyl radicals (OH) from the decomposition of the Criegee intermediate. The TOGA instrument measured a large suite of biogenic alkenes and a smaller set of fossil fuel derived alkenes (not including aromatics). Based on these observed species, alkene ozonolysis was generally negligible, being on average less than 5% of the source from ozone and formaldehyde photolysis (Figure 2.8). In the Northeastern U.S. during winter, emissions of biogenic alkenes are expected to be nearly zero in the case of isoprene, or very low in the case of monoterpenes. The fossil fuel derived alkenes, isobutene and acrolein, contributed equally to radical production as the sum of seven terpenes or their oxidation products (see Figure 2.8). Thus, it is possible that close to fossil fuel or industry related emissions, alkene ozonolysis might be a locally important radical source, but given the short lifetime of alkenes the regional importance is likely significantly less than that of the other radical precursors considered here.

Although the measured suite of alkenes presented a negligible daily integrated source of OH via ozonolysis, the oxidation of unmeasured alkenes by Cl atoms and ozone would further enhance HO_x production compared to our predictions herein, thereby reinforcing our conclusion that regional anthropogenic emissions control the wintertime radical budget. Our results therefore motivate further work to explore the types of VOC and associated Cl more broadly, OH, O_3, and NO_3 reactivity present in polluted wintertime environments.

We find HONO is most important near urban areas close to the surface (<100 m altitude) over land, contributing <8% to the projected daily radical budget within the MBL, which was typically well-mixed from the surface to ~1 km. Our measurements show some support for slower daytime production of HONO from pNO_3^- photolysis than reported by Ye et al. (2016) and more broadly consistent with that presented in Romer et al. (2018). We thus conclude that daytime HONO production and contribution to primary radicals remain uncertain, but likely smaller than previous estimates would have suggested.

The dominant sources of these less commonly considered radical precursors in polluted wintertime air arise largely from local and regional anthropogenic emissions, as opposed to background ozone. Incorporating these sources into a chemical transport model increased predicted $PM_{2.5}$ and export of NO_x to the remote troposphere via PAN, where greenhouse gases such as O_3 and CH_4 are far more sensitive to its presence [Hudman et al., 2004]. Other regions of the world, such as China, Europe, and northern India also experience elevated VOC concentrations from inefficient combustion and high NO_x during winter which may mix with reactive chlorine, especially near coasts or chlorine emissions from coal combustion [Sarwar et al., 2014; Lowe et al., 2015; Li et al., 2016]. Our findings therefore suggest important global-scale revisions to our understanding of wintertime pollution transformations, transport, and

multiphase processes.

2.11 REFERENCES

Altshuller, A. P. (1993). Production of aldehydes as primary emissions and from secondary atmospheric reactions of alkenes and alkanes during the night and early morning hours. Atmospheric Environment. Part A. General Topics, 27(1), 21–32. https://doi.org/https://doi. org/10.1016/0960-1686(93)90067-9

Anderson, L. G., Lanning, J. A., Barrell, R., Miyagishima, J., Jones, R. H., & Wolfe, P. (1996). Source and sinks of formaldehyde and acetaldehyde: An analysis of Denver's ambient concentration data. Atmospheric Environment, 30, 2113–2123. https://doi.org/10.1016/1352-2310(95)00175-1

Baergen, A. M., & Donaldson, D. J. (2013). Photochemical Renoxification of Nitric Acid on Real Urban Grime. *Environmental Science & Technology*, *47*(2), 815–820. https://doi.org/10.1021/es3037862

Bahreini, R., Dunlea, E. J., Matthew, B. M., Simons, C., Docherty, K. S., DeCarlo, P. F., … Middlebrook, A. M. (2008). Design and Operation of a Pressure-Controlled Inlet for Airborne Sampling with an Aerodynamic Aerosol Lens. *Aerosol Science and Technology*, *42*(6), 465–471. https://doi.org/10.1080/02786820802178514

Bannan, T. J., Booth, A. M., Bacak, A., Muller, J. B. A., Leather, K. E., Le Breton, M., … Percival, C. J. (2015). The first UK measurements of nitryl chloride using a chemical ionization mass spectrometer in central London in the summer of 2012, and an investigation of the role of Cl atom oxidation. *Journal of Geophysical Research: Atmospheres*, *120*(11), 5638–5657. https://doi.org/10.1002/2014JD022629

Behnke, W., George, C., Scheer, V., & Zetzsch, C. (1997). Production and decay of ClNO2 from the reaction of gaseous N2O5 with NaCl solution: Bulk and aerosol experiments. Journal of Geophysical Research, 102(D3), 3795–3804. https://doi.org/10.1029/96JD03057

Bertram, T. H., & Thornton, J. A. (2009). Toward a general parameterization of N2O5 reactivity on aqueous particles: the competing effects of particle liquid water, nitrate, and chloride. Atmospheric Chemistry and Physics, 9(21), 8351–8363. https://doi.org/10.5194/acp-9-8351-2009

Brown, S. S., Neuman, J. A., Ryerson, T. B., Trainer, M., Dubé, W. P., Holloway, J. S., et al. (2006). Nocturnal odd-oxygen budget and its implications for ozone loss in the lower troposphere. Geophysical Research Letters, 33, L08801. https://doi.org/10.1029/2006GL025900

Canagaratna, M. R., Jayne, J. T., Jimenez, J. L., Allan, J. D., Alfarra, M. R., Zhang, Q., … Worsnop, D. R. (2007). Chemical and microphysical characterization of ambient aerosols with the aerodyne aerosol mass spectrometer. *Mass Spectrometry Reviews*, *26*(2), 185–222. https://doi.org/10.1002/mas.20115

DeCarlo, P. F., Kimmel, J. R., Trimborn, A., Northway, M. J., Jayne, J. T., Aiken, A. C., … Jimenez, J. L. (2006). Field-Deployable, High-Resolution, Time-of-Flight Aerosol Mass Spectrometer. *Analytical Chemistry*, *78*(24), 8281–8289.

https://doi.org/10.1021/ac061249n

Dentener, F. J., & Crutzen, P. J. (1993). Reaction of N2O5 on tropospheric aerosols: Impact on the global distributions of NOx, O3, and OH. Journal of Geophysical Research, 98(D4), 7149–7163. https://doi.org/10.1029/92JD02979

Du, J., & Zhu, L. (2011). Quantification of the absorption cross sections of surface-adsorbed nitric acid in the 335–365nm region by Brewster angle cavity ring-down spectroscopy. *Chemical Physics Letters*, *511*(4), 213–218. https://doi.org/https://doi.org/10.1016/j.cplett.2011.06.062

Dube, W. P., Brown, S. S., Osthoff, H. D., Nunley, M. R., Ciciora, S. J., Paris, M. W., … Ravishankara, a R. (2006). Aircraft instrument for simultaneous, in situ measurement of NO3 and N2O5 via pulsed cavity ring-down spectroscopy. *Review of Scientific Instruments*, *77*(3). https://doi.org/10.1063/1.2176058

Edwards, P. M., Brown, S. S., Roberts, J. M., Ahmadov, R., Banta, R. M., deGouw, J. A., et al. (2014). High winter ozone pollution from carbonyl photolysis in an oil and gas basin. Nature, 514(7522), 351–354. https://doi.org/10.1038/nature13767

Evans, M. J., & Jacob, D. J. (2005). Impact of new laboratory studies of N2O5 hydrolysis on global model budgets of tropospheric nitrogen oxides, ozone, and OH. Geophysical Research Letters, 32, L09813. https://doi.org/10.1029/2005GL022469

Febo, A., Perrino, C., & Allegrini, I. (1996). Measurement of nitrous acid in Milan, Italy, by DOAS and diffusion denuders. Atmospheric Environment, 30(21), 3599–3609. https://doi.org/https://doi.org/10.1016/1352-2310(96)00069-6

Finlayson-Pitts, B. J., Ezell, M. J., & Pitts, J. N. (1989). Formation of chemically active chlorine compounds by reactions of atmospheric NaCl particles with gaseous N2O5 and ClONO2. Nature, 337(6204), 241–244. https://doi.org/10.1038/337241a0 Fortems-Cheiney, A., Chevallier, F., Pison, I., Bousquet, P., Saunois, M., Szopa, S., et al. (2012). The formaldehyde budget as seen by a global-scale multi-constraint and multi-species inversion system. Atmospheric Chemistry and Physics, 12(15), 6699–6721. https://doi.org/ 10.5194/acp-12-6699-2012

Fry, J. L., Draper, D. C., Zarzana, K. J., Campuzano-Jost, P., Day, D. A., Jimenez, J. L., … Grossberg, N. (2013). Observations of gas- and aerosol-phase organic nitrates at BEACHON-RoMBAS 2011. *Atmos. Chem. Phys.*, *13*(17), 8585–8605. https://doi.org/10.5194/acp-13-8585-2013

Fuchs, H., Dubé, W. P., Lerner, B. M., Wagner, N. L., Williams, E. J., & Brown, S. S. (2009). A Sensitive and Versatile Detector for Atmospheric NO2 and NOX Based on Blue Diode Laser Cavity Ring-Down Spectroscopy. *Environmental Science & Technology*, *43*(20), 7831–7836. https://doi.org/10.1021/es902067h

Fuchs, H., Dubé, W. P., Ciciora, S. J., & Brown, S. S. (2008). Determination of inlet transmission and conversion efficiencies for in situ measurements of the nocturnal nitrogen oxides, NO3, N 2O5 and NO2, via pulsed cavity ring-down spectroscopy. *Analytical Chemistry*, *80*(15), 6010–6017. https://doi.org/10.1021/ac8007253

Gao, M., Carmichael, G. R., Wang, Y., Ji, D., Liu, Z., & Wang, Z. (2016). Improving simulations of sulfate aerosols during winter haze over Northern China: the impacts of heterogeneous oxidation by NO2. Frontiers of Environmental Science & Engineering, 10(5), 1–11. https://doi.org/10.1007/s11783-016-0878-2

Haskins, J. D., Jaeglé, L., Shah, V., Lee, B. H., Lopez-Hilfiker, F. D., Campuzano-Jost, P., et al. (2018). Wintertime gas-particle partitioning and speciation of inorganic chlorine in the lower troposphere over the Northeast United States and Coastal Ocean. Journal of Geophysical Research: Atmospheres, 123, 12,897–12,916. https://doi.org/10.1029/2018JD028786

Haskins, J. D., Lee, B. H., Lopez-Hilifiker, F. D., Peng, Q., Jaeglé, L., Reeves, J. M., et al. (2019). Observational constraints on the formation of Cl2 from the reactive uptake of ClNO2 on aerosols in the polluted marine boundary layer. Journal of Geophysical Research: Atmospheres, 124, 8851–8869. https://doi.org/10.1029/2019JD030627

Hayes, P. L., Ortega, A. M., Cubison, M. J., Froyd, K. D., Zhao, Y., Cliff, S. S., … Jimenez, J. L. (2013). Organic aerosol composition and sources in Pasadena, California, during the 2010 CalNex campaign. *Journal of Geophysical Research Atmospheres*, *118*(16), 9233–9257. https://doi.org/10.1002/jgrd.50530

Heald, C. L., Collett, J. L. Jr., Lee, T., Benedict, K. B., Schwandner, F. M., Li, Y., et al. (2012). Atmospheric ammonia and particulate inorganic nitrogen over the United States. Atmospheric Chemistry and Physics, 12, 10,295–10,312. https://doi.org/10.5194/acp-12-10295-2012

Hu, W., Campuzano-Jost, P., Day, D. A., Croteau, P., Canagaratna, M. R., Jayne, J. T., … Jimenez, J. L. (2017). Evaluation of the new capture vaporizer for aerosol mass spectrometers (AMS) through field studies of inorganic species. *Aerosol Science and Technology*, *51*(6), 735–754. https://doi.org/10.1080/02786826.2017.1296104

Hudman, R. C., Jacob, D. J., Cooper, O. R., Evans, M. J., Heald, C. L., Park, R. J., et al. (2004). Ozone production in transpacific Asian pollution plumes and implications for ozone air quality in California. Journal of Geophysical Research, 109, D23S10. https://doi.org/10.1029/2004JD004974

Iyer, S., Lopez-Hilfiker, F., Lee, B. H., Thornton, J. A., & Kurtén, T. (2016). Modeling the Detection of Organic and Inorganic Compounds Using Iodide-Based Chemical Ionization. *The Journal of Physical Chemistry A*, *120*(4), 576–587. https://doi.org/10.1021/acs.jpca.5b09837

Jaeglé, L., Shah, V., Thornton, J. A., Lopez-Hilfiker, F. D., Lee, B. H., McDuffie, E. E., et al. (2018). Nitrogen oxides emissions, chemistry, deposition, and export over the northeast United States during the WINTER aircraft campaign. Journal of Geophysical Research: Atmospheres, 123, 12,368–12,393. https://doi.org/10.1029/2018JD029133

Jayne, J. T., Leard, D. C., Zhang, X., Davidovits, P., Smith, K. A., Kolb, C. E., & Worsnop, D. R. (2000). Development of an Aerosol Mass Spectrometer for Size and Composition Analysis of Submicron Particles. *Aerosol Science and Technology*, *33*(1–2), 49–70. https://doi.org/10.1080/027868200410840

Jimenez, J. L., Canagaratna, M. R., Donahue, N. M., Prevot, A. S. H., Zhang, Q., Kroll, J. H., … Worsnop, D. R. (2009). Evolution of Organic Aerosols in the Atmosphere. *Science*, *326*(5959), 1525 LP-1529. https://doi.org/10.1126/science.1180353

Kelly, T. J., Smith, D. L., & Satola, J. (1999). Emission rates of formaldehyde from materials and consumer products found in California Homes. Environmental Science & Technology, 33(1), 81–88. https://doi.org/10.1021/es980592

Kenagy, H. S., Sparks, T. L., Ebben, C. J., Wooldrige, P. J., Lopez-Hilfiker, F. D., Lee, B. H., et al. (2018). NO_x lifetime and NO_y partitioning during WINTER. *Journal of Geophysical Research: Atmospheres*, 123, 9813– 9827. https://doi.org/10.1029/2018JD028736

Kercher, J. P., Riedel, T. P., & Thornton, J. A. (2009). Chlorine activation by N_2O_5: simultaneous, in situ detection of $ClNO_2$ and N_2O_5 by chemical ionization mass spectrometry. *Atmos. Meas. Tech.*, *2*(1), 193–204. https://doi.org/10.5194/amt-2-193-2009

Kercher, J. P., Riedel, T. P., & Thornton, J. A. (2009). Chlorine activation by N_2O_5: simultaneous, in situ detection of $ClNO_2$ and N_2O_5 by chemical ionization mass spectrometry. *Atmos. Meas. Tech.*, *2*(1), 193–204. https://doi.org/10.5194/amt-2-193-2009

Kimmel, J. R., Farmer, D. K., Cubison, M. J., Sueper, D., Tanner, C., Nemitz, E., … Jimenez, J. L. (2011). Real-time aerosol mass spectrometry with millisecond resolution. *International Journal of Mass Spectrometry*, *303*(1), 15–26. https://doi.org/10.1016/j.ijms.2010.12.004

Kirchstetter, T. W., Harley, R. A., & Littlejohn, D. (1996). Measurement of nitrous acid in motor vehicle exhaust. Environmental Science & Technology, 30(9), 2843–2849. https://doi.org/10.1021/es960135y

Kleffmann, J. (2007). Daytime sources of nitrous acid (HONO) in the atmospheric boundary layer. ChemPhysChem, 8(8), 1137–1144. https://doi.org/10.1002/cphc.200700016

Lee, B. H., Lopez-Hilfiker, F. D., Mohr, C., Kurten, T., Worsnop, D. R., & J.A. Thornton (2014). Supplemental Information for: An Iodide-Adduct High-Resolution Time-of-Flight Chemical- Ionization Mass Spectrometer: Application to Atmospheric Inorganic and Organic Compounds. https://doi.org/10.1021/es500362a

Lee, B. H., Lopez-Hilfiker, F. D., Veres, P. R., McDuffie, E. E., Fibiger, D. L., Sparks, T. L., … Thornton, J. A. (2018). Flight Deployment of a High-Resolution Time-of-Flight Chemical Ionization Mass Spectrometer: Observations of Reactive Halogen and Nitrogen Oxide Species. *Journal of Geophysical Research: Atmospheres*, *123*(14), 7670–7686. https://doi.org/10.1029/2017JD028082

Levy, H. (1971). Normal atmosphere: Large radical and formaldehyde concentrations predicted. Science, 173(3992), 141–143. https://doi. org/10.1126/science.173.3992.141

Li, Q., Zhang, L., Wang, T., Tham, Y. J., Ahmadov, R., Xue, L., et al. (2016). Impacts of heterogeneous uptake of dinitrogen pentoxide and chlorine activation on ozone and reactive nitrogen partitioning: Improvement and application of the WRF-Chem model in

southern China. Atmospheric Chemistry and Physics, 16(23), 14875–14,890. https://doi.org/10.5194/acp-16-14875-2016

Lopez-Hilfiker, F. D., Iyer, S., Mohr, C., Lee, B. H., D'ambro, E. L., Kurtén, T., & Thornton, J. A. (2016). Constraining the sensitivity of iodide adduct chemical ionization mass spectrometry to multifunctional organic molecules using the collision limit and thermodynamic stability of iodide ion adducts. *Atmospheric Measurement Techniques*, *9*(4), 1505–1512. https://doi.org/10.5194/amt-9-1505-2016

Lowe, D., Archer-Nicholls, S., Morgan, W., Allan, J., Utembe, S., Ouyang, B., et al. (2015). WRF-Chem model predictions of the regional impacts of N2O5 heterogeneous processes on night-time chemistry over north-western Europe. Atmospheric Chemistry and Physics, 15(3), 1385–1409. https://doi.org/10.5194/acp-15-1385-2015

Luecken, D. J., Hutzell, W. T., Strum, M. L., & Pouliot, G. A. (2012). Regional sources of atmospheric formaldehyde and acetaldehyde, and implications for atmospheric modeling. Atmospheric Environment, 47, 477–490. https://doi.org/https://doi.org/10.1016/j.atmosenv.2011.10.005

McDonald, B. C., de Gouw, J. A., Gilman, J. B., Jathar, S. H., Akherati, A., Cappa, C. D., et al. (2018). Volatile chemical products emerging as largest petrochemical source of urban organic emissions. Science, 359(6377), 760–764. https://doi.org/10.1126/science.aaq0524

McDuffie, E. E., Fibiger, D. L., Dubé, W. P., Lopez Hilfiker, F., Lee, B. H., Jaeglé, L., et al. (2018). ClNO2 yields from aircraft measurements during the 2015 WINTER campaign and critical evaluation of the current parameterization. Journal of Geophysical Research: Atmospheres, 123, 913–994. https://doi.org/10.1029/2018JD029358

McDuffie, E. E., Fibiger, D. L., Dubé, W. P., Lopez-Hilfiker, F., Lee, B. H., Thornton, J. A., et al. (2018). Heterogeneous N2O5 uptake during winter: Aircraft measurements during the 2015 WINTER campaign and critical evaluation of current parameterizations. Journal of Geophysical Research: Atmospheres, 123, 4345–4372. https://doi.org/10.1002/2018JD028336

Michoud, V., Kukui, A., Camredon, M., Colomb, A., Borbon, A., Miet, K., et al. (2012). Radical budget analysis in a suburban European site during the MEGAPOLI summer field campaign. Atmospheric Chemistry and Physics, 12, 11,951–11,974. https://doi.org/10.5194/acp-12- 11951-2012

Mielke, L. H., Furgeson, A., & Osthoff, H. D. (2011). Observation of ClNO2 in a Mid-Continental Urban Environment. *Environmental Science & Technology*, *45*(20), 8889–8896. https://doi.org/10.1021/es201955u

Orlando, J. J., Tyndall, G. S., Apel, E. C., Riemer, D. D., & Paulson, S. E. (2003). Rate coefficients and mechanisms of the reaction of cl-atoms with a series of unsaturated hydrocarbons under atmospheric conditions. International Journal of Chemical Kinetics, 35(8), 334–353. https://doi.org/10.1002/kin.10135

Platt, U. F., Winer, A. M., Biermann, H. W., Atkinson, R., & Pitts, J. N. (1984). Measurement of nitrate radical concentrations in continental air. Environmental Science & Technology, 18(5), 365–369. https://doi.org/10.1021/es00123a015

Ridley, B. A., Grahek, F. E., & Walega, J. G. (1992). A Small High-Sensitivity, Medium-Response Ozone Detector Suitable for Measurements from Light Aircraft. *Journal of Atmospheric and Oceanic Technology*, *9*(2), 142–148. https://doi.org/10.1175/1520-0426(1992)009

Riedel, T. P., Bertram, T. H., Crisp, T. A., Williams, E. J., Lerner, B. M., Vlasenko, A., … Thornton, J. A. (2012). Nitryl chloride and molecular chlorine in the coastal marine boundary layer. *Environmental Science and Technology*. https://doi.org/10.1021/es204632r

Riedel, T. P., Wolfe, G. M., Danas, K. T., Gilman, J. B., Kuster, W. C., Bon, D. M., et al. (2014). An MCM modeling study of nitryl chloride (ClNO2) impacts on oxidation, ozone production and nitrogen oxide partitioning in polluted continental outflow. Atmospheric Chemistry and Physics, 14(8), 3789–3800. https://doi.org/10.5194/acp-14-3789-2014

Riemer, N., Vogel, H., Vogel, B., Schell, B., Ackermann, I., Kessler, C., & Hass, H. (2003). Impact of the heterogeneous hydrolysis of N2O5 on chemistry and nitrate aerosol formation in the lower troposphere under photo smog conditions. Journal of Geophysical Research: Atmospheres, 108(D4). https://doi.org/10.1029/2002JD002436

Romer, P. S., Wooldridge, P. J., Crounse, J. D., Kim, M. J., Wennberg, P. O., Dibb, J. E., et al. (2018). Constraints on aerosol nitrate photolysis as a potential source of HONO and NOx. Environmental Science & Technology, 52(23), 13,738–13,746. Sarwar, G., Simon, H., Xing, J., & Mathur, R. (2014). Importance of tropospheric ClNO2 chemistry across the Northern Hemisphere. Geophysical Research Letters, 41, 4050–4058. https://doi.org/10.1002/2014GL059962

Ryder, O. S., Ault, A. P., Cahill, J. F., Guasco, T. L., Riedel, T. P., Cuadra-Rodriguez, L. A., … Bertram, T. H. (2014). On the Role of Particle Inorganic Mixing State in the Reactive Uptake of N2O5 to Ambient Aerosol Particles. *Environmental Science & Technology*, *48*(3), 1618–1627. https://doi.org/10.1021/es4042622

Schroder, J. C., Campuzano-Jost, P., Day, D. A., Shah, V., Larson, K., Sommers, J. M., et al. (2018). Sources and secondary production of organic aerosols in the northeastern United States during WINTER. Journal of Geophysical Research: Atmospheres, 123, 7771–7796. https://doi.org/10.1029/2018JD028475

Shah, V., Jaeglé, L., Thornton, J. A., Lopez-Hilfiker, F. D., Lee, B. H., Schroder, J. C., et al. (2018). Chemical feedbacks weaken the wintertime response of particulate sulfate and nitrate to emissions reductions over the eastern United States. Proceedings of the National Academy of Sciences, 115(32), 8110–8115. https://doi.org/10.1073/pnas.1803295115

Sigsby, J. E., Tejada, S., Ray, W., Lang, J. M., & Duncan, J. W. (1987). Volatile organic compound emissions from 46 in-use passenger cars. Environmental Science & Technology, 21(5), 466–475. https://doi.org/10.1021/es00159a007

Sorgel, M., Regelin, E., Bozem, H., Diesch, J. M., Drewnick, F., Fischer, H., et al. (2011). Quantification of the unknown HONO daytime source and its relation to NO2. Atmospheric Chemistry and Physics, 11(20), 10,433–10,447. https://doi.org/10.5194/acp-

11-10433-2011

Spataro, F., & Ianniello, A. (2014). Sources of atmospheric nitrous acid: State of the science, current research needs, and future prospects. Journal of the Air & Waste Management Association, 64(11), 1232–1250. https://doi.org/10.1080/10962247.2014.952846

Stevens, P., Mather, J., H. Brune, W., Eisele, F., Tanner, D., Jefferson, A., … Williams, E. (1997). HO2/OH and RO2/HO2 ratios during the Tropospheric OH Photochemistry Experiment: Measurement and theory. Journal of Geophysical Research (Vol. 102). https://doi.org/10.1029/96JD01704

Stutz, J., Alicke, B., & Neftel, A. (2002). Nitrous acid formation in the urban atmosphere: Gradient measurements of NO2 and HONO over grass in Milan, Italy. Journal of Geophysical Research, 107(D22), 8192. https://doi.org/10.1029/2001JD000390

Sullivan, A. P., Guo, H., Schroder, J. C., Campuzano-Jost, P., Jimenez, J. L., Campos, T., et al. (2019). Biomass burning markers and residential burning in the WINTER aircraft campaign. Journal of Geophysical Research: Atmospheres, 124, 1846–1861. https://doi.org/ 10.1029/2017JD028153

Tesche, T. W., Morris, R., Tonnesen, G., McNally, D., Boylan, J., & Brewer, P. (2006). CMAQ/CAMx annual 2002 performance evaluation over the eastern US. Atmospheric Environment, 40(26), 4906–4919. https://doi.org/https://doi.org/10.1016/j.atmosenv.2005.08.046

VandenBoer, T. C., Murphy, J. G., Roberts, J. M., Middlebrook, A. M., Brock, C. A., Lerner, B., et al. (2013). Understanding the role of the ground surface in HONO vertical structure: High resolution vertical profiles during NACHTT-11. Journal of Geophysical Research: Atmospheres, 118, 10,155–10,171. https://doi.org/10.1002/jgrd.50721

Volkamer, R., Sheehy, P., Molina, L. T., & Molina, M. J. (2010). Oxidative capacity of the Mexico City atmosphere—Part 1: A radical source perspective. Atmospheric Chemistry and Physics, 10, 6969–6991. https://doi.org/10.5194/acp-10-6969-2010

Walega, J. G., Dye, J. E., Grahek, F. E., & Ridley, B. K. (1991). Compact measurement system for the simultaneous determination of NO, NO2, NOy, and O3 using a small aircraft. In *Proc.SPIE* (Vol. 1433). Retrieved from https://doi.org/10.1117/12.46167

Walker, J. M., Philip, S., Martin, R. V., & Seinfeld, J. H. (2012). Simulation of nitrate, sulfate, and ammonium aerosols over the United States. Atmospheric Chemistry and Physics, 12(22), 11,213–11,227. https://doi.org/10.5194/acp-12-11213-2012

Washenfelder, R. A., Wagner, N. L., Dube, W. P., & Brown, S. S. (2011). Measurement of Atmospheric Ozone by Cavity Ring-down Spectroscopy. *Environmental Science & Technology*, *45*(7), 2938–2944. https://doi.org/10.1021/es103340u

Weinheimer, A. J., Walega, J. G., Ridley, B. A., Sachse, G. W., Anderson, B. E., & Collins Jr., J. E. (1993). Stratospheric NOy measurements on the NASA DC-8 during AASE II. *Geophysical Research Letters*, *20*(22), 2563–2566. https://doi.org/10.1029/93GL02627

Whalley, L. K., Stone, D., Dunmore, R., Hamilton, J., Hopkins, J. R., Lee, J. D., et al. (2018). Understanding in situ ozone production in the summertime through radical observations

and modelling studies during the Clean air for London project (ClearfLo). Atmospheric Chemistry and Physics, 18, 2547–2571. https://doi.org/10.5194/acp-18-2547-2018

Wild, R. J., Edwards, P. M., Dubé, W. P., Baumann, K., Edgerton, E. S., Quinn, P. K., … Brown, S. S. (2014). A Measurement of Total Reactive Nitrogen, NOy, together with NO2, NO, and O3 via Cavity Ring-down Spectroscopy. *Environmental Science & Technology*, *48*(16), 9609–9615. https://doi.org/10.1021/es501896wWolfe, G. M., Kaiser, J., Hanisco, T. F., Keutsch, F. N., de Gouw, J. A., Gilman, J. B., et al. (2016). Formaldehyde production from isoprene oxidation across NOx regimes. Atmospheric Chemistry and Physics, 16(4), 2597–2610. https://doi.org/10.5194/acp-16-2597-2016

Wolfe, G. M., Marvin, M. R., Roberts, S. J., Travis, K. R., & Liao, J. (2016). The Framework for 0-D Atmospheric Modeling (F0AM) v3.1. Geoscientific Model Development, 9(9), 3309–3319. https://doi.org/10.5194/gmd-9-3309-2016

Wong, K. W., Tsai, C., Lefer, B., Haman, C., Grossberg, N., Brune, W. H., et al. (2012). Daytime HONO vertical gradients during SHARP 2009 in Houston, TX. Atmospheric Chemistry and Physics, 12(2), 635–652. https://doi.org/10.5194/acp-12-635-2012

Wooldridge, P. J., Perring, A. E., Bertram, T. H., Flocke, F. M., Roberts, J. M., Singh, H. B., … Cohen, R. C. (2010). Total Peroxy Nitrates (; PNs) in the atmosphere: The Thermal Dissociation-Laser Induced Fluorescence (TD-LIF) technique and comparisons to speciated PAN measurements. *Atmos. Meas. Tech.*, *3*(3), 593–607. https://doi.org/10.5194/amt-3-593-2010

Ye, C., Zhou, X., Pu, D., Stutz, J., Festa, J., Spolaor, M., et al. (2016). Rapid cycling of reactive nitrogen in the marine boundary layer. Nature, 532(7600), 489. Retrieved from–491. https://doi.org/10.1038/nature17195

Yienger, J. J., Klonecki, A. A., Levy, H., Moxim, W. J., & Carmichael, G. R. (1999). An evaluation of chemistry's role in the winter-spring ozone maximum found in the northern midlatitude free troposphere. Journal of Geophysical Research, 104(D3), 3655–3667. https://doi. org/10.1029/1998JD100043

Young, C. J., Washenfelder, R. A., Edwards, P. M., Parrish, D. D., Gilman, J. B., Kuster, W. C., et al. (2014). Chlorine as a primary radical: Evaluation of methods to understand its role in initiation of oxidative cycles. Atmospheric Chemistry and Physics, 14, 3427–3440. https://doi.org/10.5194/acp-14-3427-2014

Zhou, X., Gao, H., He, Y., Huang, G., Bertman, S. B., Civerolo, K., & Schwab, J. (2003). Nitric acid photolysis on surfaces in low-NOx environments: Significant atmospheric implications. *Geophysical Research Letters*, *30*(23). https://doi.org/10.1029/2003GL018620

Zhu, C., Xiang, B., Chu, L. T., & Zhu, L. (2010). 308 nm Photolysis of Nitric Acid in the Gas Phase, on Aluminum Surfaces, and on Ice Films. *The Journal of Physical Chemistry A*, *114*(7), 2561–2568. https://doi.org/10.1021/jp909867

2.12 TABLES

Table 2.1 Summary of WINTER Observations Used

Measured Species	Method/ Instrument	Detection limit (10s averaging period, 2σ)	Accuracy	Measurement Frequency	Reference
J-Values	HARP-AF[a]	--	***<25-40%***	10s	Shetter & Muller (1999)
		Gas Phase	***Measurements***		
NO_2	CRDS [b, c]	45-90 pptv (at 1s)	3%	1s	Fuchs et al., (2009)
	TD-LIF [d]	90 pptv	10%	1s	Day et al., (2002)
O_3	CRDS [b]	545-650 pptv (at 1s)	4%	1s	Washenfelder et al., (2011)
	CL[e]	50 pptv	10%	1s	Weinheimer et al., (1994)
NOy	CRDS	< 90 pptv	12%	1s	Wild et al., (2014)
	CL	< 90 pptv	50%	1s	Weinheimer et al., (1994)
N_2O_5	I-TOF-CIMS [f]	0.1 pptv	30%	1s	Lee et al., (2014), Lee et al., (2018)
HNO_3	I-TOF-CIMS	2.2 pptv	30%	1s	Lee et al., (2014), Lee et al., (2018)
$ClNO_2$	I-TOF-CIMS	0.1 pptv	30%	1s	Lee et al., (2014), Lee et al., (2018)
Cl_2	I-TOF-CIMS	0.1 pptv	30%	1s	Lee et al., (2014), Lee et al., (2018)
HOCl	I-TOF-CIMS	1 pptv	30%	1s	Lee et al., (2018)
HCl	I-TOF-CIMS	22 pptv	30%	1s	Lee et al., (2014), Lee et al., (2018)
HONO	I-TOF-CIMS	40 pptv	50%	1s	Lee et al., (2014), Lee et al., (2018)
HCHO	ISAF[g]	36 pptv	10%	1s	Cazorla etal., (2015)
Speciated VOCs	TOGA[h]	--	<50%	35s, 2min	Apel et al., (2015)
		Particle	***Measurements***		
Nitrate ($D_p < 4.1\mu m$)	UNH filter [i]	--	50% passing efficiency	5 min	Dibb et al., (1999), Dibb et al., (2000), McNaughton et al., 2007
Nitrate	AMS[j]	22 ng sm^{-3} [k]	35%	1s	DeCarlo et al., (2006) Schroder et al., (2018)

a HIAPER airborne radiation package-Actinic Flux. For uncertainty description, see McDuffie et al., (2018) SI, section S1.
b Excludes research flights 01–04 due to a known problem in the sampling inlet line. Detection limits are for flights used in this analysis.
c National Oceanic and Atmospheric Administration (NOAA), Cavity Ring Down Spectrometer
d University of California Berkeley, Thermal Dissociation-Laser Induced Fluorescence detector
e National Center for Atmospheric Research Chemiluminescence instrument for NO, NO_y, O_3
f University of Washington, high-resolution, Time-of-Flight, Iodide Chemical Ionization Mass Spectrometer
g In Situ Airborne Formaldehyde
h NCAR, Trace Organic Gas Analyzer
i University of New Hampshire filter measurements for $D_p < 4.1\mu m$
j University of Colorado Boulder, High-Resolution Time-of -Flight Aerosol Mass Spectrometer for $D_p < 1\mu m$
k sm^{-3} refers to cubic meters at standard temperature (273.15K) and pressure (1atm) (STP)

2.13 FIGURES

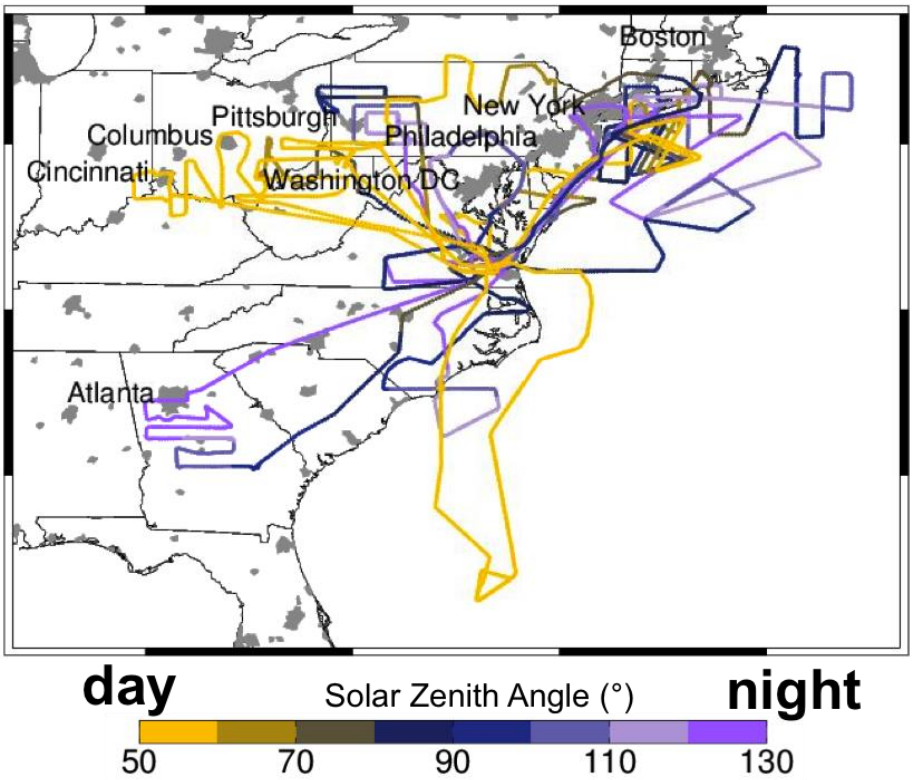

Figure 2.1 WINTER Campaign Flights

Flight tracks of the 13 research flights performed during the WINTER campaign, colored by solar zenith angle with population centers highlighted in grey.

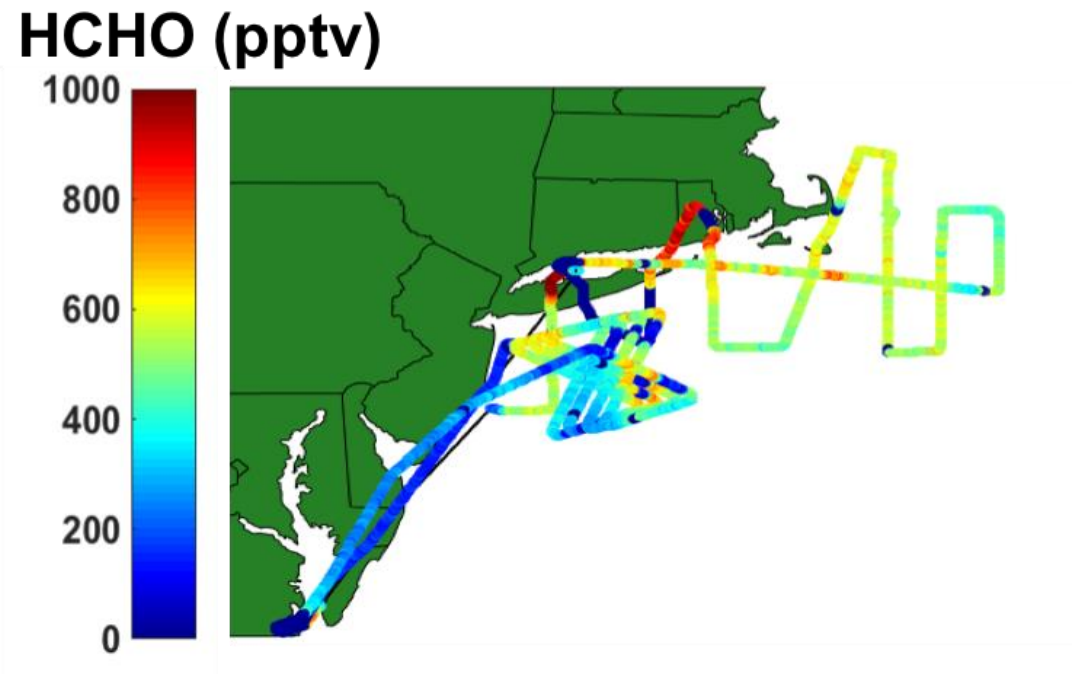

Figure 2.2 WINTER Nighttime HCHO

Measurements of HCHO from the nighttime Research Flights 3, and 8 made below 2000 m

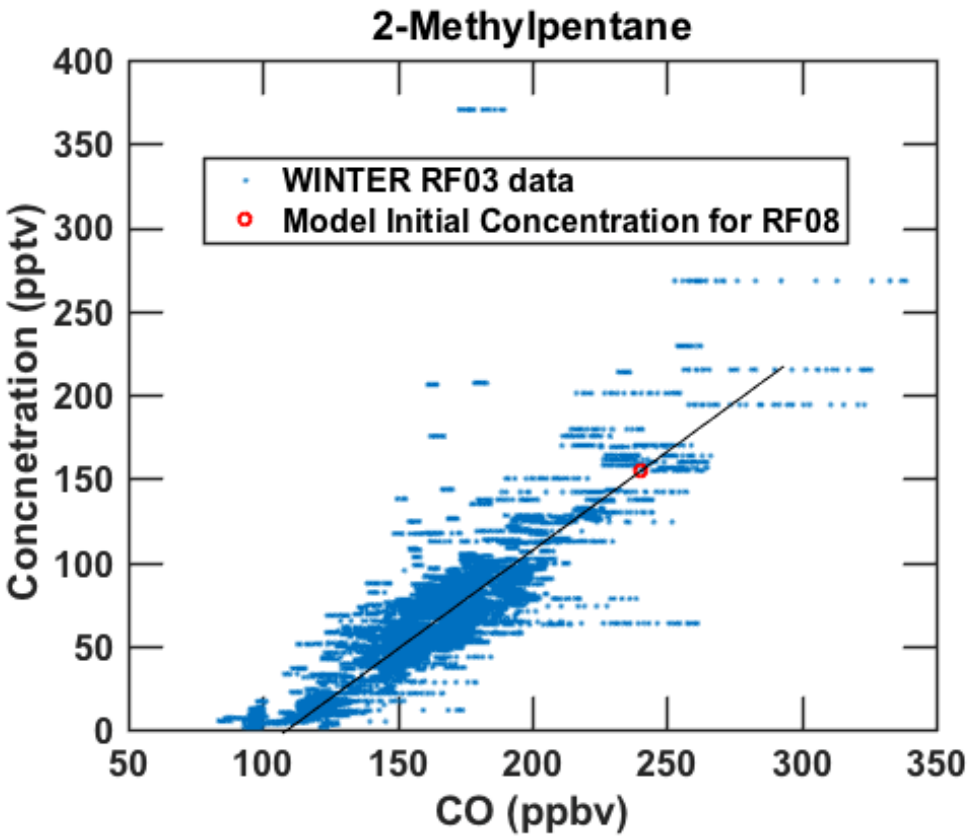

Figure 2.3 Determining VOC Concentrations from CO

Example of method used to estimate a particular VOC's concentration from observed CO on RF08 during the TDLIF instrument malfunction from RF03 data.

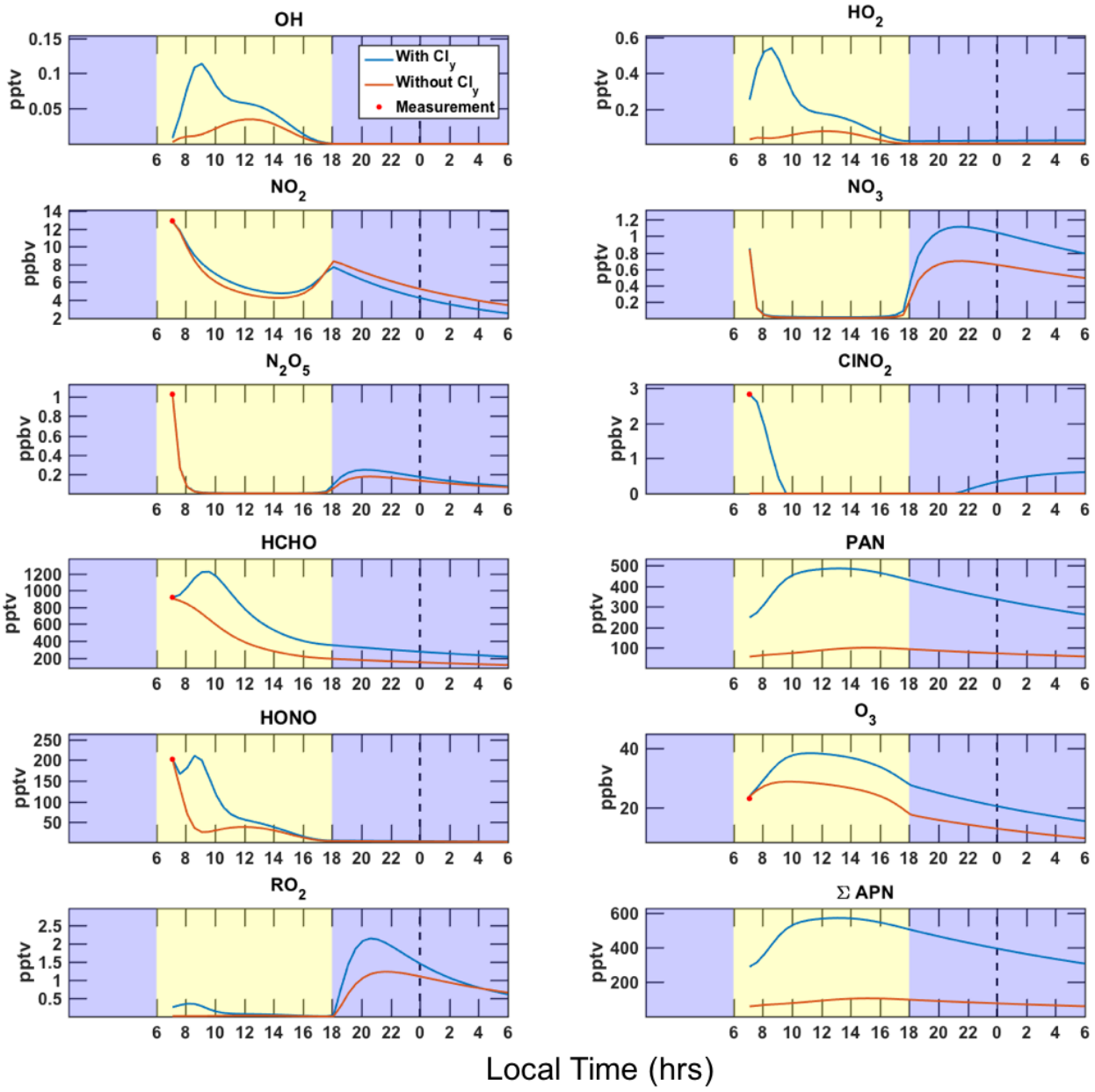

Figure 2.4 F0AM Gas Phase Concentrations

Time series of F0AM modeled gas phase concentrations initialized at peak ClNO2 observation at 6:36 local time considering reactions with chloride and without them during the free evolution period and measurements at the point of observation. Daytime hours are shown in yellow and nighttime hours in purple.

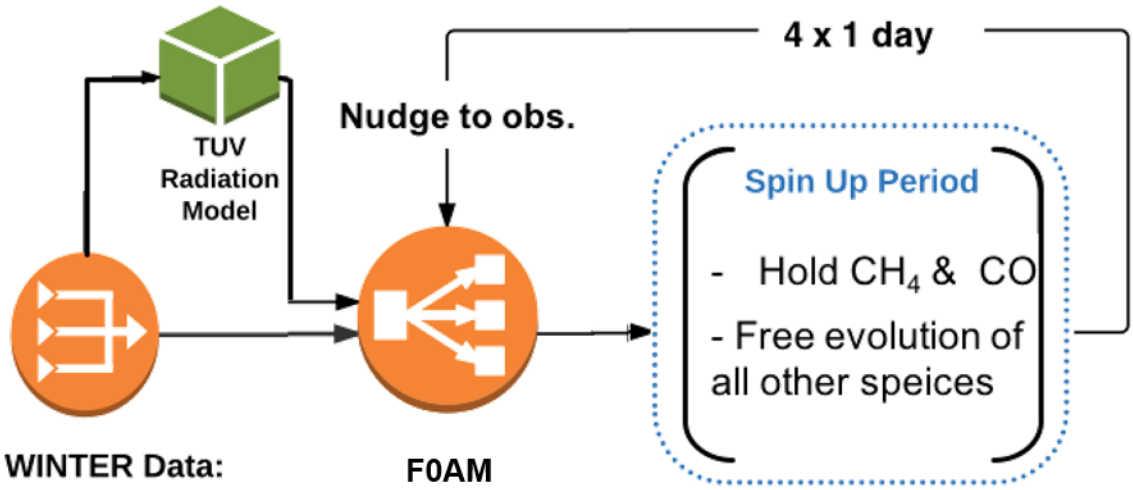

Figure 2.5 Summary of F0AM Operation

Summary of F0AM operation, using WINTER data, TUV radiation model input for cases with and without Cl chemistry.

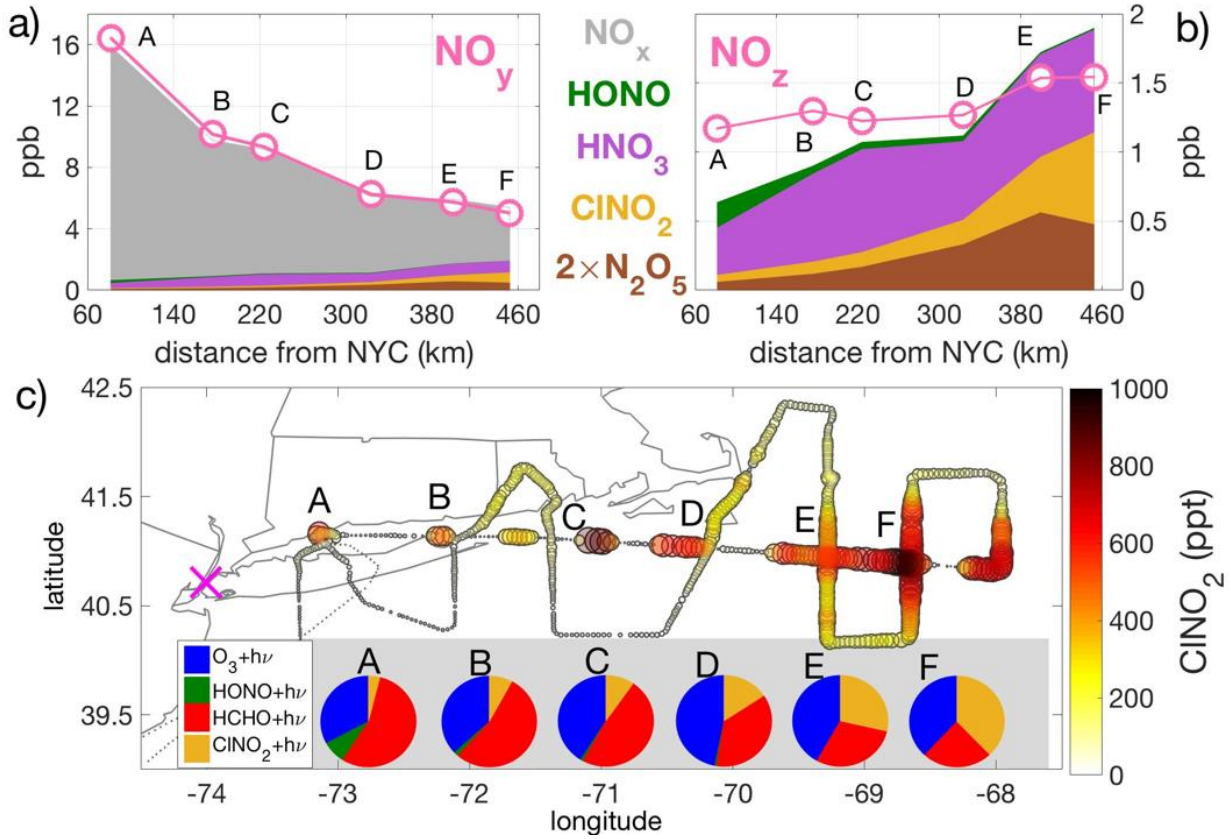

Figure 2.6 Downwind NO_x & $ClNO_2$ Evolution

Evolution of nitrogen oxide reservoir species downwind of New York City (purple x) observed during Research Flight 3 of the WINTER campaign. a) NOy is the sum of all forms of reactive nitrogen oxides that can be converted to NO at high temperatures. b) NOz is the sum of higher oxides of all reactive nitrogen oxides species excluding NOx (NOz = NOy - NOx). The gap between NOz and the sum of the individual components that occurs near NYC is likely explained by a combination of particle nitrates and gaseous peroxynitrates (see SI). c) Map of the flight track colored and sized by the measured mixing ratio of ClNO2. The pie charts show the observationally constrained contributions of different radical precursors to the integrated daytime radical source (see text). The six intercepts of the New York City plume, labeled as A-F in (a), (b) and (c), occurred between 7 pm to 11 pm local time, between 250 and 400 m pressure altitude (c). The plume intercept F was excluded due to a higher altitude (750 m) than the first six.

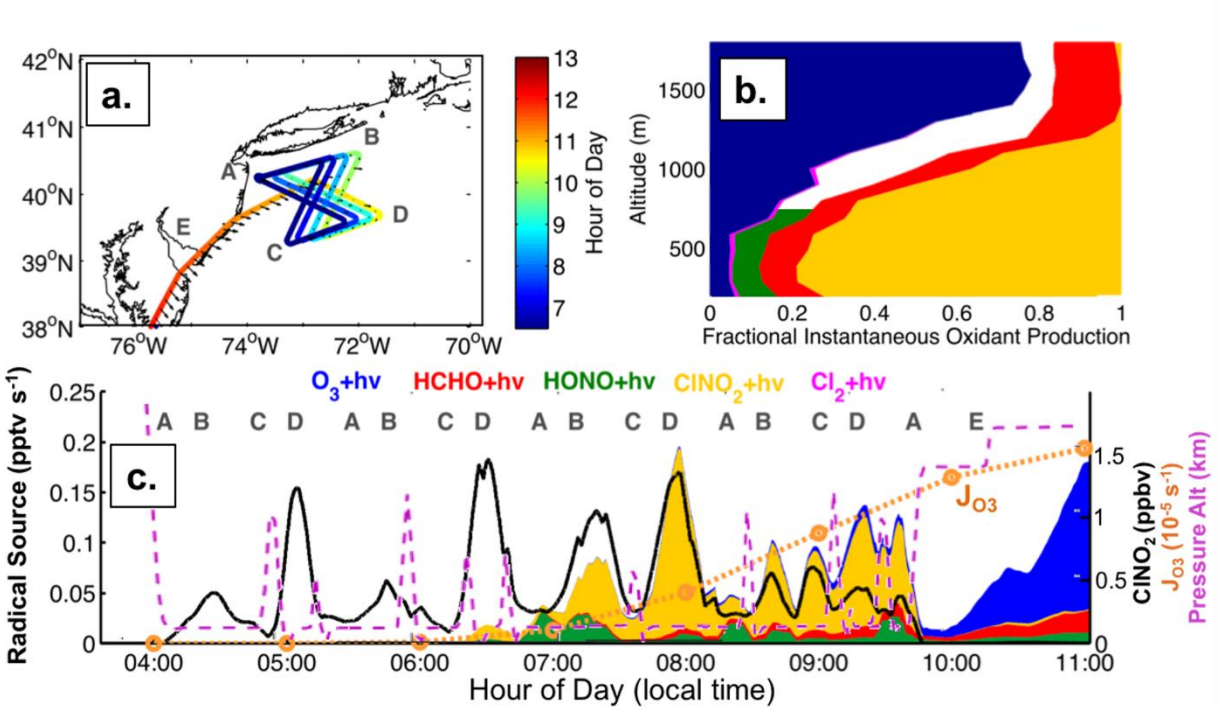

Figure 2.7 Instantaneous Morning Estimates of $ClNO_2$ Photolysis

(a) Flight track of the NSF/NCAR C-130 on Research Flight 8 of the WINTER campaign, colored by local time of day. Sunrise occurred at approximately 6:30 AM local time. Only portions with altitudes <2000 m are shown. (b) Vertical profiles of the instantaneous radical source calculated from observations of solar radiation and radical precursors. White space indicates HONO measurements at these altitudes were below instrument detection limits. (c) Time series of the instantaneous radical source (left axis, stacked color), ClNO2 mixing ratios (right axis, ppbv), the measured O3 photolysis frequency (orange circles, right axis, 10 -5 s-1), and pressure altitude (right axis, km)

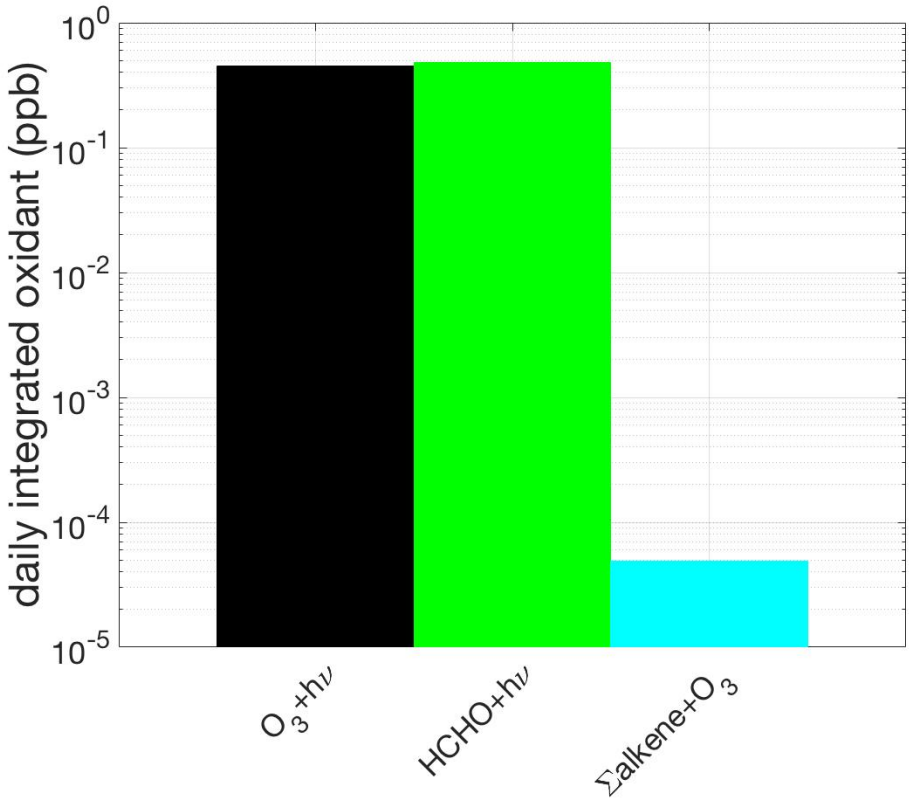

Figure 2.8 Contribution of Alkene Ozonolysis to Radical Budget

Comparison of the relative contributions of O3 and HCHO photolysis and the alkene ozonoylsis reactions to the daily integrated radical budget during WINTER

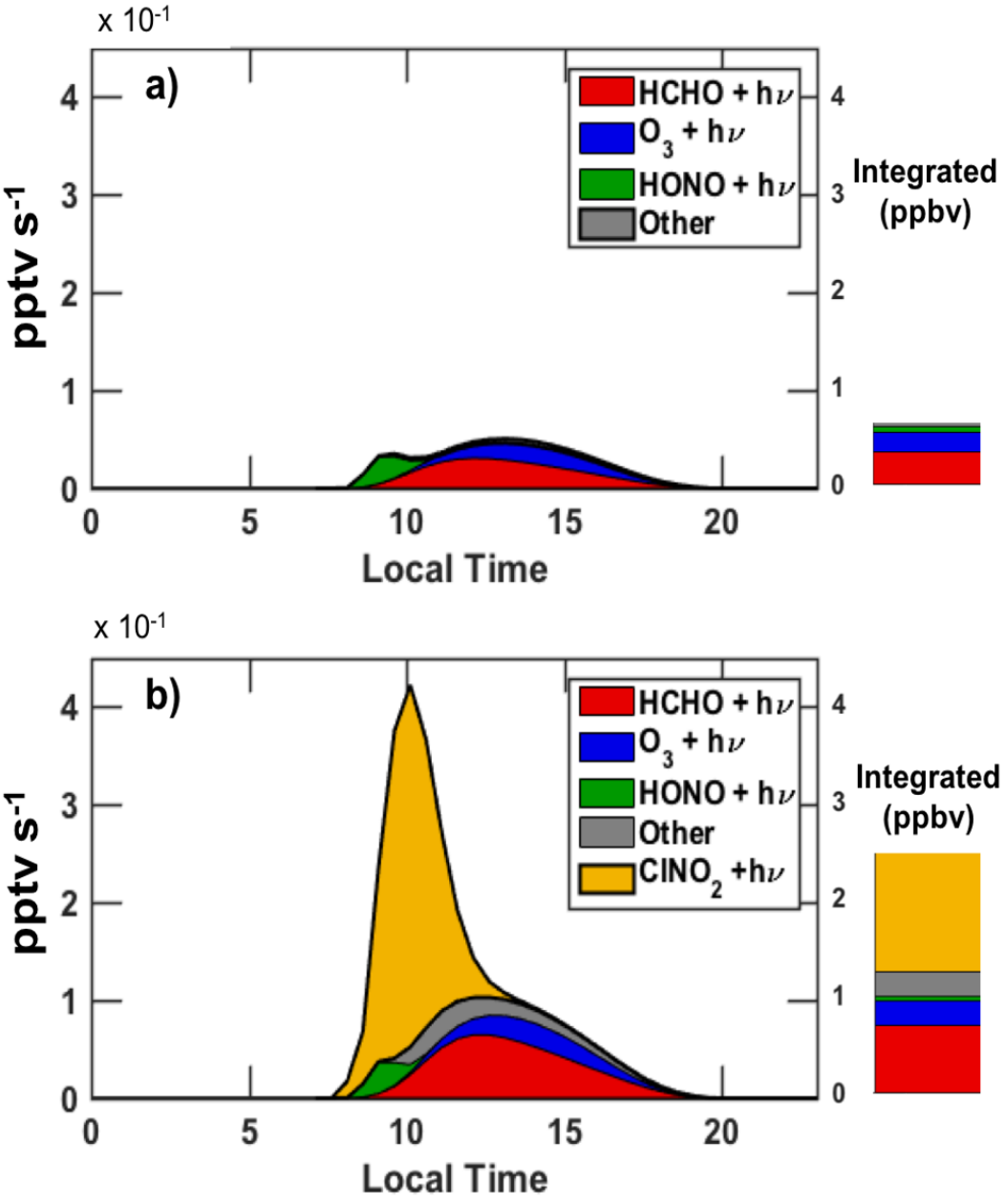

Figure 2.9 F0AM Radical Production

Summary of daily integrated primary radical production rates calculated the day following our interception of the peak $ClNO_2$ concentrations on RF08 using the F0AM box model initialized with WINTER observations without including chlorine reactions (a) and including chlorine reactions (b). Bar charts show the integrated daily radical source from each precursor.

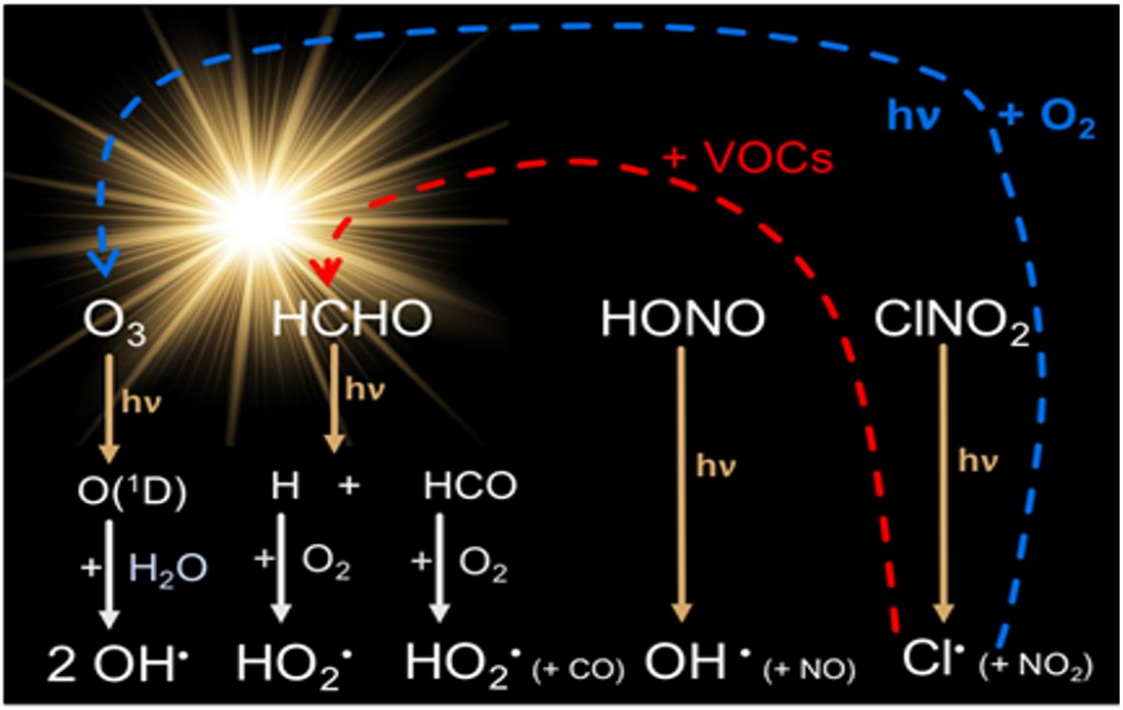

Figure 2.10 Mechanism for O_3, HCHO Enhancements from Cl

Summary of the mechanism by which increased Cl atom production can secondarily enhance OH production via enhancing O_3 and HCHO concentrations.

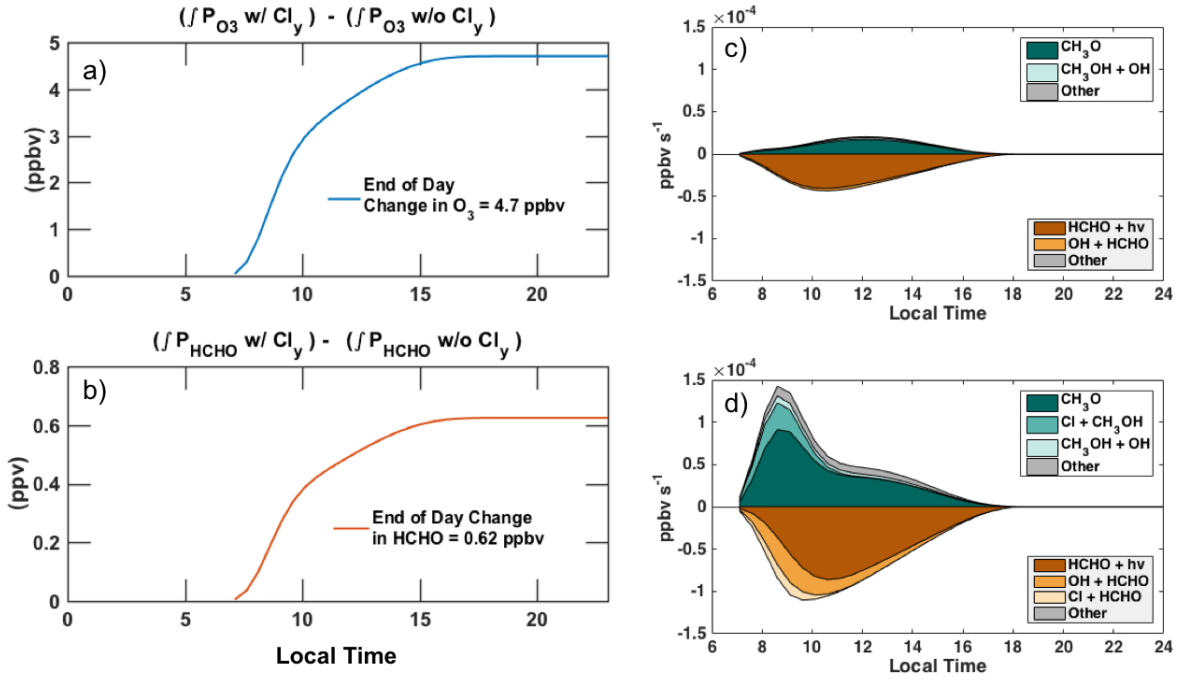

Figure 2.11 F0AM Enhancements in O_3, HCHO Production

a) Difference in the daily Integrated production of O3 that results from including Cly reactions for the simulation initialized at the peak observed ClNO2 concentration. b) Difference in the daily integrated production of HCHO that results from including Cl_y reactions. c) Top production and loss mechanisms of HCHO in the simulation not considering Cl_y reactions compared to d) the top production and loss mechanisms of HCHO in the simulation considering Cl_y reactions.

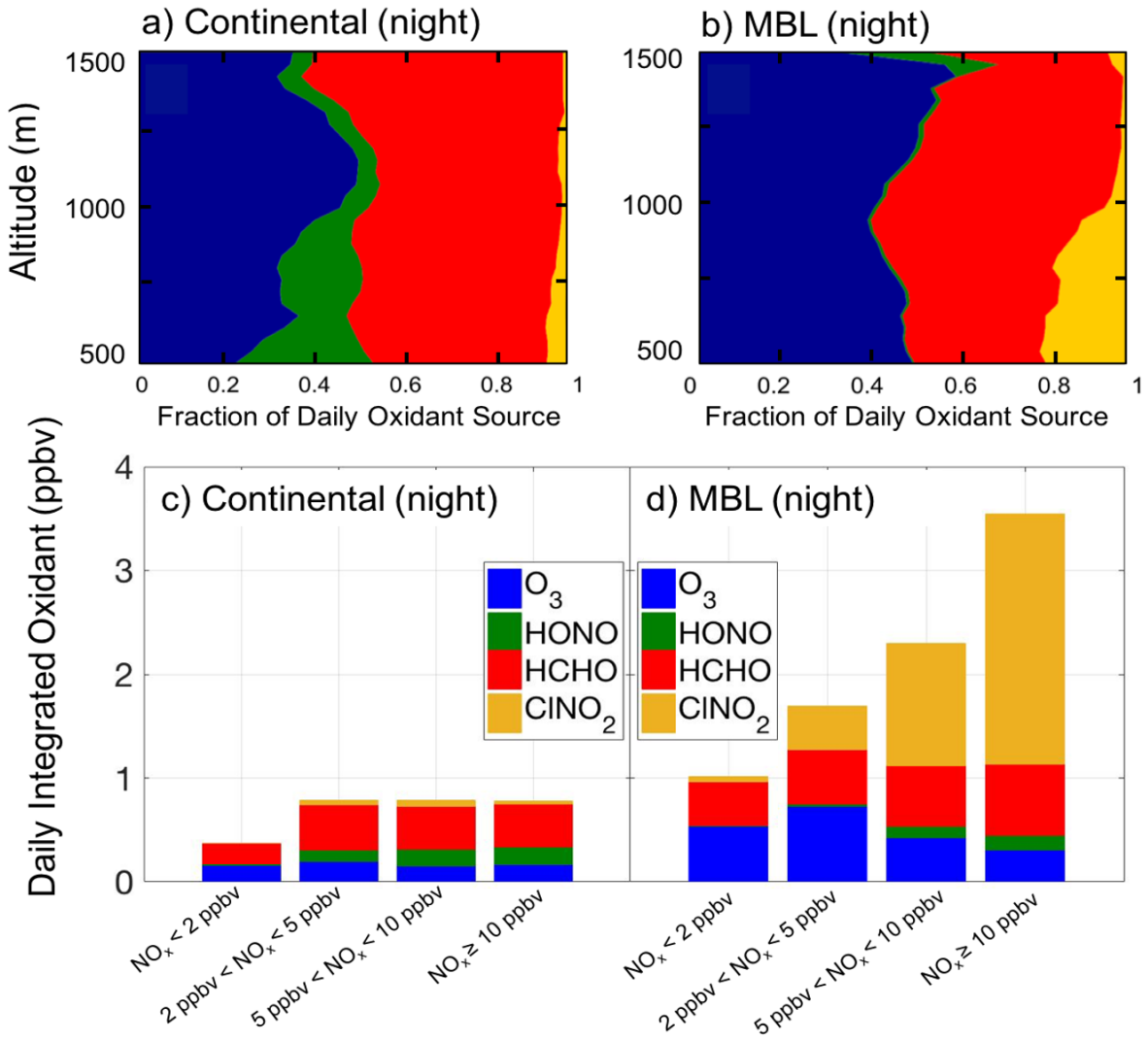

Figure 2.12 Daily Integrated Oxidants from Precursors

Vertical profiles of the daily integrated primary radical sources calculated from observations of O_3, $H_2O_,$, $ClNO_2$, HONO, and HCHO made throughout the campaign in vertical profiling maneuvers during the night below 1.5 km over (a) the continental boundary layer, and (b) within the marine boundary layer (MBL). Averaging over these vertical profiles during the night and binning them as a function of their observed NO_x mixing ratios, we show the calculated the daily integrated primary radical source from each radical precursor that would result the following day over (c) the continental boundary layer and (d) within the MBL as calculated using the methodology in Section 2.5.

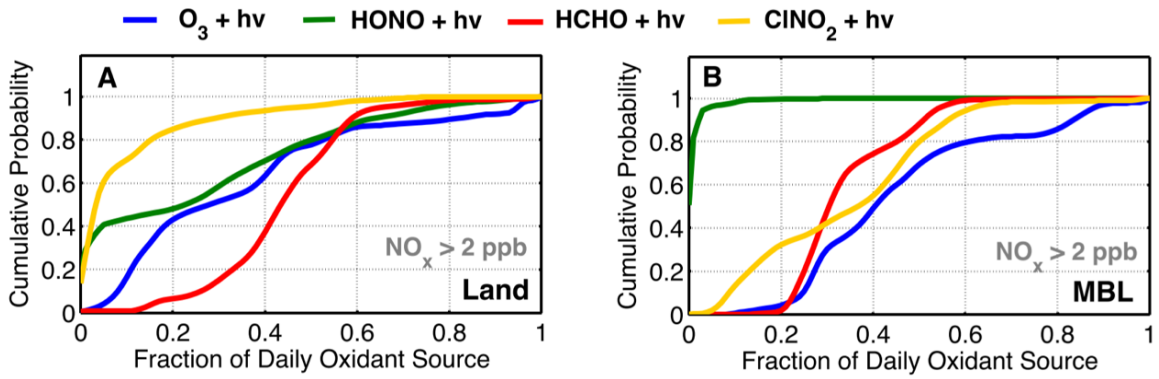

Figure 2.13 Cumulative Distribution of Radical Sources

The cumulative distribution functions for the contribution of each specific radical source to the total daily integrated source derived from measurements (a) over land and (b) in the marine boundary layer at all points during the campaign where NO_x > 2ppbv.

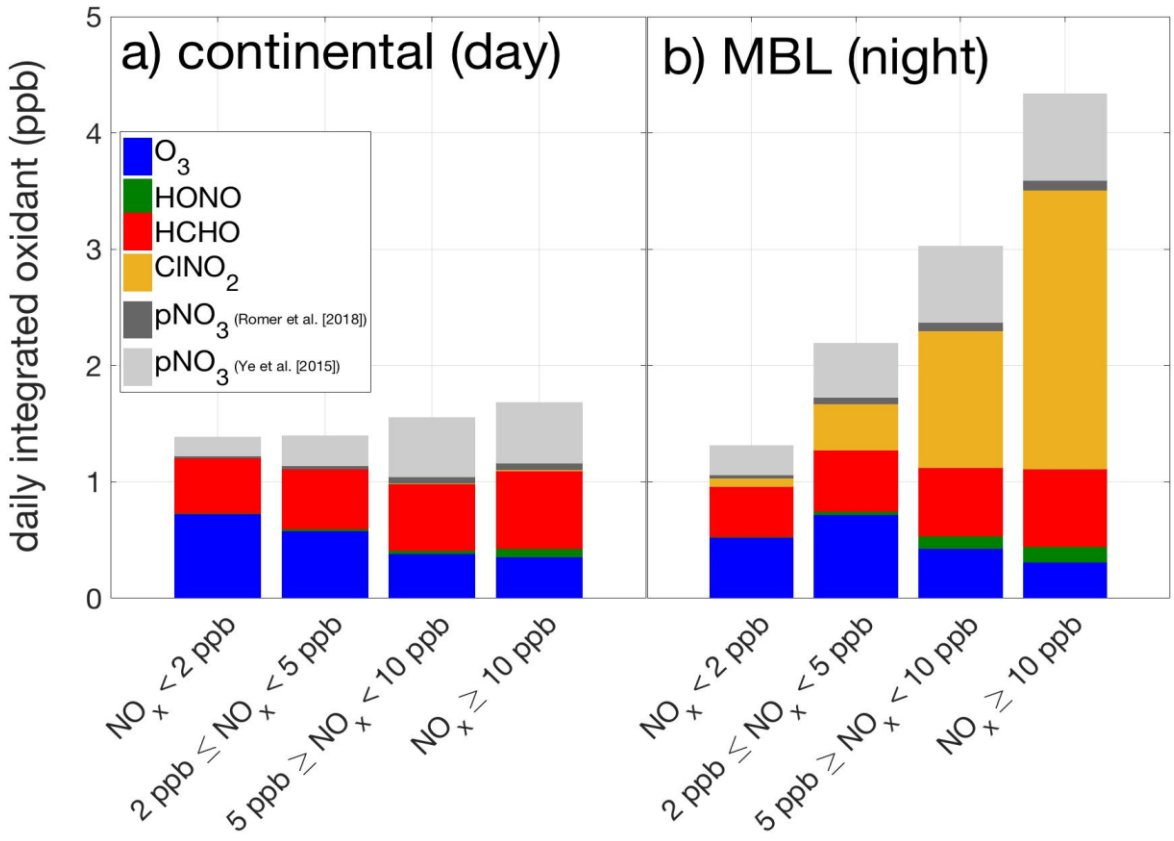

Figure 2.14 Daily Integrated Oxidants, Including pNO_3 Photolysis

The predicted contribution of each radical precursor to the daily integrated oxidant budget when considering daytime production of HONO following pNO_3^- photolysis at rates prescribed by Ye et al., (2016) and Romer et al., (2018) during winter, binned by NO_x concentration at the time of early morning observation during the day over continental regions and during the night in the MBL when we were sampling within the boundary layer.

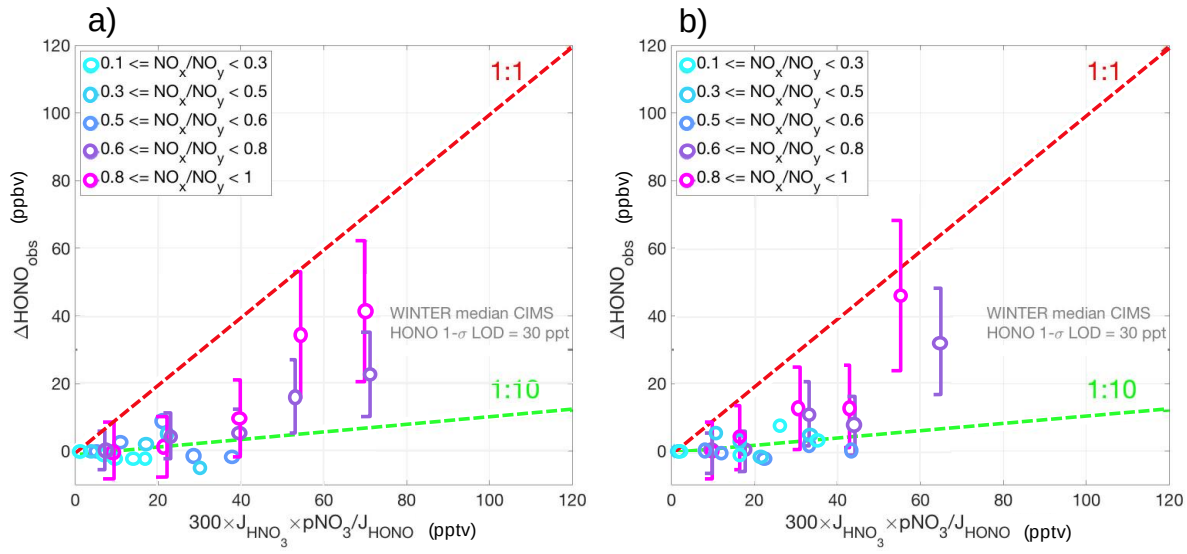

Figure 2.15 pNO_3 and HONO Compared to Parameterizations

The median observed enhancement in HONO concentrations relative to the lowest binned observation during the day in WINTER below 1 km, compared to the predicted values of HONO using the parameterization from Ye et al., (2016). Comparisons are binned and colored by the NOx to NOy ratio as an indicator of plume age. Predictions are calculated with observed photolysis frequencies and either (a) AMS particle nitrate concentrations or (b) filter particle nitrate concentrations, using a photolysis enhancement factor of 300 (red line) from Ye et al., (2016) or an enhancement factor of 30 (green line) from Romer et al., (2018). Error bars shown indicate the 50% uncertainty in I^- CIMS HONO measurements and are shown only for cases where observed HONO concentrations included in the analysis were greater than the HONO detection limit.

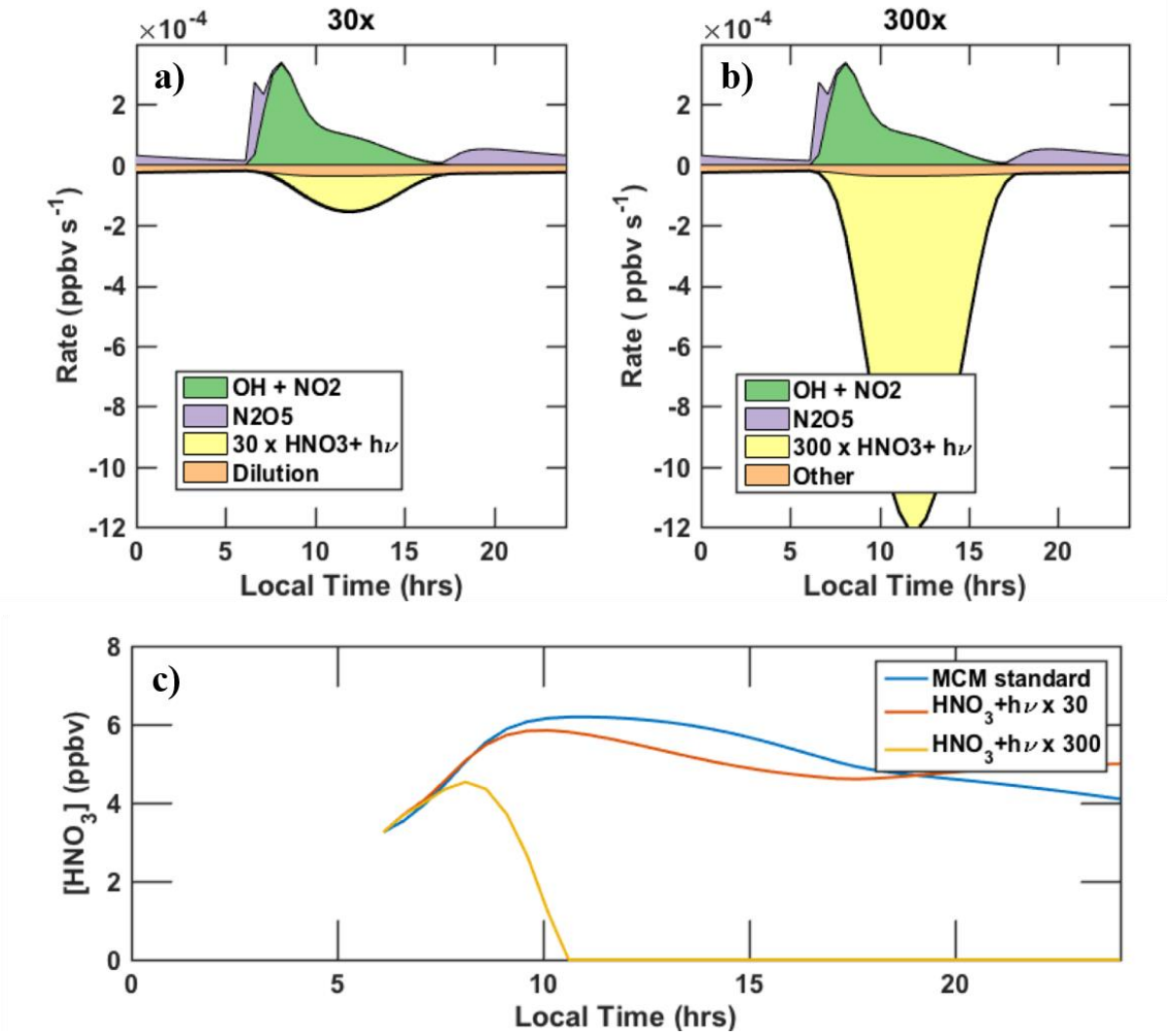

Figure 2.16 Impact of pNO_3^- photolysis on HNO_3 concentrations

The rates of HNO_3 production and loss within F0AM during WINTER if a loss process from aerosol photolysis is included with an enhancement factor of (a) 30 from Romer et al., 2018 or (b) 300 from Ye et al., 2016. c) The resulting concentrations of HNO_3 considering no photolysis of pNO_3^- to form HONO but including other production and loss pathways (blue), with an enhancement factor of 30 (orange), or with an enhancement factor of 300 (yellow).

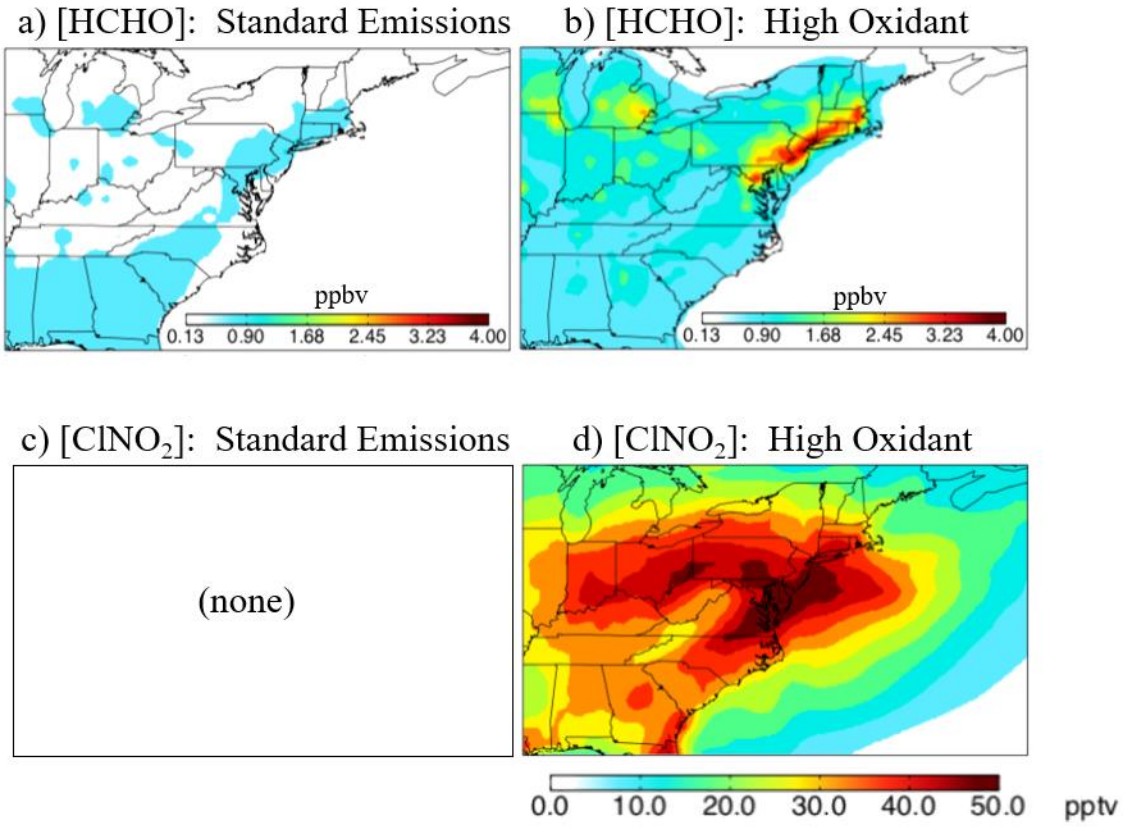

Figure 2.17 Standard Emissions vs. High Oxidant Simulations

Differences in HCHO (top) and $ClNO_2$ (bottom) concentrations for the standard emissions case (left column) and the high oxidant case (right column)

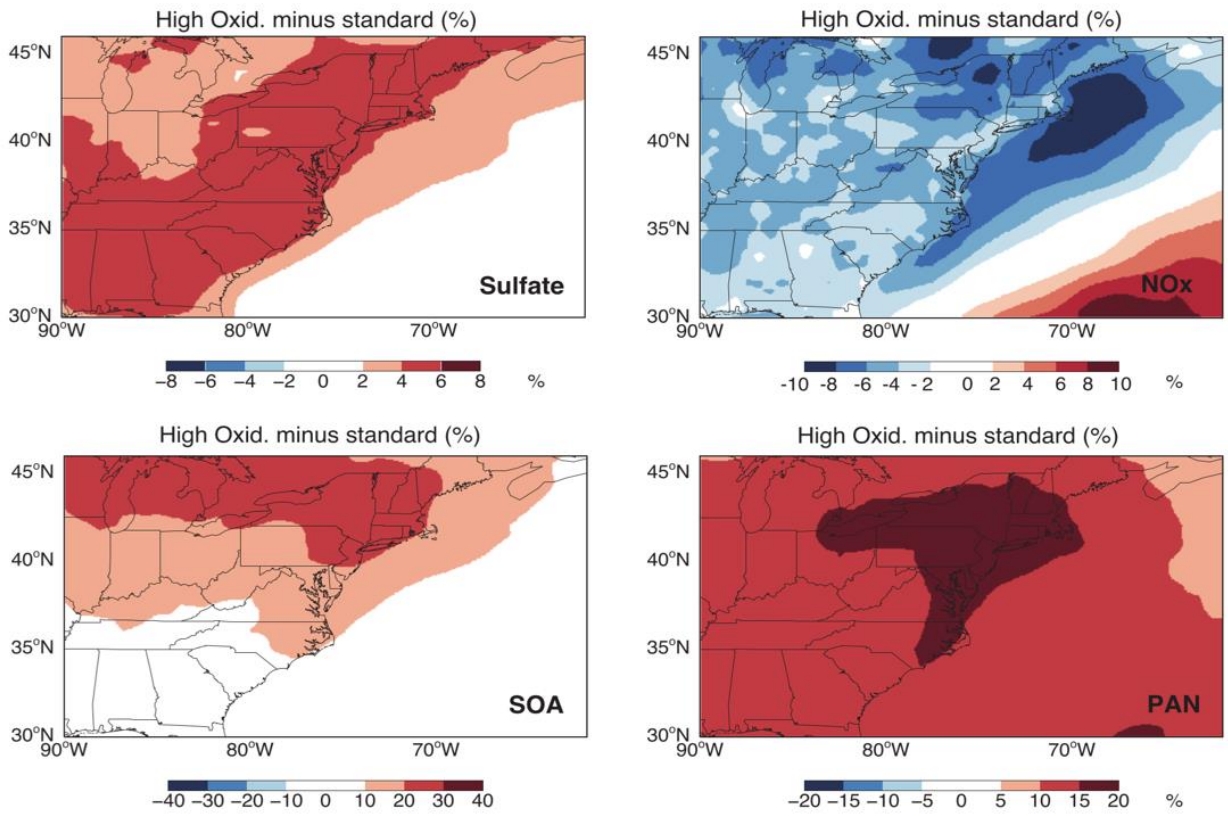

Figure 2.18 Changes in GEOS-Chem from Enhanced Oxidants

Relative changes in GEOS-Chem model predicted particulate sulfate, SOA, NOx, and PAN abundances between runs using standard emissions and chemistry, and those using updated emissions of HCHO and updated $ClNO_2$ chemistry (described in Jaegle et al., (2018)) based on the WINTER observations. Enhanced oxidative capacity in the boundary layer from enhanced HCHO (over land) and $ClNO_2$ (in the MBL) leads to increased conversion of SO_2 to sulfate aerosol mass, VOC to secondary organic aerosol mass, and increased conversion of NO_x into reservoirs such as PAN which in turn affects its global distribution.

Chapter 3

Observational Constraints on the Formation of Cl_2 From the Reactive Uptake of $ClNO_2$ on Aerosols in the Polluted Marine Boundary Layer

3.1 INTRODUCTION

The largest source of inorganic chlorine gases (Cl_y=HCl+$ClNO_2$+HOCl+2Cl_2) to the troposphere is from the volatilization of particle chloride (pCl^-) from sea salt aerosols (SSA) (Graedel and Keene, 1995; Finlayson-Pitts, 2003). In polluted regions, reactions of nitrogen oxides (NO_x= NO_2+ NO) and volatile organic compounds (VOCs) can enhance the liberation of pCl^- from particles. This chlorine activation impacts air quality by increasing oxidant sources through the formation of Cl-atom precursors such as nitryl chloride ($ClNO_2$) and molecular chlorine (Cl_2), which rapidly photolyze during the day (von Glasow et al., 2004; Saiz-Lopez and von Glasow, 2012; Simpson et al., 2015; Schmidt et al., 2016; Sherwen et al., 2016).

Cl atoms are highly reactive towards ozone (O_3) and VOC and have rate coefficients orders of magnitude larger than the hydroxyl radical (OH) for reactions with most alkanes. Although concentrations of Cl atoms in the troposphere are orders of magnitude lower than that of OH, their high reaction rates with O_3 and VOCs make Cl atoms an atmospherically important oxidizer. Several recent observational studies have concluded that in summertime coastal urban areas, reactions with Cl atoms dominated the early morning oxidation of alkanes before ~10 am, surpassing OH reactions, and that 15%-25% of the total daily alkane oxidation was driven by Cl atoms (Riedel et al., 2012; Bannan et al., 2014). On a global scale, Wang et al., (2018) estimated that Cl atoms were responsible for 1% of the global oxidation of methane, and 20% of ethane, among other alkanes. Ultimately, because of the importance of Cl atoms to the overall oxidant

budget in the lower troposphere, sources of Cl atoms are important to constrain.

Roberts et al. (2008) proposed a mechanism for in-situ Cl_2 production where the nocturnal production of $ClNO_2$ from dinitrogen pentoxide (N_2O_5) uptake leads to Cl_2 via reaction on acidic aerosols (R1) following a mechanism analogous to the formation of Br_2 from $BrNO_2$ on Br^- containing substrates.

$$Cl^-(aq) + N_2O_5(g) + H^+(aq) \xrightarrow[\gamma_{N_2O_5}]{} \phi\, ClNO_2(g) + (2-\phi)HNO_3(g) \qquad (R1a)$$

$$Cl^-(aq) + ClNO_2(g) + H^+(aq) \xrightarrow[\gamma_{ClNO_2}]{} Cl_2(g) + HONO(aq) \qquad (R1b)$$

In a series of experiments, they showed that the uptake of $ClNO_2$ proceeded with 60-100% efficiency resulting in ~1 ppbv of Cl_2 for ~1-1.5 ppbv of $ClNO_2$ reacted, when $ClNO_2$ was passed over a film of deliquesced oxalic acid and NaCl (pH ~1.8). On a variety of acidic surfaces with pH ≤ 2, they estimated $\gamma(ClNO_2)$ values of 6×10^{-3} ($\pm 2 \times 10^{-3}$) with $[Cl^-]$ as low as 0.05 M, while on less acidic surfaces, they found that $ClNO_2$ was relatively unreactive with $\gamma(ClNO_2) = 0.3 \times 10^{-6}$ to 5×10^{-6} (Roberts et al., 2008; Roberts et al., 2009). Additional studies have investigated the uptake of $ClNO_2$ without observing specific products or controlling pH, and have shown that $\gamma(ClNO_2)$ on pure water is $< 10^{-5}$ and on the order of 10^{-6} on low concentration halide surfaces, with no temperatures dependence between 177- 291 K (George et al., 1995; Behnke et al., 1997; Frenzel et al., 1998; Schweitzer et al., 1998; Burkeholder et al., 2015;).

Given that $ClNO_2$ has routinely been observed in the troposphere exceeding 1 ppbv (Osthoff et al., 2008; Thornton et al., 2010; Mielke et al., 2011, 2013; Phillips et al., 2012; Riedel et al., 2012; Riedel et al., 2013; Tham et al., 2014; Bannan et al., 2015; Faxon et al., 2015; Wang et al., 2016; Haskins et al., 2017; Yun et al., 2018), this production channel (R1) suggests significant Cl_2 production, on the order of 1 ppbv. Since, concentrations of $ClNO_2$ can be an order of magnitude larger than HOCl concentrations in polluted regions, and the literature values

for $\gamma(ClNO_2)$ on acidic aerosol are larger than $\gamma(HOCl)$, production of Cl_2 from $ClNO_2$ uptake is potentially far greater than from HOCl. Therefore, this mechanism of Cl_2 production would be essential to include in models to simulate tropospheric production of Cl atoms and the oxidative capacity of the atmosphere.

Despite the implication that $ClNO_2$ uptake could contribute up to 1 ppbv of Cl_2, the only recent measurements observing tropospheric Cl_2 exceeding ~150 pptv in the troposphere were attributed to large, direct emissions of Cl_2 from coal fired power plants in China, occurring in the daytime, when $ClNO_2$ chemistry is not prominent (Liu et al., 2017; Liu et al., 2018). All other recent measurements of Cl_2 in the troposphere have shown concentrations on the order of 10-20 pptv, with maxima at night, even with simultaneous $ClNO_2$ observations > 1 ppbv (Finley & Saltzman, 2006; Haskins et al., 2018; Lawler et al., 2011; Riedel et al., 2012;). Although the pioneering measurements of Keene et al., (1993) and Spicer et al. (1998) showed Cl_2* (Cl_2* = Cl_2 + HOCl) in excess of 120 pptv peaking at night, those high concentrations of Cl_2* are thought to be driven more by HOCl, than Cl_2 at night (Pszenny et al., 1993). Furthermore, Wang et al., (2018) significantly overestimated nighttime aircraft observations of Cl_2 during the 2015 Wintertime Investigation of Transportation, Emissions, & Reactivity (WINTER) campaign, using the global chemistry model, GEOS-Chem, when including Cl_2 production from $ClNO_2$ uptake on acidic aerosols. Therefore, observations suggest that Cl_2 production from heterogeneous $ClNO_2$ reaction on acidic particles either occurs with a lower efficiency in the atmosphere than was measured in the laboratory, that Cl_2 production from $ClNO_2$ in the atmosphere is limited by a lack of aerosol having both sufficient acidity and pCl^-, or no observations reported to date have been made in areas where this chemistry is relevant.

Recent studies have shown that submicron aerosols across the globe are acidic, with pH

ranging from -0.5 to 3, suggesting that the conditions for efficient $ClNO_2$ uptake and Cl_2 production are often satisfied, at least in submicron aerosols (Guo et al., 2015; Guo et al., 2016; Guo et al., 2017). However, a large majority of the chloride mass is expected in the super-micron (> 1 μm) range (Keene et al., 1999). This super-micron SSA is more likely to be present in less acidic particles and is less likely to be internally mixed than acidic submicron aerosols. Indeed, a few studies determined that the uptake of $ClNO_2$ was unlikely as a source of their observed Cl_2 since thermodynamic calculations showed the aerosols sampled had pH> 2, which was not acidic enough to catalyze efficient $ClNO_2$ uptake (Riedel et al., 2012; Riedel et al., 2013; Mielke et al., 2011). However, Guo et al. (2016) showed that submicron particles offshore from New York City during WINTER were predicted to have pH ≤ 2. Furthermore, Haskins et al. (2018) showed that both predicted and observed submicron pCl^- was sufficient to promote chloride activation chemistry. Elevated concentrations of gas-phase HCl and $ClNO_2$ in the marine boundary layer indicated internally mixed chloride was activated via heterogeneous chemistry, with submicron aerosols present that contained chloride and had low calculated pH at the time of aircraft sampling. Therefore, the condition of coexisting aerosol acidity and available pCl^- necessary to catalyze $ClNO_2$ uptake does appear exist in the troposphere, and the WINTER campaign provides an opportunity to evaluate laboratory parameterizations of Cl_2 formation from $ClNO_2$ uptake.

In this work, we use WINTER observations of Cl_2, $ClNO_2$, HOCl, N_2O_5, HNO_3, O_3, NO_2, pCl^-, among others in a box model to derive an upper limit to the reaction probability of $ClNO_2$, $\gamma(ClNO_2)$, needed to explain the Cl_2 concentrations observed in specific plumes where the two are highly correlated. We use a reacto-diffusive length framework (Hansen et al., 1994) to reconcile differences between these field derived reaction probabilities on ambient aerosol with

those derived in the laboratory using macroscopic salt films. Observed correlations between the box model derived $\gamma(ClNO_2)$ and parameters such as relative humidity, aerosol pH, aerosol diameter, and pCl^- concentrations are evaluated, and we present a simple empirical parameterization of Cl_2 production from $ClNO_2$ reactive uptake based on these observed relationships.

3.2 WINTER CAMPAIGN & OBSERVATIONS

The WINTER campaign took place in February and March of 2015 using the NSF/NCAR C-130 aircraft. This campaign sampled a broad suite of chemical compounds in 13 flights over the eastern US during both day and night above marine, rural, and highly populated areas. Observations of halogen trace gases, reactive nitrogen oxides, O_3, aerosol composition, and aerosol size distributions were made, some with duplicate techniques. A summary of the instrument accuracy, detection limit, measurement frequency, and operational technique references for the observations used in this work from the WINTER campaign and additional instrument details are given in Chapter 2,Table 2.1. All observations presented in this work are 10s averages of the data collected at 1-2 Hz to improve the signal to noise ratio while maintaining temporal resolution. More information on the WINTER campaign and instrumentation can be found in papers published as a special collection [Guo et al., 2016; Salmon et al., 2017; Fibiger et al., 2018; Jaegle et al., 2018; Haskins et al., 2018; Kenagy et al., 2018; Lee et al., 2018ab; McDuffie et al., 2018ab; Ren et al., 2018; Salmon et al., 2018; Schroder et al., 2018; Sullivan et al., 2019].

The Ultra High Sensitivity Aerosol Spectrometer (UHSAS) was used to measure dry submicron particle surface area density during WINTER. Wet aerosol surface area (cm^2/cm^3)

and volume (cm^3/cm^3) densities are calculated by summing the product of the dry surface area or volume density by relative humidity-dependent, hygroscopic growth factors for particles <1 μm in diameter. Surface and volume growth factors were obtained using the E-AIM model, assuming pure ammonium nitrate submicron particles and no solid formation.

3.3 Calculating Aerosol Growth Factors

We infer total dry aerosol surface area density and total dry aerosol volume density based on the dry number concentrations measured on board the C-130 during the WINTER campaign, by summing the particle surface area with D_p< 3μm and those with D_p< 1μm from the UHSAS measurements when available.

$$\mathbf{SA}^{\mathbf{dry}} = \boldsymbol{SA}_{\boldsymbol{subm}}^{\boldsymbol{dry}} + \boldsymbol{SA}_{\boldsymbol{superm}}^{\boldsymbol{dry}} \quad (3.1)$$

$$\mathbf{V}^{\mathbf{dry}} = \boldsymbol{V}_{\boldsymbol{subm}}^{\boldsymbol{dry}} + \boldsymbol{V}_{\boldsymbol{superm}}^{\boldsymbol{dry}} \quad (3.2)$$

If unavailable, measurements from the PCASP are used after multiplying by a scaling factor. This scaling factor is the median of the ratio of the derived surface area or volume densities derived from the UHSAS and PCASP when simultaneous measurements of number concentrations were being made during the WINTER campaign. It represents the reduced resolution of the PCASP in the submicron size range relative to the UHSAS instrument. The scaling factor used for the surface area density scaling is 1.216 and that for the volume density scaling is 1.34.

From these dry aerosol surface area and volume densities the wet aerosol surface area and volume densities are calculated by summing the product of the dry surface area or volume density by a growth factor for particles with D_p <1 μm and the product of the dry surface area or volume density by a growth factor for particles with D_p <3 μm as follows:

$$\mathbf{SA^{wet}} = \boldsymbol{SA_{subm}^{dry}} * \boldsymbol{GF_{subm}} + \boldsymbol{SA_{superm}^{dry}} * \boldsymbol{GF_{superm}} \quad (3.3)$$

$$\mathbf{V^{wet}} = \boldsymbol{V_{subm}^{dry}} * \boldsymbol{GF_{subm}^{3/2}} + \boldsymbol{V_{superm}^{dry}} * \boldsymbol{GF_{superm}^{3/2}} \quad (3.4)$$

Where GF_{subm} and GF_{superm} are the relative humidity dependent growth factors for submicron and super micron particles, respectively. We calculate the growth factors using the E-AIM model for ammonium nitrate submicron particles and sodium chloride super micron particles assuming no solid formation (metastable mode). Some of the relative humidity dependence for the growth factors used are given below, though growth factors measured at a specific relative humidity were obtained by interpolation. This calculation does not consider the impact of aerosol organics on hygroscopic growth, and a comparison between the two approaches for calculating diameter growth factors during WINTER is presented in Figure S1 of McDuffie et al., (2018a).

3.4 Estimating Wet Surface Area Density from AMS mass

For some plumes of interest, the UHSAS was not functioning. So, a linear model was used to predict the wet aerosol surface area concentration using a parameterization based on the Aerosol Mass Spectrometer (AMS) total submicron mass concentration, derived from collocated measurements when both instruments were sampling. The plumes where aerosol surface area concentration is estimated using this parameterization are denoted in all figures and tables with an asterisk.

In the case where neither the UHSAS or PCASP measurements were available to calculate wet surface area density or wet volume for use within a specific plume (max ~10 minutes), we fit a line to the calculated wet surface area or volume density and the total measured AMS aerosol mass for the entire flight for points measured at a pressure altitude <

400m and separately for those measured at pressure altitude > 400m. For points where neither the UHSAS or PCASP measurements were made, we use these linear fits to predict the wet surface area or volume density based on the measured total AMS aerosol mass during the time when the number distribution measurements are unavailable as shown in Figure 3.1. A separate fit is used for each flight analyzed. A similar process is used to determine when we may be sampling in cloud. When the calculated surface area or volume density spikes without a corresponding increase in total measured aerosol mass from the AMS, we assume we are in cloud, a condition for which the box model analysis is not run.

To investigate the nocturnal uptake of $ClNO_2$ and subsequent production of Cl_2, we examine three nighttime flights that sampled the polluted marine boundary layer downwind of New York City. Figure 3.2 shows a time series of the concentrations of Cl_2 and $ClNO_2$ from each of these flights and an inlaid map of the flight track, highlighting 18 plumes we examine here. These plumes do not include those where $ClNO_2$ and Cl_2 are correlated due to plane altitude changes, or observations that occurred before sunset or after sunrise when photolytic loss of Cl_2 and $ClNO_2$ are important. More information on plumes where these compounds appear correlated in time, but are not included due to these factors, can be found in the Supplemental Information. General trends in Cl_2, $ClNO_2$, HOCl, and HCl concentrations observed throughout the WINTER campaign can be found in Haskins et. al., (2018), and trends in these halogen species observed within power-plant plumes during WINTER can be found in Lee et al., (2018a).

As shown in Figure 3.3, Cl_2 was positively correlated with $ClNO_2$ (r^2=0.88), and with HOCl to a lesser degree (r^2=0.52), implying Cl_2, like $ClNO_2$, is formed by nocturnal heterogeneous chemistry, rather than direct emission. Although these plumes are downwind of

several significant anthropogenic sources of Cl_2, as reported to the Environmental Protection Agency (EPA), these specific plumes of Cl_2 do not show a pattern of direct emission from a point source, which Riedel et al., (2012) demonstrates is distinguishable in a time series from a pattern of in-situ formation, since plumes influenced by direct emission of Cl_2 are not expected to show correlation with $ClNO_2$. Inlet and inner instrument conversion of HOCl or $ClNO_2$ to Cl_2 is unlikely, as Lee et al. (2018) showed that conversion of directly injected, isotopically labeled N_2O_5 to $ClNO_2$ yielded only of 1 pptv $ClNO_2$ per 100 pptv of N_2O_5 during WINTER. The assumption that all Cl_2 plumes are from in-situ production via $ClNO_2$ uptake alone, rather than uptake of HOCl or instrument artifacts will be discussed below in Section 3.8, but would tend to bias our estimates of $\gamma(ClNO_2)$ high relative to the true value. While we cannot rule out that the simultaneous uptake of $ClNO_2$ and HOCl in these plumes is contributing to the elevated Cl_2 concentrations, observations in Figure 3.3 suggest that the production and loss of Cl_2 is more highly correlated with $ClNO_2$ than with HOCl.

3.5 Aerosol Thermodynamics

The aerosol thermodynamics model ISORROPIA II was used to calculate submicron bulk particle pH and liquid water content during WINTER as described in Haskins et al. (2018) and Guo et al., (2016). Previous evaluations of the gas-particle partitioning of chlorine and nitrate predicted by ISORROPIA II against the WINTER data set provide confidence in the ISORROPIA II prediction of bulk-average pH and liquid water content used in this work for submicron particles (Haskins et al., 2018; Guo et al., 2016; Shah et al., 2018). Given the low temperatures observed during WINTER, partitioning of HNO_3 into particles was high, thereby driving submicron particle pH low for much of the campaign (Guo et al., (2016). In all plumes

where Cl_2 and $ClNO_2$ were simultaneously elevated, calculated submicron particle pH was < 2, so comparison of this chemistry at higher pH is not possible with this data set.

Given that submicron aerosols are often acidic, but most pCl^- mass is in the super micron, we employed the Model for Simulation Aerosol Interactions and Chemistry (MOSAIC) (Zaveri et al., 2008) to investigate whether it was possible for sufficient acidity and pCl^- to coexist in particles. The inputted aerosol size distribution was constrained using WINTER measurements of the size distribution by 3 instruments (UHASA, PCASP, FSSP, see Table 2.1) across the size distribution counting particle with dry diameters (D_p) between 0.01-10µm. We constrain the inputted particle masses using the percentage of each aerosol component in the AMS for particles with D_p< 1um for the composition of particles sampled in plume #15, selected because it corresponds to the peak $ClNO_2$ observed during the WINTER campaign, also the same case study plume examined in Chapter 2. Inputted gas phase concentrations of HNO_3HCl were taken as the average within the defined plume. We assume particles with D_p> 2.5µm are pure NaCl and interpolate the mass composition of aerosols with D_p between 1-2.5µm between these two. The resulting inputs to MOSAIC compared with observations are shown in Figure 3.4.

The output of MOSAIC for this case study in whether collocated pH<2 is possible within particles still containing pCl^- is displayed in Figure 3.5. The model captures the expected depletion in pCl^- across the size distribution, with pCl^- located in submicron aerosols becoming more rapidly depleted than those located in larger particles. MOSAIC output of size resolved pH shows that within 6 hours, particle pH for aerosols with D_p between 1-2µm can drop below 2, (with timescales longer for larger aerosols), a timescale before which pCl^- is expected to be completely depleted. Additionally, the pCl^- located within the submicron particles, while small in absolute mass, is still persistent for some time, with equilibrium pH <2 within 30 minutes of

allowing evolution. These results suggest that aerosols with D_p up to 2μm may provide conditions under which laboratory tests suggest the production of Cl_2 from uptake of $ClNO_2$ may be reasonable within minutes to several hours since the onset chemical evolution. Unlike ISORROPIA II, MOSAIC is not as easy to verify field measurements with, since required inputs, such as the composition across the size distribution, are not easily measured. Therefore, while this model provides valuable insight into whether it is theoretically possible to have collocated acidity and pCl^- sufficient to promote the uptake of $ClNO_2$ and production of Cl_2, these results should be taken with some skepticism, given the large underlying uncertainties in model input.

3.6 Multiphase Chemical Box Model

A simple zero-dimensional box model was developed to simulate the nocturnal chemical evolution of an air parcel at constant temperature, pressure, and relative humidity. Table 3.1 summarizes the reactions included in this model and their rate coefficient expressions. The model was run from 5pm local time, considered the onset of N_2O_5 production, for 16.5 hours until 9:30am local time on the following day, for each of the identified plumes. Assuming loss due only to N_2O_5 formation (i.e., no deposition or dilution), the initial concentrations of O_3 and NO_2 at sunset were iteratively adjusted until their modeled loss matched the observations of NO_2 and O_3 at the time the C-130 aircraft intercepted the plume within measurement uncertainty, similar to previous studies of nocturnal reactive nitrogen chemistry [Brown et al., 2003; Thornton et al., 2010; Mielke et al., 2011; Wagner et al., 2013; Phillips et al., 2016; McDuffie et al., 2018a; Tham et al., 2018;]. The amount of reacted O_3 and NO_2 sets a maximum amount of N_2O_5 formed during the time since sunset. The reaction probability of N_2O_5, $\gamma(N_2O_5)$, is then adjusted until the modeled concentrations matched the observation of N_2O_5 for the wet aerosol

surface area observed at the time of intercept. The yield of $ClNO_2$, $\varphi(ClNO_2)$, from R1a is then adjusted until modeled concentrations of $ClNO_2$ match observations, after which, the total nitrate deposition velocity is adjusted until the initial concentration of total nitrate ($^{T}NO_3$= HNO_3 + pNO_3^-(D_p<4.1μm)) matches its concentration at the point of observation. Finally, $\gamma(ClNO_2)$ is iteratively adjusted with extremely small changes in $\varphi(ClNO_2)$ (e.g. typically < 0.01) until Cl_2 and $ClNO_2$ concentrations predicted by the model match the observations within 5% of [Cl_2]. Figure 3.6 shows a collection of all 18 of the box model runs performed and the WINTER observations at the time since the previous 5pm local.

The inferred values for $\gamma(ClNO_2)$ reported here are not strongly dependent upon $\gamma(N_2O_5)$, $\phi(ClNO_2)$, or the deposition velocity of $^{T}NO_3$, used to match the observed concentrations of $ClNO_2$, N_2O_5, and $^{T}NO_3$, nor are they sensitive to other loss mechanisms of nitrate radical (NO_3) that are not included in this simple model (see Section 3.8). By using the observed concentration of [$ClNO_2$] at a given time since sunset, the inferred $\gamma(ClNO_2)$ does not change as $\gamma(N_2O_5)$ or $\phi(ClNO_2)$ are adjusted so long as the model accurately reproduces the observed [$ClNO_2$]. The values used for $\gamma(N_2O_5)$ and $\varphi(ClNO_2)$ in analysis are generally constrained in that they must range between 0 and 1 and should agree with independent estimates from other field-based studies (Bannan et al., 2015, Faxon et al., 2015; Mielke et al., 2011, 2013; McDuffie et al., 2018ab, Osthoff et al., 2008; Phillips et al., 2012; Riedel et al., 2012; Riedel et al., 2013; Tham et al., 2014, Thornton et al., 2010). The range of values for $\gamma(N_2O_5)$ and $\varphi(ClNO_2)$ used in our box model are 0.002 – 0.02 and 0.2 – 0.6, respectively, and are in good agreement with the study of these quantities during the WINTER campaign by McDuffie et al., (2018a, 2018b). Values for $\gamma(ClNO_2)$ obtained by our box model analysis are mainly a function of aerosol surface area, temperature, concentrations of $ClNO_2$ and Cl_2, time since sunset, and dilution, the sensitivities to

all of which are discussed below in Section 3.8.

3.7 Results & Discussion

To match the observed Cl_2 concentrations from $ClNO_2$ uptake in all plumes, $\gamma(ClNO_2)$ ranging from $6x10^{-6}$ to $7x10^{-5}$, with a mean value of $2.3x10^{-5}$ ($\pm$ $1.8x10^{-5}$) were required. Table 3.2 gives a summary of the derived values for $\gamma(ClNO_2)$ for each of the plumes analyzed using the box model, a list of corresponding observations, and the correlation coefficient for each observation with the modeled $\gamma(ClNO_2)$. Despite the ambient environment satisfying all the conditions at which Roberts et al. (2008) found conversion of $ClNO_2$ to Cl_2 to be 60-100% efficient, the values derived from the box model approach (γ $(ClNO_2)$ $2.3x10^{-5}$ $\pm$ $1.8x10^{-5}$) are at least 2 orders of magnitude below that reported on acidic laboratory films (γ $(ClNO_2) = 6x10^{-3}$ $\pm$ $2x10^{-3}$).

There are several possible reasons for the much slower conversion of $ClNO_2$ to Cl_2 in acidic ambient particles compared to that found in the laboratory. One possibility is that $ClNO_2$ is taken up into particles as quickly as described in Roberts et al. (2008), but that the yield of reaction is significantly lower in atmospheric particles that contain reactants other than chloride. Our simulations inherently assume the yield of R1b is unity, but competition of R1b with others that consume Cl^- (aq), like the formation of $ClNO_2$, HCl, HOCl, or BrCl, would lower the yield of the reaction to form Cl_2 (Fickert et al., 1998; Frenzel et al., 1998). Our observations ultimately constrain the product of the $\gamma(ClNO_2)$ and $\varphi(Cl_2)$ from reaction 1b. Figure 3.7 shows the range of $\gamma(ClNO_2)$ that would be consistent with observations of $ClNO_2$ and Cl_2 by assuming different $\varphi(Cl_2) < 1$. In the median, if $ClNO_2$ uptake occurs as efficiently as found in Roberts et al. (2008), the observations require a yield of reaction 1b of 0.001, indicating only a small fraction of the

absorbed $ClNO_2$ results in production of Cl_2. Such a low $\varphi(Cl_2)$ with high $\gamma(ClNO_2)$ implies a large flux of pCl^- into different products. However, in four of the 18 plumes (plume #2, 3, 10, 16), requiring such high uptake of $ClNO_2$ would simultaneously require a non-physically large yield of $ClNO_2$ (i.e. $\varphi(ClNO_2) > 1$) in R1a to match the observed [$ClNO_2$]. Thus, our results imply that reactive uptake of $ClNO_2$ as efficient as was observed in the laboratory cannot simultaneously explain all observations of $ClNO_2$ and Cl_2 during the WINTER campaign without invoking a major gap in our understanding of reactive chlorine chemistry.

A second possibility is that sufficient acidity to promote the reaction is not often collocated with available pCl^-. However, the ISORROPIA II calculations used in this work and examined in detail in Haskins et al., (2018), show that for the WINTER flights examined here submicron particles were predicted to have both $pH \leq 2$ and significant pCl^- and thus do not support this explanation. These ISORROPIA II calculations only examine bulk submicron aerosol pH under an assumption of internal mixing. Therefore, it is possible that particle pH is size dependent with submicron aerosols having lower pH, and super micron aerosols having a higher concentration of pCl^- and a higher pH, perhaps higher than the $pH \leq 2$ threshold observed by Roberts et al., 2008, that would not be captured by this prediction of particle pH. This could imply that the formation of Cl_2 was occurring efficiently only on a fraction of the particles instead of inefficiently on all of them, as we find.

If we assume that production of Cl_2 takes place on only a fraction of the coarse mode aerosol population (D_p > 1μm- 3μm) where most of the mass of chloride is expected, and further assume that these particles are acidic enough to promote the formation of Cl_2, the required $\gamma(ClNO_2)$ are on the order of $1x10^{-4}$, which is not large enough to explain the discrepancy with laboratory results. We argue that internally mixed pCl^- in fact must exist in the submicron mode,

as assuming that pCl^- only exists in the coarse mode implies both the production of $ClNO_2$ and subsequent uptake to form Cl_2 only occurs in the coarse mode. Under this situation, we require unrealistic physical values for $\gamma(N_2O_5)$ and φ $(ClNO_2)$ in all plumes (e.g. φ $(ClNO_2)>1$, $\gamma(N_2O_5)$ > 0.1) to reproduce the full suite of observations. Furthermore, HCl was observed in elevated concentrations during these three flights (Haskins et al., 2018), which is primarily formed via acid displacement at pH 1-3. In addition, the HNO_3 partitioning is highly sensitive to pH and the observed partitioning is consistent with the same thermodynamic models that predict pH [Guo et al., 2016; Haskins et al., 2018]. Thus, we conclude that the plumes examined in this work do simultaneously contain pCl^- and acidity sufficient to promote the reaction as observed in Roberts et al., (2008).

We have inherently assumed uptake occurs on all aerosols at the same rate, when it is possible that reactive uptake occurs with varying efficiency on particles of different sizes (e.g. submicron vs. super-micron particles), composition, and mixing state. However, without quantitative, size-resolved aerosol composition measurements across the size distribution, it is not possible to assess these issues beyond the sensitivity simulations presented in Section 3.8, as our results represent an aerosol population-averaged value.

Given that a potential lack of co-located particle acidity and pCl^- seems unlikely to explain the discrepancy between field and laboratory derived $\gamma(ClNO_2)$, we examined the relationship between the derived values for $\gamma(ClNO_2)$ and other potential predictor variables, including pH, pCl^- mass concentration and Cl^- molarity, liquid water content, and volume-weighted mean wet particle diameter (wet D_p). We used a forward and backward linear stepwise regression model to add or remove the variables listed in Table 3.2, and weighted the observations that had estimated surface area densities from the AMS mass concentrations at half

that of other observations due to larger uncertainties in the corresponding $\gamma(ClNO_2)$. Parameters were added or removed from the model by determining if a *p*-value for an *F*-test of the change in the sum of squared error for the model was significant or not at the 95% level.

We found a rather simple result that wet D_p, and submicron pCl^- mass concentration, could explain 90% of the observed variance in the model derived $\gamma(ClNO_2)$, within the 99% confidence level. In order to make the ISORROPIA II predicted chlorine partitioning consistent with measurements, Haskins et al., 2018 assumed a small fraction of refractory sea-salt was present in particles with $D_p < 1\mu m$, amounting to ~3% of UNH filter chloride in the median during WINTER. Therefore, the pCl^- measurement used in this work is the sum of the AMS non-refractory chloride for dry $D_p < 1\mu m$ and 3% of the UNH filter chloride for dry $D_p < 4.1\ \mu m$. Values of AMS pCl^- lower than the detection limit (0.024 $\mu g/m^3$) were set to ½ of the detection limit. The variations in the AMS non-refractory chloride alone are enough to make pCl^- a significant predictor variable, while adding some refractory chloride from sea salt does statistically significantly improve the fit. D_p and pCl^- are not expected to be independent variables but using them together provided a statistically significant change in the linear model's ability to predict the required $\gamma(ClNO_2)$. The stepwise linear regression function that provided the best fit was $\gamma(ClNO_2) = 6.67x10^{-5}\ D_p + 2.22x10^{-4}\ pCl^- - 1.0x10^{-5}$ where D_p is in μm and pCl^- is in $\mu g\ m^{-3}$, and should be considered valid only over the range of $D_p < 0.6\ \mu m$ and $pCl^- < 0.2\ \mu g\ m^{-3}$. It should be noted that the values of D_p and pCl^- used to calculate this empirical parameterization are not direct measurements of these values in the atmosphere, but rely on estimates of aerosol growth factors and an equilibrium partitioning based estimate of refractory chloride contributions to submicron pCl^-. The validity of this empirical parameterization beyond conditions sampled during the WINTER campaign remains to be determined.

Figure 3.8 shows the variance of $\gamma(ClNO_2)$ with wet D_p and pCl^-, and the multi-linear fit estimated using the forward and backward linear stepwise regression model. The dependence on pCl^- availability of $\gamma(ClNO_2)$ is reasonable as several processes compete to volatilize pCl^- into the gas phase in acidic aerosols. As such, the colocation of sufficient acidity to promote the reaction and available chloride may generally limit the production of Cl_2 from this mechanism, even if particles are not completely depleted in chloride. The trend in increasing $\gamma(ClNO_2)$ with wet D_p is an indicator of a potentially volume-limited aqueous phase reaction, where the reaction rate in the particle phase is slow compared to diffusion, which has the form of equation 3.5.

$$\frac{\mathbf{1}}{\boldsymbol{\gamma}} = \frac{\mathbf{1}}{\boldsymbol{\alpha}} + \frac{\mathbf{3\omega}}{\mathbf{4HRTR_p k_{aq}^I}} \qquad 3.5$$

where α is the mass accommodation coefficient, ω is mean thermal speed (m s^{-1}), *H* is the Henry's law constant (M atm^{-1}), *R* is the gas constant (L atm mol^{-1} K^{-1}), *T* is temperature (K), R_p is particle radius (m), and $k_{aq}{}^I$ is the first order reaction rate (s^{-1}).

Several trends of note were observed in the other predictor variables listed in Table 3.2. Like the positive correlation with pCl^-, a positive correlation was found with HCl. HCl can serve as a reservoir of pCl^- via reversible equilibrium partitioning, such that in the presence of high HCl and higher pH, pCl^- could be replenished if this process could be competitive with the equilibrium partitioning of chloride to the gas phase under such acidic conditions. No statistically significant correlation was found with submicron aerosol pH, or liquid water content, presumably because the bulk calculated pH <2 in all plumes and because particles were likely at least partially deliquesced in the humid marine boundary layer, such that acidity or presence of an aqueous phase was not a limiting factor in Cl_2 production..

A slight negative correlation, though not statistically significant, was found between $\gamma(ClNO_2)$ and both submicron particle nitrate (pNO_3^-) and organic content (pOA), (both known to

suppress absolute $ClNO_2$ formation via N_2O_5 uptake suppression) and likely to impact $ClNO_2$ uptake directly or indirectly (Bertram and Thornton 2009; McDuffie et al., 2018ab; Ryder et al., 2015). There was a distinct negative correlation between the required $\gamma(ClNO_2)$ and the time after sunset at which the observations were made. It is possible this is due to a sampling bias in our measurements as the four plumes with the highest $\gamma(ClNO_2)$ are those intercepted earliest in the night, where surface area was estimated with the total AMS mass and uncertainty is high. However, we cannot rule out that it could arise from a mechanism that either promotes uptake early in the evening, such as near source emissions, or a mechanism that suppresses uptake later in the night, such as chloride availability after particle processing.

Given the above finding that volume-weighted wet D_p is a strong predictor of the $\gamma(ClNO_2)$, we hypothesize that the $ClNO_2$ reacto-diffusive length (ℓ), a measure of the characteristic distance an accommodated molecule must travel before reaction (Hanson et al., 1994), is larger than the mean D_p of sufficiently acidic aerosol particles sampled during WINTER. This hypothesis, summarized in Figure 3.9, provides an explanation of the much lower $\gamma(ClNO_2)$ derived from ambient measurements compared to those measured in the laboratory. In small atmospheric particles, $ClNO_2$ could be accommodated but diffuse out before reacting with pCl^- to form Cl_2, thereby leading to a lower net $\gamma(ClNO_2)$ in smaller aerosol particles than on the thicker laboratory films, which had aqueous volumes with effective thicknesses > 100's of microns (Roberts et al., 2009].

To test this hypothesis, we estimate ℓ by extracting an observationally derived estimate for $k_{aq}{}^{I}$ using equation 3.5 and the box model derived values for $\gamma(ClNO_2)$, and subsequently solving for ℓ in equation (3.6 by assuming a liquid diffusion coefficient (D_l) of 1 x 10^{-5} cm^2 s^{-1} (Poling et al., 2001; Cussler, 2009).

$$\ell = \left(\frac{D_l}{k_{aq}^I}\right)^{1/2} \quad (3.6)$$

Using the observed wet particle radius, R_p, temperature, a Henry's law constant of 4.6 x 10^{-2} M atm^{-1} (Frenzel et al., 1997), and assuming that $\alpha >> \gamma(ClNO_2)$, over all plumes, we require a mean $k_{aq}{}^I$ of 3.7x10 ^{4} s^{-1} ± 3.5x10 ^{4} s^{-1} and ℓ of 0.2 μm ± 0.05 μm to match the box model derived values of $\gamma(ClNO_2)$.

With ℓ on the same order of magnitude as observed wet D_p, and $k_{aq}{}^I$ competitive with the liquid phase diffusion rate, these values imply some fraction of accommodated $ClNO_2$ diffuses out of aerosol particles before reaction. This result explains why observationally constrained values of the $\gamma(ClNO_2)$ are orders of magnitude lower than their estimated values on thick (~375 μm) laboratory films. Figure 3.10 **Determining First and Second Order Rate Coefficients**

a) The minimum, median, and maximum values for γ(ClNO2) calculated from the required kaqI as a function of wet Dp (lines) compared to the box model derived values of γ(ClNO2) at the observed wet Dp (points) b) Scatter plot of the first order rate coefficients needed to match the box model derived γ(ClNO2) versus the chloride molarity determined from the concentration of pCl- (AMS + 3% filter) and UHSHS particle volume concentrations. The slope of the linear least squared fit (line), with plumes having estimated surface area (denoted with *) weighted at 50%, is the corresponding second order rate coefficient.

Figure 3.11 Time series of HOCl, Cl2, ClNO2

Time series of altitude (first row), concentrations of ClNO2 (second row), and concentrations of HOCl and Cl2 (third row), with each of the 18 plumes examined in this work highlighted and numbered for each of the 3 nighttime flights (columns). Note: Cl2 concentrations are offset by +12 pptv for comparison Figure 3.12 a) The minimum, median, and maximum values for γ(ClNO2) calculated from the required kaqI as a function of wet Dp (lines) compared to the box model derived values of γ(ClNO2) at the observed wet Dp (points) b)

Scatter plot of the first order rate coefficients needed to match the box model derived $\gamma(ClNO2)$ versus the chloride molarity determined from the concentration of pCl- (AMS + 3% filter) and UHSHS particle volume concentrations. The slope of the linear least squared fit (line), with plumes having estimated surface area (denoted with *) weighted at 50%, is the corresponding second order rate coefficient. **Figure 3.13**a shows the minimum, median, and maximum values for $\gamma(ClNO_2)$ calculated from k_{aq}^{I} as a function of wet D_p compared to the box model derived values of $\gamma(ClNO_2)$ at the observed wet D_p. The box model derived $\gamma(ClNO_2)$ exhibit a similar trend with D_p as that expected from equation 3.5 for a volume-limited process having ℓ on the order of 0.2 μm. If ambient particles were more viscous than pure water, or contained organics slowing liquid phase diffusion such that D_l was lower than the assumed value, the estimated ℓ would decrease promoting a faster k_{aq}^{I}. However, the presence of elevated $ClNO_2$ concentrations, formed from reactive uptake of N_2O_5 to aerosol, indicates that the ambient aerosol population sampled within these plumes are not strongly impacted by diffusion limiting conditions, like viscous organic coatings. The assumed α will not impact the values presented here, since α would have to be on the order of $1x10^{-5}$, uncharacteristically low for liquid aerosols containing salt, to significantly impact $\gamma(ClNO_2)$.

Our observationally constrained values for k_{aq}^{I} of $3.7x10^{4}$ s^{-1}± $3.5x10^{4}$ s^{-1} are orders of magnitude lower than those reported in Roberts et al., (2008) ($k_{aq}^{I} = 1.6x10^{7}$ s^{-1}). To investigate if this difference arises from a fundamentally slower reaction in ambient aerosols or because of lower chloride molarity in ambient aerosols, we use the derived k_{aq}^{I} and measured $[Cl^-]$ to extract a second order rate coefficient, $\left(k_{aq}^{II} \equiv \frac{k_{aq}^{I}}{[Cl^-]}\right)$. Notably, the experiments preformed in Roberts et al., 2008 were done at low chloride molarity to simulate atmospheric particle concentrations ($[Cl^-]$= 0.05 M), and are comparable to the range estimated from the plumes examined here (0.03 M <

[Cl^-] < 0.35 M). However, as shown in Figure 3.10 **Determining First and Second Order Rate Coefficients**

a) The minimum, median, and maximum values for γ(ClNO2) calculated from the required kaqI as a function of wet Dp (lines) compared to the box model derived values of γ(ClNO2) at the observed wet Dp (points) b) Scatter plot of the first order rate coefficients needed to match the box model derived γ(ClNO2) versus the chloride molarity determined from the concentration of pCl- (AMS + 3% filter) and UHSHS particle volume concentrations. The slope of the linear least squared fit (line), with plumes having estimated surface area (denoted with *) weighted at 50%, is the corresponding second order rate coefficient.

Figure 3.11 Time series of HOCl, Cl2, ClNO2

Time series of altitude (first row), concentrations of ClNO2 (second row), and concentrations of HOCl and Cl2 (third row), with each of the 18 plumes examined in this work highlighted and numbered for each of the 3 nighttime flights (columns). Note: Cl2 concentrations are offset by +12 pptv for comparison Figure 3.12 a) The minimum, median, and maximum values for γ(ClNO2) calculated from the required kaqI as a function of wet Dp (lines) compared to the box model derived values of γ(ClNO2) at the observed wet Dp (points) b) Scatter plot of the first order rate coefficients needed to match the box model derived γ(ClNO2) versus the chloride molarity determined from the concentration of pCl- (AMS + 3% filter) and UHSHS particle volume concentrations. The slope of the linear least squared fit (line), with plumes having estimated surface area (denoted with *) weighted at 50%, is the corresponding second order rate coefficient. **Figure 3.13**b as the slope of the linear least square regression line, we find a median k_{aq}^{II} of 5.7x10^4 M^{-1} s^{-1}. This value is considerably lower than that reported in Roberts et al., (2008), suggesting that the difference in chloride molarity is not enough to explain the difference in implied reaction rates between the field measurements (k_{aq}^{II} = 5.7x10^4 M^{-1} s^{-1}) and laboratory experiments (k_{aq}^{II} ~10^7 M^{-1} s^{-1}). Given that [Cl^-] used is an average over the

aerosol size distribution calculated from three separate instruments data (AMS pCl^-, UNH pCl^-, UHSAS particle volume density), there is considerable uncertainty associated with this parameter, likely giving rise to deviations from the linear least square regression fit shown in Figure 3.10 **Determining First and Second Order Rate Coefficients**

a) The minimum, median, and maximum values for γ(ClNO2) calculated from the required kaqI as a function of wet Dp (lines) compared to the box model derived values of γ(ClNO2) at the observed wet Dp (points) b) Scatter plot of the first order rate coefficients needed to match the box model derived γ(ClNO2) versus the chloride molarity determined from the concentration of pCl- (AMS + 3% filter) and UHSHS particle volume concentrations. The slope of the linear least squared fit (line), with plumes having estimated surface area (denoted with *) weighted at 50%, is the corresponding second order rate coefficient.

Figure 3.11 Time series of HOCl, Cl2, ClNO2

Time series of altitude (first row), concentrations of ClNO2 (second row), and concentrations of HOCl and Cl2 (third row), with each of the 18 plumes examined in this work highlighted and numbered for each of the 3 nighttime flights (columns). Note: Cl2 concentrations are offset by +12 pptv for comparison Figure 3.12 a) The minimum, median, and maximum values for γ(ClNO2) calculated from the required kaqI as a function of wet Dp (lines) compared to the box model derived values of γ(ClNO2) at the observed wet Dp (points) b) Scatter plot of the first order rate coefficients needed to match the box model derived γ(ClNO2) versus the chloride molarity determined from the concentration of pCl- (AMS + 3% filter) and UHSHS particle volume concentrations. The slope of the linear least squared fit (line), with plumes having estimated surface area (denoted with *) weighted at 50%, is the corresponding second order rate coefficient. **Figure 3.13**b, though these uncertainties are unlikely to explain 3 orders of magnitude difference in k_{aq}^{II}. Ultimately, our results suggest the reaction is fundamentally slower in small atmospheric particles (D_p ~ 1μm) than inferred from thick

(~375μm) laboratory films.

Hanson et al. (1994) derived the following expression to relate the effective uptake coefficient of a gas on small drops (γ_e) relative to its uptake coefficient on thick (~100s μm) laboratory films (γ_m) as follows:

$$\frac{1}{\gamma_e} = \frac{1}{\alpha} + \frac{1}{\gamma_m[coth(D_p/\ell) - \ell/D_p]} \quad (3.7)$$

where α is the mass accommodation coefficient. If α >> γ, equation (3.7 becomes:

$$\gamma_e \cong \left[coth\left(D_p/\ell\right) - \ell/D_p\right]\gamma_m \quad (3.8)$$

In order to further test our hypothesis, we use equation 3.8, γ_m measured by Roberts et al. (2008), and the box model derived values for γ_e with the measured D_p, to iteratively determine the implied ℓ and k_{aq}^{I} for each of the 18 plumes that would explain the difference in our model derived $\gamma(ClNO_2)$ and the laboratory measured $\gamma(ClNO_2)$. Using this method, we estimated a mean ℓ of on the order of 15 μm (compared to 0.2 μm using equation (3.6) and values of k_{aq}^{I} considerably slower than our previous calculation. We attribute the discrepancy between our two methods of estimating ℓ to the uncertainty in the laboratory measured value, γ_m. The hyperbolic cotangent function in equation (3.8 is nonlinear, so small changes in γ_m result in orders of magnitude changes in the estimated ℓ and k_{aq}^{I} values. This result ultimately provides additional qualitative support for our hypothesis that the difference between our observationally constrained value of $\gamma(ClNO_2)$ and those reported from laboratory measurements in Roberts et al., (2008) arise because R1b is volume limited.

3.8 Model Sensitivity

Here we consider to what degree the inputs or assumptions used in the model may have

influenced the field derived reactive uptake coefficients. Several of the input uncertainties would lead to an overestimation in the box model derived $\gamma(ClNO_2)$ which is the opposite direction needed to explain the discrepancy between those observed in the laboratory and in our observations. We do not consider the possibility of direct emission of Cl_2 from anthropogenic point sources in any of the plumes analyzed here. While no plumes show clear evidence of being influenced by anthropogenic point sources of Cl_2, neglecting such a source would lead us to overestimate the $\gamma(ClNO_2)$ needed to explain the observed Cl_2. Similarly, if the onset of N_2O_5 production were earlier than our assumed 5pm, we would also overestimate the $\gamma(ClNO_2)$. The $\gamma(ClNO_2)$ had to be decreased by ~8% if the sunset time was moved back an hour to 4 pm.

We also reran the model setting sunset forward an hour to 6pm. After accounting for the changes in the initial concentrations of NO_2 and O_3 needed to match the observations at plume intercept, the yield of $ClNO_2$ from R1a had to be increased to match observations of $ClNO_2$, after which the $\gamma(ClNO_2)$ had to be increased to match Cl_2 concentrations. For a typical plume, the $\gamma(ClNO_2)$ had to be increased by ~10% if the sunset time was moved forward an hour, and for plume #1, $\gamma(ClNO_2)$ increased by ~40%, resulting a maximum value of 9.5×10^{-5}, which implied a ℓ of 0.09 μm and k_{aq}^{I} of 1.2×10^{5} s^{-1}, still consistent with the discrepancies between the field and laboratory studies resulting from a size limited uptake coefficient. Moving the onset of N_2O_5 chemistry even later eventually leads to unrealistic values for $\gamma(N_2O_5)$ and $\phi(ClNO_2)$.

Our 0-D model does not include NO_3+ VOC reactions, though these reactions would not significantly bias the results herein. Biogenic emissions, which often constitute the largest loss of NO_3, are greatly reduced in winter due to total lack of isoprene emissions and the strong temperature dependence of monoterpene emissions (Janson et al., 1993). Under WINTER conditions, McDuffie et al., (2018a) calculated that the predicted equilibrium concentrations of

NO_3 were typically more than 100 times lower than N_2O_5 and predicted only small fractional contributions of NO_3 to the total loss of NO_3 + N_2O_5. The box model approach employed in McDuffie et al., (2018a), similar to that presented in our work, shows that despite the large number of uncertainties associated with direct NO_3 loss, 10% changes in total loss rates for NO_3 had a small impact on the box model predicted values of $\gamma(N_2O_5)$. We expect the impact on the values of $\gamma(ClNO_2)$ to be even smaller than that on $\gamma(N_2O_5)$ because while including NO_3+ VOC reactions may slow N_2O_5 and $ClNO_2$ formation temporally, we only report instantaneous values of $\gamma(ClNO_2)$, which are not dependent on the temporal evolution of N_2O_5 and $ClNO_2$, but their absolute concentrations, which we require the box model to reproduce at the time of intercept.

Another consideration is that Cl_2 may be produced from HOCl or $ClONO_2$ uptake, instead of from $ClNO_2$ uptake alone as we currently assume. Figure 3.14 **Time series of HOCl, Cl2, ClNO2**

Time series of altitude (first row), concentrations of ClNO2 (second row), and concentrations of HOCl and Cl2 (third row), with each of the 18 plumes examined in this work highlighted and numbered for each of the 3 nighttime flights (columns). Note: Cl2 concentrations are offset by +12 pptv for comparison Figure 3.15 a) The minimum, median, and maximum values for γ(ClNO2) calculated from the required kaqI as a function of wet Dp (lines) compared to the box model derived values of γ(ClNO2) at the observed wet Dp (points) b) Scatter plot of the first order rate coefficients needed to match the box model derived γ(ClNO2) versus the chloride molarity determined from the concentration of pCl- (AMS + 3% filter) and UHSHS particle volume concentrations. The slope of the linear least squared fit (line), with plumes having estimated surface area (denoted with *) weighted at 50%, is the corresponding second order rate coefficient.

Figure 3.16 Changes in HCl emissions and NSS Cl- deposition

Changes in anthropogenic SO2 emissions (a) and HCl emissions (b) by EPA regions for 1998-2018 compared to the precipitation weighted, three-year annual average of the weekly NADP observations of NSS SO42-(c,e) and NSS Cl- deposition (d,f) for 1998-2001

(middle row) and 2016-2019 (bottom row) at 128 sites. Dark outlines show the EPA regions, which are labeled numerically. Circles indicate sites where the 3-year mean absolute value of NSS component exceeds 5% of that period's 3-year mean in either the total SO42- or Cl- and diamonds show sites where the 3-year mean absolute value of NSS component is less than 5% of that period's 3-year mean in either the total SO42- or Cl-.Figure 3.17 shows plane altitude and concentrations of HOCl along with that of Cl_2 and $ClNO_2$ (from Figure 3.2). It is apparent that Cl_2 is correlated with both $ClNO_2$ and HOCl in time on all nocturnal flights examined here. Figure 3.3 shows a scatter plot of Cl_2 against both HOCl and $ClNO_2$, from which it is apparent that Cl_2 is more highly correlated with $ClNO_2$ than HOCl in the plumes examined here. Furthermore, using estimated uptake coefficients from Lawler et al., (2011), there is not enough HOCl present to explain the Cl_2 concentrations in 6 of the 18 plumes observed, suggesting that this mechanism could be contributing to Cl_2 concentrations in some cases presented here, but not all. Using that of Pratte & Rossi (2006), none of the Cl_2 concentrations could be explained from HOCl concentrations. It is impossible to completely rule out the conversion of HOCl to Cl_2 on surfaces, in all plumes analyzed here, but if it was occurring, it would bias our box model derived $\gamma(ClNO_2)$ values high, thereby pushing the ratio of D_p/ℓ even lower, further increasing the discrepancy between the field and laboratory measurements.

Measurements of $ClONO_2$ were not available during WINTER, so estimates of its contributions to observed Cl_2 concentrations cannot be made. However, Breton et al., (2018) report 15 pptv of $ClONO_2$ throughout the night in a polluted region of China. Under the conditions observed during WINTER, the relevant uptake coefficients, $4.6x10^{-3}$ - 0.14 (Burkholder et al., 2015) of $ClONO_2$, would predict complete conversion of 15 pptv of $ClONO_2$ into Cl_2 within 15 minutes to 6 hours, and the production of >40 pptv Cl_2 if such concentrations

of $ClONO_2$ were sustained throughout the night, which is significantly higher than WINTER observations. Such a rapid turnover of $ClONO_2$ would imply a nighttime formation mechanism of $ClONO_2$, of which we have no knowledge. Thus, we conclude that $ClONO_2$ heterogeneous chemistry was not an important source of Cl_2 during WINTER, and to the extent it was occurring, we would need to further slow $ClNO_2$ conversion to Cl_2, increasing the discrepancy between laboratory and field.

Due to large flight-by-flight uncertainties in dilution rates, dilution was not included in the initial box model analysis. Therefore, a sensitivity simulation was run where dilution was represented as an additional first order loss process for all chemical species in the mechanism (Table 3.2). Following McDuffie et al., (2018), the dilution rate constant was set to a constant value of 3.1×10^{-5} s^{-1} as calculated from NO_y mixing ratio changes in a single air parcel measured at multiple times during RF03. For all species except O_3, concentrations in background air outside plumes was set to zero. Background levels of O_3 were calculated on a flight-by-flight basis as the intercept of the O_3/NO_y correlation plot. Considering dilution increased $\gamma(ClNO_2)$ by only 5% in the median, requiring a maximum $\gamma(ClNO_2)$ of 6.8×10^{-5}, which does not significantly change the results presented herein.

Uncertainty in the calculated aerosol growth factors can affect the available surface area for heterogeneous chemistry. Instead of using a surface area concentration based on deliquesced particles, we reran the model using the aerosol dry surface area. At most, $\gamma(ClNO_2)$ had to be increased by 30 to 60%. Even together with the maximum uncertainty in the time for onset of N_2O_5 production and dilution used in the model, this was not enough to significantly impact the results presented here. Therefore, we conclude the uncertainties in our model inputs are not enough to explain the discrepancy in the observationally constrained values and laboratory

measurements of $\gamma(ClNO_2)$, and that the strong correlations between model-derived $\gamma(ClNO_2)$, particle size and pCl^- suggest that this chemistry may be size and chloride limited in the atmosphere thereby serving to reduce the production efficiency of Cl_2 compared to that inferred from laboratory studies on macroscopic films.

3.9 CONCLUSIONS

We have presented simultaneous observations of Cl_2 and $ClNO_2$ in 18 highly correlated plumes from the WINTER campaign where in-situ production of Cl_2 is more likely than direct emission. Using a simple zero-dimensional box model to simulate the nocturnal chemical evolution of an air parcel, we derived values for $\gamma(ClNO_2)$ required to explain observed Cl_2 from $ClNO_2$ uptake ranging from $6.5x10^{-6}$ to $6.7x10^{-5}$, with a mean value of $2.3x10^{-5}$ ($\pm 1.8x10^{5}$). These uptake coefficients are 2 orders of magnitude lower than previous laboratory observations on acidic surfaces, despite independent indications that submicron particle pH was less than 2 and pCl^- was non-zero, the conditions under which this reaction was seen to proceed with 60-100% efficiency (Roberts et al., 2008). Assuming $ClNO_2$ uptake as efficient as observed in the laboratory, but occurring with a very low yield of Cl_2 ($\varphi(Cl_2) = 0.001$), we were unable to match the observed [$ClNO_2$] and [Cl_2] concentrations in 4 of the 18 plumes analyzed. We cannot rule out the simultaneous uptake of HOCl or $ClONO_2$ contributing to the observed Cl_2 concentrations, though these would bias our derived values for $\gamma(ClNO_2)$ high, the opposite direction needed for agreement with laboratory values.

We found a strong dependence of the observationally-constrained values for $\gamma(ClNO_2)$ on both pCl^- and volume-weighted wet D_p, indicating that the efficiency with which $ClNO_2$ is

converted to Cl_2 is both dependent on the availability of collocated pCl^- and sufficient acidity to promote the reaction, and that $\gamma(ClNO_2)$ is volume limited. We hypothesize the most plausible explanation for the discrepancy in our field derived $\gamma(ClNO_2)$ and those measured in the laboratory stems from the different length scales in macroscopic films or salt beds used in the laboratory compared to submicron particles. We estimate that the first order reaction rate constant in the 18 plumes examined here is k_{aq}^{I} of 3.7×10^4 $s^{-1} \pm 3.5 \times 10^4$ s^{-1}, which implies a second order reaction rate constant of $k_{aq}^{II} = 5.7 \times 10^4$ M^{-1} s^{-1} using the observationally constrained chloride molarity.

Ultimately, our work suggests a need for direct laboratory studies of $ClNO_2$ reactive uptake on acidic submicron aerosol particles. It is possible that our inference of a size dependence is rather a result of some other limitation not considered here, such as an equilibrium between particle chloride, nitrite, Cl_2 and $ClNO_2$. A laboratory experiment using acidic submicron particles would directly test these hypotheses. Currently, our observations suggest models use a much lower $\gamma(ClNO_2)$ on the order of 2.3×10^{-5} ($\pm 1.8 \times 10^5$), to simulate Cl_2 production on acidic aerosols from nocturnal reactive nitrogen chemistry.

3.10 REFERENCES

Bahreini, R., Dunlea, E. J., Matthew, B. M., Simons, C., Docherty, K. S., DeCarlo, P. F., et al. (2008). Design and operation of a pressure- controlled inlet for airborne sampling with an aerodynamic aerosol lens. Aerosol Science and Technology, 42(6), 465–471. https://doi.org/ 10.1080/02786820802178514

Bannan, T. J., Booth, A. M., Bacak, A., Muller, J. B. A., Leather, K. E., Le Breton, M., et al. (2015). The first UK measurements of nitryl chloride using a chemical ionization mass spectrometer in central London in the summer of 2012, and an investigation of the role of Cl atom oxidation. Journal of Geophysical Research: Atmospheres, 120, 1–20. https://doi.org/10.1002/2014JD022629

Behnke, W., George, C., Scheer, V., & Zetzsch, C. (1997). Production and decay of ClNO2 from the reaction of gaseous N2O5 with NaCl solution: Bulk and aerosol experiments. Journal of Geophysical Research, 102, 3795–3804.

Bertram, T. H., & Thornton, J. A. (2009). Toward a general parameterization of N2O5 reactivity on aqueous particles: the competing effects of particle liquid water, nitrate, and chloride. Atmospheric Chemistry and Physics, 9, 8351–8363. https://doi.org/10.5194/acp-9-8351-2009

Brown, S. S., Dubé, W. P., Peischl, J., Ryerson, T. B., Atlas, E., Warneke, C., et al. (2011). Budgets for nocturnal VOC oxidation by nitrate radicals aloft during the 2006 Texas Air Quality Study. Journal of Geophysical Research, 116, D24305.

Brown, S. S., Stark, H., & Ravishankara, A. R. (2003). Applicability of the steady state approximation to the interpretation of atmospheric observations of NO3 and N2O5. Journal of Geophysical Research, 108(D17), 4539. https://doi.org/10.1029/2003JD003407

Burkholder, J. B., Sander, S. P., Abbatt, J. P. D., Barker, J. R., Huie, R. E., Kolb, C. E., et al. (2015). Chemical kinetics and photochemical data for use in atmospheric studies: Evaluation number 18. Pasadena, CA: Jet Propulsion Laboratory, National Aeronautics and Space Administration.

Cai, Y., Montague, D. C., Mooiweer-Bryan, W., & Deshler, T. (2008). Performance characteristics of the ultra-high sensitivity aerosol spectrometer for particles between 55 and 800 nm: Laboratory and field studies. Journal of Aerosol Science, 39(9), 759–769. https://doi. org/10.1016/j.jaerosci.2008.04.007

Cussler, E. L. (2009). Diffusion: Mass transfer in fluid systems (3rd ed.). Cambridge, UK: Cambridge University Press.

Custard, K. D., Raso, A. R. W., Shepson, P. B., Staebler, R. M., & Pratt, K. A. (2017). Production and release of molecular bromine and chlorine from the Arctic coastal snowpack. ACS Earth and Space Chemistry, 1(3), 142–151. https://doi.org/10.1021/ acsearthspacechem.7b00014

Day, D. A., Wooldridge, P. J., Dillon, M. B., Thornton, J. A., & Cohen, R. C. (2002). A thermal

dissociation laser-induced fluorescence instrument for in situ detection of NO2, peroxy nitrates, alkyl nitrates, and HNO3. Journal of Geophysical Research, 107(D6), 4046. https://doi.org/10.1029/2001JD000779

DeCarlo, P. F., Kimmel, J. R., Trimborn, A., Northway, M. J., Jayne, J. T., Aiken, A. C., et al. (2006). Field-deployable, high-resolution, time- of-flight aerosol mass spectrometer. Analytical Chemistry, 78, 8281–8289. https://doi.org/10.1021/ac061249n

DeMore, W. B., Sander, S. P., Golden, D. M., Hampson, R. F., Kurylo, M. J., Howard, C. J., et al. (1997). Chemical kinetics and photochemical data for use in stratospheric modeling: Eval. 12. Pasadena, Calif: Jet Propul. Lab.

Dibb, J. E., Talbot, R. W., & Scheuer, E. M. (2000). Composition and distribution of aerosols over the North Atlantic during the Subsonic Assessment Ozone and Nitrogen Oxide Experiment (SONEX). Journal of Geophysical Research, 105(D3), 3709–3717. https://doi.org/ 10.1029/1999JD900424

Dibb, J. E., Talbot, R. W., Scheuer, E. M., Blake, D. R., Blake, N. J., Gregory, G. L., et al. (1999). Aerosol chemical composition and distribution during the Pacific Exploratory Mission (PEM) tropics. Journal of Geophysical Research, 104(D5), 5785–5800. https://doi.org/ 10.1029/1998JD100001

Faxon, C., Bean, J., & Hildebrandt-Ruiz, L. (2015). Inland concentrations of ClNO2 in Southeast Texas suggest chlorine chemistry significantly contributes to atmospheric reactivity. Atmosphere, 6 (Atmospheric Composition Observations), 1487–1506. https://doi.org/ 10.3390/atmos6101487

Fibiger, D. L., McDuffie, E. E., Dubé, W. P., Aikin, K. C., Lopez-Hilfiker, F. D., Lee, B. H., et al. (2018). Wintertime overnight NOx removal in a Southeastern United States coal-fired power plant plume: A model for understanding winter NOx processing and its implications. Journal of Geophysical Research: Atmospheres, 123, 1412–1425. https://doi.org/10.1002/2017JD027768

Fickert, S., Helleis, F., Adams, J. W., Moortgat, G. K., & Crowley, J. N. (1998). Reactive uptake of ClNO2 on aqueous bromide solutions. The Journal of Physical Chemistry. A, 102, 10,689–10,696. Finlayson-Pitts, B., Ezell, M., & Pitts, J. (1989). Formation of chemically active chlorine compounds by reactions of atmospheric NaCl particles with gaseous N2O5 and ClONO2. Nature, 337(6204), 241–244. https://doi.org/10.1038/337241a0

Finley, B. D., & Saltzman, E. S. (2006). Measurement of Cl2 in coastal urban air. Geophysical Research Letters, 33, L11809. https://doi.org/ 10.1029/2006gl025799

Frenzel, A., Scheer, V., Sikorski, R., George, C., Behnke, W., & Zetzsch, C. (1998). Heterogeneous interconversion reactions of BrNO2, ClNO2, Br2, and Cl2. The Journal of Physical Chemistry A, 102(8), 1329–1337. https://doi.org/10.1021/jp973044b

Fuchs, H., Dube, W. P., Lerner, B. M., Wagner, N. L., Williams, E. J., & Brown, S. S. (2009). A sensitive and versatile detector for atmospheric NO2 and NOx based on blue diode laser cavity ring-down spectroscopy. Environmental Science & Technology, 43(20), 7831–7836. https://doi.org/10.1021/es902067h

George, C., Behnke, W., Scheer, V., Zetzsch, C., Magi, L., Ponche, J. L., & Mirabel, P. (1995). Fate of ClNO2 over aqueous solutions containing iodide. Geophysical Research Letters, 22, 1505–1508.

Graedel, T. E., & Keene, W. C. (1995). Tropospheric budget of reactive chlorine. Global Biogeochemical Cycles, 9(1), 47–77. https://doi.org/ 10.1029/94GB03103

Guo, H., Liu, J., Froyd, K. D., Roberts, J. M., Veres, P. R., Hayes, P. L., et al. (2017). Fine particle pH and gas-particle phase partitioning of inorganic species in Pasadena, California, during the 2010 CalNex campaign. Atmospheric Chemistry and Physics, 17, 5703–5719. https:// doi.org/10.5194/acp-17-5703-2017

Guo, H., Sullivan, A. P., Campuzano-Jost, P., Schroder, J. C., Lopez-Hilfiker, F. D., Dibb, J. E., et al. (2016). Fine particle pH and the partitioning of nitric acid during winter in the northeastern United States. Journal of Geophysical Research: Atmospheres, 121, 10,355–10,376. https://doi.org/10.1002/2016JD025311

Guo, H., Xu, L., Bougiatioti, A., Cerully, K. M., Capps, S. L., Hite, J. R. Jr., et al. (2015). Fine-particle water and pH in the southeastern United States. Atmospheric Chemistry and Physics, 15(9), 5211–5228. https://doi.org/10.5194/acp-15-5211-2015

Hanson, D. R., & Ravishankara, A. R. (1994). Reactive uptake of ClONO2 onto sulfuric acid due to reaction with HCl and H2O. The Journal of Physical Chemistry, 98(22), 5728–5735. https://doi.org/10.1021/j100073a026

Hanson, D. R., Ravishankara, A. R., & Solomon, S. (1994). Heterogeneous reactions in sulfuric acid aerosols: A framework for model calculations. Journal of Geophysical Research, 99(D2), 3615–3629. https://doi.org/10.1029/93JD02932

Haskins, J. D., Jaeglé, L., Shah, V., Lee, B. H., Lopez-Hilfiker, F. D., Campuzano-Jost, P., et al. (2018). Wintertime gas-particle partitioning and speciation of inorganic chlorine in the lower troposphere over the Northeast United States and coastal ocean. Journal of Geophysical Research: Atmospheres, 123. https://doi.org/10.1029/2018JD028786

Hayes, P. L., Ortega, A. M., Cubison, M. J., Froyd, K. D., Zhao, Y., Cliff, S. S., et al. (2013). Organic aerosol composition and sources in Pasadena, California, during the 2010 CalNex campaign. Journal of Geophysical Research: Atmospheres, 118, 9233–9257. https://doi.org/ 10.1002/jgrd.50530

Jaeglé, L., Shah, V., Thornton, J. A., Lopez-Hilfiker, F. D., Lee, B. H., McDuffie, E. E., et al. (2018). Nitrogen oxides emissions, chemistry, deposition, and export over the Northeast United States during the WINTER aircraft campaign. Journal of Geophysical Research: Atmospheres, 123, 12,368–12,393. https://doi.org/10.1029/2018JD029133

Janson, R. W. (1993). Monoterpene emissions from Scots pine and Norwegian spruce. Journal of Geophysical Research, 98(D2), 2839–2850. https://doi.org/10.1029/92JD02394 Keene, W. C., Maben, J. R., Pszenny, A. A. P., & Galloway, J. N. (1993). Measurement technique for inorganic chlorine gases in the marine boundary layer. Environmental Science & Technology, 27, 866–874. https://doi.org/10.1021/es00042a008

Keene, W. C., Stutz, J., Pszenny, A. A., Maben, J. R., Fischer, E. V., Smith, A. M., et al. (2007).

Inorganic chlorine and bromine in coastal New England air during summer. Journal of Geophysical Research, 112, D10S12. https://doi.org/10.1029/2006JD007689

Kenagy, H. S., Sparks, T. L., Ebben, C. J., Wooldrige, P. J., Lopez-Hilfiker, F. D., Lee, B. H., et al. (2018). NOx lifetime and NOy partitioning during WINTER. Journal of Geophysical Research: Atmospheres, 123, 9813–9827. https://doi.org/10.1029/2018JD028736

Knipping, E. M., Lakin, M. J., Foster, K. L., Jungwirth, P., Tobias, D. J., Gerber, R. B., et al. (2000). Experiments and simulations of ion-enhanced interfacial chemistry on aqueous NaCl aerosols. Science, 288(5464), 301–306. https://doi.org/10.1126/science.288.5464.301

Laskin, A., Moffet, R. C., Gilles, M. K., Fast, J. D., Zaveri, R. A., Wang, B., et al. (2012). Tropospheric chemistry of internally mixed sea salt and organic particles: Surprising reactivity of NaCl with weak organic acids. Journal of Geophysical Research, 117, D15302. https://doi. org/10.1029/2012JD017743

Lawler, M. J., Sander, R., Carpenter, L. J., Lee, J. D., Von Glasow, R., Sommariva, R., & Saltzman, E. S. (2011). HOCl and Cl2 observations in marine air. Atmospheric Chemistry and Physics, 11(15), 7617–7628. https://doi.org/10.5194/acp-11-7617-2011

Lee, B. H., Lopez-Hilfiker, F. D., Mohr, C., Kurten, T., Worsnop, D. R., & Thornton, J. A. (2014). An iodide-adduct high-resolution time-of- flight chemical- ionization mass spectrometer: Application to atmospheric inorganic and organic compounds. Environmental Science & Technology, 48(11), 6309–6317. https://doi.org/10.1021/es500362a

Lee, B. H., Lopez-Hilfiker, F. D., Schroder, J. C., Campuzano-Jost, P., Jimenez, J. L., McDuffie, E. E., et al. (2018). Airborne observations of reactive inorganic chlorine and bromine species in the exhaust of coal-fired power plants. Journal of Geophysical Research: Atmospheres, 123(19), 11,211–225,237. https://doi.org/10.1029/2018JD029284

Lee, B. H., Lopez-Hilfiker, F. D., Veres, P. R., McDuffie, E. E., Fibiger, D. L., Sparks, T. L., et al. (2018). Flight deployment of a high- resolution time-of-flight chemical ionization mass spectrometer: Observations of reactive halogen and nitrogen oxide species. Journal of Geophysical Research: Atmospheres, 123(14), 7670–7686. https://doi.org/10.1029/2017JD028082

Liao, J., Huey, L. G., Liu, Z., Tanner, D. J., Cantrell, C. A., Orlando, J. J., et al. (2014). High levels of molecular chlorine in the Arctic atmosphere. Nature Geoscience, 7, 91. https://doi.org/10.1038/ngeo2046

Liu, X., Qu, H., Huey, L. G., Wang, Y., Sjostedt, S., Zeng, L., et al. (2017). High levels of daytime molecular chlorine and nitryl chloride at a rural site on the North China Plain. Environmental Science & Technology, 51(17), 9588–9595. https://doi.org/10.1021/acs.est. 7b03039

Liu, Y., Fan, Q., Chen, X., Zhao, J., Ling, Z., Hong, Y., et al. (2018). Modeling the impact of chlorine emissions from coal combustion and prescribed waste incineration on tropospheric ozone formation in China. Atmospheric Chemistry and Physics, 18, 2709–2724. https://doi. org/10.5194/acp-18-2709-2018

McDuffie, E. E., Fibiger, D. L., Dubé, W. P., Lopez Hilfiker, F., Lee, B. H., Jaeglé, L., et al. (2018). ClNO2 Yields from aircraft measurements during the 2015 WINTER campaign and critical evaluation of the current parameterization. Journal of Geophysical Research: Atmospheres, 123(22), 12,15,913–12,15,994. https://doi.org/10.1029/2018JD029358

McDuffie, E. E., Fibiger, D. L., Dubé, W. P., Lopez-Hilfiker, F., Lee, B. H., Thornton, J. A., et al. (2018). Heterogeneous N2O5 uptake during winter: Aircraft measurements during the 2015 WINTER campaign and critical evaluation of current parameterizations. Journal of Geophysical Research: Atmospheres, 123, 4345–4372. https://doi.org/10.1002/2018JD028336

McNaughton, C., Clarke, A. D., Howell, S. G., Pinkerton, M., Anderson, B., Thornhill, L., et al. (2007). Results from the DC-8 inlet characterization experiment (DICE): Airborne versus surface sampling of mineral dust and sea salt aerosols. Aerosol Science and Technology, 41(2), 136–159. https://doi.org/10.1080/02786820601118406

Mielke, L. H., Furgeson, A., & Osthoff, H. D. (2011). S.I.: Observation of ClNO in a mid-continental urban environment. Environmental Science & Technology, 45, 8889–8896. https://doi.org/10.1021/es201955u

Osthoff, H. D., Roberts, J. M., Ravishankara, A. R., Williams, E. J., Lerner, B. M., Sommariva, R., et al. (2008). High levels of nitryl chloride in the polluted subtropical marine boundary layer. Nature Geoscience, 1(5), 324–328. https://doi.org/10.1038/ngeo177

Pechtl, S., & von Glasow, R. (2007). Reactive chlorine in the marine boundary layer in the outflow of polluted continental air: A model study. Geophysical Research Letters, 34, L11813. https://doi.org/10.1029/2007GL029761

Phillips, G. J., Tang, M. J., Thieser, J., Brickwedde, B., Schuster, G., Bohn, B., et al. (2012). Significant concentrations of nitryl chloride observed in rural continental Europe associated with the influence of sea salt chloride and anthropogenic emissions. Geophysical Research Letters, 39, L10811. https://doi.org/10.1029/2012GL051912

Phillips, G. J., Thieser, J., Tang, M., Sobanski, N., Schuster, G., Fachinger, J., et al. (2016). Estimating N2O5 uptake coefficients using ambient measurements of NO3, N2O5, ClNO2 and particle-phase nitrate. Atmospheric Chemistry and Physics, 16, 13,231–13,249. https:// doi.org/10.5194/acp-16-13231-2016

Poling, B. E., Prausnitz, J. M., & O'connell, J. P. (2001). The properties of gases and liquids (Vol. 5). New York: Mcgraw-Hill. Pratt, K. A., Custard, K. D., Shepson, P. B., Douglas, T., Pöhler, D., General, S., et al. (2013). Photochemical production of molecular bromine in Arctic surface snowpacks. Nature Geoscience, 6(5), 351–356.

Pszenny, A. A. P., Keene, W. C., Jacob, D. J., Fan, S., Maben, J. R., Zetwo, M. P., et al. (1993). Evidence of inorganic chlorine gases other than hydrogen chloride in marine surface air. Geophysical Research Letters, 20(8), 699–702. https://doi.org/10.1029/93gl00047

Pszenny, A.A.P., Moldanová, J., Keene, W.C., Sander, R., Maben, J.R., Martinez, M., et al. (2004). Halogen cycling and aerosol pH in the Hawaiian marine boundary layer. Atmospheric Chemistry and Physics, 4(1), 147–168. Retrieved from https://hal.archives-ouvertes.fr/ hal-00295390

Ren, X., Salmon, O. E., Hansford, J. R., Ahn, D., Hall, D., Benish, S. E., et al. (2018). Methane emissions from the Baltimore-Washington area based on airborne observations: Comparison to emissions inventories. Journal of Geophysical Research: Atmospheres, 123, 8869–8882. https://doi.org/10.1029/2018JD028851

Riedel, T. P., Bertram, T. H., Crisp, T. A., Williams, E. J., Lerner, B. M., Vlasenko, A., et al. (2012). Nitryl chloride and molecular chlorine in the coastal marine boundary layer. Environmental Science and Technology. https://doi.org/10.1021/es204632r

Riedel, T. P., Wagner, N. L., Dubé, W. P., Middlebrook, A. M., Young, C. J., Öztürk, F., et al. (2013). Chlorine activation within urban or power plant plumes: Vertically resolved ClNO2 and Cl2 measurements from a tall tower in a polluted continental setting. Journal of Geophysical Research: Atmospheres, 118, 8702–8715. https://doi.org/10.1002/jgrd.50637

Riedel, T. P., Wolfe, G. M., Danas, K. T., Gilman, J. B., Kuster, W. C., Bon, D. M., et al. (2014). An MCM modeling study of nitryl chloride (ClNO2) impacts on oxidation, ozone production and nitrogen oxide partitioning in polluted continental outflow. Atmospheric Chemistry and Physics, 14(8), 3789–3800. https://doi.org/10.5194/acp-14-3789-2014

Roberts, J. M., Osthoff, H. D., Brown, S. S., & Ravishankara, A. R. (2008). N2O5 Oxidizes Chloride to Cl2 in Acidic Atmospheric Aerosol. Science, 321(5892), 1059.

Roberts, J. M., Osthoff, H. D., Brown, S. S., Ravishankara, A. R., Coffman, D., Quinn, P., & Bates, T. (2009). Laboratory studies of products of N2O5 uptake on Cl- containing substrates. Geophysical Research Letters, 36, L20808. https://doi.org/10.1029/2009GL040448

Ryder, O. S., Campbell, N. R., Shaloski, M., Al-Mashat, H., Nathanson, G. M., & Bertram, T. H. (2015). Role of organics in regulating ClNO2 production at the air–sea interface. The Journal of Physical Chemistry A, 119(31), 8519–8526. https://doi.org/10.1021/jp5129673

Saiz-Lopez, A., & von Glasow, R. (2012). Reactive halogen chemistry in the troposphere. Chemical Society Reviews, 41(19), 6448–6472. https://doi.org/10.1039/C2CS35208G

Salmon, O. E., Shepson, P. B., Ren, X., He, H., Hall, D. L., Dickerson, R. R., et al. (2018). Top-down estimates of NOx and CO emissions from Washington, D.C.-Baltimore during the WINTER campaign. Journal of Geophysical Research: Atmospheres, 123, 7705–7724. https://doi. org/10.1029/2018JD028539

Salmon, O. E., Shepson, P. B., Ren, X., Marquardt Collow, A. B., Miller, M. A., Carlton, A. G., et al. (2017). Urban emissions of water vapor in winter. Journal of Geophysical Research: Atmospheres, 122, 9467–9484. https://doi.org/10.1002/2016JD026074

Sander, S. P., Finlayson-Pitts, B. J., Friedl, R. R., Golden, D. M., Huie, R. E., Kolb, C. E., et al. (2003). Chemical kinetics and photochemical data for use in atmospheric studies, Evaluation Number 14. Pasadena, CA: JPL Publication 02-25, Jet Propulsion Laboratory.

Sander, S. P., Golden, D. M., Kurylo, M. J., Moortgat, G. K., Wine, P. H., Ravishankara, A. R., et al. (2006). Chemical kinetics and photochemical data for use in atmospheric studies, Evaluation Number 15. Pasadena, CA: JPL Publication 07-10, Jet Propulsion Laboratory.

Schmidt, J. A., Jacob, D. J., Horowitz, H. M., Hu, L., Sherwen, T., Evans, M. J., et al. (2016). Modeling the observed tropospheric BrO background: Importance of multiphase chemistry and implications for ozone, OH, and mercury. Journal of Geophysical Research: Atmospheres, 121, 11,811–11,819, 835. https://doi.org/10.1002/2015JD024229

Schroder, J. C., Campuzano-Jost, P., Day, D. A., Shah, V., Larson, K., Sommers, J. M., et al. (2018). Sources and secondary production oforganic aerosols in the northeastern United States during WINTER. Journal of Geophysical Research: Atmospheres, 123, 7771–7796.https://doi.org/10.1029/2018JD028475

Schweitzer, F., Mirabel, P., & George, C. (1998). Multiphase chemistry of N2O5, ClNO2 and BrNO2. The Journal of Physical Chemistry. A,102, 3942–3952.

Shah, V., Jaeglé, L., Thornton, J. A., Lopez-Hilfiker, F. D., Lee, B. H., Schroder, J. C., et al. (2018). Chemical feedbacks weaken the wintertime response of particulate sulfate and nitrate to emissions reductions over the eastern United States. Proceedings of the NationalAcademy of Sciences, 115(32), 8110 LP–8115. https://doi.org/10.1073/pnas.1803295115

Sherwen, T., Schmidt, J. A., Evans, M. J., Carpenter, L. J., Großmann, K., Eastham, S. D., et al. (2016). Global impacts of tropospheric halogens (Cl, Br, I) on oxidants and composition in GEOS-Chem. Atmospheric Chemistry and Physics, 16, 12,239–12,271. https://doi.org/10.5194/acp-16-12239-2016

Simpson, W. R., Brown, S. S., Saiz-Lopez, A., Thornton, J. A., & Von Glasow, R. (2015). Tropospheric halogen chemistry: Sources, cycling, and impacts. Chemical Reviews, 115(10), 4035–4062. https://doi.org/10.1021/cr5006638

Spicer, C. W., Chapman, E. G., Finlayson-Pitts, B. J., Plastridge, R. A., Hubbe, J. M., Fast, J. D., & Berkowitz, C. M. (1998). Unexpectedly high concentrations of molecular chlorine in coastal air. Nature, 394(6691), 353–356. https://doi.org/10.1038/28584

Sullivan, A. P., Guo, H., Schroder, J. C., Campuzano-Jost, P., Jimenez, J. L., Campos, T., Shah, V., Jaeglé, L., Lee, B. H., Lopez-Hilfiker, F. D., Thornton, J. A., Brown, S. S., Weber, R. J. (2019). Biomass burning markers and residential burning in the WINTER aircraft campaign. Journal of Geophysical Research: Atmospheres, 124, 1846– 1861. https://doi.org/10.1029/2017JD028153

Tanaka, P. L., Oldfield, S., Neece, J. D., Mullins, C. B., & Allen, D. T. (2000). Anthropogenic sources of chlorine and ozone formation in urban atmospheres. Environmental Science & Technology, 34(21), 4470–4473. https://doi.org/10.1021/es991380v

Tham, Y. J., Wang, Z., Li, Q., Wang, W., Wang, X., Lu, K., et al. (2018). Heterogeneous N2O5 uptake coefficient and production yield of ClNO2 in polluted northern China: Roles of aerosol water content and chemical composition. Atmospheric Chemistry and Physics Discussions. https://doi.org/10.5194/acp-2018-313

Tham, Y. J., Yan, C., Xue, L., Zha, Q., Wang, X., & Wang, T. (2014). Presence of high nitryl chloride in Asian coastal environment and its impact on atmospheric photochemistry. Chinese Science Bulletin, 59(4), 356–359. https://doi.org/10.1007/s11434-013-0063-y

Thornton, J. A., Kercher, J. P., Riedel, T. P., Wagner, N. L., Cozic, J., Holloway, J. S., et al. (2010). A large atomic chlorine source inferred from mid-continental reactive nitrogen chemistry. Nature, 464(7286), 271–274. https://doi.org/10.1038/nature08905

Vogt, R., Crutzen, P. J., & Sander, R. (1996). A mechanism for halogen release from sea salt aerosol in the remote marine boundary layer. Nature, 383(6598), 327–330. http://doi.org/10.1038/383327a0

von Glasow, R., von Kuhlmann, R., Lawrence, M. G., Platt, U., & Crutzen, P. J. (2004). Impact of reactive bromine chemistry in the troposphere. Atmospheric Chemistry and Physics, 4, 2481–2497. https://doi.org/10.5194/acp-4-2481-2004

Wagner, N. L., Riedel, T. P., Young, C. J., Bahreini, R., Brock, C. A., Dubé, W. P., et al. (2013). N2O5 uptake coefficients and nocturnal NO2 removal rates determined from ambient wintertime measurements. Journal of Geophysical Research: Atmospheres, 118, 9331–9350. https://doi.org/10.1002/jgrd.50653

Washenfelder, R. A., Wagner, N. L., Dube, W. P., & Brown, S. S. (2011). Measurement of atmospheric ozone by cavity ring-down spectroscopy. Environmental Science & Technology, 45(7), 2938–2944. https://doi.org/10.1021/es103340u

Wang, X., Jacob, D. J., Eastham, S. D., Sulprizio, M. P., Zhu, L., Chen, Q., et al. (2018). The role of chlorine in tropospheric chemistry. Atmospheric Chemistry and Physics Discussions. https://doi.org/10.5194/acp-2018-1088

Wang, X., Wang, H., Xue, L., Wang, T., Wang, L., Gu, R., et al. (2017). Observations of N2O5 and ClNO2 at a polluted urban surface site in North China: High N2O5 uptake coefficients and low ClNO2 product yields. Atmospheric Environment, 156, 125–134. https://doi.org/10.1016/J.ATMOSENV.2017.02.035

Weinheimer, A. J., Walega, J. G., Ridley, B. A., Gary, B. L., Blake, D. R., Blake, N. J., et al. (1994). Meridional distributions of NOx, NOy, and other species in the lower stratosphere and upper troposphere during AASE II. Geophysical Research Letters, 21, 2583–2586. https://doi. org/10.1029/94GL01897

Wennberg, P. (1999). Bromine explosion. Nature, 397, 299. https://doi.org/10.1038/16805

Yun, H., Wang, W., Wang, T., Xia, M., Yu, C., Wang, Z., et al. (2018). Nitrate formation from heterogeneous uptake of dinitrogen pentoxide during a severe winter haze in southern China. Atmospheric Chemistry and Physics, 18, 17,515–17,527. https://doi.org/10.5194/acp-18-17515-2018

Zaveri, R. A., Easter, R. C., Fast, J. D., & Peters, L. K. (2008). Model for Simulating Aerosol Interactions and Chemistry (MOSAIC). *Journal of Geophysical Research: Atmospheres*, *113*(D13). https://doi.org/10.1029/2007JD008782

3.11 TABLES

Table 3.1 Reactions & Rate Constants included in 0-D Box Model.

SA is defined as wet aerosol surface area concentration (m2 m-3), ω as mean thermal velocity (m s-1), φ as the yield of a reaction, and γ as the reaction probability of a reaction. Values of k0, k∞, and F can be found in the given reference.

Reaction No.	Reaction	Rate coefficient expression (cm^3 $molecules^{-1}$ s^{-1})	Reference
R10	$NO_2 + O_3 \xrightarrow{k_{10}} NO_3^{\bullet} + O_2$	$k_{10} = 1.2e^{-13} \exp(-2450/T)$	Sander et al., 2003
R11f	$NO_3^{\bullet} + NO_2 \underset{k_{11r}}{\overset{k_{11f}}{\rightleftharpoons}} N_2O_5$	$k_{11f} = (k_0/k_\infty)*F/(k_0+k_\infty)$	DeMore et al., 1997
R11r		$k_{11r} = k_{11f} / [2.7e\text{-}27 \exp(11000/T)]$	Sander et al., 2006
R9a	$Cl^-(aq) + N_2O_5 + H_2O \xrightarrow[\gamma_{N_2O_5}]{k_{9a}} \Phi\ ClNO_2 + (2\text{-}\Phi)\ HNO_3$	$k_{9a} = (\gamma_{N2O5}\ \omega_{N2O5}\ SA\ ) /4$	Model derived
R9b	$Cl^-(aq) + ClNO_2 + H_2O \xrightarrow[\gamma_{ClNO_2}]{k_{9b}} Cl_2 + HONO$	$k_{9b} = (\gamma_{ClNO2}\ \omega_{ClNO2}\ SA\ ) /4$	Model derived

Table 3.2 Summary of Box Model Results & Corresponding Observations

Plume No.	Flight	γ_{ClNO_2}	pCl$^-$ (μg m^{-3}) [a]	D_p (μm) [b]	Time since sunset (hrs) [c]	HCl (pptv)	[Cl$^-$] (M)[d]	$ClNO_2$ (pptv)	LWC (M) [e]	pOrg (μg m^{-3}) [f]	pNO_3 (μg m^{-3}) [f]	Cl_2 (pptv)	Aerosol pH [e]	SA (μm^2 cm^{-3}) [g]	HOCl (pptv)	T (K)
1*	3	6.69 x 10^{-5}	0.137	0.47	3.72	1352	0.20	812.6	30.5	2.05	1.27	4.47	1.45	227.3	9.3	273
2*	3	3.73 x 10^{-5}	0.112	0.47	4.07	861	0.16	724.5	28.4	2.02	1.47	2.46	1.48	269	7.3	273
3*	3	3.87 x 10^{-5}	0.083	0.48	4.22	952	0.12	967.3	30.9	2.15	1.73	3.31	1.38	273.8	6.9	273
4*	3	4.35 x 10^{-5}	0.085	0.42	4.53	712	0.18	565	27.3	1.51	0.83	1.75	1.53	212	5.2	274
5	6	1.74 x 10^{-5}	0.053	0.27	7.54	539	0.08	931.1	28.5	5.32	0.80	3.82	-0.15	412.9	8.3	274
6	6	1.67 x 10^{-5}	0.04	0.27	8.76	699	0.06	863	27.3	5.46	1.64	4.92	0.1	424.3	7.5	277
7	6	1.39 x 10^{-5}	0.02†	0.29	9.44	583	0.03	248.2	40.2	2.12	0.07	1.18	-0.41	322	6.9	278
8	6	1.62 x 10^{-5}	0.03	0.26	11.20	623	0.06	387	35.6	1.83	0.04	2.01	-0.48	229	9.7	279
9	6	1.14 x 10^{-5}	0.03	0.28	11.43	517	0.04	994.9	31.6	3.31	0.30	4.58	-0.33	360.2	9.9	279
10	6	1.55 x 10^{-5}	0.043	0.29	12.25	574	0.09	232.2	40.2	1.40	0.01	1.44	-0.42	208.6	8.8	279
11	6	1.71 x 10^{-5}	0.07	0.23	13.48	348	0.35	196.6	36.5	1.31	0.03	1.01	-0.52	156.7	8.8	282
12*	8	1.60 x 10^{-5}	0.015†	0.25	12.54	395	0.11	551.8	19.3	1.40	1.03	1.38	1.98	142	3.2	269
13	8	1.10 x 10^{-5}	0.028	0.17	13.17	433	0.10	2022.9	18.5	3.76	3.45	6.35	1.96	275.9	8.5	270
14	8	1.22 x 10^{-5}	0.015†	0.27	13.88	306	0.10	765.3	20.4	1.54	1.28	1.53	1.84	128.8	4.7	269
15	8	6.5 x 10^{-6}	0.02†	0.18	14.58	465	0.05	2336.4	17.2	3.19	3.80	6.59	2.0	317.2	6.9	270
16	8	8.3 x 10^{-6}	0.021†	0.19	15.29	619	0.13	1276.3	21.5	2.00	1.77	2.8	1.9	240.7	5.8	269
17	8	9.1 x 10^{-6}	0.02†	0.2	15.50	770	0.09	1546.6	18.4	2.35	2.42	5.86	1.39	213.5	6.4	270
18	8	8.1 x 10^{-6}	0.027	0.21	16.08	1003	0.12	1610	14.1	2.46	3.12	7.36	1.55	246.5	8.9	271
r with γ_{ClNO_2}			**0.93‡**	**0.89‡**	**-0.86**	**0.70**	**0.44**	**-0.31**	**0.29**	**-0.21**	**-0.20**	**-0.18**	**0.14**	**-0.08**	**0.07**	**0.06**

a Sum of AMS non-refractory pCl$^-$ for D_p^{dry}< 1 μm + 3% UNH filter pCl$^-$ for D_p^{dry}< 4 μm
b Wet particle diameter, derived from the calculated wet volume density to wet surface area density ratio
c Time of intercept of plume after 5pm, the "model sunset"
d Calculated chlorine molarity from measurements of a and b
e Calculated using ISORROPIA II following Haskins et al., 2018
f AMS measurements for D_p^{dry}< 1 μm
g Calculated wet surface area density from UHSAS measurements

† Denotes the AMS component of the pCl- measurement shown here was below detection limit (0.024 μg m^{-3}) and set to ½ detection limit.
‡ Denotes statistical significance at the 95% level

3.12 FIGURES

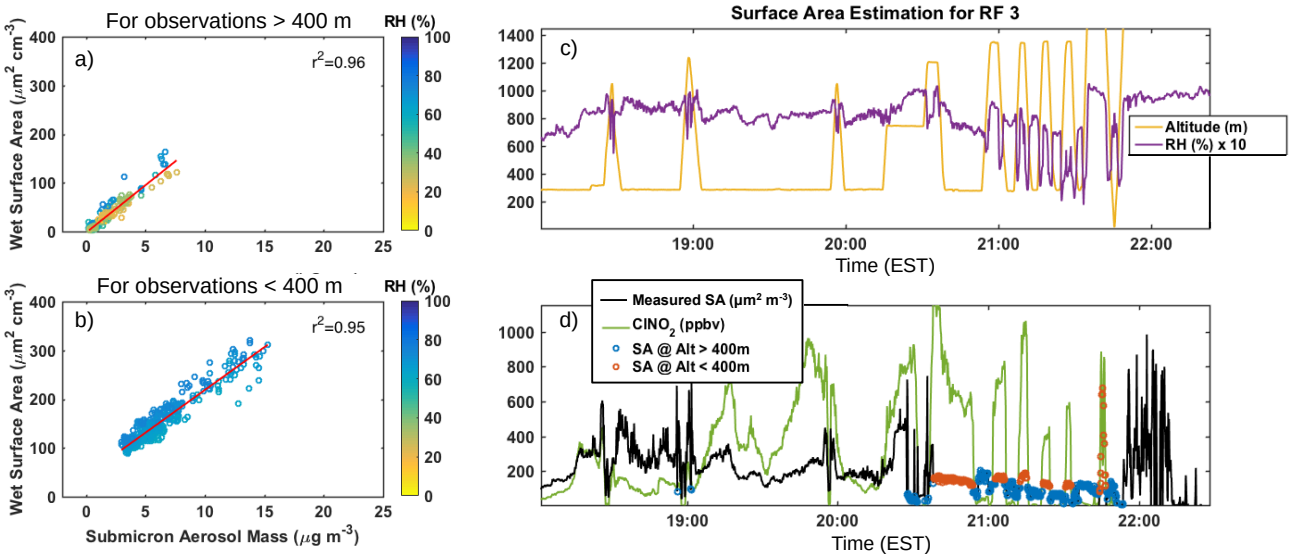

Figure 3.1 Estimating Particle Surface Area from Total AMS Mass

a) Scatterplots of total submicron aerosol mass, measured by the AMS versus wet surface area from the UHSAS for altitudes > 400m (a) and < 400m (b) on RF 03, colored by relative humidity. c) Time series of aircraft altitude and relative humidity d) time series of measured $ClNO_2$, measured wet aerosol surface area density, and the estimated aerosol wet surface area density from the linear fits shown on a) and b)

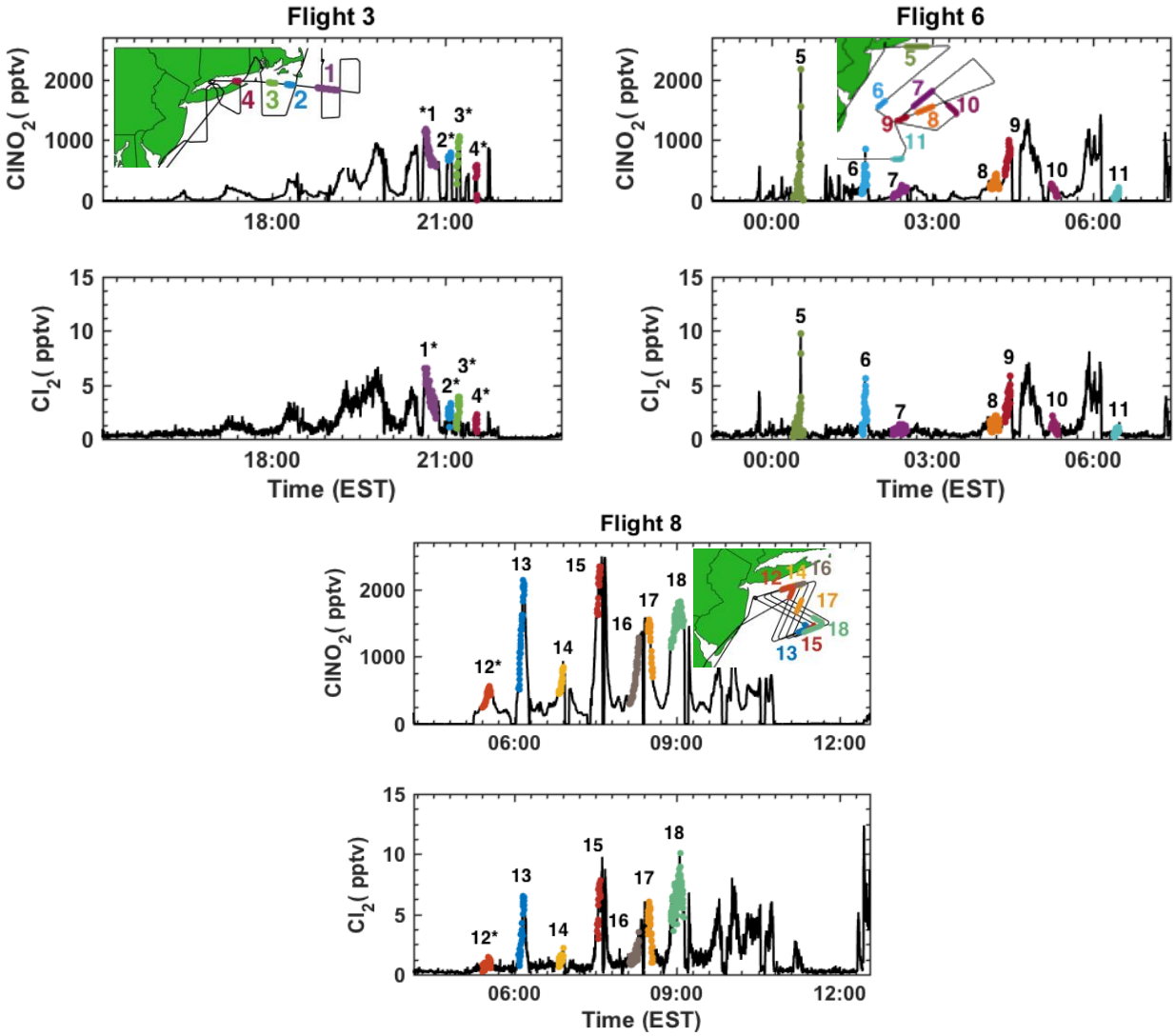

Figure 3.2 Timeseries of $ClNO_2$ and Cl_2 during 3 Flights

Time series of $ClNO_2$ and Cl_2 from Research Flight 3 on February 7th, 2015 (a, b), Research Flight 6 on February 23rd, 2015 (c, d), and Research Flight 8 on March 1st, 2015 (e, f) with inlaid flight tracks off the coast of New York City, highlighting the 18 plumes (numbered for reference) used in the box model analysis presented in this work. Enhancements in Cl_2 and $ClNO_2$ not highlighted are those where all measurements necessary for the box model analysis were not available, were during daytime, in-cloud, or where correlations are caused by plane altitude changes. In all figures, asterisks denote plumes where wet aerosol surface area was estimated using the AMS total mass. See text for details.

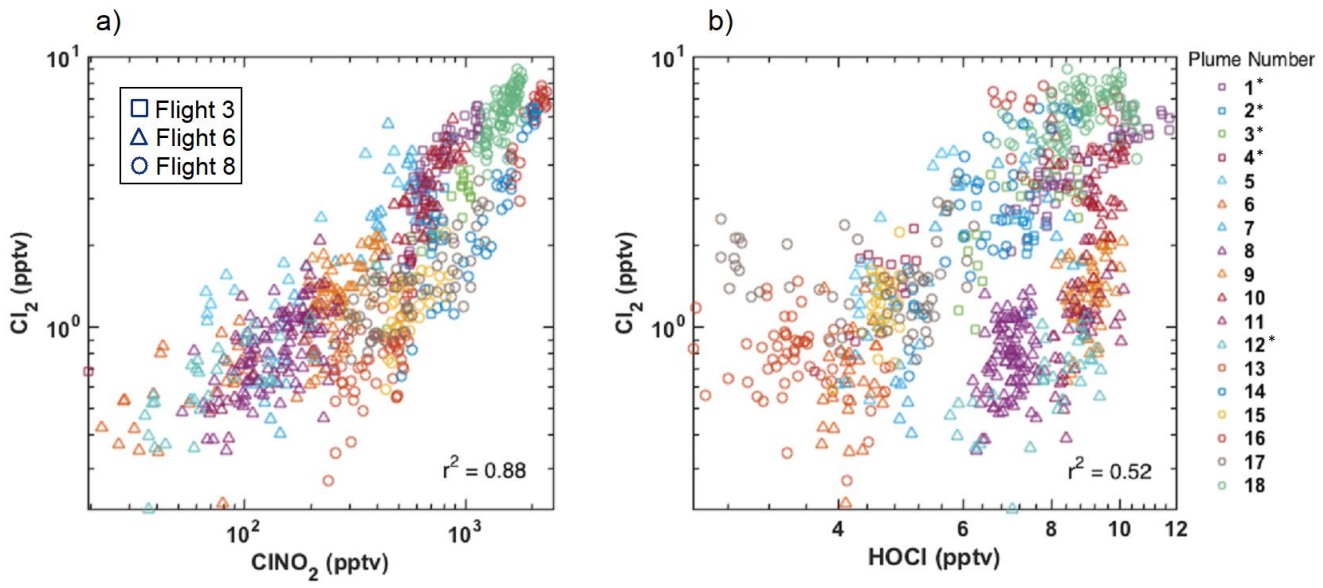

Figure 3.3 Correlations between Cl_2, $ClNO_2$, and HOCl

Scatterplots of measured Cl_2 as a function of a) $ClNO_2$ and b) HOCl within each plume using 10s averages colored by plume number with markers indicating flight number

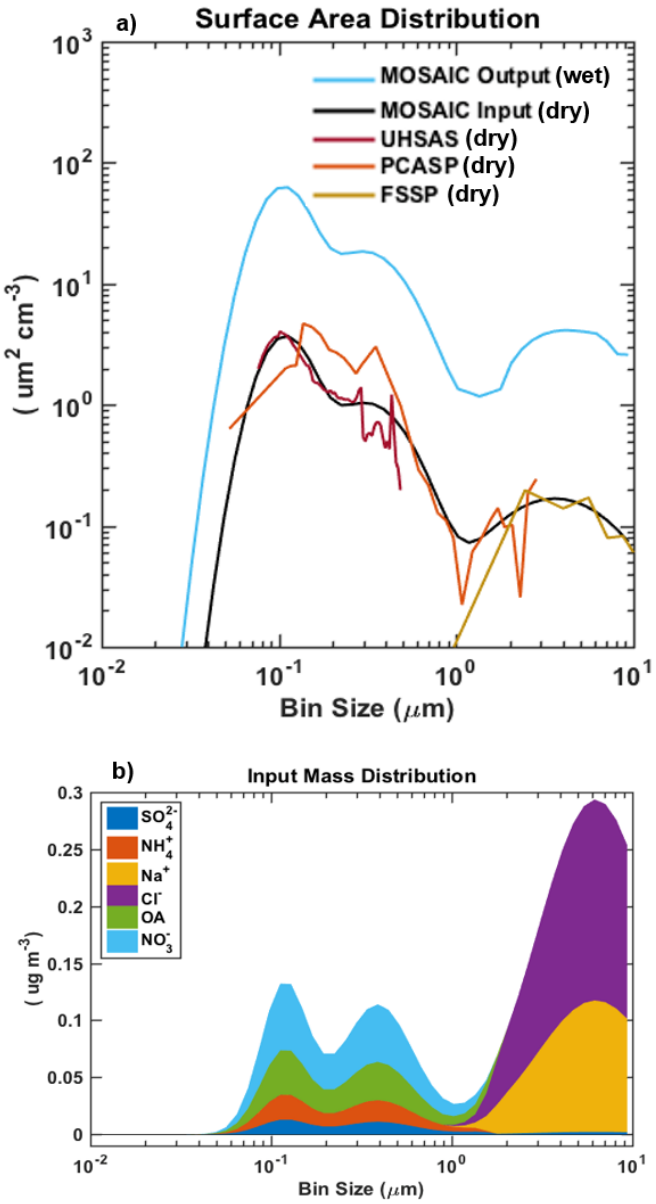

Figure 3.4 MOSAIC Input Constraints from WINTER

Figure showing MOSAIC inputs. a) A comparison between the measured dry aerosol surface area size distribution during plume #15 on RF08 on March 1st, 2015 during WINTER and the MOSAIC inputted dry aerosol surface area size distribution, as well as the outputted wet aerosol surface area size distribution. B) The inputted mass distribution, using the percentage of measured compounds from the AMS for submicron aerosols, assuming pure NaCl using the seasalt mass ratio of the two for aerosols with D_p>2µm, and interpolating between the two for aerosols with D_p between 1-2 µm.

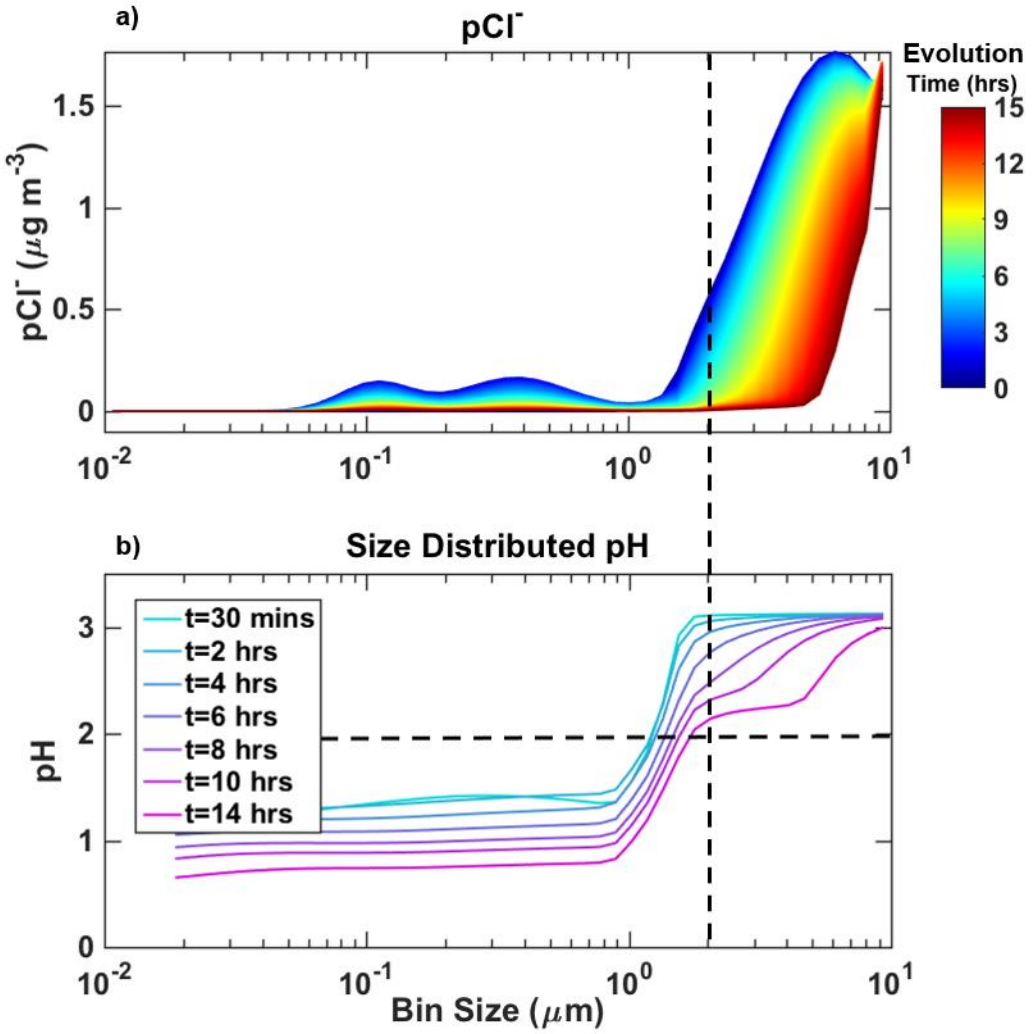

Figure 3.5 MOSAIC Outputted Size Resolved pCl^- and Aerosol pH

Figure displaying MOSAIC output of (a) the pCl^- mass distribution, as it evolves in time, and (b) the mean size resolved aerosol pH at different times of plume evolution

.

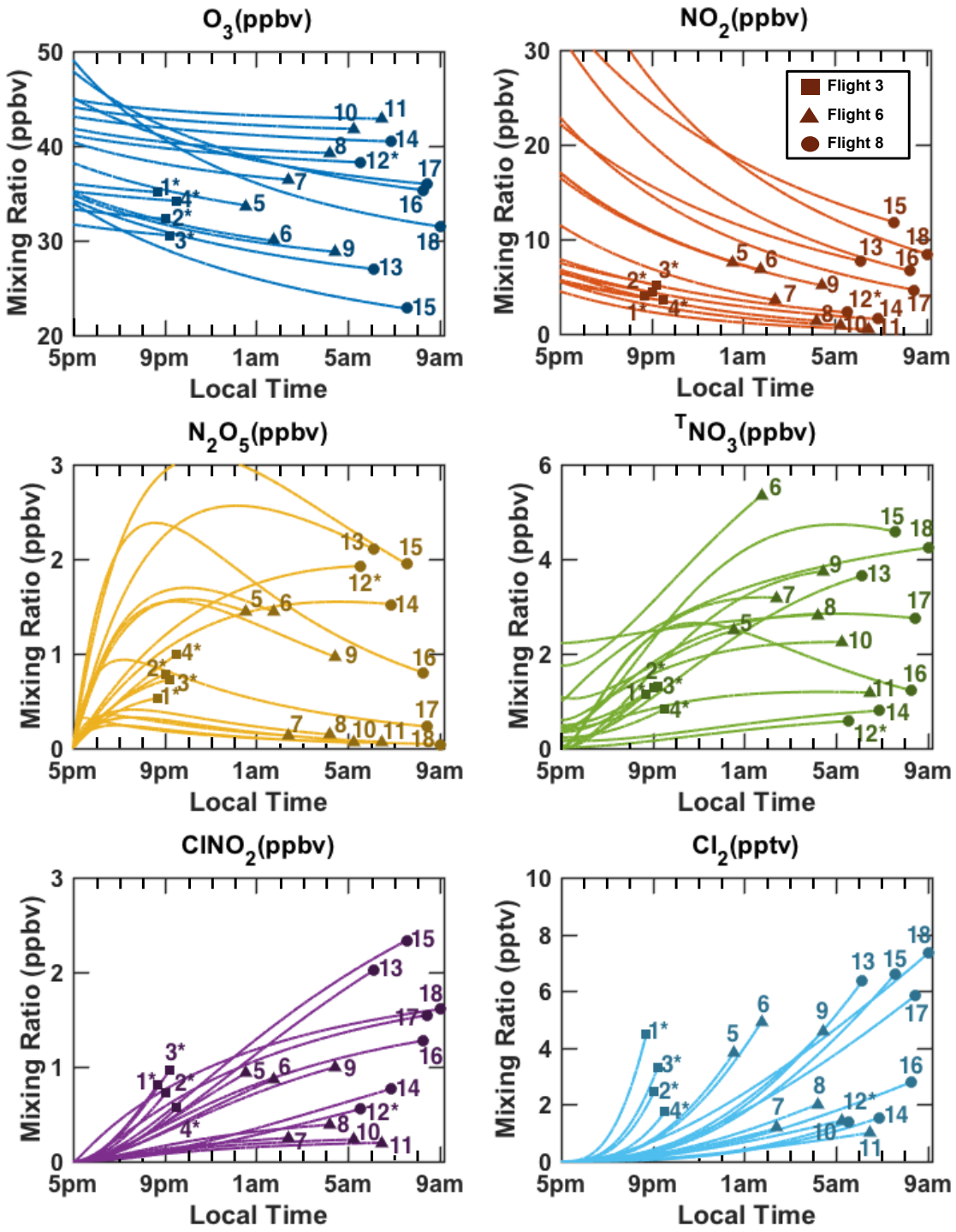

Figure 3.6 Modeled Evolution of Selected Plumes

WINTER observations at the time of intercept (points) and the box model predictions (lines) for the concentrations of (a) O_3, (b) NO_2, (c) N_2O_5, (d) TNO_3, (e) $ClNO_2$, and (f) Cl_2 and for each analyzed plume, noted with the referenced plume number.

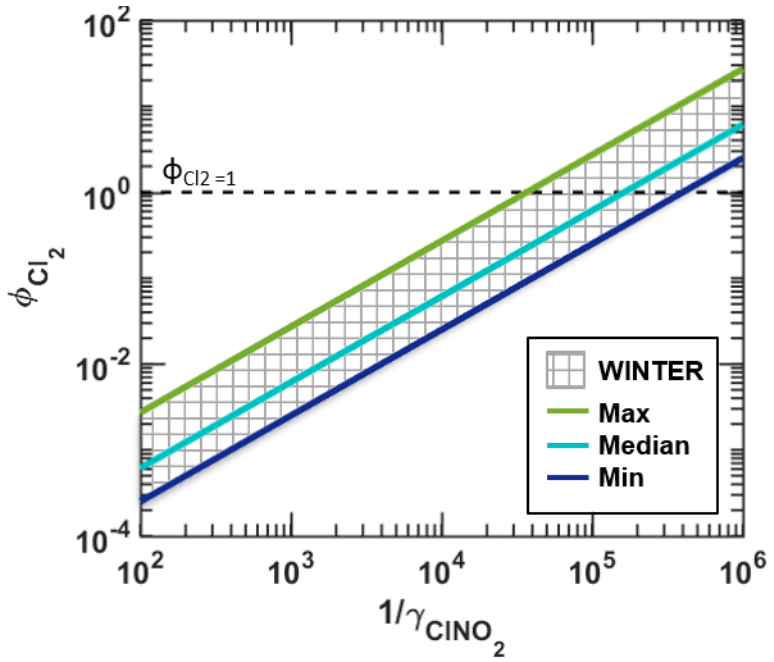

Figure 3.7 WINTER Constraints on φ_{Cl2} and γ_{ClNO2}

The range of WINTER constraints on the product of φ_{Cl2} and γ_{ClNO2} in all plumes.

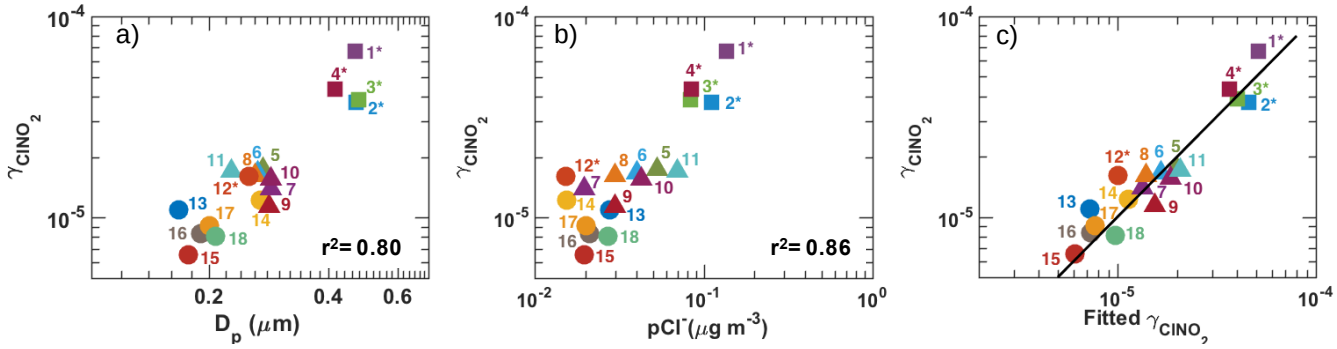

Figure 3.8 Multi-linear fits of Modeled γ($ClNO_2$)

Scatter plots on a log scale of a) the box model derived γ($ClNO_2$) and wet D_p and b) the box model derived γ($ClNO_2$) and measured pCl^- (AMS + 3% filter), which are used in c) the multi-linear fit (x-axis) of the box model derived γ($ClNO_2$) (y-axis), assuming the yield of Cl_2 is 1.

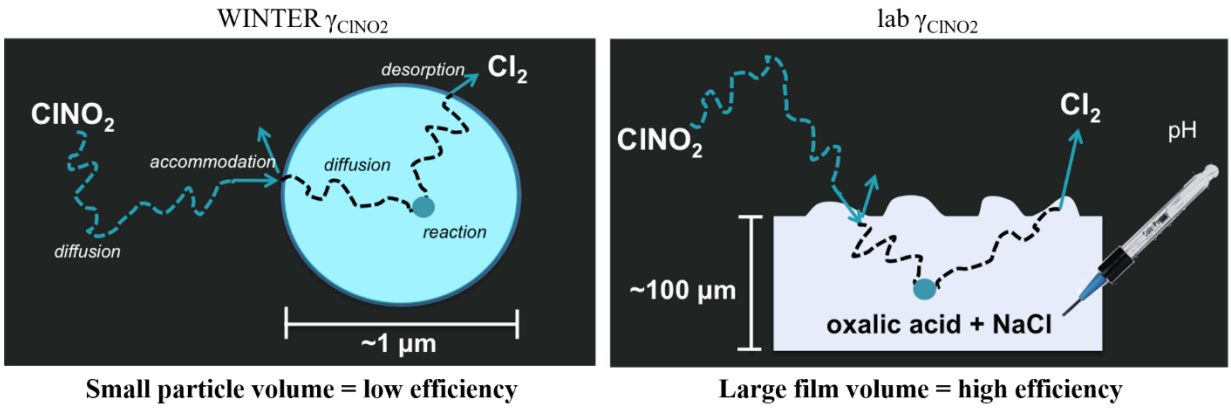

Figure 3.9 Mechanistic Differences between Atmosphere & Lab

Figure summarizing how the differing length scales between the ambient atmosphere in small aerosol particles (left) and in the laboratory on thick films may affect liquid phase diffusion of $ClNO_2$ before reaction, thereby effecting the effective uptake coefficient.

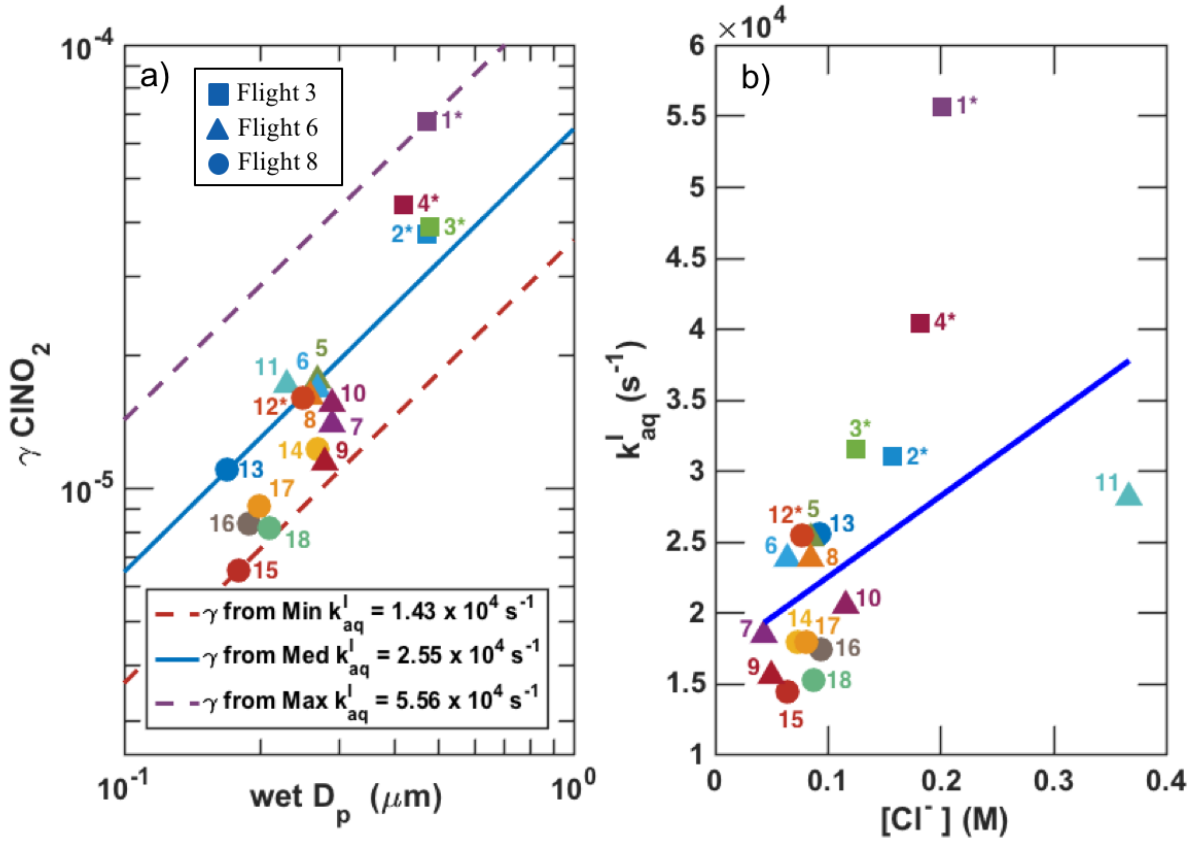

Figure 3.10 Determining First and Second Order Rate Coefficients

a) The minimum, median, and maximum values for $\gamma(ClNO_2)$ calculated from the required k_{aq}^I as a function of wet D_p (lines) compared to the box model derived values of $\gamma(ClNO_2)$ at the observed wet D_p (points) b) Scatter plot of the first order rate coefficients needed to match the box model derived $\gamma(ClNO_2)$ versus the chloride molarity determined from the concentration of pCl^- (AMS + 3% filter) and UHSHS particle volume concentrations. The slope of the linear least squared fit (line), with plumes having estimated surface area (denoted with *) weighted at 50%, is the corresponding second order rate coefficient.

Figure 3.11 Time series of HOCl, Cl_2, $ClNO_2$

Time series of altitude (first row), concentrations of $ClNO_2$ (second row), and concentrations of HOCl and Cl_2 (third row), with each of the 18 plumes examined in this work highlighted and numbered for each of the 3 nighttime flights (columns). Note: Cl_2 concentrations are offset by +12 pptv for comparison Figure 3.12 a) The minimum, median, and maximum values for $\gamma(ClNO_2)$ calculated from the required k_{aq}^I as a function of wet D_p (lines) compared to the box model derived values of $\gamma(ClNO_2)$ at the observed wet D_p (points) b) Scatter plot of the first order rate coefficients needed to match the box model derived $\gamma(ClNO_2)$ versus the chloride molarity determined from the

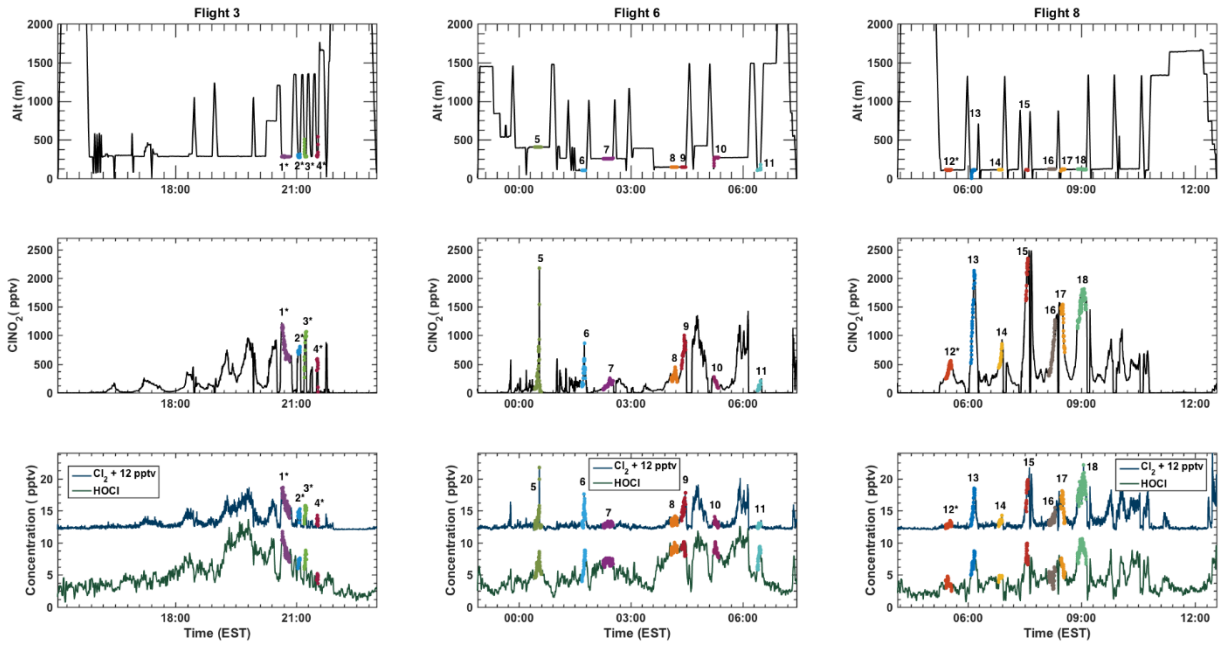

Figure 3.14 Time series of HOCl, Cl_2, $ClNO_2$

Time series of altitude (first row), concentrations of $ClNO_2$ (second row), and concentrations of HOCl and Cl_2 (third row), with each of the 18 plumes examined in this work highlighted and numbered for each of the 3 nighttime flights (columns). Note: Cl_2 concentrations are offset by +12 pptv for comparison Figure 3.15 a) The minimum, median, and maximum values for $\gamma(ClNO_2)$ calculated from the required k_{aq}^{I} as a function of wet D_p (lines) compared to the box model derived values of $\gamma(ClNO_2)$ at the observed wet D_p (points) b) Scatter plot of the first order rate coefficients needed to match the box model derived $\gamma(ClNO_2)$ versus the chloride molarity determined from the concentration of pCl^- (AMS + 3% filter) and UHSHS particle volume concentrations. The slope of the linear least squared fit (line), with plumes having estimated surface area (denoted with *) weighted at 50%, is the corresponding second order rate coefficient.

Chapter 4

Significant U.S. decreases in deposition of anthropogenic chloride from emission controls

4.1 INTRODUCTION

The main source of tropospheric gas-phase inorganic chlorine (Cl_y= HCl + $ClNO_2$ + $2Cl_2$ + HOCl) is mobilization of chloride (Cl^-) from sea salt aerosol (SSA) (Graedel and Keene, 1995; Keene et al., 1999). Wang et al. (2019) estimate that 3.6% of the global flux of SSA is mobilized as Cl_y (resulting in 64 Tg Cl^- yr^{-1}) through acid displacement or other heterogenous reactions. They find that nearly 80% of the mobilized SSA Cl^- is released as hydrochloric acid (HCl) (51 Tg Cl yr^{-1}), with the remaining (13 Tg Cl yr^{-1}) released as reactive chlorine (Cl^*= $ClNO_2$ + $2Cl_2$ + HOCl + $ClNO_3$), cycling to eventually return as HCl (Wang et al., 2019). Outside of coastal regions, direct emissions of HCl into the atmosphere can influence Cl_y concentrations and can be emitted through coal combustion, industrial processes, waste incineration, road salt application, fugitive dust, and biomass burning (Andreae et al., 1996; Keene et al., 1999; Lobert et al., 1999; McCulloch et al., 1999; Sarwar et al., 2012; WMO, 2014; Kolesar et al., 2018). Once emitted, global models estimate 19% of HCl goes onto become further mobilized to Cl^* via reaction with OH (Wang et al., 2019). Although these non-sea salt (NSS) emissions of Cl_y are much smaller in magnitude (together < 6.6 Tg yr^{-1}, globally in 1999 ; Keene et al., 1999;) relative to the source

from SSA, they are potentially important as inland sources of Cl* (Haskins et al., 2018; Thornton et al., 2010;).

The amount of Cl^- deposited via wet deposition in an area is affected by both the local and upwind sources of Cl^- and the concentrations of gases which mobilize Cl^-, all of which have changed in the past two decades. Since the 1990 U.S. Clean Air Act Amendments, anthropogenic emissions from power generation, industry, transportation, and waste incineration have decreased significantly, thereby affecting the NSS sources of Cl_y and the mobilization of Cl^- from SSA. On average between 1990 and 2018, SO_2 emissions have decreased by more than 88% and NO_x emissions have decreased by more than 59% in the U.S. (U.S EPA, 2018). Similarly, between 2002 and 2014, anthropogenic mercury emissions have decreased by more than 79% and NH_3 emissions have slightly decreased by 1.9% (U.S EPA, 2014). These anthropogenic emissions changes have led to significant, and well documented decreases in SO_4^{2-} deposition to the environment, increases in rainwater pH, and the recovery of previously devastated ecosystems (Butler et al., 200l; Giang et al., 2016; Lehmann et al., 2007; Lajtha et al., 2013; Paulot et al., 2017; Fedkin et al., 2019).

These emissions reductions can largely be attributed to wide spread installation of flue-gas desulphurization (FGD) technologies and selective catalytic reactors (SCR) across industries, which were designed to remove SO_2, NO_x, and mercury as part of the 1990 Acid Rain Program, the 2005 Clean Air Interstate Rule, the 2011 Cross State Air Pollution Rule, and the 2012 Mercury and Air Toxics Standards rule. As a co-benefit of NO_x, SO_2, and mercury targeted reductions, these emissions control technologies have been shown to be effective at removing gas phase HCl, which can be emitted from burning chloride-containing items (e.g. biomass, waste, coal) (McCulloch et al., 1999; Lee et al., 2004). FGD use an alkaline sorbent to remove

SO_2, which also reacts readily with other acid gases such as HCl, and is used to control SO_2 and HCl emissions at municipal and industrial facilities with a removal efficiency estimated to be greater than 95% (McCulloch et al., 1999;). Emission controls through SCR convert insoluble elemental mercury (Hg^0) to oxidized mercury (Hg^{2+}) via the heterogenous reaction of Hg^0 with HCl on various metal oxide surfaces to form $HgCl_2$, which is then captured, thereby removing mercury and HCl as a co-benefit (Lee et al., 2004).

The widespread installation of these emissions control technologies has led to a 95% decrease in anthropogenic HCl emissions across the US, from a maximum in 1999 of 303 Gg yr^{-1} to 15 Gg yr^{-1} in 2018 (U.S. EPA, 2018, Figure 4.1 **Changes in HCl emissions and NSS Cl- deposition**

Changes in anthropogenic SO2 emissions (a) and HCl emissions (b) by EPA regions for 1998-2018 compared to the precipitation weighted, three-year annual average of the weekly NADP observations of NSS SO42-(c,e) and NSS Cl- deposition (d,f) for 1998-2001 (middle row) and 2016-2019 (bottom row) at 128 sites. Dark outlines show the EPA regions, which are labeled numerically. Circles indicate sites where the 3-year mean absolute value of NSS component exceeds 5% of that period's 3-year mean in either the total SO42- or Cl- and diamonds show sites where the 3-year mean absolute value of NSS component is less than 5% of that period's 3-year mean in either the total SO42- or Cl-.b). The most significant decreases have occurred in the midwestern states (U.S. EPA, 2018; Figure 4.1 **Changes in HCl emissions and NSS Cl- deposition**

Changes in anthropogenic SO2 emissions (a) and HCl emissions (b) by EPA regions for 1998-2018 compared to the precipitation weighted, three-year annual average of the weekly NADP observations of NSS SO42-(c,e) and NSS Cl- deposition (d,f) for 1998-2001 (middle row) and 2016-2019 (bottom row) at 128 sites. Dark outlines show the EPA regions, which are labeled numerically. Circles indicate sites where the 3-year mean absolute value of NSS component exceeds 5% of that period's 3-year mean in either the total SO42- or Cl- and diamonds show sites where the 3-year mean absolute value of NSS component is less than 5% of that period's 3-year mean in either the total SO42- or Cl-.), where energy generation from coal burning is most common. In this work, we examine whether these anthropogenic HCl emission deceases are reflected in measurements of wet deposition fluxes of Cl^- over the United States in the past

two decades. We contrast the contributions to changes in Cl^- wet deposition from decreases in the primary sources of anthropogenic HCl, versus decreases in the secondary mobilization of SSA from reduced NO_x and SO_2 concentrations.

4.2 METHODOLOGY

The National Atmospheric Deposition Program/ National Trends Network (NADP/NTN) has measured the concentrations of acids, nutrients, and base cations in weekly United States (US) precipitation samples since 1978 to characterize the chemical climate of the US and its temporal and spatial trends (Lamb & Bowersox, 2000) having collected data at 380 different sites, as of January 1st, 2020. The NADP reported measurements include concentrations of Cl^-, sulfate (SO_4^{2-}), nitrate (NO_3^-), ammonium (NH_4^+), potassium (K^+), sodium (Na^+), calcium (Ca^{2+}), and magnesium (Mg^{2+}), as well as pH, specific conductivity, and precipitation (National Atmospheric Deposition Program (NADP), 2005). The Toxic Release Inventory (TRI) at the Environmental Protection Agency (EPA), established in 1986, tracks the release of certain toxic chemicals, including HCl as of 1995, released from large industry facilities that may pose a threat to human health and the environment (US EPA, 2018). We compare trends in NADP Cl^- deposition data to total air emissions of HCl from across all reported sectors, as reported to the TRI over the period Jan. 1, 1998- Dec. 31, 2018. The National Emissions Inventory (NEI) estimates air emissions of criteria pollutants, criteria precursors, and hazardous air pollutants from air emissions sources, including SO_2, since 1990 until the most recent report which covers emissions until the end of 2017 (US EPA, 2018). We compare trends in NADP SO_4^{2-} deposition data to total air emissions of SO_2 from across all reported sectors, as reported to the NEI over the period Jan. 1998- Dec. 31, 2017.

In order to separate natural and anthropogenic contributions to Cl^- deposition, we calculate the non-sea salt (NSS) contribution using NADP observations of Na^+. Previous comparisons of the Cl^- to Na^+ ratio in sea spray have shown it to be conserved, with a measured mass ratio of 1.80, corresponding to bulk sea water composition (Keene et al., 1986). Therefore, the contribution of NSS sources to total Cl^- deposition can be calculated by subtracting the measured Cl^- from the maximum possible amount of chloride present in sea salt particles or the product of the measured amount of Na^+, and the Cl^- to Na^+ mass-ratio in sea-water, $(Cl^-/Na^+)_{seawater}$ = 1.80. Similarly, NSS SO_4^{2-} can be calculated using the SO_4^{2-} to Na^+ mass ratio in seawater (0.507; Keene et al., 1986).

$$NSS\ Cl^- = Cl^- - Na^+ \left(\frac{Cl^-}{Na^+}\right)_{seawater}$$

$$NSS\ SO_4^{2-} = SO_4^{2-} - Na^+ \left(\frac{SO_4^{2-}}{Na^+}\right)_{seawater}$$

Using weekly SO_4^{2-}, Cl^-, Na^+ and precipitation data from the NADP/ National Trends Network, we calculate the NSS Cl^- and NSS SO_4^{2-} deposition at all 380 sites. Only samples flagged as valid by the NADP were used in our analysis. Valid samples are defined as those collected following standard procedures, not flagged as being significantly contaminated, those not exposed to excess dry deposition, those with a sampling interval less than 8 days and 2 hours, and those samples with a reported rain gauge depth or sample volume (NADP, 2016). We require data to meet three completeness criteria as defined by the NADP, on a monthly basis throughout the period of analysis (NADP, 2016): 1) there are valid samples for at least 75% of the summary period, 2) that there must be precipitation amounts (including zeros) for at least 90% of the summary period, either from the rain gage or from the sample volume, and 3) that there must be valid samples for at least 75% of the total precipitation amount reported for the

month. The first two criteria ensure that measurements on valid wet deposition samples and of precipitation amounts were reported for a minimum acceptable fraction of the summary period (i.e. functioning equipment handling), while the third ensures that there are valid precipitation chemistry data to represent a majority of the precipitation that was estimated to have occurred (i.e. unbiased towards a single, large precipitation event).

We performed a Seasonal Kendall Test (SKT) using Sen's method on the weekly data at individual sites to detect trends underlying seasonal deposition patterns from 1998-2019 (Marchetto et al., 2013; Burkey, 2020). The SKT trends were applied to NADP sites that fulfilled the 3 criteria described above on a monthly basis and, in addition, we exclude sites that had more than a 3-month gap in meeting the completeness criteria. Between 1998-2019, 124 sites met these criteria, and we only show analysis and summary statistics for these 128 sites throughout this work. Seasons in the SKT test are based on the annual year, so seasonality trends are assessed from January-December. The null hypotheses were that the trend was zero (Kendall's tau-b statistic was 0) and the statistical significance level was set at 90%. The magnitude of the trend was determined by taking the Sen's slope of the weekly deposition data.

Throughout this work, to separate sites with and without large relative contributions from NSS sources, we determine whether the 3-year average, absolute value of the NSS Cl^- deposition flux is greater than 5% of the 3-year average of the total Cl^- deposition flux at the beginning of the period between 1998-2001 or end of the period, 2016-2019. NADP sites where the total deposition pattern isn't overwhelmed by the deposition of sea salt, using this definition, are hereafter referred to as sites with non-negligible NSS Cl^- deposition flux. These sites tend to be located near industrial centers where anthropogenic Cl^- sources might be expected to contribute to total Cl^- deposition (e.g. Midwest, Northeast), or those where the sea salt Cl^- deposition is so

small that even a small amount of deposited NSS Cl^- would be relevant (e.g. central, western US). Sites with less than 5% contributions to total Cl^- from NSS Cl^- over a 3-year averaging period referred to as sites with negligible NSS Cl^- and tend to be located in coastal regions where sea salt deposition is large or where there is little anthropogenic Cl_y contribution to deposition. We denote whether an individual site has negligible or non-negligible NSS Cl^- in all figures using different symbol shapes. Figure 4.2 **Total Cl- Deposition**

Figure showing the 3 year mean Total Cl- wet deposition flux at the 128 sites analyzed from 1998-2001 (a) and between 2016-2019 (b). EPA regions are shown as dark outlines and are numerically labeled. shows the showing the 3 year mean Total Cl^- wet deposition flux at the 128 sites analyzed from 1998-2001 and between 2016-2019, highlighting the dominance of the coastal sea salt Cl^- signal to the total Cl^- signal.

4.3 Results & Discussion

Figure 4.1 **Changes in HCl emissions and NSS Cl- deposition**

Changes in anthropogenic SO2 emissions (a) and HCl emissions (b) by EPA regions for 1998-2018 compared to the precipitation weighted, three-year annual average of the weekly NADP observations of NSS SO42-(c,e) and NSS Cl- deposition (d,f) for 1998-2001 (middle row) and 2016-2019 (bottom row) at 128 sites. Dark outlines show the EPA regions, which are labeled numerically. Circles indicate sites where the 3-year mean absolute value of NSS component exceeds 5% of that period's 3-year mean in either the total SO42- or Cl- and diamonds show sites where the 3-year mean absolute value of NSS component is less than 5% of that period's 3-year mean in either the total SO42- or Cl-.a and 4.1b show the anthropogenic

emission changes in SO_2 and HCl by EPA region. The well documented reduction in SO_2 emissions (Figure 4.1 **Changes in HCl emissions and NSS Cl- deposition**

Changes in anthropogenic SO2 emissions (a) and HCl emissions (b) by EPA regions for 1998-2018 compared to the precipitation weighted, three-year annual average of the weekly NADP observations of NSS SO42-(c,e) and NSS Cl- deposition (d,f) for 1998-2001 (middle row) and 2016-2019 (bottom row) at 128 sites. Dark outlines show the EPA regions, which are labeled numerically. Circles indicate sites where the 3-year mean absolute value of NSS component exceeds 5% of that period's 3-year mean in either the total SO42- or Cl- and diamonds show sites where the 3-year mean absolute value of NSS component is less than 5% of that period's 3-year mean in either the total SO42- or Cl-.a) is seen to largely occur in EPA Regions 3-5, which include the Midwest, Southeast, and mid-Atlantic states where coal burning is most common, with the steepest decreases between 2005 and 2011. Similarly, the largest anthropogenic HCl emissions (Figure 4.1 **Changes in HCl emissions and NSS Cl- deposition**

Changes in anthropogenic SO2 emissions (a) and HCl emissions (b) by EPA regions for 1998-2018 compared to the precipitation weighted, three-year annual average of the weekly NADP observations of NSS SO42-(c,e) and NSS Cl- deposition (d,f) for 1998-2001 (middle row) and 2016-2019 (bottom row) at 128 sites. Dark outlines show the EPA regions, which are labeled numerically. Circles indicate sites where the 3-year mean absolute value of NSS component exceeds 5% of that period's 3-year mean in either the total SO42- or Cl- and diamonds show sites where the 3-year mean absolute value of NSS component is less than 5% of that period's 3-year mean in either the total SO42- or Cl-.b) occur in EPA regions 3,4, and 5. However, HCl emissions decrease faster over time than SO_2, particularly from 2008-2010. One explanation for this trend is the widespread installation of emissions controls technologies across

industries (including those that don't co-emit SO_2) in anticipation of the 2012 Mercury and Air Toxics Standards rule and the 2009 enactment of the Clean Air Interstate Rule (CAIR). CAIR required scrubbing technologies to run year-round, and not just in the summer months, for all states in EPA regions 2-6 except Oklahoma, Arkansas, Louisiana, Mississippi, and Florida. He et al., (2013) shows that prior to 2009 stack emissions of NO_x from CEMS data, exhibited a square wave seasonality with peaks in the winter in Maryland, Ohio and Pennsylvania from industry SCRs (which also remove HCl) being turned on and off in the summer and winter months, respectively. After the 2009 enactment of CAIR, this seasonality was completely diminished, demonstrating the power these emissions controls across industries had on local NO_x concentrations, and therefore, likely on anthropogenic HCl concentrations given their co-removal within SCRs.

Figure 4.1 **Changes in HCl emissions and NSS Cl- deposition**

Changes in anthropogenic SO2 emissions (a) and HCl emissions (b) by EPA regions for 1998-2018 compared to the precipitation weighted, three-year annual average of the weekly NADP observations of NSS SO42-(c,e) and NSS Cl- deposition (d,f) for 1998-2001 (middle row) and 2016-2019 (bottom row) at 128 sites. Dark outlines show the EPA regions, which are labeled numerically. Circles indicate sites where the 3-year mean absolute value of NSS component exceeds 5% of that period's 3-year mean in either the total SO42- or Cl- and diamonds show sites where the 3-year mean absolute value of NSS component is less than 5% of that period's 3-year mean in either the total SO42- or Cl-.c-f shows the spatial distribution of the 3 year average wet deposition flux of NSS SO_4^{2-} and NSS Cl^- for the beginning (Jan. 1, 1998 - Jan. 1, 2001) and end (Jan. 1, 2016 - Jan. 1, 2019) of the analysis period at 128 sites that meet the completeness criteria. Figure 4.1 **Changes in HCl emissions and NSS Cl- deposition**

Changes in anthropogenic SO2 emissions (a) and HCl emissions (b) by EPA regions for 1998-2018 compared to the precipitation weighted, three-year annual average of the weekly NADP observations of NSS SO42-(c,e) and NSS Cl- deposition (d,f) for 1998-2001 (middle row) and 2016-2019 (bottom row) at 128 sites. Dark outlines show the EPA regions, which are labeled numerically. Circles indicate sites where the 3-year mean absolute value of NSS component exceeds 5% of that period's 3-year mean in either the total SO42- or Cl- and diamonds show sites where the 3-year mean absolute value of NSS component is less than 5% of that period's 3-year mean in either the total SO42- or Cl-.c, e highlights the well documented reduction in NSS SO_4^{2-} deposition from targeted anthropogenic SO_2 emissions controls across the eastern US in EPA Regions 2-5. The largest decreases between 1998-2019 occur in Maryland, New Jersey, New York, North Carolina, Ohio, Pennsylvania, Virginia, and West Virginia. We find that between 1998-2019, average annual NSS SO_4^{2-} deposition at all sites in EPA regions 2-5 in the eastern US decreased from an average 27.4 kg ha^{-1} between 1998-2001 to 8.0 kg ha^{-1} by 2016-2019, for a total average decrease of 19.4 kg ha^{-1}. This agrees well with results from Fedkin et al., (2019) who showed decreases up to 20 kg ha^{-1} in annual sulfate deposition between 2005-2015 centered around the Ohio, West Virginia, and Pennsylvania border.

Similarly, the largest reductions in NSS Cl^- deposition (Figure 4.1 **Changes in HCl emissions and NSS Cl- deposition**

Changes in anthropogenic SO2 emissions (a) and HCl emissions (b) by EPA regions for 1998-2018 compared to the precipitation weighted, three-year annual average of the weekly NADP observations of NSS SO42-(c,e) and NSS Cl- deposition (d,f) for 1998-2001 (middle row) and 2016-2019 (bottom row) at 128 sites. Dark outlines show the EPA regions, which are

labeled numerically. Circles indicate sites where the 3-year mean absolute value of NSS component exceeds 5% of that period's 3-year mean in either the total SO42- or Cl- and diamonds show sites where the 3-year mean absolute value of NSS component is less than 5% of that period's 3-year mean in either the total SO42- or Cl-.d,f) are seen in EPA Regions 2-5 with the largest decreases in Maryland, New Jersey, New York, North Carolina, Ohio, Pennsylvania, Virginia, and West Virginia. Between 1998-2019, average annual NSS Cl^- deposition flux at all sites in EPA Regions 2-5 in the eastern US decreased from an average 0.11 kg ha^{-1} between 1998-2001 to -0.05 kg ha^{-1} by 2016-2019. Of the 90 sites across the US which had non-negligible NSS Cl^- from 1998-2001, 51% of sites (n=46) had positive values in NSS Cl^- deposition (red circles), indicating areas where more Cl^- was measured than would be expected from sea salt influence alone and are likely indicative of anthropogenic sources of Cl_y. However, by 2016-2019, only 22% of sites with non-negligible NSS Cl^- had positive, or excess NSS Cl^- deposition flux (n=15), indicating that far fewer sites are impacted by anthropogenic Cl_y sources now than in the past two decades. Additionally, between 1998-2019, the percentage of sites across the US with non-negligible NSS Cl^- deposition decreased from 72% (n=90) to 56% (n=68), indicating that the number of sites experiencing a significant anthropogenic influence on NSS Cl^- deposition relative to sea salt Cl^- deposition has significantly decreased over time. Or that the number of sites whose Cl^- deposition pattern is consistent with SSA deposition alone, has increased over time.

We find 44 sites with non-negligible NSS Cl^- between 1998-2001 had negative values in NSS Cl^- deposition flux (blue circles). These are sites where less Cl^- was measured than would be expected from sea salt emission or are depleted in Cl^- relative Na^+ in SSA. They are areas where Na^+ presumably from sea salt has been deposited, but where the co-emitted Cl^- from sea salt has

been displaced from the particle into the gas phase as Cl_y either through acid displacement by HNO_3 or H_2SO_4, or through heterogenous reactions with N_2O_5. Concentrations of HNO_3, H_2SO_4, and N_2O_5 are enhanced by anthropogenic activities, and therefore areas with large negative or depleted values of NSS Cl^- can be thought of as regions where anthropogenic activity is mobilizing natural sources of Cl^-. Between 1998-2001, displacement of Cl^- can be seen to occur in all regions outside the Midwest and northeast US, but to the largest degree in the southeast, particularly in Alabama, Arkansas, Mississippi, Missouri, and Texas.

The Sen's slopes of the trends underlying seasonal wet deposition patterns in annual NSS SO_4^{2-} and NSS Cl^- deposition for individual sites between 1998-2019 are shown in Figure 4.3

Sen's Slopes in NSS Cl- and SO42-

Maps of the calculated Sen's slopes at 128 NADP stations for the period 1998-2019 in NSS SO42- (a) and NSS Cl- (b). Dark outlines show the EPA regions, which are labeled numerically. Shapes indicate whether absolute value of the 3-year mean NSS SO42- (a) or NSS Cl- (b, c) is >5% of the 3-year mean, Total SO42- or Cl- from 1998-2001, whether the calculated Sen's slope in NSS SO42- (a) or NSS Cl- (b, c) is statistically significant or not at the 90% level. A scatter plot of the data in (a) vs (b) is shown in panel (c) with a weighted linear least squares fit (red line) to the data with statistically significant Sen's slopes in NSS Cl- and with a 3-year mean NSS Cl- greater than 5% of the 3-year mean Total Cl- from 1998-2003 (red circles), using the calculated standard error in the Sen's slopes for NSS Cl- and NSS SO42. The expected NSS Cl- decrease from the average HCl:SO2 emissions factor in EPA regions 1-5 is shown as a purple line.. All but 3 of the 128 NADP sites analyzed display negative trends in NSS SO_4^{2-} deposition, reflecting the well documented environmental impact of decreases in anthropogenic SO_2 emissions, with the trends at the remaining 3 sites not being statistically significant (Lehmann et al., 2007; Lajtha et al., 2013; Paulot et al., 2017; Fedkin et al., 2019). Sites having the largest decreases in annual NSS SO_4^{2-} deposition are in the midwestern and northeastern US in EPA regions 2-5. The mean change in annual NSS SO_4^{2-} wet deposition at sites with statistically significant trends (circles, n=109) is -339 g ha^{-1} yr^{-1}, though changes at individual sites in the Ohio River Valley range up to -952 g ha^{-1} yr^{-1}, broadly consistent with other studies (Lehmann

et al., 2007; Fedkin et al., 2019;).

Similarly, the largest and statistically significant changes in NSS Cl^- deposition are seen in the midwestern and northeastern US in EPA Regions 2-5. The mean change at all sites with statistically significant trends in NSS Cl^- (n=88) is -6.1 g ha^{-1} yr^{-1}, with decreases at 85% of these sites. Considering only sites with a statistically significant decrease and non-negligible NSS Cl^- between 1998-2001 (n=63, red circles), this decrease becomes -10.2 g ha^{-1} yr^{-1}, with these sites largely located in Maryland, New Jersey, New York, North Carolina, Ohio, Pennsylvania, Virginia, and West Virginia. These sites are spatially correlated with the largest NSS SO_4^{2-} deposition decreases during this time period (Figure 4.3 **Sen's Slopes in NSS Cl- and SO42-**

Maps of the calculated Sen's slopes at 128 NADP stations for the period 1998-2019 in NSS SO42- (a) and NSS Cl- (b). Dark outlines show the EPA regions, which are labeled numerically. Shapes indicate whether absolute value of the 3-year mean NSS SO42- (a) or NSS Cl- (b, c) is >5% of the 3-year mean, Total SO42- or Cl- from 1998-2001, whether the calculated Sen's slope in NSS SO42- (a) or NSS Cl- (b, c) is statistically significant or not at the 90% level. A scatter plot of the data in (a) vs (b) is shown in panel (c) with a weighted linear least squares fit (red line) to the data with statistically significant Sen's slopes in NSS Cl- and with a 3-year mean NSS Cl- greater than 5% of the 3-year mean Total Cl- from 1998-2003 (red circles), using the calculated standard error in the Sen's slopes for NSS Cl- and NSS SO42. The expected NSS Cl- decrease from the average HCl:SO2 emissions factor in EPA regions 1-5 is shown as a purple line.c). Additionally, they are in or downwind of EPA regions with the highest anthropogenic emissions of HCl. We find that 46% of the 128 sites analyzed were experiencing excess (positive) NSS Cl^- deposition flux from anthropogenic sources of Cl_y between 1998-2001, but which are now depleted (negative) in Cl^- relative to Na^+ deposited due to the statistically significant decreases in the anthropogenic sources such that these sites' Cl^- deposition can be explained entirely by sea salt contributions by 2016-2019.

Conversely, statistically significant increases in NSS Cl^- deposition are seen in the southeastern and northwestern US at a total of 13 sites. Of these 13 sites, only 6 had non-negligible, NSS Cl^- between 1998-2001, and all saw statistically significant increases in NSS Cl^-

deposition, located in Florida, Georgia, Mississippi and Texas. For the remaining 7 sites in the Pacific Northwest and coastal Florida, the amount of NSS Cl^- deposited is negligible relative to the sea salt signal in these areas, such that these increases are occurring for a very small amount of deposited NSS Cl^-. The average increase in NSS Cl^- at the 6 sites with non-negligible NSS Cl^- wet deposition flux was 7.9 g ha^{-1} yr^{-1}. However, this increase is not enough to change the 3-year mean annual NSS Cl^- wet deposition flux from a negative value of -0.55 kg ha^{-1} between 1998-2001 to a positive value. By 2016-2019, these areas are still depleted in Cl^-, but to a lesser degree (-0.19 kg ha^{-1}). In EPA Region 4, encompassing these sites with statistically significant increases in NSS Cl^-, Na^+ wet deposition flux decreased slightly, despite increasing precipitation, indicating that sea salt Cl^- deposition likely decreased slightly over this time period (Figure 4.4

Regional Changes in Na+, Cl- and Precipitation

Figure comparing the median change in the annual deposition flux of Na+, Cl- precipitation, (a), NSS Cl- (b), and NSS SO42- (c) at all 128 sites where data was analyzed subdivided by EPA region.

). Therefore, the increase in NSS Cl^- deposition is indicative that a larger percentage of the total Cl^- is co-deposited with the Na^+ with which it was co-emitted, but not that the total sea salt Cl^- deposition has been increasing. These results suggest that at least in some places in the southeast are experiencing less displacement of natural Cl^-, presumably a side effect of reduced NO_x and SO_2 concentrations.

Our results suggest a decrease in the sources of NSS Cl^- in the Midwest and Northeast US, or a decrease in the amount of Cl_y deposited there from other regions. As shown in Figure

4.3 **Sen's Slopes in NSS Cl- and SO42-**

Maps of the calculated Sen's slopes at 128 NADP stations for the period 1998-2019 in NSS SO42- (a) and NSS Cl- (b). Dark outlines show the EPA regions, which are labeled numerically. Shapes indicate whether absolute value of the 3-year mean NSS SO42- (a) or NSS Cl- (b, c) is >5% of the 3-year mean, Total SO42- or Cl- from 1998-2001, whether the calculated Sen's slope in NSS SO42- (a) or NSS Cl- (b, c) is statistically significant or not at the 90% level. A scatter

plot of the data in (a) vs (b) is shown in panel (c) with a weighted linear least squares fit (red line) to the data with statistically significant Sen's slopes in NSS Cl- and with a 3-year mean NSS Cl- greater than 5% of the 3-year mean Total Cl- from 1998-2003 (red circles), using the calculated standard error in the Sen's slopes for NSS Cl- and NSS SO42. The expected NSS Cl- decrease from the average HCl:SO2 emissions factor in EPA regions 1-5 is shown as a purple line.c, sites in the Midwest with the largest and statistically significant decreases in NSS Cl^- are well correlated (r^2=0.68) with those having the largest decreases in NSS SO_4^{2-} deposition. Correlated decreases in NSS SO_4^{2-} and NSS Cl^- wet deposition fluxes are what would be expected if emissions control technologies are removing SO_2 and HCl at common industry sources or are decreasing the downwind deposition of displaced sea salt Cl^-, but would not be expected if trends in other potential sources of NSS Cl^- like road-salting practices (Denby et al., 2016; Loelsar et al., 2018), biomass burning (Andreae et al., 2019), or fugitive dust (Sarwar et al., 2012), were driving the decreases in NSS Cl^- wet deposition flux.

It is possible that the decrease in mobilized Cl^- from these regions is driving the decrease in excess Cl^- deposited in the Midwest, and mid-Atlantic states. Sites with the largest NSS SO_4^{2-} decreases have driven the highest rainwater pH increases observed in the NADP dataset. However, decreases in NSS Cl^- wet deposition fluxes are not as well correlated with rainwater pH increases (r^2=0.39) as they are with NSS SO_4^{2-} decreases (r^2=0.68, Figure 4.3 **Sen's Slopes in NSS Cl- and SO42-**

Maps of the calculated Sen's slopes at 128 NADP stations for the period 1998-2019 in NSS SO42- (a) and NSS Cl- (b). Dark outlines show the EPA regions, which are labeled numerically. Shapes indicate whether absolute value of the 3-year mean NSS SO42- (a) or NSS Cl- (b, c) is >5% of the 3-year mean, Total SO42- or Cl- from 1998-2001, whether the calculated Sen's slope in NSS SO42- (a) or NSS Cl- (b, c) is statistically significant or not at the 90% level. A scatter plot of the data in (a) vs (b) is shown in panel (c) with a weighted linear least squares fit (red line) to the data with statistically significant Sen's slopes in NSS Cl- and with a 3-year mean NSS Cl- greater than 5% of the 3-year mean Total Cl- from 1998-2003 (red circles), using the calculated standard error in the Sen's slopes for NSS Cl- and NSS SO42. The expected NSS Cl- decrease from the average HCl:SO2 emissions factor in EPA regions 1-5 is shown as a purple line.). Given that HCl is thermodynamically favored to partition into the particle phase at pH>3 (Sander et al., 2015), even acidic rainwater, typical of areas downwind of industrial centers in the

Midwest in 1998 (pH~4), is a good wet scavenger of HCl. Therefore, increases in rainwater pH between 1998-2019 are unlikely to have impacted the wet scavenging of HCl over this time period. Although fine mode aerosol pH (D_p < 2.5 μm) is not expected to be significantly increased until atmospheric SO_4^{2-} concentrations reach near pre-anthropogenic levels (Guo et al., 2017; Weber et al., 2016), because the majority of sea salt Cl^- is found in externally mixed coarse mode particles (Graedel and Keene, 1995; Keene et al., 1999), changes in HNO_3, N_2O_5, and H_2SO_4 production from NO_x and SO_2 decreases that have occurred since 1998 should favor coarse mode sea salt Cl^- to remain in the particle phase, rather than to partition out as Cl_y, more often in 2019. It is unclear how much this would impact the lifetime of Cl^- against deposition given that the atmospheric lifetimes of Cl_y vary from timescales on the order of days-weeks (HCl) to hours-seconds ($ClNO_2$, Cl_2), and that the ultimate sink of displaced Cl^- may or may not be sensitive to wet deposition (HCl vs chlorinated VOCs). However, because global models estimate that the Cl_y from displaced sea salt Cl^- eventually cycles back as HCl (Wang et al., 2019), it is possible that less displacement of Cl^-, from decreased production of HNO_3, H_2SO_4, and N_2O_5 from reductions in NO_x and SO_2 concentrations, have reduced the lifetime against deposition of Cl^- over this time period, by reducing the cycling of Cl_y through the gas phase before deposition. This would explain the increase in wet deposition flux of NSS Cl^- at sites in the central south that had large negative NSS Cl^- deposition fluxes between 1998-2003.

In order to determine if the observed HCl emissions decreases are enough to explain the observed decreases in NSS Cl^- wet deposition flux or whether other mechanisms, such as reduced Cl- mobilization are needed, we calculate the expected annual NSS Cl^- deposition change from the observed annual NSS SO_4^{2-} deposition changes using an emissions factor from the yearly anthropogenic SO_2 and HCl data in each EPA Region, as follows.

$$\Delta \text{NSS } Cl^- = \Delta \text{NSS } SO_4^{2-} \text{ x } \left(\frac{m_S}{m_{SO_4^{2-}}}\right) \text{ x EF}\left(\frac{Cl}{S}\right)$$

where $\Delta NSS\ SO_4^{2-}$ is the observed annual NSS SO_4^{2-} deposition flux change (shown in Figure

4.3 **Sen's Slopes in NSS Cl- and SO42-**

Maps of the calculated Sen's slopes at 128 NADP stations for the period 1998-2019 in NSS SO42- (a) and NSS Cl- (b). Dark outlines show the EPA regions, which are labeled numerically. Shapes indicate whether absolute value of the 3-year mean NSS SO42- (a) or NSS Cl- (b, c) is >5% of the 3-year mean, Total SO42- or Cl- from 1998-2001, whether the calculated Sen's slope in NSS SO42- (a) or NSS Cl- (b, c) is statistically significant or not at the 90% level. A scatter plot of the data in (a) vs (b) is shown in panel (c) with a weighted linear least squares fit (red line) to the data with statistically significant Sen's slopes in NSS Cl- and with a 3-year mean NSS Cl- greater than 5% of the 3-year mean Total Cl- from 1998-2003 (red circles), using the calculated standard error in the Sen's slopes for NSS Cl- and NSS SO42. The expected NSS Cl- decrease from the average HCl:SO2 emissions factor in EPA regions 1-5 is shown as a purple line.a), m is the molar mass of Sulfur and SO_4^{2-}, respectively, and EF is the calculated emissions factor for the mass of Cl emitted per mass of S. Emissions of SO_2 and HCl were well correlated throughout time in EPA Regions 1-5 in the eastern US ($r^2 > 0.947$), and the average emission factor in these regions was 0.044 +/-0.021 Tg Cl Tg S^{-1}. We use the NEI SO_2 emissions and the TRI HCl emissions in each EPA region on an annual basis to calculate an average emissions factor of the annual mass of Cl emitted from anthropogenic sources of HCl over the annual mass of S emitted from anthropogenic SO_2 sources between Jan. 1, 1998- Dec. 31, 2017. We use an orthogonal distance regression to calculate the average emissions factor in each region used in the calculation, which are all shown in Figure 4.5 **Determining Regional Emissions Factors**

Scatter plots showing the emission of Cl from anthropogenic HCl against the emission of S from anthropogenic SO2 on a yearly basis (colors) from Jan. 1, 1998- Dec. 31, 2017 in each EPA region. The emissions factor (slope) used in each region is displayed with the correlation coefficient.

Figure 4.6 Predicted Changes in NSS Cl- from HCl Emissions

The change in (a) the observed annual NSS Cl- deposition flux from Figure 4.3b compared to (b)

the predicted change in NSS Cl- deposition calculated from multiplying the observed annual NSS SO42- deposition flux in Figure 4.3a by a regional emissions factor of Cl/S, and (c) the difference between them for the period Jan 1. 1998- Dec. 31 2017 (since NEI SO2 emissions data is not available after this date). EPA regions are shown as dark outlines and are labeled numerically. **Figure 4.7**. EPA Regions 1-5 had correlation coefficients between emitted anthropogenic S and Cl greater than 0.947 with an average emission factor of with an average of 0.044 +/-0.021 Tg Cl Tg S^{-1}. Regions 6-10, with less industry emissions overall, had lower correlations, all greater than 0.828, and a lower mean emission factor of 0.0084 +/-0.0052 Tg Cl^- Tg S^{-1}.

Figure 4.3 **Sen's Slopes in NSS Cl- and SO42-**

Maps of the calculated Sen's slopes at 128 NADP stations for the period 1998-2019 in NSS SO42- (a) and NSS Cl- (b). Dark outlines show the EPA regions, which are labeled numerically. Shapes indicate whether absolute value of the 3-year mean NSS SO42- (a) or NSS Cl- (b, c) is >5% of the 3-year mean, Total SO42- or Cl- from 1998-2001, whether the calculated Sen's slope in NSS SO42- (a) or NSS Cl- (b, c) is statistically significant or not at the 90% level. A scatter plot of the data in (a) vs (b) is shown in panel (c) with a weighted linear least squares fit (red line) to the data with statistically significant Sen's slopes in NSS Cl- and with a 3-year mean NSS Cl- greater than 5% of the 3-year mean Total Cl- from 1998-2003 (red circles), using the calculated standard error in the Sen's slopes for NSS Cl- and NSS SO42. The expected NSS Cl- decrease from the average HCl:SO2 emissions factor in EPA regions 1-5 is shown as a purple line.c shows this calculated predicted change in annual NSS Cl^- deposition using the average EF in EPA Regions 1-5, compared to the individual site changes. This estimation inherently assumes that Cl^- and SO_4^{2-} have the same lifetime against wet deposition and that all HCl decreases come from facilities that co-emit SO_2 and HCl. While on the same order of magnitude (days), the lifetime against wet deposition between Cl^- and SO_4^{2-} can vary, given that Cl^- can repartition to the gas phase as Cl_y, while SO_4^{2-} cannot. Additionally, industries like municipal waste incineration or various mining processes may emit HCl, but not SO_2. Therefore, while HCl and SO_2 are co-emitted across many industries including power generation, this is not expected to be

the case for all industrial emitters of HCl.

Figure 4.8 **Predicted Changes in NSS Cl- from HCl Emissions**

The change in (a) the observed annual NSS Cl- deposition flux from Figure 4.3b compared to (b) the predicted change in NSS Cl- deposition calculated from multiplying the observed annual NSS SO42- deposition flux in Figure 4.3a by a regional emissions factor of Cl/S, and (c) the difference between them for the period Jan 1. 1998- Dec. 31 2017 (since NEI SO2 emissions data is not available after this date). EPA regions are shown as dark outlines and are labeled numerically.

Figure 4.9 Temporal Correlation in HCl Emissions & NSS Cl- deposition

Percent decrease in anthropogenic HCl emissions (orange line) and NSS Cl- deposition (blue line) relative to 1998 for EPA regions 1-5. We only consider deposition data from NADP sites with statistically significant, negative Sen's slopes and non-negligible NSS Cl- between 1998-2003. Included sites and the corresponding change in their annual NSS Cl- between 1998-2019 from Figure 4.3 on the same color axis, are shown as inlays. The NSS Cl- deposition trends are calculated by taking the 3-year running time average and standard deviation centered around each year at each site, and then taking the median trend of all sites included. The median of all sites' individual change magnitudes as percentage of mean in wet deposition flux of NSS Cl-, calculated from the Sen's slopes, is shown as a blue 'X' at 2018.Figure **4.10** shows the observed annual NSS Cl^- deposition flux compared to this predicted change in annual NSS Cl^- deposition flux and the difference between the observations and predictions. In EPA regions 1-3, the predicted NSS Cl^- deposition change from emissions changes are lower than the observed decreases in annual NSS Cl^- deposition, explaining 28% of the observed decreases in Regions 1-2 on average where the absolute value of the decreases are small. The emissions explain up to 85% of the observed decreases in Region 3, where the absolute value of the decrease is largest. This indicates that in Regions 1-3, the anthropogenic HCl emissions decreases can explain at

least some of the observed annual NSS Cl^- deposition decreases but are not nearly enough to explain the most extreme decreases in Ohio and Pennsylvania. Predictions of annual NSS Cl^- deposition change could be lower than observations in EPA Regions 1-3 as a result of the underlying assumptions that all anthropogenic HCl is co-emitted with SO_2. In EPA Region 5, encompassing Illinois, Indiana, Michigan, Minnesota, Ohio, and Wisconsin, on average, the HCl emissions decreases explain 103% of the observed NSS Cl^- deposition decreases, having the best agreement between predictions and observations throughout the US. Across the central and western US in EPA Regions 6-9, the predicted decreases explain only 33% of the deposition changes on average, though the value of the observed deposition changes in this region are small in absolute value and not always significant. Conversely, across the southeast in Region 4, but particularly in Mississippi, Alabama, Georgia and Florida, predictions indicate that annual NSS Cl^- should have decreased by 5-15 g ha^{-1} yr^{-1}, when observations show they have increased by 2-13 g ha^{-1} yr^{-1}. This discrepancy between predicted and observed annual NSS Cl^- deposition can be interpreted as areas where other mechanisms, such as reduced mobilization of Cl_y, is affecting the NSS Cl^- deposition. It is possible that some of the decrease in annual NSS Cl^- deposition in EPA Regions 1-3 is occurring because of the decrease in Cl^- mobilization in Region 4.

Figure 4.11 **Temporal Correlation in HCl Emissions & NSS Cl- deposition**

Percent decrease in anthropogenic HCl emissions (orange line) and NSS Cl- deposition (blue line) relative to 1998 for EPA regions 1-5. We only consider deposition data from NADP sites with statistically significant, negative Sen's slopes and non-negligible NSS Cl- between 1998-2003. Included sites and the corresponding change in their annual NSS Cl- between 1998-2019 from Figure 4.3 on the same color axis, are shown as inlays. The NSS Cl- deposition trends are calculated by taking the 3-year running time average and standard deviation centered around each year at each site, and then taking the median trend of all sites included. The median of all sites' individual change magnitudes as percentage of mean in wet deposition flux of NSS Cl-, calculated from the Sen's slopes, is shown as a blue 'X' at 2018.

Figure 4.12Figure 4.13 compares 1998-2018 changes in NSS Cl^- wet deposition to

changes in anthropogenic emissions of HCl for EPA regions 1-5 located in the eastern US. In this figure, we only consider deposition data from NADP sites with statistically significant, negative Sen's slopes and non-negligible NSS Cl^- between 1998-2001, or sites where we might expect emissions changes to have impacted deposition patterns. Because small absolute values of NSS Cl^- deposition flux between 1998-2001 can bias the percent change relative to this period to large numbers (e.g. > 500%), we also show the change magnitude as a percentage of the mean in deposition, calculated from the Sen's slopes on Figure 4.3 **Sen's Slopes in NSS Cl- and SO42-**

Maps of the calculated Sen's slopes at 128 NADP stations for the period 1998-2019 in NSS SO42- (a) and NSS Cl- (b). Dark outlines show the EPA regions, which are labeled numerically. Shapes indicate whether absolute value of the 3-year mean NSS SO42- (a) or NSS Cl- (b, c) is >5% of the 3-year mean, Total SO42- or Cl- from 1998-2001, whether the calculated Sen's slope in NSS SO42- (a) or NSS Cl- (b, c) is statistically significant or not at the 90% level. A scatter plot of the data in (a) vs (b) is shown in panel (c) with a weighted linear least squares fit (red line) to the data with statistically significant Sen's slopes in NSS Cl- and with a 3-year mean NSS Cl- greater than 5% of the 3-year mean Total Cl- from 1998-2003 (red circles), using the calculated standard error in the Sen's slopes for NSS Cl- and NSS SO42. The expected NSS Cl- decrease from the average HCl:SO2 emissions factor in EPA regions 1-5 is shown as a purple line. for comparison to end points in calculated percent change. The change magnitude as a percentage of the mean, displayed in Figure 4.11 **Temporal Correlation in HCl Emissions & NSS Cl- deposition**

Percent decrease in anthropogenic HCl emissions (orange line) and NSS Cl- deposition (blue line) relative to 1998 for EPA regions 1-5. We only consider deposition data from NADP sites with statistically significant, negative Sen's slopes and non-negligible NSS Cl- between 1998-2003. Included sites and the corresponding change in their annual NSS Cl- between 1998-2019 from Figure 4.3 on the same color axis, are shown as inlays. The NSS Cl- deposition trends are calculated by taking the 3-year running time average and standard deviation centered around each year at each site, and then taking the median trend of all sites included. The median of all sites' individual change magnitudes as percentage of mean in wet deposition flux of NSS Cl-, calculated from the Sen's slopes, is shown as a blue 'X' at 2018.

Figure 4.12Figure 4.13 between 1998-2018 and compared to the yearly percent change in annual NSS Cl- deposition relative to 1998 is calculated as:

$$\% \Delta \text{NSS } Cl^- = \left(\frac{m_{Sen's} \text{ x } \Delta t}{mean(\text{NSS } Cl^- (\Delta t))}\right)$$

where $m_{sen's}$ is the calculated Sen's slope, Δt is the number of years over which the change has occurred (Δt =20 years), and $NSS\ Cl^-\ (t_O)$ is the mean NSS Cl^- deposition flux over the entire time period (1998-2018). The smaller concentrations of total Cl^- in EPA Region 5 in Minnesota and Wisconsin biasing the calculated percent change significantly lower than the change magnitude as a percentage of the mean is largely responsible for the greater variability in the percent change in NSS Cl^- deposition flux seen in Region 5 (in addition to a larger number of sites considered in this region).

Figure 4.11 **Temporal Correlation in HCl Emissions & NSS Cl- deposition**

Percent decrease in anthropogenic HCl emissions (orange line) and NSS Cl- deposition (blue line) relative to 1998 for EPA regions 1-5. We only consider deposition data from NADP sites with statistically significant, negative Sen's slopes and non-negligible NSS Cl- between 1998-2003. Included sites and the corresponding change in their annual NSS Cl- between 1998-2019 from Figure 4.3 on the same color axis, are shown as inlays. The NSS Cl- deposition trends are calculated by taking the 3-year running time average and standard deviation centered around each year at each site, and then taking the median trend of all sites included. The median of all sites' individual change magnitudes as percentage of mean in wet deposition flux of NSS Cl-, calculated from the Sen's slopes, is shown as a blue 'X' at 2018.

Figure 4.12Figure 4.13 shows that the median of the 3-year running average percent change in NSS Cl^- wet deposition flux declines at a rate like HCl emissions throughout the comparison period, also having the steepest declines between 2007 and 2011. All correlation coefficients between HCl emissions reductions and deposition decreases in NSS Cl^- deposition decreases in regions 1-5 are greater than 0.74. Temporal correlations between HCl emissions and NSS Cl^- deposition were largest in Maryland, Pennsylvania, Virginia, and West Virginia, (Region 3, r^2=0.96, n=8). These states are where anthropogenic HCl emissions were 61 Gg yr^{-1} in 1998, or 22% of the national anthropogenic HCl emissions that year, and where the 3 year

average annual NSS Cl^- wet deposition flux decreased from 33 g ha^{-1} between 1998-2001 to -7.4 g ha^{-1} by 2016-2019. This is the largest absolute value change in NSS Cl^- wet deposition flux since in all EPA regions between 1998 and 2018. Given the significance of the magnitude of these decreases in both HCl emissions and NSS Cl^- deposition, the excellent temporal correlation at sites in Region 3, strongly supports our conclusion that decreases in anthropogenic HCl emissions are driving the NSS Cl^- deposition decreases in the Midwest.

However, this support extends beyond just Region 3. In total, 87% of the total reported anthropogenic HCl emissions occur within EPA regions 3, 4 and 5. In EPA Regions 2-4,with land mass immediately downwind of those with large HCl emissions, the percent change in HCl emissions are most closely correlated, temporarily and spatially, with the percent change in deposited NSS Cl^-. The impact of upwind HCl emissions can be seen particularly in New York and New Jersey in Region 2, which has minimal direct anthropogenic HCl emissions from industry, but experiences some of the largest decreases in the wet deposition flux of NSS Cl^- both in absolute value and percentage. Ultimately, these results suggest that the observed decrease in the absolute value of NSS Cl^- wet deposition flux in EPA Regions 1-5 are, at least in part, the result of decreases in anthropogenic HCl emissions.

4.4 CONCLUSIONS

We have shown that between 1998-2019, the average annual NSS Cl^- deposition flux has decreased significantly in the Midwest and northeastern US and slightly increased in the southeastern US with evidence that both changes are driven by decreases in anthropogenic HCl, SO_2, and NO_x emissions. On average in the eastern US, the average annual NSS Cl^- deposition decreased from an average excess value of 0.11 kg ha^{-1} between 1998-2001 to an average

depleted value of -0.05 kg ha^{-1} by 2016-2019, with the most extreme decreases occurring in the Midwest. At sites with non-negligible average annual NSS Cl^- deposition between 1998-2001, the percentage of sites with excess NSS Cl^- deposition flux decreased from 51% to 22% by 2016-2019. Though, statistically significant decreases in NSS Cl^- deposition flux were found at 58% of all sites analyzed, decreases at sites with non-negligible NSS Cl^- between 1998-2001, largely located in Maryland New Jersey, New York, North Carolina, Ohio, Pennsylvania, Virginia, and West Virginia saw the largest decreases of -10.2 g ha^{-1} yr^{-1}, on average. The observed decreases in NSS Cl^- in these states was spatially well correlated with SO_4^{2-} deposition decreases (r^2=0.68), and temporally well correlated with HCl emissions decreases ($r^2 \geq 0.74$). The predicted decreases in NSS Cl^- from HCl emissions decreases was able to explain 85% on average of the observed decrease in Pennsylvania, Virginia, and West Virginia on average and up to 103% on average of the decrease in Illinois, Indiana, Michigan, Minnesota, Ohio, and Wisconsin. Therefore, we propose that the 95% decrease in anthropogenic HCl emissions across the US, from a maximum in 1999 of 303 Gg yr^{-1} to 15 Gg yr^{-1} in 2018, has driven a majority of the decrease in observed NSS Cl^- deposition in the Midwest from excess values in the late 1990s to depleted values by 2019. This reflects a trend of reduced anthropogenic impacts on Cl^- deposition with more Cl^- deposition explained by a sea salt source alone from 2016-2019 than in 1998-2001, with most sites returning to deposition patterns that would occur naturally.

Conversely, sites located in Florida, Georgia, Mississippi and Texas with statistically significant trends and non-negligible NSS Cl^- wet deposition flux saw an average increase in the mean annual NSS Cl^- deposition flux from -0.55 kg ha^{-1} between 1998-2001 to -0.19 kg ha^{-1} by 2016-2019. We propose that the increase in depleted NSS Cl^- deposition flux in the southeast is indicative of less mobilization of SS Cl^- occurring because of reduced SO_2 and NO_x emissions in

these regions. In these states, predictions from HCl emissions indicate that annual NSS Cl^- should have decreased by 5-15 g ha^{-1} yr^{-1}, when observations show they have increased by 2-13 g ha^{-1} yr^{-1}. This result suggests mechanisms other than direct HCl emissions changes are impacting the NSS Cl^- annual deposition pattern in this region, such as reduced mobilization of Cl^- from lower SO_2 and NO_x emissions. It is possible that the decrease in mobilized Cl^- from these regions is contributing in part to the decrease in excess Cl^- deposited in the Midwest, and mid-Atlantic state. Regardless of the exact mechanism for the decrease in the absolute value of NSS Cl^- wet deposition flux across the US, whether reductions in primary emission of anthropogenic HCl from industry sources, or reductions in primary emissions of SO_2 and NO_x promoting less Cl- mobilization are responsible, our conclusion that emissions control technologies have reduced the anthropogenic impact on the deposition of NSS Cl^- to the environment remains the same.

Ultimately, our results suggest that the tropospheric atmospheric Cl_y burden was distinctly larger over the US in the past than it is today, both from higher direct HCl emissions and perhaps, larger mobilization of sea salt Cl^-, to the degree that this trend is identifiable in NSS Cl^- deposition data across the US. Anthropogenic emissions of HCl are a factor of 20 lower today than they were in 1998. If 19% of HCl gets converted to reactive Cl_y (as estimated by Wang et al., (2019), this could result in an additional source of Cl_y of 45 Gg a^{-1} in 1998 than today, which could be significant on a local level. We hypothesize that emissions controls on the direct emission of HCl, SO_2, and NO_x are responsible for the changes presented here. A similar decrease in anthropogenic HCl emissions from coal burning (95%) in the U.K. has been shown to have resulted in a 66% decrease in deposition of NSS Cl^- (Evans et al., 2011). The degree to which reductions in direct anthropogenic HCl emissions verses how much NO_x and SO_2

reductions have impacted HNO_3, H_2SO_4, and N_2O_5 mobilization of sea salt Cl^-, have caused this decrease in the NSS Cl^- deposition and the implied Cl_y burden remain to be quantified. We hypothesize that year-round usage of emissions controls technologies may reduce the downwind transport of NOx and corresponding O_3 formation resulting from reduced Cl_y cycling, though the magnitude of these implied benefits remains to be assessed. Ultimately, our results suggest that anthropogenic activity emitting NO_x and Cl_y, and the subsequent multiphase reactions that result and impact the oxidant budget may have played an even larger role in the past than they do today.

4.5 REFERENCES

Abbatt, J. P. D., Lee, A. K. Y., and Thornton, J. A.: Quantifying trace gas uptake to tropospheric aerosol: recent advances and remaining challenges, Chem. Soc. Rev., 41, 6555–6581, https://doi.org/10.1039/C2CS35052A, 2012.

Andreae, M. O.: Emission of trace gases and aerosols from biomass burning – an updated assessment, Atmos. Chem. Phys., 19, 8523–8546, https://doi.org/10.5194/acp-19-8523-2019, 2019.

Atkinson, R.: Gas-Phase Tropospheric Chemistry of Volatile Organic Compounds: 1. Alkanes and Alkenes, J. Phys. Chem. Ref. Data, 26, 215–290, 1997.

Behnke, W., George, C., Scheer, V., and Zetzsch, C.: Production and decay of $ClNO_2$ from the reaction of gaseous N_2O_5 with NaCl solution: Bulk and aerosol experiments, J. Geophys. Res.-Atmos., 102, 3795–3804, https://doi.org/10.1029/96JD03057, 1997.

Butler, T. J., Likens, G. E., & Stunder, B. J. B. (2001). Regional-scale impacts of Phase I of the Clean Air Act Amendments in the USA: the relation between emissions and concentrations, both wet and dry. Atmospheric Environment, 35(6), 1015–1028. https://doi.org/https://doi.org/10.1016/S1352-2310(00)00386-1

Burkey, Jeff (2020). Mann-Kendall Tau-b with Sen's Method (enhanced) (https://www.mathworks.com/matlabcentral/fileexchange/11190-mann-kendall-tau-b-with-sen-s-method-enhanced), MATLAB Central File Exchange.

Chen, Q., Schmidt, J. A., Shah, V., Jaeglé, L., Sherwen, T., and Alexander, B.: Sulfate production by reactive bromine: Implications for the global sulfur and reactive bromine budgets, Geophys. Res. Lett., 44, 7069–7078, https://doi.org/10.1002/2017GL073812, 2017.

Denby, B. R., Ketzel, M., Ellermann, T., Stojiljkovic, A., Kupiainen, K., Niemi, J. V, … Sundvor, I. (2016). Road salt emissions: A comparison of measurements and modelling using the NORTRIP road dust emission model. Atmospheric Environment, 141, 508–522. *https://doi.org/https://doi.org/10.1016/j.atmosenv.2016.07.027*

Erickson, D. J., Seuzaret, C., Keene, W. C., & Gong, S. L. (1999). A general circulation model-based calculation of HCl and ClNO2 production from sea salt dechlorination: Reactive Chlorine Emissions Inventory. Journal of Geophysical Research: Atmospheres, 104(D7), 8347–8372. https://doi.org/10.1029/98JD01384

Evans, C. D., Monteith, D. T., Fowler, D., Cape, J. N., & Brayshaw, S. (2011). Hydrochloric Acid: An Overlooked Driver of Environmental Change. Environmental Science & Technology, 45(5), 1887–1894. https://doi.org/10.1021/es103574u

Fedkin, N. M., Li, C., Dickerson, R. R., Canty, T., & Krotkov, N. A. (2019). Linking improvements in sulfur dioxide emissions to decreasing sulfate wet deposition by combining satellite and surface observations with trajectory analysis. *Atmospheric Environment*, *199*, 210–223. https://doi.org/https://doi.org/10.1016/j.atmosenv.2018.11.039

Fickert, S., Adams, J. W., and Crowley, J. N.: Activation of Br_2 and BrCl via uptake of HOBr

onto aqueous salt solutions, J. Geophys. Res.-Atmos., 104, 23719–23727, https://doi.org/10.1029/1999JD900359, 1999.

Finlayson-Pitts, B. J.: The Tropospheric Chemistry of Sea Salt: A Molecular-Level View of the Chemistry of NaCl and NaBr, Chem. Rev., 103, 4801–4822, https://doi.org/10.1021/cr020653t, 2003.

Finley, B. D., and E. S. Saltzman (2006), Measurement of Cl_2 in coastal urban air, *Geophys. Res. Lett.*, **33**, L11809, doi:10.1029/2006GL025799.

Giang, A., & Selin, N. E. (2016). Benefits of mercury controls for the United States. Proceedings of the National Academy of Sciences, 113(2), 286 LP – 291. https://doi.org/10.1073/pnas.1514395113

Graedel, T. E., & Keene, W. C. (1995). Tropospheric budget of reactive chlorine. Global Biogeochemical Cycles, 9(1), 47–77. https://doi.org/10.1029/94GB03103

Guo H, Weber RJ, Nenes A. High levels of ammonia do not raise fine particle pH sufficiently to yield nitrogen oxide-dominated sulfate production. *Sci Rep*. 2017;7(1):12109. Published 2017 Sep 21. doi:10.1038/s41598-017-11704-0

Haskins, J. D., Jaeglé, L., Shah, V., Lee, B. H., Lopez-Hilfiker, F. D., Campuzano-Jost, P., Schroder, J. C., Day, D. A., Guo, H., Sullivan, A. P., Weber, R., Dibb, J., Campos, T., Jimenez, J. L., Brown, S. S., and Thornton, J. A.: Wintertime Gas-Particle Partitioning and Speciation of Inorganic Chlorine in the Lower Troposphere Over the Northeast United States and Coastal Ocean, J. Geophys. Res.-Atmos., 123, 12897–12916, https://doi.org/10.1029/2018JD028786, 2018.

Haskins, J. D., Lopez-Hilfiker, F. D., Lee, B. H., Shah, V., Wolfe, G. M., DiGangi, J., … Thornton, J. A. (2019). Anthropogenic Control Over Wintertime Oxidation of Atmospheric Pollutants. Geophysical Research Letters, 46(24), 14826–14835. https://doi.org/10.1029/2019GL085498

He, H., Stehr, J. W., Hains, J. C., Krask, D. J., Doddridge, B. G., Vinnikov, K. Y., Canty, T. P., Hosley, K. M., Salawitch, R. J., Worden, H. M., and Dickerson, R. R.: Trends in emissions and concentrations of air pollutants in the lower troposphere in the Baltimore/Washington airshed from 1997 to 2011, Atmos. Chem. Phys., 13, 7859–7874, https://doi.org/10.5194/acp-13-7859-2013, 2013.

Hoffmann, E. H., Tilgner, A., Schrödner, R., Bräuer, P., Wolke, R., and Herrmann, H.: An advanced modeling study on the impacts and atmospheric implications of multiphase dimethyl sulfide chemistry, P. Natl. Acad. Sci. USA, 113, 11776–11781, https://doi.org/10.1073/pnas.1606320113, 2016.

Horowitz, H. M., Jacob, D. J., Zhang, Y., Dibble, T. S., Slemr, F., Amos, H. M., Schmidt, J. A., Corbitt, E. S., Marais, E. A., and Sunderland, E. M.: A new mechanism for atmospheric mercury redox chemistry: implications for the global mercury budget, Atmos. Chem. Phys., 17, 6353–6371, https://doi.org/10.5194/acp-17-6353-2017, 2017.

Hossaini, R., Chipperfield, M. P., Saiz-Lopez, A., Fernandez, R., Monks, S., Feng, W., Brauer, P., and von Glasow, R.: A global model of tropospheric chlorine chemistry: Organic

versus inorganic sources and impact on methane oxidation, J. Geophys. Res.-Atmos., 121, 14271-14297, https://doi.org/10.1002/2016JD025756, 2016.

Jaeglé, L., Quinn, P. K., Bates, T. S., Alexander, B., and Lin, J.-T.: Global distribution of sea salt aerosols: new constraints from in situ and remote sensing observations, Atmos. Chem. Phys., 11, 3137–3157, https://doi.org/10.5194/acp-11-3137-2011, 2011.

Johnke, B., Hoppaus R., Lee, E., Irving, B., Martinsen, T., & Mareckova, K. (2000). Emissions from Waste Incineration. Good Practice Guidance and Uncertainty Management in National Greenhouse Gas Inventories. *International Panel on Climate Change*. Montreal. Retrieved from: https://www.ipcc-nggip.iges.or.jp/public/gp/english/

Keene, W. C., Pszenny, A. A. P., Galloway, J. N., and Hawley, M. E. (1986), Sea-salt corrections and interpretation of constituent ratios in marine precipitation, J. Geophys. Res., 91(D6), 6647– 6658, doi:10.1029/JD091iD06p06647.

Keene, W. C., Aslam, @bullet M, Khalil, K., Erickson Iii, D. J., Mcculloch, A., Graedel, T. E., … @bullet, L. (1999). Composite global emissions of reactive chlorine from anthropogenic and natural sources: Reactive Chlorine Emissions Inventory. JOURNAL OF GEOPHYSICAL RESEARCH, 104(20), 8429–8440. https://doi.org/10.1029/1998JD100084

Kercher, J. P., T. P. Riedel, and J. A. Thornton (2009), Chlorine activation by N_2O_5: Simultaneous, in situ detection of $ClNO_2$ and N_2O_5 by chemical ionization mass spectrometry, Atmos. Meas. Tech., 2(1), 193– 204, doi:10.5194/amt-2-193-2009.

Kolesar, K. R., Mattson, C. N., Peterson, P. K., May, N. W., Prendergast, R. K., and Pratt, K. A.: Increases in wintertime $PM_{2.5}$ sodium and chloride linked to snowfall and road salt application, Atmos. Environ., 177, 195–202, https://doi.org/10.1016/j.atmosenv.2018.01.008, 2018.

Lajtha, K., Jones, J. Trends in cation, nitrogen, sulfate and hydrogen ion concentrations in precipitation in the United States and Europe from 1978 to 2010: a new look at an old problem. Biogeochemistry 116, 303–334 (2013). https://doi.org/10.1007/s10533-013-9860-2

Lamb, D., & Bowersox, V. (2000). The national atmospheric deposition program: An overview. Atmospheric Environment, 34, 1661–1663.

Lawler, M. J., R. Sander, L. J. Carpenter, J. D. Lee, R. von Glasow, R. Sommariva, and E. S. Saltzman (2011), HOCl and Cl_2 observations in marine air, Atmos. Chem. Phys., 11(15), 7,617– 7,628, doi:10.5194/acp-11-7617-2011.

Lee, C. W., Srivastava, R. K., Ghorishi, S. B., Hastings, T. W., & Stevens, F. M. (2004). Investigation of selective catalytic reduction impact on mercury speciation under simulated N [O.sub.x] emission control conditions. Journal of the Air & Waste Management Association, 54(12), 1560+.

Lee, B. H., Lopez-Hilfiker, F. D., Schroder, J. C., Campuzano-Jost, P., Jimenez, J. L., McDuffie, E. E., Fibiger, D. L., Veres, P. R., Brown, S. S., Campos, T. L., Weinheimer, A. J., Flocke, F. F., Norris, G., O'Mara, K., Green, J. R., Fiddler, M. N., Bililign, S., Shah, V.,

Jaeglé, L., and Thornton, J. A.: Airborne Observations of Reactive Inorganic Chlorine and Bromine Species in the Exhaust of Coal-Fired Power Plants, J. Geophys. Res.-Atmos., 123, 11225–11237, https://doi.org/10.1029/2018jd029284, 2018.

Lehmann, C.M.B., Bowersox, V.C., Larson, R.S. et al. Monitoring Long-term Trends in Sulfate and Ammonium in US Precipitation: Results from the National Atmospheric Deposition Program/National Trends Network. Water Air Soil Pollution: Focus 7, 59–66 (2007). https://doi.org/10.1007/s11267-006-9100-z

Lobert, J. M., Keene, W. C., Logan, J. A., and Yevich, R. (1999), Global chlorine emissions from biomass burning: Reactive Chlorine Emissions Inventory, J. Geophys. Res., 104(D7), 8373– 8389, doi:10.1029/1998JD100077.

Marchetto, A., Rogora, M., & Arisci, S. (2013). Trend analysis of atmospheric deposition data: A comparison of statistical approaches. Atmospheric Environment, 64, 95–102. https://doi.org/https://doi.org/10.1016/j.atmosenv.2012.08.020

Massucci, M., Clegg, S. L., and Brimblecombe, P.: Equilibrium Partial Pressures, Thermodynamic Properties of Aqueous and Solid Phases, and Cl_2 Production from Aqueous HCl and HNO_3 and Their Mixtures, J. Phys. Chem. A, 103, 4209–4226, https://doi.org/10.1021/jp9847179, 1999.

McCulloch, A., Aucott, M. L., Benkovitz, C. M., Graedel, T. E., Kleiman, G., Midgley, P. M., and Li, Y.-F. (1999), Global emissions of hydrogen chloride and chloromethane from coal combustion, incineration and industrial activities: Reactive Chlorine Emissions Inventory, J. Geophys. Res., 104(D7), 8391– 8403, doi:10.1029/1999JD900025.

National Atmospheric Deposition Program (2016). NADP Network Quality Assurance Plan. v.1.8 Retrieved from: nadp.slh.wisc.edu/lib/qaplans/NADP_Network_Quality_Assurance_Plan.pdf

Osthoff, H. D., et al. (2008), High levels of nitryl chloride in the polluted subtropical marine boundary layer, Nat. Geosci., 1(5), 324– 328, doi:10.1038/ngeo177.

Paulot, F., Fan, S., and Horowitz, L. W. (2017), Contrasting seasonal responses of sulfate aerosols to declining SO2 emissions in the Eastern U.S.: Implications for the efficacy of SO2 emission controls, Geophys. Res. Lett., 44, 455– 464, doi:10.1002/2016GL070695.

Pszenny, A. A. P., W. C. Keene, D. J. Jacob, S. Fan, J. R. Maben, M. P. Zetwo, M. Springer-Young, and J. N. Galloway (1993), Evidence of inorganic chlorine gases other than hydrogen chloride in marine surface air, Geophys. Res. Lett., 20(8), 699– 702, doi:10.1029/93GL00047.

Riedel, T. P., Wolfe, G. M., Danas, K. T., Gilman, J. B., Kuster, W. C., Bon, D. M., Vlasenko, A., Li, S.-M., Williams, E. J., Lerner, B. M., Veres, P. R., Roberts, J. M., Holloway, J. S., Lefer, B., Brown, S. S., and Thornton, J. A.: An MCM modeling study of nitryl chloride ($ClNO_2$) impacts on oxidation, ozone production and nitrogen oxide partitioning in polluted continental outflow, Atmos. Chem. Phys., 14, 3789–3800, https://doi.org/10.5194/acp-14-3789-2014, 2014.

Saiz-Lopez, A. and von Glasow, R.: Reactive halogen chemistry in the troposphere, Chem. Soc.

Rev., 41, 6448–6472, https://doi.org/10.1039/c2cs35208g, 2012

Sarwar, G., Simon, H., Bhave, P., and Yarwood, G.: Examining the impact of heterogeneous nitryl chloride production on air quality across the United States, Atmos. Chem. Phys., 12, 6455–6473, https://doi.org/10.5194/acp-12-6455-2012, 2012.

Schmidt, J. A., Jacob, D. J., Horowitz, H. M., Hu, L., Sherwen, T., Evans, M. J., Liang, Q., Suleiman, R. M., Oram, D. E., Le Breton, M., Percival, C. J., Wang, S., Dix, B., and Volkamer, R.: Modeling the observed tropospheric BrO background: Importance of multiphase chemistry and implications for ozone, OH, and mercury, J. Geophys. Res.-Atmos., 121, 11819–11835, https://doi.org/10.1002/2015jd024229, 2016.

Sherwen, T., Schmidt, J. A., Evans, M. J., Carpenter, L. J., Großmann, K., Eastham, S. D., Jacob, D. J., Dix, B., Koenig, T. K., Sinreich, R., Ortega, I., Volkamer, R., Saiz-Lopez, A., Prados-Roman, C., Mahajan, A. S., and Ordóñez, C.: Global impacts of tropospheric halogens (Cl, Br, I) on oxidants and composition in GEOS-Chem, Atmos. Chem. Phys., 16, 12239–12271, https://doi.org/10.5194/acp-16-12239-2016, 2016.

Simpson, W. R., Brown, S. S., Saiz-Lopez, A., Thornton, J. A., & Von Glasow, R. (2015). Tropospheric Halogen Chemistry: Sources, Cycling, and Impacts. Chemical Reviews, 115(10), 4035–4062. https://doi.org/10.1021/cr5006638

Thornton, J. A., Kercher, J. P., Riedel, T. P., Wagner, N. L., Cozic, J., Holloway, J. S., Dubé, W. P., Wolfe, G. M., Quinn, P. K., Middlebrook, A. M., Alexander, B., and Brown, S. S.: A large atomic chlorine source inferred from mid-continental reactive nitrogen chemistry, Nature, 464, 271–274, https://doi.org/10.1038/nature08905, 2010.

US Energy Information Administration (2019). Existing Electric Generating Units in the United States (EIA 860M). Retrieved from: https://www.eia.gov/electricity/data/eia860m/

US Energy Information Administration (2002). Inventory of Electric Utility Power Plants in the United States 2000. Retrieved from: https://www.eia.gov/electricity/archive/009500.pdf

US Environmental Protection Agency (2018). Inventory of U.S. Greenhouse Gas Emissions and Sinks: 1990-2018 (EPA-HQ-OAR-2019-0706). Retrieved from: https://www.epa.gov/ghgemissions/inventory-us-greenhouse-gas-emissions-and-sinks

US Environmental Protection Agency. (2018). TRI Explorer (2018 National Analysis Dataset (released November 12, 2019)) [Internet database] for All Industry Air Releases of Hydrochloric Acid (after 1995 and after "Acid Aerosols" only). Retrieved from: https://enviro.epa.gov/triexplorer/).

US Environmental Protection Agency. (2014). 2014 National Emissions Inventory, available at: https://www.epa.gov/air-emissions-inventories/2014-national-emissions-inventory-nei-data.

Wang, X., Jacob, D. J., Eastham, S. D., Sulprizio, M. P., Zhu, L., Chen, Q., Alexander, B., Sherwen, T., Evans, M. J., Lee, B. H., Haskins, J. D., Lopez-Hilfiker, F. D., Thornton, J. A., Huey, G. L., and Liao, H.: The role of chlorine in global tropospheric chemistry, Atmos. Chem. Phys., 19, 3981–4003, https://doi.org/10.5194/acp-19-3981-2019, 2019

Weber, R., Guo, H., Russell, A. et al. High aerosol acidity despite declining atmospheric sulfate

concentrations over the past 15 years. Nature Geosci 9, 282–285 (2016). https://doi-org.offcampus.lib.washington.edu/10.1038/ngeo2665

4.6 FIGURES

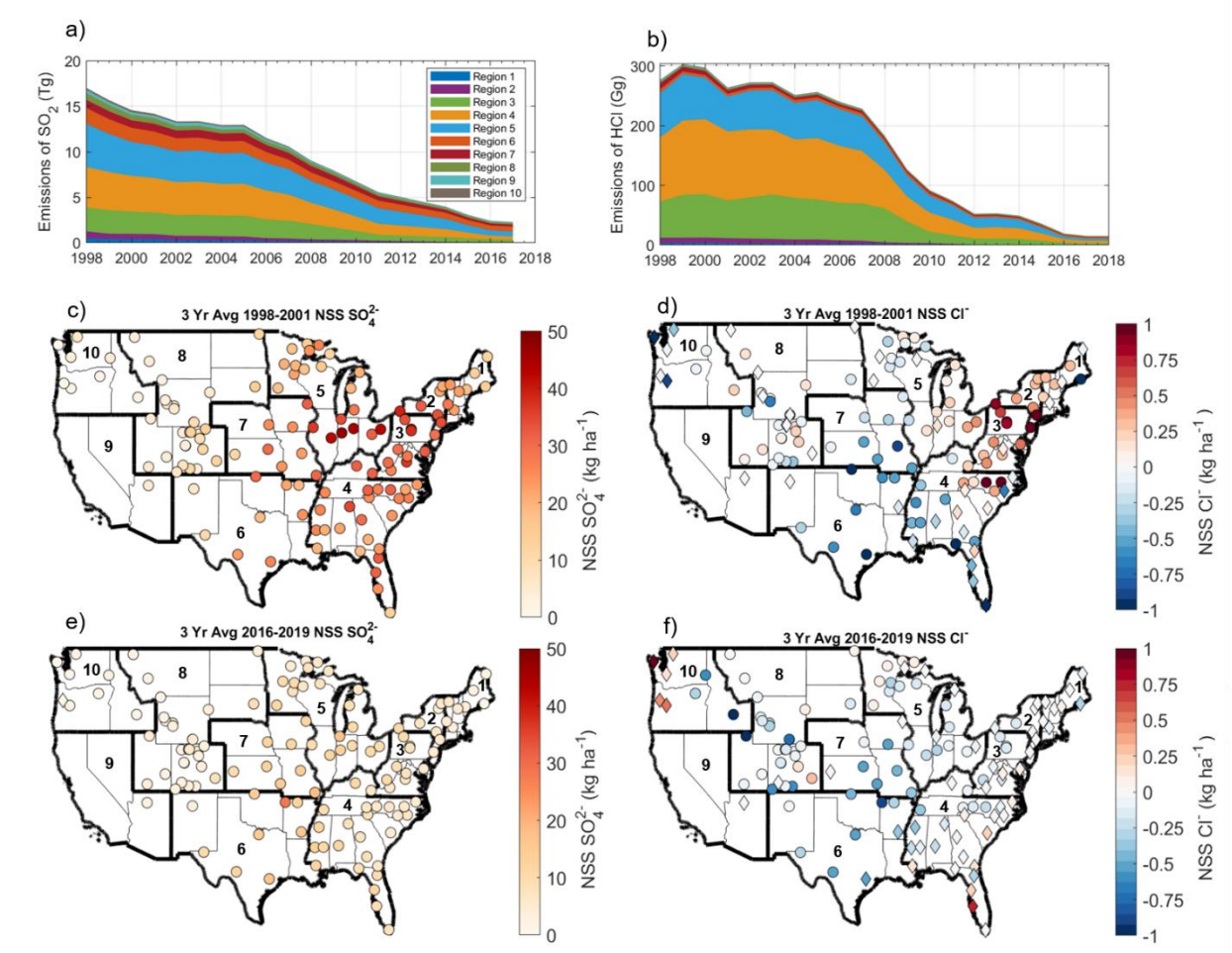

Figure 4.1 Changes in HCl emissions and NSS Cl^- deposition

Changes in anthropogenic SO_2 emissions (a) and HCl emissions (b) by EPA regions for 1998-2018 compared to the precipitation weighted, three-year annual average of the weekly NADP observations of NSS SO_4^{2-}(c,e) and NSS Cl^- deposition (d,f) for 1998-2001 (middle row) and 2016-2019 (bottom row) at 128 sites. Dark outlines show the EPA regions, which are labeled numerically. Circles indicate sites where the 3-year mean absolute value of NSS component exceeds 5% of that period's 3-year mean in either the total SO_4^{2-} or Cl^- and diamonds show sites where the 3-year mean absolute value of NSS component is less than 5% of that period's 3-year mean in either the total SO_4^{2-} or Cl^-.

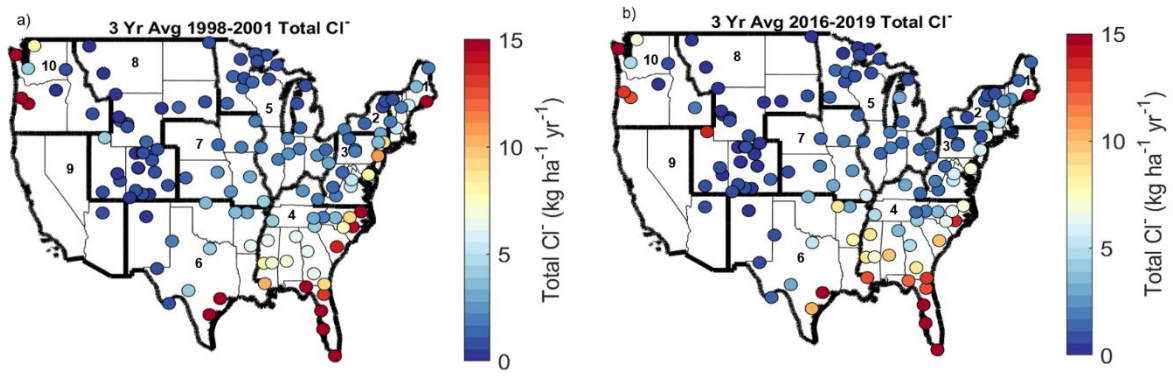

Figure 4.2 Total Cl^- Deposition

Figure showing the 3 year mean Total Cl^- wet deposition flux at the 128 sites analyzed from 1998-2001 (a) and between 2016-2019 (b). EPA regions are shown as dark outlines and are numerically labeled.

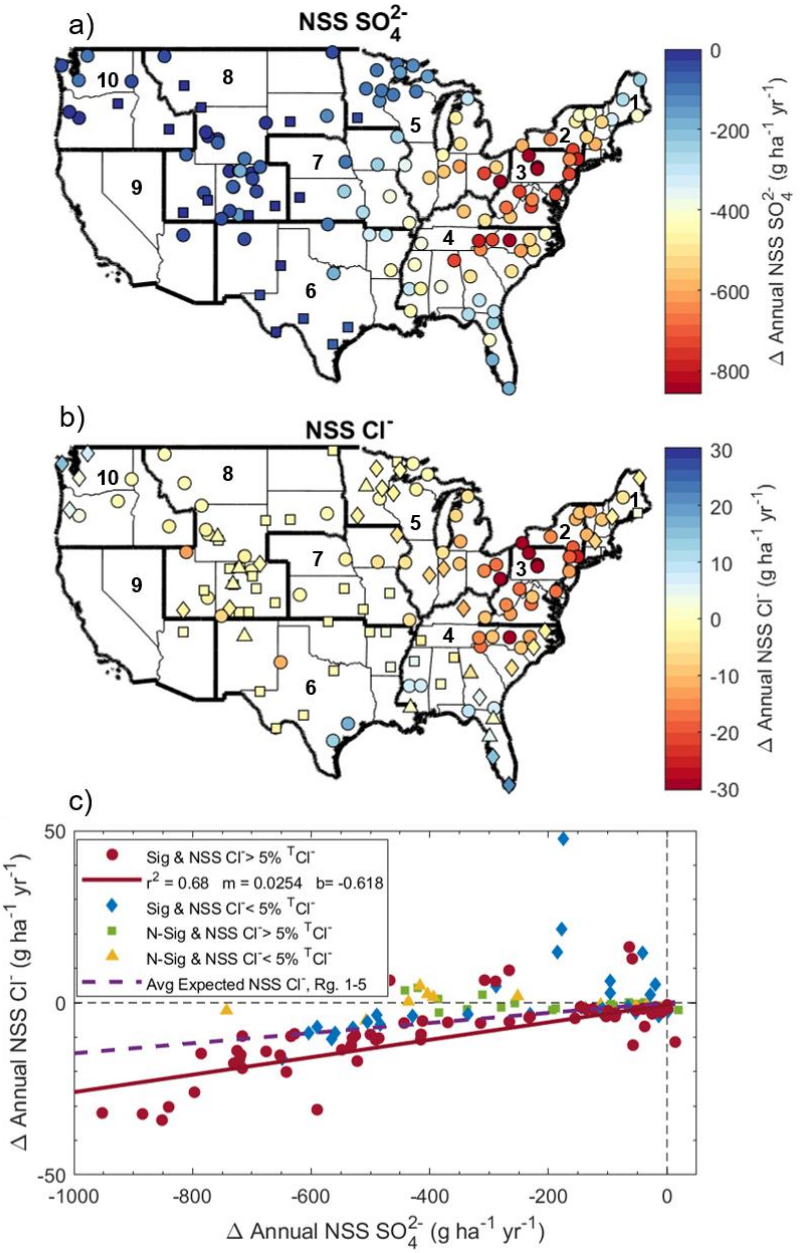

Figure 4.3 Sen's Slopes in NSS Cl^- and SO_4^{2-}

Maps of the calculated Sen's slopes at 128 NADP stations for the period 1998-2019 in NSS SO_4^{2-} (a) and NSS Cl^- (b). Dark outlines show the EPA regions, which are labeled numerically. Shapes indicate whether absolute value of the 3-year mean NSS SO_4^{2-} (a) or NSS Cl^- (b, c) is >5% of the 3-year mean, Total SO_4^{2-} or Cl^- from 1998-2001, whether the calculated Sen's slope in NSS SO_4^{2-} (a) or NSS Cl^- (b, c) is statistically significant or not at the 90% level. A scatter plot of the data in (a) vs (b) is shown in panel (c) with a weighted linear least squares fit (red line) to the data with statistically significant Sen's slopes in NSS Cl^- and with a 3-year mean NSS Cl^- greater than 5% of the 3-year mean Total Cl^- from 1998-2003 (red circles), using the calculated standard error in the Sen's slopes for NSS Cl^- and NSS SO_4^2. The expected NSS Cl^- decrease from the average HCl:SO_2 emissions factor in EPA regions 1-5 is shown as a purple line.

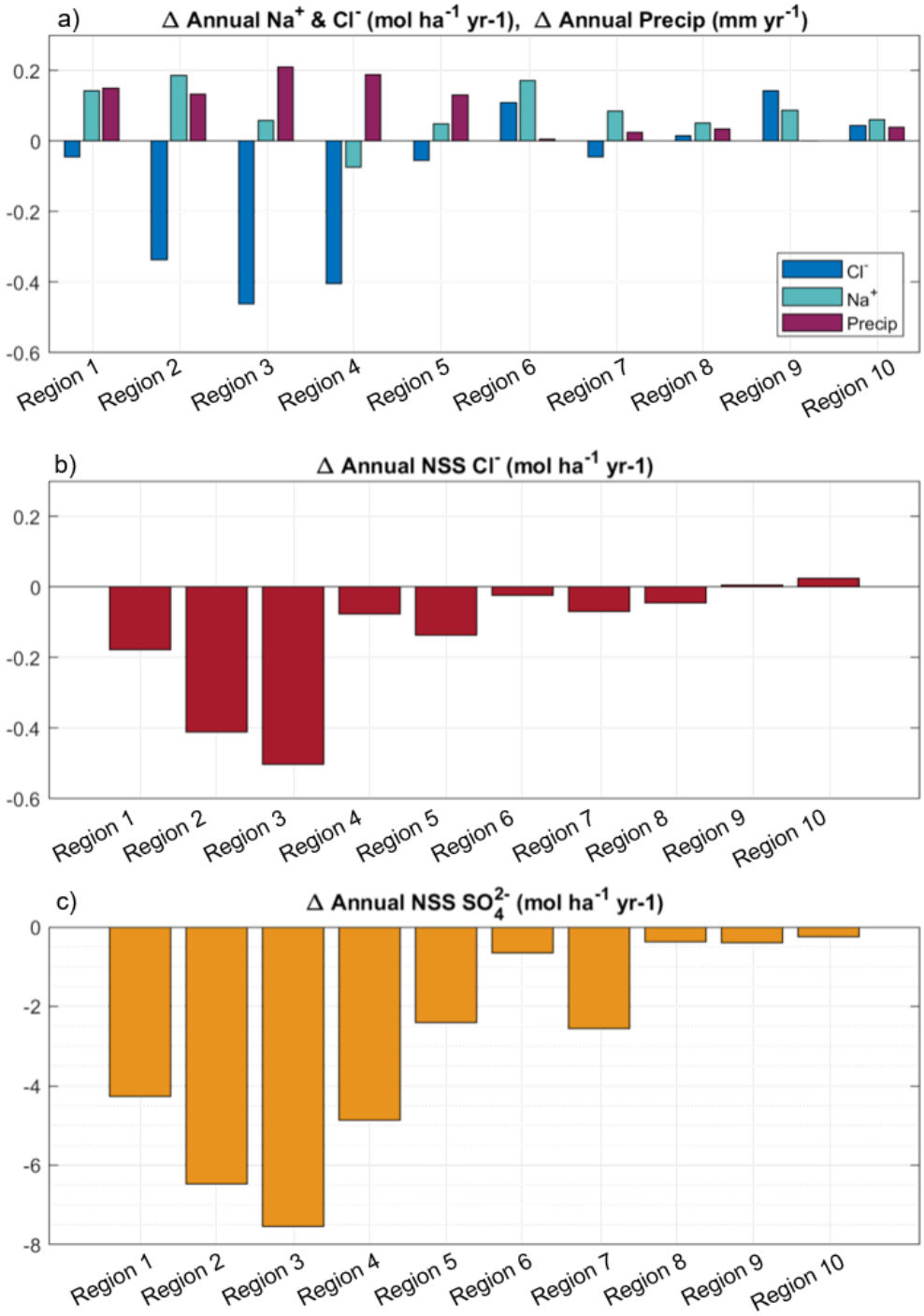

Figure 4.4 Regional Changes in Na^+, Cl^- and Precipitation

Figure comparing the median change in the annual deposition flux of Na^+, Cl^- precipitation, (a), NSS Cl^- (b), and NSS SO_4^{2-} (c) at all 128 sites where data was analyzed subdivided by EPA region.

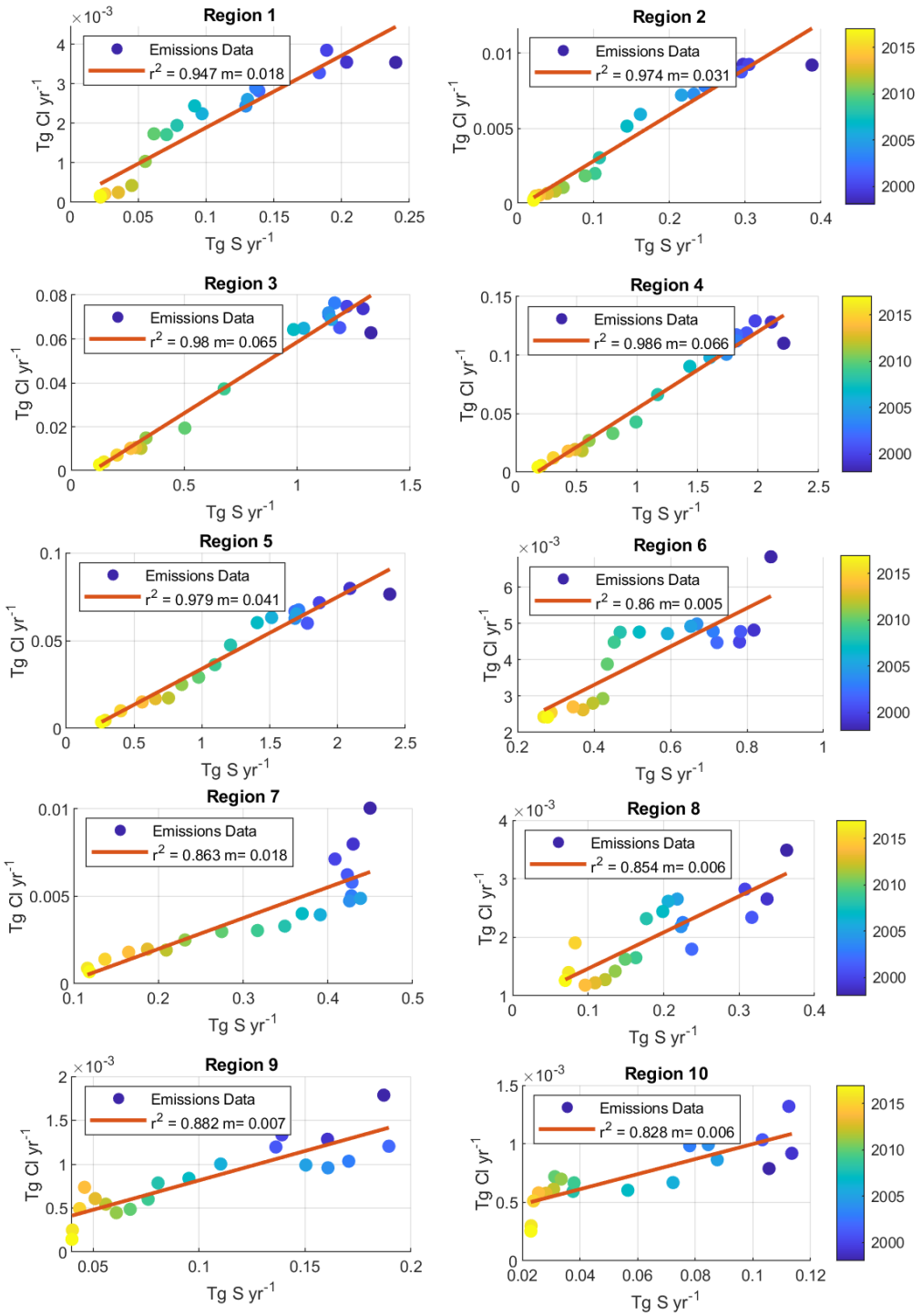

Figure 4.5 Determining Regional Emissions Factors

Scatter plots showing the emission of Cl from anthropogenic HCl against the emission of S from anthropogenic SO_2 on a yearly basis (colors) from Jan. 1, 1998- Dec. 31, 2017 in each EPA region. The emissions factor (slope) used in each region is displayed with the correlation coefficient.

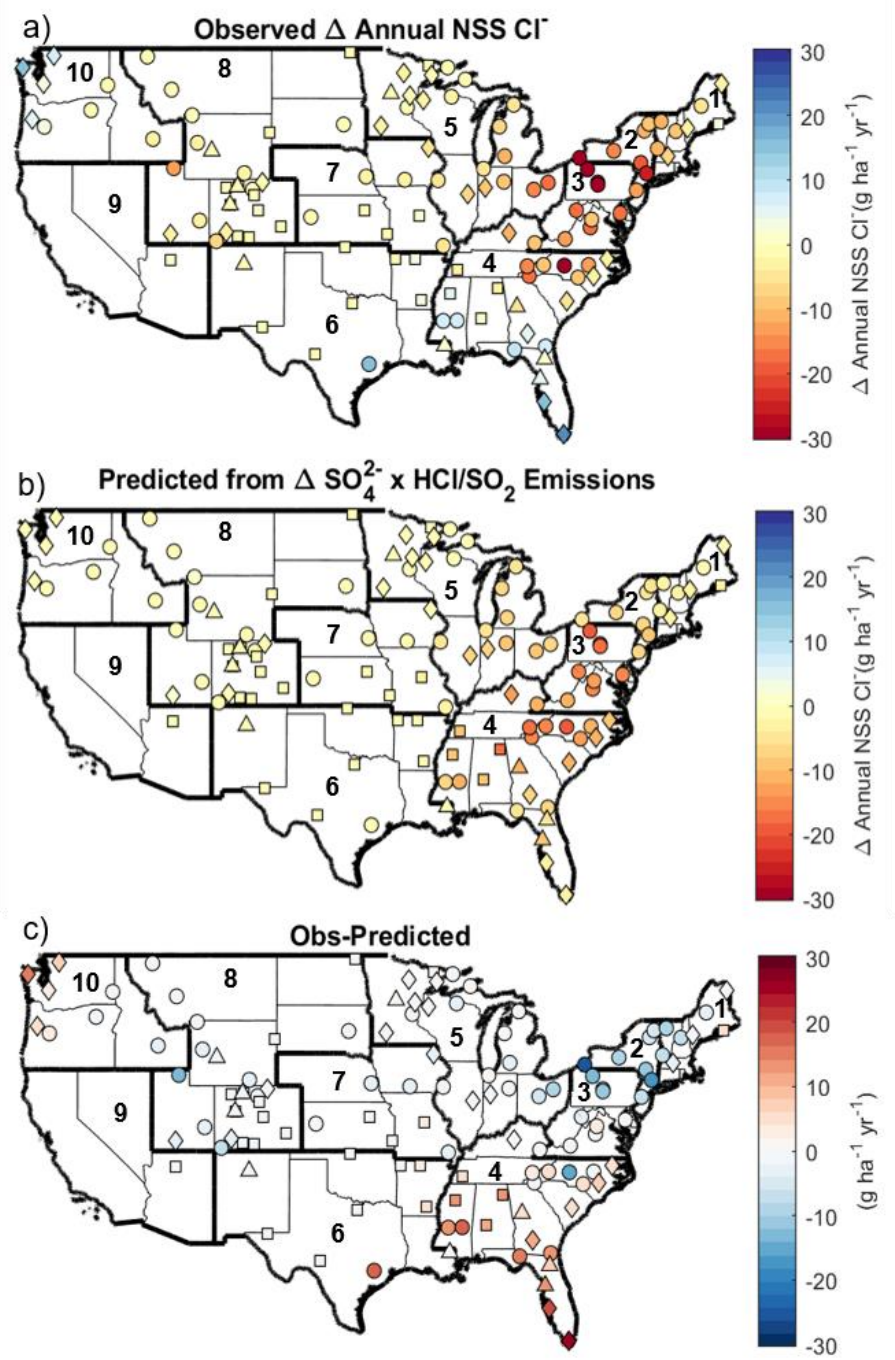

Figure 4.8 Predicted Changes in NSS Cl^- from HCl Emissions

The change in (a) the observed annual NSS Cl^- deposition flux from Figure 4.3b compared to (b) the predicted change in NSS Cl^- deposition calculated from multiplying the observed annual NSS SO_4^{2-} deposition flux in Figure 4.3a by a regional emissions factor of Cl/S, and (c) the difference between them for the period Jan 1. 1998- Dec. 31 2017 (since NEI SO_2 emissions data is not available after this date). EPA regions are shown as dark outlines and are labeled numerically.

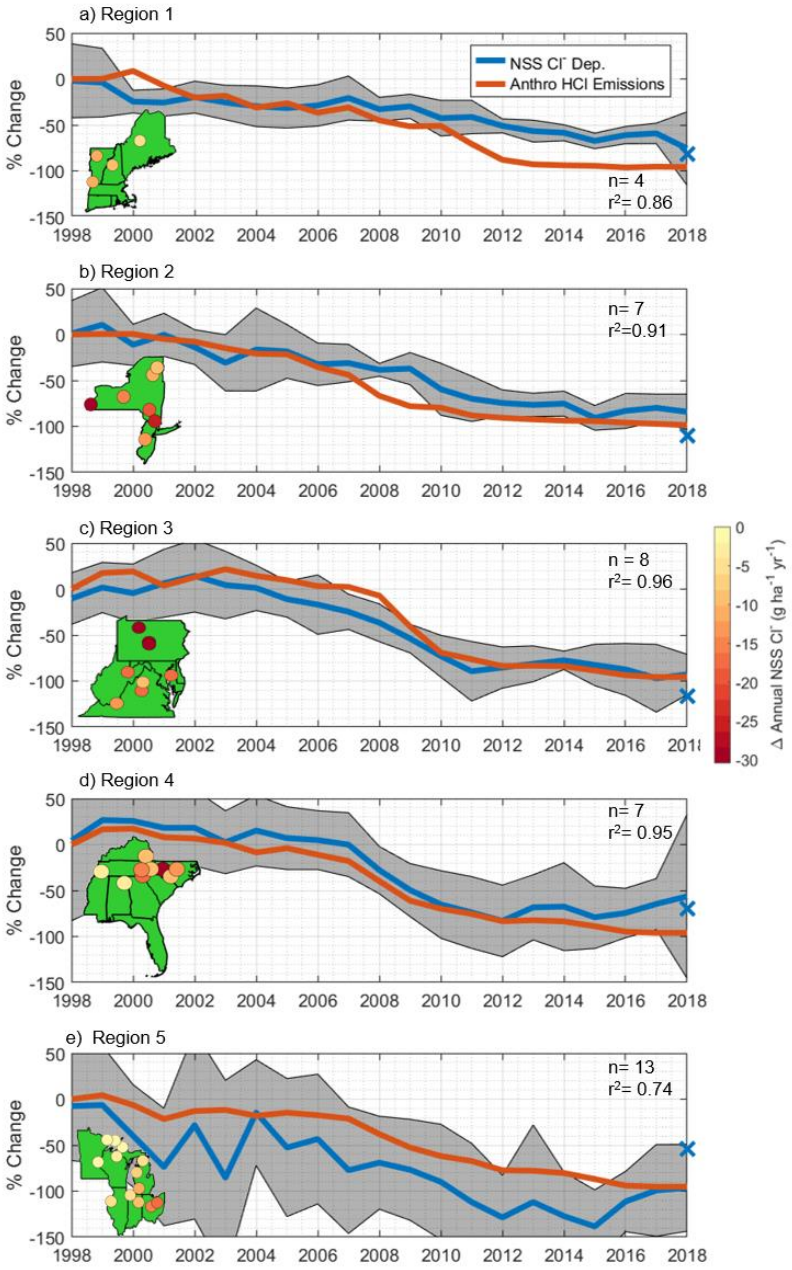

Figure 4.11 Temporal Correlation in HCl Emissions & NSS Cl^- deposition

Percent decrease in anthropogenic HCl emissions (orange line) and NSS Cl^- deposition (blue line) relative to 1998 for EPA regions 1-5. We only consider deposition data from NADP sites with statistically significant, negative Sen's slopes and non-negligible NSS Cl^- between 1998-2003. Included sites and the corresponding change in their annual NSS Cl^- between 1998-2019 from Figure 4.3 on the same color axis, are shown as inlays. The NSS Cl^- deposition trends are calculated by taking the 3-year running time average and standard deviation centered around each year at each site, and then taking the median trend of all sites included. The median of all sites' individual change magnitudes as percentage of mean in wet deposition flux of NSS Cl^-, calculated from the Sen's slopes, is shown as a blue 'X' at 2018.

Chapter 5

Conclusions

When I began graduate school, the number of tropospheric observations of chlorine containing species was extremely limited, and of the existing global chemistry climate models, very few included tropospheric chlorine chemistry (CMAQ, ECHAM-Messy) (Sarwar et al., 2007; Wetzel et al., 2012). Existing observations were largely taken at ground and ship-based platforms over short time periods, often in the summer, when the impacts of chlorine chemistry were expected to be more muted than they would be in the winter. Yet, the WINTER campaign took place only 6 months after I began graduate school, and peaked my interest when I learned that $ClNO_2$ could shift the downwind impact on anthropogenic emissions from net ozone destroying to net ozone producing (Yienger et al., 1999). Chemical mechanisms like the production of Cl_2 from the uptake of $ClNO_2$ on acidic aerosols had been suggested to be important in the atmosphere from laboratory measurements but had never been verified by observations in the atmosphere (Roberts et al., 2008; Roberts et al., 2009). The degree to which global models with existing aerosol partitioning models could correctly simulate the acid displacement of HCl and pCl^- had never been verified using observations, posing questions like whether or not implementing laboratory parameterizations of the production of $ClNO_2$, which rely on pCl^-, would even be realistic. Although emissions inventories of anthropogenic HCl emissions existed (Keene et al., 1999), there were few observations to verify their continued efficacy. The observations necessary to test proposed mechanisms and constrain global models' representations of chlorine chemistry did not

yet exist in the season where their impacts were expected to be largest.

During my time at UW, I have been fortunate enough to contribute to the advance of knowledge on all these subjects. During my master's degree, I was able to publish work on the abundance of HOCl, HCl, $ClNO_2$, Cl_2 and pCl^- over the eastern United States, contrasting differences in their concentrations over land and over the ocean, and during the day and night, observations which represented the broadest collection of many of these species, at the time (Haskins et al., 2018). These observations were used to constrain the new GEOS-Chem Halogen mechanism in Wang et al., (2019), on which I was a coauthor.

5.1 Summary of Results

Using data from the most expansive data set of inorganic chlorine compounds taken to date from the 2015 WINTER aircraft campaign, the contribution of various oxidants, including Cl atoms from $ClNO_2$ photolysis, on a regional basis during winter is quantified in this work, enabling improved chemical descriptions of wintertime air pollution transformations. $ClNO_2$ concentrations during the WINTER campaign were observationally confirmed to reach upwards of 2.5 ppbv in the polluted marine boundary layer. Several flights which took place as the sun rose, showed that Cl atoms from direct $ClNO_2$ photolysis are both the dominant early morning radical source and the dominant integrated daily radical source, observationally confirming what was only a hypothesis before this analysis (Riedel et al., 2014). The F0AM box model simulations I did showed that the impact of Cl atoms on the oxidant budget is not only primary but also plays an important secondary role amplifying OH production through increased HCHO formation from VOC + Cl reactions (+0.62 ppbv), and increased O_3 production (+4.7 ppbv), which we able to quantify for the first time using observations during winter. Together,

multiphase reactions between gas-phase NO_x reservoirs and chlorine containing aerosol particles are shown to control greater than 70% of the oxidizing capacity of polluted air during winter. This analysis underscores the role that tropospheric chlorine cycling plays in amplifying of the impact of anthropogenic emissions and demonstrates that including $ClNO_2$ formation and Cl atom cycling connecting O_3 and VOC oxidation by Cl atoms is paramount for correctly representing the oxidant budget in polluted marine areas during winter.

It was found that HCHO was the largest radical source on a regional basis over land, with implications that HCHO sources are dominated by local or regional anthropogenic contributions, either through direct emissions and/or emissions of short-lived precursors, such as primary alkenes. This was a somewhat surprising result considering that previous studies in summer show that biogenic HCHO sources typically dominate (Wofle et al., 2016). This result underscores the importance of including correct anthropogenic emissions of HCHO and of VOC in global models, which often result in secondary HCHO formation after oxidation. If models simulate the impact of biogenic VOC alone, especially during winter, these results imply underestimates in OH will be persistent over land, especially.

Furthermore, I showed that the dominant sources of these the commonly considered radical precursors in polluted wintertime air arise largely from local and regional anthropogenic emissions, as opposed to background ozone. Incorporating these sources into a chemical transport model increased predicted $PM_{2.5}$ and export of NO_x to the remote troposphere via PAN, where greenhouse gases such as O_3 and CH_4 are far more sensitive to its presence [Hudman et al., 2004]. Other regions of the world, such as China, Europe, and northern India also experience elevated VOC concentrations from inefficient combustion and high NO_x during winter which may mix with reactive chlorine, especially near coasts or chlorine emissions from coal

combustion [Sarwar et al., 2014; Lowe et al., 2015; Li et al., 2016]. These findings suggest important global-scale revisions to our understanding of wintertime pollution transformations, transport, and multiphase processes and motivate further work to more broadly explore the types of VOC and associated Cl, OH, O_3, and NO_3 reactivity present in polluted wintertime environments.

Given the abundance of $ClNO_2$ within the polluted marine boundary layer, I used observations from the 2015 WINTER aircraft campaign in a chemical box model to constrain a laboratory-based mechanism of chlorine gas (Cl_2) production from $ClNO_2$ reaction in acidic particles. Because of the potential of this mechanism to double the Cl atom concentration, shown to have such a large impact on the oxidant budget in polluted marine regions, verifying the degree to which this mechanism occurs in the atmosphere was paramount to understanding the full impact of chlorine compounds in the troposphere. To reproduce Cl_2 concentrations observed during WINTER, the model required the $ClNO_2$ reaction probability to be more than an order of magnitude lower than those determined in previous laboratory experiments on acidic surfaces, even when calculated particle pH is ≤2. It is the availability of Cl^- and particle volume which limit the efficiency of the reaction in the atmosphere, compared to the laboratory. However, this mechanism can still be responsible for the nocturnal formation of 10–20 pptv of Cl_2 in polluted regions, yielding an atmospherically relevant concentration of Cl atoms the following morning.

The analysis done in Chapter 4, showing that significant decreases in NSS Cl^- deposition particularly within the Midwest, suggests that by 2015 when the WINTER campaign took place, the total Cl_y budget was lower than it was in the past. Global model simulations by Wang et al., (2019) recently showed that SSA Cl^- provided a Cl* source of 12 Tg Cl yr^{-1} in 2016, which was much higher than previous estimates of 5.6 Tg Cl yr−1 (Hossaini et al., 2016) and 6.1 Tg Cl yr^{-1}

(Schmidt et al., 2016), even neglecting anthropogenic HCl concentrations (given their small contribution to total Cl_y by the model run year of 2016). These results suggest that this number may have been even higher in the past over the US when HNO_3 and H_2SO_4 production was larger and when anthropogenic HCl concentrations were a more significant inland source of Cl_y.

5.2 Recommendations For Future Research Directions

5.2.1 *Implications for more impacts of Cly chemistry in the past over the US*

The degree to which increased Cl_y from either increased anthropogenic HCl emissions or increased mobilization from higher NO_x and SO_2 in the US in the past impacted the past oxidant budget, downwind O_3 formation, methane and VOC oxidation, dimethyl sulfide and mercury concentrations remains to be assessed. Given the conclusion in Chapter 2, that Cl atoms can be the dominant early morning oxidant in winter in select polluted coastal regions as recently as 2015, the results in Chapter 4 suggest that the impact of tropospheric halogens may have played an even larger role in the past on air quality and climate. Perhaps more relevant to the future, as China continues to implement NO_x and SO_2 control technologies across industries (Zhao et al., 2019), researchers interested in prescribing policy best suited to mitigate ozone formation should be cognizant of the benefits of utilizing emissions control technologies even during winter, to reduce the impacts of Cl_y amplifying the downwind transfer of NO_2.

Together this work shows that anthropogenic activity and multiphase reactions play a larger role than previously thought in determining the available oxidant budget, particularly in polluted coastal region in winter, which may have been even larger in the past. Global modeling work in GEOS-Chem by Wang et al. (2019) showed the global average annual impacts of including comprehensive chlorine chemistry in GEOS-Chem with results from two simulations;

one which included anthropogenic HCl emissions the global inventory compiled in 1999 by McCulloch et al. (1999), and one simulation which did not include these contributions. Given the trends discussed in Chapter 4 of how HCl emissions have decreased significantly in the past 20 years, for the model simulation year of 2015, unsurprisingly, they found that the global anthropogenic source of 6.7 Tg Cl a^{-1} greatly overestimated atmospheric observations of HCl over the US. They argue that this overestimated is because modern national inventories of anthropogenic HCl emissions in both China and the US are 6 to 7 times than lower than estimates given in McCulloch et al. (1999). Compared to a global source of 6.7 Tg Cl a^{-1} in 1990, in China modern inventories suggest emissions of 236 Gg Cl a^{-1} in 2012 [Liu et al., 2018] and in the US emissions of 69 Gg Cl a^{-1} in 2014 [US EPA, 2018].

Figure **5.1** Vertical profiles of HCl, nighttime $ClNO_2$, HOCl, and Cl_2 mixing ratios during the WINTER campaign over the eastern US and offshore in February–March 2015. Observations from Haskins et al. (2018) are shown as individual 1 min data points, with medians and 25th–75th percentiles in 500 m vertical bins. Measurements below the detection limit are treated as the median of 0 and detection limit. $ClNO_2$ data exclude daytime (10:00–16:00 local) when mixing ratios are near zero in both the observations and the model. Model values are shown as medians sampled along the flight tracks. Also shown are results from a sensitivity simulation including the anthropogenic chlorine inventory of McCulloch et al. (1999). *Figure from Wang et al., (2019)*. shows the over-estimate in the simulated concentrations of HCl from including a larger anthropogenic source from Wang et al., (2019). These results suggest that HCl concentrations over the WINTER domain could have been nearly double on average in the past, particularly below 1.5 km, which does have some impact on HOCl and Cl_2 concentrations in the bottom 500m of the model. Future insights on how decreases in the anthropogenic contributions of HCl

have impacted the prevalence of halogen initiated chemistry, could be gained by contrasting export of NO_x, the oxidant budget, and PM formation in a simulation utilizing the McCulloch inventory in 1999 compared to a model simulation with scaled down HCl emissions to match those in 2018.

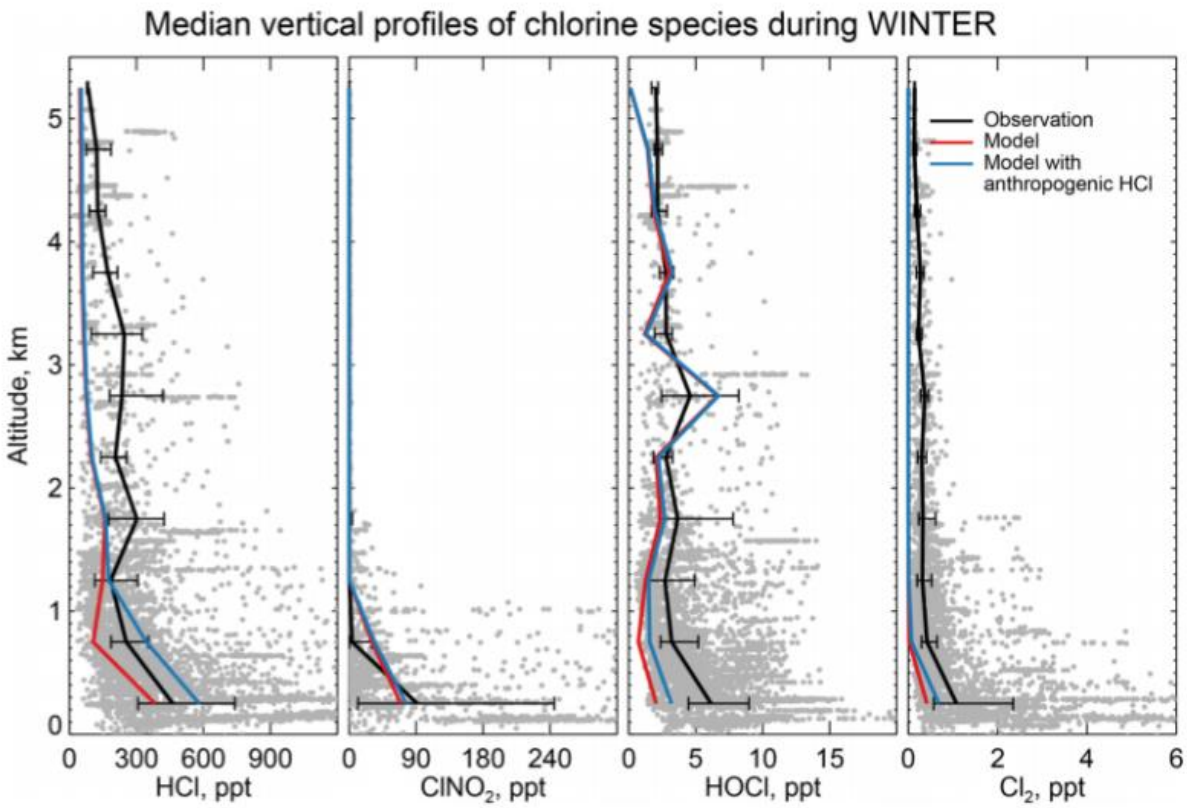

Figure 5.1 Vertical profiles of HCl, nighttime $ClNO_2$, HOCl, and Cl_2 mixing ratios during the WINTER campaign over the eastern US and offshore in February–March 2015. Observations from Haskins et al. (2018) are shown as individual 1 min data points, with medians and 25th–75th percentiles in 500 m vertical bins. Measurements below the detection limit are treated as the median of 0 and detection limit. $ClNO_2$ data exclude daytime (10:00–16:00 local) when mixing ratios are near zero in both the observations and the model. Model values are shown as medians sampled along the flight tracks. Also shown are results from a sensitivity simulation including the anthropogenic chlorine inventory of McCulloch et al. (1999). *Figure from Wang et al., (2019).*

5.2.1 *HONO*

Through simultaneous observations of HONO and pNO_3^-, I was able to provide the critical observational constraints on the production of HONO from pNO_3^- photolysis, a topic of continued intense debate (Ye et al., 2016; Romer et al., 2018). I showed that the ubiquity of HONO during winter in the troposphere is confined to, approximately, the lower 100m of the troposphere with minimal contributions to the oxidant budget within the marine boundary layer, even considering a pNO_3^- source. Furthermore, this analysis showed that considering pNO_3^- photolysis during WINTER with an enhancement factor (EF) of 300 would imply loss of HNO_3 so quickly that HNO_3 would become entirely depleted before the days end, at odds with direct observations, suggesting a lower EF is more appropriate.

Because observed HONO concentrations were often at or below the detection limit of CIMS during WINTER, we were not able to derive an EF from these observations. One limit of the simultaneous observations of HONO from the CIMS and pNO_3^- from the AMS's operation during WINTER was the particle inlet sampling cut off at D_p <1μm, which forced us to use sums of pNO_3^- from other instruments with lower time resolution, and which can be subject to contamination via acid displacement. Attempts to derive an EF from observations in the future would need to account for pNO_3^- on larger particles which are important for HONO production from this multiphase reaction. The difficulty in making inter-comparisons of AMS data with a cut off of D_p< 1μm to other particle data collected for D_p <2.5μm is not a new complaint, and development of a new lens to focus on larger particles is a topic of intense current interest within the AMS community (Peck et al., 2016;). Given these limitations in measuring both HONO and pNO_3, further efforts to derive an appropriate EF from direct observations are more likely to be successful at ground based stations (low altitudes) in nitrate rich environments where HONO

concentrations could exceed the 15pptv detection limit of the CIMS, and where the operation of an AMS with an aerodynamic lens that would allow analysis of larger particles is more feasible.

5.2.2 *High Time Resolution Refractory Chloride Measurements*

It is important to note that the AMS measurements of pCl^-, heavily relied upon in this work, typically do not include refractory Cl^- and thus contributions from NaCl. To support the conclusions drawn, it was critical to have PILS and UNH filter measurements of pCl^- to compare to, though differences in time resolution, size cut sampled, and degree of acid displacement contamination made firm comparisons difficult. While it is possible that certain AMS measurement methods may be able to tease out the degree to which observations include NaCl samples (Nuaaman et al., 2015) the development of a high frequency measurement of pCl^- which includes contributions from refractory NaCl, such as the Extractive Electrospray Ionization (Lopez-Hilfiker et al., 2019) would be highly useful in future campaigns looking to probe the multiphase chemistry of Cl^-. Such an analysis method that was also capable of scanning across different size distributions (discussed below) would be ideal. In the absence of such instrument capabilities or operational modes, it is critical for campaigns wanting to investigate $Cl_{y\ chemistry}$ to have an instrument which *does* include refractory particulate Cl^- contributions.

5.2.3 *Particle Composition Across the Size Distribution*

Developing observations and a more complete understating of particle composition, and degree of phase separation across the size distribution and how that varies in the ambient atmosphere is perhaps the largest research area, I have come to realize, that has the potential to

further progress our understanding of multiphase chemistry in the troposphere. Given that multiphase chemistry is what allows the cycling of Cl_y (and other halogens) to have such large impacts on the oxidant budget both upwind and downwind, such progress would undoubtedly advance quantifications of this chemistry in global models. Assumptions of internally mixed aerosol composition without phase separations should be tested, as these assumptions will have a significant impact upon calculated aerosol pH. Nearly all multiphase reactions in the troposphere of note are pH dependent and given our knowledge that particle composition does indeed change across the aerosol size distribution, we should expect aerosol pH to change across the size distribution, as well. For pCl^- particularly, this topic was an area of continued frustration for me, as readers will find a discussion about how assumptions about the phase state and mixing of pCl^- would impact the conclusions drawn in each chapter, herein. It is unclear how much and in what phase state pCl^- is present in within particles within the transition regime between internally mixed submicron aerosols, which may contain small amounts of pCl^- from thermodynamic partitioning of HCl, and large externally mixed sea salt particles. However, results from Chapter 3 indicate that particles large enough to still contain large masses of Cl^- and small enough to be transported longer distances and be impacted by other multiphase chemistry such as acid displacement, may be particularly important to low pH mobilization processes.

In a small project not described herein, I utilized an aerosol thermodynamics model to predict size resolved pH by assuming different compositions of various sized particles, like that shown in Chapter 3. I found that the size resolved pH differences were enough to drastically change the parameterized uptake of IEPOX based on the size of the particle. This result reinforced my conviction that instruments enabling particle composition measurements across the size distribution could have potential insights on multiphase chemistry well beyond halogen

chemistry that could advance the field.

Recently, McNamara et al., (2020) demonstrated that only a fraction of the particulate surface area contains chloride in an inland suburban area, and taking that inhomogeneous distribution of chloride concentrations across the particle surface area led to significantly lower predictions of $ClNO_2$ concentrations. Furthermore, they argue that road salt aerosol is the primary chloride aerosol source, accounting for 80–100% of $ClNO_2$ formation, at an inland urban area in the wintertime. This recent work underscores the impact that considering particle composition across the size distribution can have on heterogenous chlorine chemistry, with implications for other uptake processes that activate chlorine from the particle phase. Future work is needed to consider chloride content across the size distribution.

5.2.4 *Bromine & Other Halogens*

Of particular interest to me, is the degree to which WINTER CIMS observations provide insight into coupled bromine and chlorine chemistry, which would appear to be more globally significant to O_3 and OH concentrations than the immediate downwind impact of $ClNO_2$ in polluted marine regions, according the recent GEOS-Chem full halogen simulations in Wang et al., (2019). Peaks were fit within the CIMS during WINTER for Br_2, $BrNO_2$, HBr, HOBr and BrCl, with corresponding sensitivities reported in Lee et al., (2018). I suspect insights could be gained from analyzing the interplay between the observed bromine and chlorine compounds, particularly for BrCl, which to my knowledge, has not yet been done with the WINTER data set, outside of enhancements within powerplant plumes. Although HBr and HOBr are detected at the same nominal masses as two sulfur containing ions, SO_3I^- and SO_4I^-, within the CIMS respectively, analysis of the measurements of these compounds from the flights in cleaner

marine regions would be very interesting as it relates to which chemical cycles are most important for mobilizing Br^-.

5.3 REFERENCES

Haskins, J. D., Jaeglé, L., Shah, V., Lee, B. H., Lopez-Hilfiker, F. D., Campuzano-Jost, P., Schroder, J. C., Day, D. A., Guo, H., Sullivan, A. P., Weber, R., Dibb, J., Campos, T., Jimenez, J. L., Brown, S. S., and Thornton, J. A.: Wintertime Gas-Particle Partitioning and Speciation of Inorganic Chlorine in the Lower Troposphere Over the Northeast United States and Coastal Ocean, J. Geophys. Res.-Atmos., 123, 12897–12916, https://doi.org/10.1029/2018JD028786, 2018.

Keene, W. C., Aslam, M, Khalil, K., Erickson Iii, D. J., Mcculloch, A., Graedel, T. E., (1999). Composite global emissions of reactive chlorine from anthropogenic and natural sources: Reactive Chlorine Emissions Inventory. JOURNAL OF GEOPHYSICAL RESEARCH, 104(20), 8429–8440. https://doi.org/10.1029/1998JD100084

Lee, B. H., Lopez-Hilfiker, F. D., Veres, P. R., McDuffie, E. E., Fibiger, D. L., Sparks, T. L., et al. (2018). Flight deployment of a high-resolution time-of-flight chemical ionization mass spectrometer: Observations of reactive halogen and nitrogen oxide species. Journal of Geophysical Research: Atmospheres, 123, 7670– 7686. https://doi.org/10.1029/2017JD028082

Lopez-Hilfiker, F. D., Pospisilova, V., Huang, W., Kalberer, M., Mohr, C., Stefenelli, G., Thornton, J. A., Baltensperger, U., Prevot, A. S. H., and Slowik, J. G.: An extractive electrospray ionization time-of-flight mass spectrometer (EESI-TOF) for online measurement of atmospheric aerosol particles, Atmos. Meas. Tech., 12, 4867–4886, https://doi.org/10.5194/amt-12-4867-2019, 2019.

McNamara, S. M., Kolesar, K. R., Wang, S., Kirpes, R. M., May, N. W., Gunsch, M. J., … Pratt, K. A. (2020). Observation of Road Salt Aerosol Driving Inland Wintertime Atmospheric Chlorine Chemistry. ACS Central Science, 6(5), 684–694. https://doi.org/10.1021/acscentsci.9b00994

Nuaaman, I., Li, S.-M., Hayden, K. L., Onasch, T. B., Massoli, P., Sueper, D., Worsnop, D. R., Bates, T. S., Quinn, P. K., and McLaren, R.: Separating refractory and non-refractory particulate chloride and estimating chloride depletion by aerosol mass spectrometry in a marine environment, Atmos. Chem. Phys. Discuss., 15, 2085–2118, https://doi.org/10.5194/acpd-15-2085-2015, 2015.

Peck, J., Gonzalez, L. A., Williams, L. R., Xu, W., Croteau, P. L., Timko, M. T., … Smith, K. A. (2016). Development of an aerosol mass spectrometer lens system for PM2.5. *Aerosol Science and Technology*, *50*(8), 781–789. https://doi.org/10.1080/02786826.2016.1190444

Riedel, T. P., Wolfe, G. M., Danas, K. T., Gilman, J. B., Kuster, W. C., Bon, D. M., Vlasenko, A., Li, S.-M., Williams, E. J., Lerner, B. M., Veres, P. R., Roberts, J. M., Holloway, J. S., Lefer, B., Brown, S. S., and Thornton, J. A.: An MCM modeling study of nitryl chloride (ClNO2) impacts on oxidation, ozone production and nitrogen oxide partitioning in

polluted continental outflow, Atmos. Chem. Phys., 14, 3789–3800, https://doi.org/10.5194/acp-14-3789-2014, 2014.

Roberts, J. M., Osthoff, H. D., Brown, S. S., & Ravishankara, A. R. (2008). N2O5 Oxidizes Chloride to Cl2 in Acidic Atmospheric Aerosol. Science, 321(5892), 1059.

Roberts, J. M., Osthoff, H. D., Brown, S. S., Ravishankara, A. R., Coffman, D., Quinn, P., & Bates, T. (2009). Laboratory studies of products of N2O5 uptake on Cl- containing substrates. Geophysical Research Letters, 36, L20808. https://doi.org/10.1029/2009GL040448

Sarwar, G., & Bhave, P. V. (2007). Modeling the Effect of Chlorine Emissions on Ozone Levels over the Eastern United States. Journal of Applied Meteorology and Climatology, 46(7), 1009–1019. https://doi.org/10.1175/JAM2519.1

Wang, X., Jacob, D. J., Eastham, S. D., Sulprizio, M. P., Zhu, L., Chen, Q., Alexander, B., Sherwen, T., Evans, M. J., Lee, B. H., Haskins, J. D., Lopez-Hilfiker, F. D., Thornton, J. A., Huey, G. L., and Liao, H.: The role of chlorine in global tropospheric chemistry, Atmos. Chem. Phys., 19, 3981–4003, https://doi.org/10.5194/acp-19-3981-2019, 2019

Wetzel, G., Oelhaf, H., Kirner, O., Friedl-Vallon, F., Ruhnke, R., Ebersoldt, A., Kleinert, A., Maucher, G., Nordmeyer, H., and Orphal, J.: Diurnal variations of reactive chlorine and nitrogen oxides observed by MIPAS-B inside the January 2010 Arctic vortex, Atmos. Chem. Phys., 12, 6581–6592, https://doi.org/10.5194/acp-12-6581-2012, 2012.

Wolfe, G. M., Kaiser, J., Hanisco, T. F., Keutsch, F. N., de Gouw, J. A., Gilman, J. B., Graus, M., Hatch, C. D., Holloway, J., Horowitz, L. W., Lee, B. H., Lerner, B. M., Lopez-Hilifiker, F., Mao, J., Marvin, M. R., Peischl, J., Pollack, I. B., Roberts, J. M., Ryerson, T. B., Thornton, J. A., Veres, P. R., and Warneke, C.: Formaldehyde production from isoprene oxidation across NOx regimes, Atmos. Chem. Phys., 16, 2597–2610, https://doi.org/10.5194/acp-16-2597-2016, 2016.

Yienger, J. J., Klonecki, A. A., Levy, H., Moxim, W. J., & Carmichael, G. R. (1999). An evaluation of chemistry's role in the winter-spring ozone maximum found in the northern midlatitude free troposphere. Journal of Geophysical Research, 104(D3), 3655–3667. https://doi. org/10.1029/1998JD100043

Zhao, Y., Chan, J. K., Lopez-Hilfiker, F. D., McKeown, M. A., D'Ambro, E. L., Slowik, J. G., Riffell, J. A., and Thornton, J. A.: An electrospray chemical ionization source for real-time measurement of atmospheric organic and inorganic vapors, Atmos. Meas. Tech., 10, 3609–3625, https://doi.org/10.5194/amt-10-3609-2017, 2017.

APPENDIX

List of Coauthors/Contributors

Portions of Chapter 1 have been previously published:

J. D. Haskins[1], L. Jaeglé[1], V.Shah[1††], B. H. Lee[1], F. D. Lopez-Hilfiker[1†], P. Campuzano-Jost[5.6], J.C. Schroder[5,6], D.Day[5,6], H.Guo[10], A.Sullivan[9], R. Weber[10], J. Dibb[14], T. Campos[7], J. L. Jimenez[5,6], S. S. Brown[6,13], J.A. Thornton[1] (2018). *Wintertime gas-particle partitioning and speciation of inorganic chlorine in the lower troposphere over the Northeast United States and Coastal Ocean*. Journal of Geophysical Research: Atmospheres, 123, 12,897–12,916. https://doi.org/10.1029/2018JD028786

Chapter 2 has been previously published:

J. D. Haskins[1], F. D. Lopez-Hilfiker,[1†] B. H. Lee,[1] V. Shah,[1††] G. M. Wolfe,[2,3] J. DiGangi,[4] D. Fibiger,[5,13 †††] E. E. McDuffie,[5,6,13 ‡] P. Veres,[5] J. C. Schroder,[5,6] P. Campuzano-Jost,[5,6] D. A. Day,[5,6] J. L. Jimenez,[5,6] A. Weinheimer,[7] T. Sparks,[8] R. C. Cohen,[8] T. Campos,[7] A. Sullivan,[9] H. Guo,[10] R. Weber,[10] J. Dibb,[11] J. Green,[12] M. Fiddler,[12] S. Bililign,[12] L. Jaeglé,[1] S. S. Brown,[6, 13] J. A. Thornton[1] (2019b). *Anthropogenic Control Over Wintertime Oxidation of Atmospheric Pollutants*. Geophysical Research Letters, 46(24), 14826–14835. https://doi.org/10.1029/2019GL085498

Chapter 3 was previously published:

J. D. Haskins[1], B. H. Lee[1], F.D. Lopez-Hilifiker[1†], Q. Peng[1], L.Jaegle[1], J. M. Reeves[7], J. C. Schroder[5,6], P. Campuzano-Jost[5,6], D. Fibiger[5,13†††], E.E. McDuffie[5,6,13‡], J. L. Jimenez[5,6] , S. S. Brown[6,13], J. A. Thornton[1] (2019a). *Observational constraints on the formation of Cl_2 from the reactive uptake of $ClNO_2$ on aerosols in the polluted marine boundary layer*. Journal of Geophysical Research: Atmospheres, 124, 8851–8869. https://doi.org/10.1029/2019JD030627

Chapter 4 is currently in preparation for publication:

J.D. Haskins[1], L. Jaeglé[1], J.A. Thornton[1] (2020). *Significant U.S. decreases in deposition of anthropogenic chloride from emission controls*

Coauthor/Contributor Affiliations:

[1] Department of Atmospheric Sciences, University of Washington, Seattle, WA USA

[2] Joint Center for Earth Systems Technology, University of Maryland, Baltimore, MD USA
[3]Atmospheric Chemistry & Dynamics Laboratory, NASA GSFC, Greenbelt, MD USA
[4] NASA Langley Research Center, Hampton, VA USA
[5] Cooperative Institute for Research in Environmental Sciences, University of Colorado, Boulder, CO, USA
[6] Department of Chemistry, University of Colorado, Boulder, CO USA
[7] Earth Observing Laboratory, National Center for Atmospheric Research, Boulder, CO USA
[8] Department of Chemistry, University of California, Berkeley CA USA
[9] Department of Atmospheric Sciences, Colorado State University, Fort Collins, CO USA
[10] School of Earth and Atmospheric Sciences, Georgia Institute of Technology, Atlanta, GA USA
[11] Department of Earth Sciences, University of New Hampshire, Durham, NH USA
[12] Department of Physics, North Carolina A&T State University, Greensboro, NC USA
[13] Chemical Sciences Division, NOAA Earth System Research Laboratory, Boulder, CO USA
[14] College of Engineering & Physical Science, University of New Hampshire, Durham, NH, USA

† Now at Tofwerk AG, Switzerland
†† Now at Harvard School of Engineering and Applied Sciences, Harvard University, Cambridge, USA
††† Now at California Air Resources Board, Sacramento, USA
‡ Now at the Department of Physics and Atmospheric Science, Dalhousie University, Halifax, NS, Canada

Vita

Jessica D. Haskins was born in central Georgia and found her interest in Atmospheric Chemistry in 7th grade, with her Social Studies Fair topic, “What are the harmful effects of auto emissions and how can we prevent them?”. After continuing her interest in the topic throughout high school, and finding a passion for chemistry, she quickly escaped Georgia and majored in Earth, Atmosphere, and Planetary Sciences at MIT, where she successfully lost her southern accent and became the first undergraduate at MIT to be awarded a minor in Atmospheric Chemistry. Working with mentor Susan Solomon for 2 years on research involving chlorine chemistry in the stratosphere as an undergraduate, Jessica took Susan’s advice and applied to the University of Washington for graduate school. Being particularly interested in learning to integrate observations and models, Jessica was lucky to find two advisors with expertise in each. Though the Cascades, Olympic Peninsula, and Seattle’s thriving brass band community provided Jessica with welcome distractions, it was COVID-19 which forced her to finish her Ph’D in 2020 during quarantine.